Development of a Small Ring Specimen Cyclic Testing Technique

Julija Kazakeviciute

2021-03-07

Abstract

Efficient system design is important in engineering in order to reduce costs, waste, and energy consumption. The goal of efficient system design is to maximize the use of material. This means ensuring critical material elements are not underloaded such that they perform no real function while simultaneously ensuring no material element is overloaded such that it prematurely fails. Foundational to make this type of assessment is a detailed understanding of material properties informed by robust characterization methods. Traditionally this required a large amount of testing to be performed which is expensive and uses a large amount of source material. Small specimen testing is an active area of research that replaces large conventional specimens with smaller novel designs, thereby allowing for a more efficient use of source material, localized material property investigations, and the development of larger test databases. The increased volume of data that small specimen testing enables could improve confidence in predictive models by allowing for more accurate representation of statistical measures, however at present small specimen testing is used simplistically. The present work advances small specimen testing by developing experimental and analytical methods to determine fundamental material response characteristics.

Historically small specimens have been used in industry to rank the performance of in-service components and acquire simple material properties, such as yield stress and ultimate tensile strength. In order to further the use of small specimens, their capabilities should be extended for more complex material properties, such as full elastic-plastic behaviour and response to cyclic loading. A large number of components in mechanical systems experience cyclic loading in service, making it necessary to fully characterize the response for flexible operation. Small ring specimens were initially developed for creep testing. Due to their easy alignment, manufacture and high testing sensitivity they were chosen for the development of tensile and cyclic testing techniques.

Aerospace aluminium alloys 7175-T7153, 2014A-T6, 6082-T6 and a power plant chromium steel P91 were chosen for tensile testing as power generation and aerospace industries particularly benefit from small specimen testing. Effective operation in the power generation industry

requires maintenance inspection of in-service components, allowing a small amount of material to be removed for testing in order to not compromise the integrity of the component. Aerospace components, such as turbine blade roots, are too small for standard specimens. The temperatures and loading rates for standard tests were chosen to compliment established tests, as a database was needed for comparison with small ring testing results. As copper is commonly used for the development of fatigue testing techniques and is well characterized in the literature, it was chosen for the development of a cyclic small ring specimen testing technique.

Despite the many advantages, small ring specimen tensile testing also poses challenges, especially for data interpretation. Unlike standard test results, small ring specimen test results cannot be easily correlated to material properties due to a combination of material and geometry non-linearity. Small ring specimens were tested in tension under conditions corresponding to standard tests so that the response could be compared. The trends for rate dependency and failure were found to agree, also, small ring specimens were found to be easier to mount and keep aligned when setting up the test, resulting in around 20 % lower scatter. Analytical and finite element models were developed for interpreting the small ring specimen tensile test results. The analytical model, based on Euler-Bernoulli beam theory, was suitable for finding Young's modulus. The FEA model (representative of small ring specimen tensile test results) was used to evaluate how varying material and geometry parameters affects the results. Several methods to interpret the small ring specimen tensile test results using the FEA model were investigated, with inverse analysis proving to be superior. It was found to be capable of calculating Young's modulus and yield stress within 10 %, with the hardening behaviour evaluated within 20 % of standard test results. This is similar to other established small specimen testing methods.

An additional challenge when developing the small ring specimen cyclic testing technique was that the tensile setup was not suitable for fully reversible loading. This required a new setup to be designed and a testing methodology to be developed, with displacement control used to cycle the ring. The shape of the small ring hysteresis loops was similar to standard specimen hysteresis loops. The small ring specimen cyclic test peak loads increased for up to two cycles, then began to drop until the specimen eventually failed. Repeatability was good, the results also showed potential for evaluating fatigue life, as the shape of the life curve was similar to the standard life curve, with increasing loading amplitude reducing the number of cycles to failure. Weak correlations were noted between the loading amplitude and a variety of parameters from small ring specimen cyclic test results, such as maximum tensile and compressive forces.

Small ring specimen tensile testing technique was successfully developed, with capability to calculate bulk material stress-strain behaviour which can be described using a Ramberg-Osgood material model. The methodology for testing small ring specimen under cyclic loading was also developed, showing small ring specimen cyclic testing technique to be promising for evaluating cyclic plasticity and fatigue properties. Cyclic loading data interpretation is difficult due to the complex evolution of the stress state in the small ring specimen as it is being loaded and uncertainty in contact conditions, which need to be investigated and quantified. Developing a representative model of the small ring specimen under cyclic loading would be the first step towards it.

Acknowledgements

I would like to thank my supervisors, Dr Chris Hyde, Dr Davide De Focatiis and Dr James Rouse for their support.

I would like to thank the IMPaCT CDT staff, in particular Prof Graham McCartney and Dr Katy Voisey.

I would also like to thank Rolls-Royce plc. and Engineering and Physical Sciences Research Council (EPSRC) for funding my research.

For technical support I would like to thank Mr Shane Maskill, Mr Andrew Plummer and Mr Kieran Orange.

Lastly, I would like to thank my friends and family.

Nomenclature

Roman Symbols

A - cross-sectional area

a - transition offset

a_c - centred transition offset

a_d - distance in compliance calculations

a_{el} - semi-major radius of the ellipse

A_{gauge} - equivalent gauge section

A_{tot} - total cross-sectional area for compliance calculations

b - speed of transition

B - integration constant for compliance

b_c - centred speed of transition

b_d - length of a flat surface for compliance calculations

b_{di} - distance in compliance calculations

b_{el} - semi-minor radius of the ellipse

b_I - width for the second moment of are calculations

b_i - isotropic hardening parameter

b_r - lateral thickness of the ring

C - kinematic hardening model parameter

c - initial slope

c_c - centred initial slope

c_f - fatigue ductility exponent, empirical constant

D - integration constant for compliance

d - second slope

d_c - centred second slope

d_r - radial thickness of the ring

E - Young's modulus

E_c - centred Young's modulus

E_{new} - recalculated Young's modulus

F - applied force

G - shear modulus

h - height for calculating the second moment of area

I - second moment of area

L - length

L' - distance between the centres of the pins, when offset misalignment is considered

L_{gauge} - equivalent gauge length

L_{lat1} - original lateral distance

L_{lat2} - final lateral distance

L_{long1} - final longitudinal distance

L_{long2} - original longitudinal distance

M_0 - reaction moment

M_1 - reaction moment for compliance calculations

M_θ - moment at angle θ

n - Ramberg-Osgood material model parameter

N_f - half of the load reversals to failure for low cycle fatigue

n_r - offset between centroid and neutral axis

P - applied load

Q - dummy load for calculating horizontal displacement

Q_∞ - saturation stress for cyclic loading

R - ratio between minimum and maximum stress for cyclic loading

R_1 - initial radius

R_2 - final radius

R_{curve} - radius of curvature

R_i - internal radius of the ring

R_{in} - radius of the hole in the cyclic loading setup

R_n - radius of the neutral axis

R_o - external radius of the ring

R_{out} - radius of the lower end of the cyclic loading setup

r_{pin} - radius of the pin

R_r - radius of the ring

r_s - radius of the cross-section of the standard creep specimen

S - internal shear force

T - internal tensile force

U - left-singular vectors

U_b - bending strain energy

u_{hb} - bending contribution to horizontal displacement

u_{hs} - shear contribution to horizontal displacement

u_{ht} - tensile contribution to horizontal displacement

u_{htot} - total horizontal displacement

U_s - shear strain energy

U_t - tensile strain energy

u_{vb} - bending contribution to vertical displacement

u_{vs} - shear contribution to vertical displacement

u_{vt} - tensile contribution to vertical displacement

u_{vtot} - total vertical displacement

V - right-singular vectors

W - data projected onto principal components

w - pin bending deformation

w_d - distance between flat surfaces for compliance calculations

y - distance from the neutral axis

Greek Symbols

α - parameter from Ramberg-Osgood material model

$\boldsymbol{\alpha}$ - backstress tensor

$\dot{\boldsymbol{\alpha}}$ - rate of the backstress tensor

β_{OLS} - coefficients calculated using ordinary least squares

β_{PCA} - coefficients calculated using principal component analysis

γ - kinematic hardening parameter

γ_{PCA} - intermediate coefficients calculated using principal component analysis

Δ - singular values

$\Delta\varepsilon_p$ - plastic strain range

$\Delta\sigma$ - stress range during cyclic loading

ε - strain

$\varepsilon_{bending}$ - bending strain

ε_{eng} - engineering strain

ε'_f - empirical constant, fatigue ductility coefficient

ε_{lat} - lateral strain

ε_{long} - longitudinal strain

$\bar{\varepsilon_{pl}}$ - equivalent plastic strain

$\dot{\bar{\varepsilon_{pl}}}$ - equivalent plastic strain rate

ε_{true} - true strain

$\varepsilon_{uniaxial}$ - uniaxial strain

ε_X - strain in the X direction

ε_Y - strain in the Y direction

ε_Z - strain in the Z direction

ζ - angle between ξ and the x-axis

θ - angle

θ' - angle when calculating offset misalignment

ν - Poisson's ratio

ξ - distance between the ends of the arc

σ - stress

$\boldsymbol{\sigma}$ - second order stress tensor

σ_0 - size of the yield surface

$\sigma|_0$ - size of the yield surface at zero plastic strain

$\sigma_1, \sigma_2, \sigma_3$ - principal stresses

$\sigma_{11}, \sigma_{22}, \sigma_{33}$ - stress components

σ_a - cyclic loading stress amplitude

σ_{eng} - engineering stress

σ_{MAX} - maximum stress per cycle

σ_{MEAN} - mean stress

σ_{MIN} - minimum stress per cycle

σ_{true} - true stress

σ_X - stress in the X direction

σ_y - yield strength

σ_Y - stress in the Y direction

σ_Z - stress in the Z direction

$\tau_{12}, \tau_{23}, \tau_{31}$ - shear stresses

ϕ - tangent to the ellipse

Abbreviations

Bal - Balance

LVDT - Linear Variable Differential Transformer

MAPE - Mean Average Percentage Error

OLS - Ordinary Least Squares

PCA - Principal Component Analysis

PCR - Principal Component Regression

Contents

1 Introduction

1.1 Background

Small specimens are specimens that are smaller than the specimens conventionally used to test the material properties for the particular application. For example, if the standard specimen is a whole railway axle, anything smaller than that could be considered a small specimen. Usually, this term is applied to specimens which are smaller than standard specimens used to test the relevant material properties, such as tensile properties, cyclic plasticity or fatigue.

Small specimen testing is becoming increasingly relevant in industry and new capabilities are continuously being developed for identifying a wide range of material properties. Generally, small specimens are used in situations where there is insufficient material to make full size specimens, where handling full size specimens is undesirable or when properties of a small amount of material are of interest.

There could be insufficient material to make full size specimens when a new material is being developed, as due to large costs only small amounts of material are initially made. Another reason could be that a part of an in-use component is tested, such as when a scoop sample is taken from a steam pipe. Sometimes the components, the properties of which are of interest, are too small to make a full size specimen, for example the airfoil parts of the service-exposed gas turbine blades, requiring to reduce the size of the specimen tested.

Handling full size specimens may be undesirable when irradiated material is being tested, as irradiating large amounts of material might be difficult in test reactors due to the test reactor size limits, also, transporting large amounts of irradiated materials is a safety issue. Due to in-service conditions, sometimes materials need to be tested in combustible liquids, so small specimens need to be used in order to minimize the amount of liquid needed. When precise temperature control is needed, such as when testing in cryogenic temperatures, small specimens are preferable, as temperature control on a small amount of material is easier.

Properties of small components may be of particular interest when the effect of a coating is investigated, such as when fatigue performance of nitrided small gear teeth is investigated. Some processing techniques, such as spot welding, result in locally changed properties. In order to investigate them specifically small specimens have to be used. Another reason to use small specimens would be when single crystal properties are investigated, for example, when the effect of loading on the activation of slip systems is of interest. Currently small specimens are mostly used in power generation, nuclear and aerospace industries, however, they usually do not replace standard specimen testing only supplement it.

An important challenge in small specimen testing is that much of it depends on correlating force-displacement measurements to stress-strain states in non-uniaxial load conditions. Correlations are often valid for only one material (equivalent gauge sections and lengths depend on small specimen stiffness rather than simply geometry), so new ones must be developed for different materials (for example, different correlations for steels and copper alloys). Generally, properties can be directly obtained from sub-size standard specimens, while all other specimens (such as small punch specimens) require correlations in order to get information comparable to data from standard specimens (i.e. uniaxial equivalent results). Creep is the most commonly researched material property, followed by fracture, then tensile properties, fatigue and lastly crack growth.

Small ring specimens were developed by Hyde and Sun at the University of Nottingham as small specimens for creep testing [1]. In comparison to other commonly used small specimen techniques for creep testing (indentation testing, small punch testing and sub-size standard specimen testing), they have a long equivalent gauge length, meaning high sensitivity for creep strain, is easy to manufacture, and align as they are self aligning [1].

1.2 Thesis Layout

The thesis begins with a Literature review section, which gives a general overview of microstructures, how they affect material properties, then a general overview of tensile material properties, cyclically loaded material properties and fatigue properties, as well as the factors influencing the material behaviour relevant to this thesis. As well as that, standard specimen testing techniques for tensile and cyclic/fatigue testing are discussed, as well as the small specimen testing techniques used by other researchers for a wide variety of purposes.

Methodology follows, which describes the established techniques used in this project, including materials, specimens, microscopy, as well as the established testing techniques for tensile testing and cyclic testing.

The chapters on tensile testing (Chapter 4 and Chapter 5) are concerned with the small ring tensile modelling and testing, comparing the results and drawing parallels between the conventional and ring results. The chapter on tensile modelling (Chapter 4) is concerned with making a representative model, using that model to evaluate how varying material and geometry model parameters affect the force-displacement curves. The chapter on tensile testing and data interpretation (Chapter 5) describes the small ring specimen testing methodology, results, the development several interpretation methods and evaluation of their performance on experimental results.

Similarly to how the chapters on the tensile small ring loading are structured, the chapters on cyclic small ring loading are structured. The chapter on cyclic modelling (Chapter 6) talks about the representative model of the small ring specimen under cyclic loading, how varying material and geometry parameters affects the results. The chapter on cyclic testing (Chapter 7) has conventional cyclic testing results, the development of the small ring specimen cyclic testing technique and setup, then it shows the test results and the trends in them, as well as drawing parallels between conventional and small ring cyclic test results alongside with discussing the development of an interpretation technique.

Afterwards an overview of conclusions and future work about both small ring specimen tensile loading and cyclic loading is given, with a focus on what future work is useful to expand on which objective of the project.

2 Literature Review

2.1 Introduction

When a novel small specimen cyclic testing technique is being developed, it is important to have an overview of relevant material behaviour and previously used small specimen testing techniques. A small ring specimen tensile testing technique had to be developed as a step towards developing a small ring specimen cyclic testing technique, similarly to how other small specimen cyclic testing techniques were extensions of small specimen tensile testing techniques.

Crystalline material structure is important to understand, as the small specimen testing technique being developed is for testing metallic materials, which usually have crystalline structures. General material tensile behaviour, as well as conventional methods to test the materials to acquire it, have to be understood as background knowledge to appreciate the complexity of small specimen tensile testing techniques.

The same reasoning applies to understanding cyclic and fatigue material behaviour, as well as the methods used to acquire it. Then, small specimen tensile, cyclic and fatigue testing techniques are reviewed to appreciate the work already gathered in this field. As the small ring specimen tensile and cyclic testing techniques are based on existing small ring specimen creep testing technique, it is reviewed as well.

2.2 Background on Crystalline Materials

Different types of materials are used for various engineering applications: metal alloys, ceramics, polymers and others, with metal alloys being particularly relevant. Varying the composition and the processing method can change the microstructure, which largely governs the material behaviour [2].

Metal alloy structures can be categorized into crystalline and amorphous. Crystalline structures are orderly, with a unit cell repeated throughout the material, while amorphous structures lack that order. In metallic materials FCC (face-centered-cubic) and BCC (body-centered-cubic) unit cells (shown in Figure 2.1) are common [3].

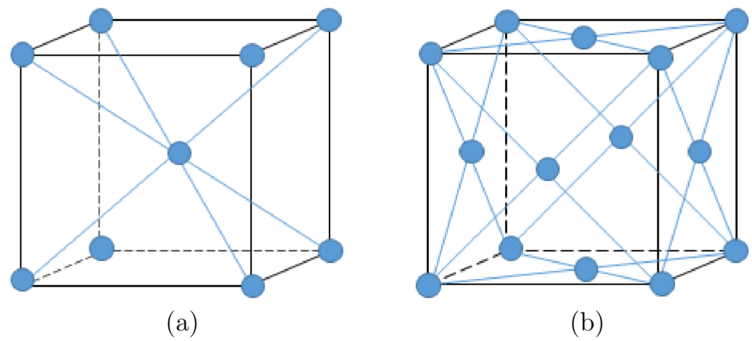

Figure 2.1: (a) BCC (body-centered-cubic) crystal cell; (b) FCC (face-centered-cubic) crystal cell

When metal alloys solidify, crystals nucleate and grow into grains. If grains that impinge on each other during growth have different orientations a grain boundary forms, illustrated in Figure 2.2 [3]. Polycrystalline materials with the grains randomly oriented tend to have largely isotropic properties, with a very small amount of anisotropy, while materials with grains oriented in one direction or single crystals tend to have anisotropic properties [4].

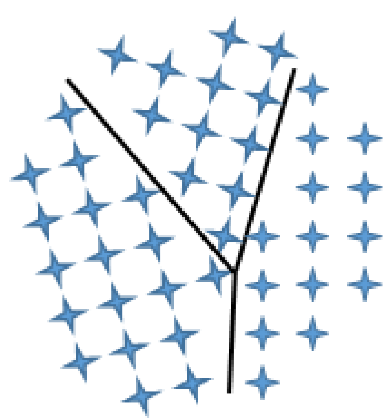

Figure 2.2: Grains with different orientations touching and forming grain boundaries.

Crystal structures usually are not perfect, they have defects. The defects can be classified into point defects, such as vacancies or self-interstitials, line defects (dislocations), planar defects, such as stacking faults, and volume defects, such as voids. The presence of vacancies makes it easier for dislocations to move as less material needs to be displaced. Dislocations are extra half-planes of atoms in the otherwise orderly crystal structure. They enable the deformation of the material without breaking the crystal structure. Dislocations are generated when material is deformed and stresses are introduced. Planar defects can also be grain boundaries, which impede dislocation motion due to misorientation between grains. Voids can be formed during solidification or due to clustering of dislocations and they play an important part during ductile fracture, when voids coalesce and material tears [4].

2.3 Mechanical Response of Materials

2.3.1 Monotonic Behaviour

Elastic Behaviour When a material is deformed the dimensions of it change. Strain is the measure of how much the dimensions of the body change when a load is applied to it, the ratio of the change in the dimension to the original dimension, illustrated by Equation 2.1, where ε is strain, ΔL is the change in length and L is the original length, and Figure 2.3 [5].

$$\varepsilon = \frac{\Delta L}{L} \tag{2.1}$$

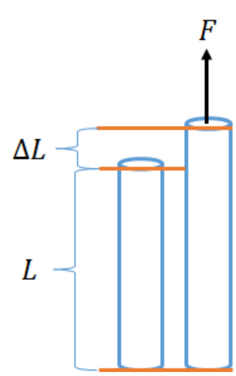

Figure 2.3: Illustration of strain. Change in length results in strain.

Stress is the measure of applied force over the unit cross-sectional area, it is illustrated by Equation 2.2, where σ is stress, F is the applied load and A is the cross-section [5]. It results from a body being deformed.

$$\sigma = \frac{F}{A} \tag{2.2}$$

Initial deformation is elastic, which means that when the load is removed the material returns to its original shape and no residual stresses remain. Young's modulus describes the elastic behaviour of a material, it is the coefficient of proportionality between stress and strain on the initial part of the stress-strain curve, illustrated by Equation 2.3, where E is Young's modulus, and Figure 2.4. The equation is also called Hooke's law [6].

$$E = \frac{\sigma}{\varepsilon} \tag{2.3}$$

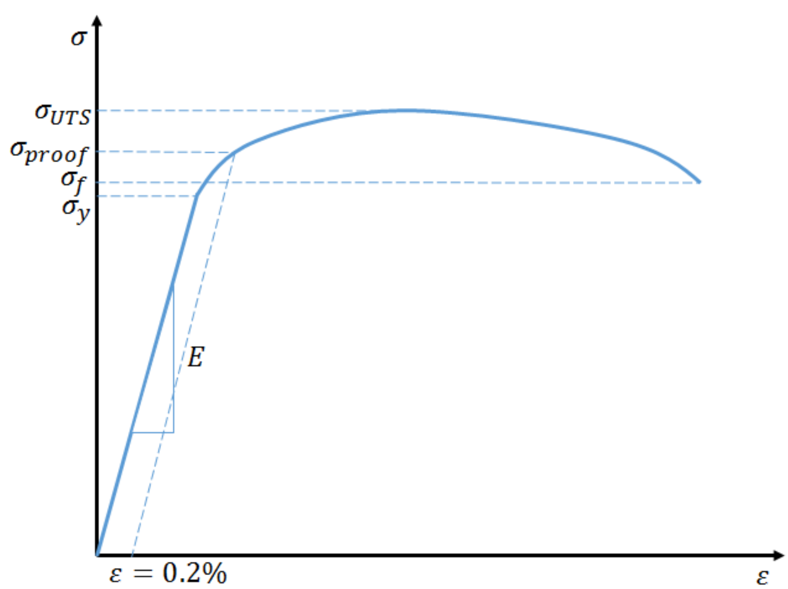

Figure 2.4: Stress-strain curve.

Generally when a body is strained in one direction, it develops a strain in other two directions as a reaction. This phenomenon is described by Poisson's ratio and illustrated by Equation 2.4, where ν is Poisson's ratio, ε_{lat} is lateral strain and ε_{long} is longitudinal strain, and Figure 2.5 [7]. If the body shown is stretched longitudinally it contracts in the other two dimensions proportionally to Poisson's ratio. This concept also results in a 3 dimensional version of Hooke's law, shown in

Equation 2.5 to 2.7.

$$\nu = \frac{\varepsilon_{lat}}{\varepsilon_{long}} = \frac{\frac{L_{lat1}-L_{lat2}}{L_{lat1}}}{\frac{L_{long2}-L_{long1}}{L_{long2}}} \tag{2.4}$$

$$\varepsilon_x = \frac{1}{E}\left(\sigma_x - \nu\left(\sigma_y + \sigma_z\right)\right) \tag{2.5}$$

$$\varepsilon_y = \frac{1}{E}\left(\sigma_y - \nu\left(\sigma_x + \sigma_z\right)\right) \tag{2.6}$$

$$\varepsilon_z = \frac{1}{E}\left(\sigma_z - \nu\left(\sigma_y + \sigma_x\right)\right) \tag{2.7}$$

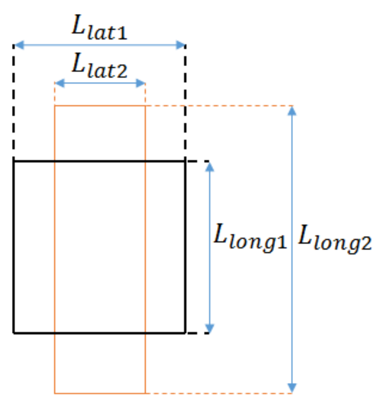

Figure 2.5: Poisson's ratio. Due to a load applied in the longitudinal direction the dimensions in both lateral and longitudinal directions change.

Hooke's law stops being valid when material yields. The point on the stress-strain curve where it occurs is called the yield strength. When it not exactly clear where that point is, proof stress is used instead. It can be at either 0.1 % or 0.2 % plastic strain, and is determined by drawing a line parallel to the elastic line from the selected strain value and the point where the line intersects the stress-strain curve proof stress is identified [5].

For yield to occur the stress state in the material has to meet a yield criterion. There are several yield criteria commonly used, such as von Mises (illustrated by Equation 2.8) [8] and Tresca (illustrated by Equations 2.9 to 2.11) [9]. The comparison of them is shown in Figure 2.6, yield occurs when the stress is outside of the boundaries drawn by the yield criteria. If stress in one direction is significantly higher than in other two uniaxial yield can be used.

$$\sigma_y^2 = \frac{1}{2}\left((\sigma_{11}-\sigma_{22})^2 + (\sigma_{22}-\sigma_{33})^2 + (\sigma_{33}-\sigma_{11})^2 + 6\left(\tau_{12}^2+\tau_{23}^2+\tau_{31}^2\right)\right) \tag{2.8}$$

$$|\sigma_1 - \sigma_2| > \sigma_y \tag{2.9}$$

$$|\sigma_2 - \sigma_3| > \sigma_y \tag{2.10}$$

$$|\sigma_3 - \sigma_1| > \sigma_y \tag{2.11}$$

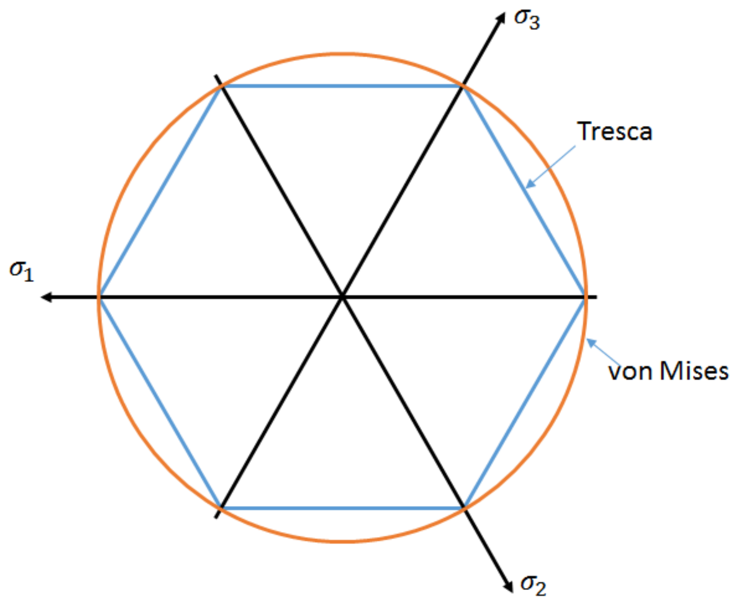

Figure 2.6: Illustration of von Mises and Tresca yield criteria.

Plastic Behaviour The material behaviour after yielding is called plastic behaviour, as when the material is unloaded it does not return to its initial state but remains deformed. The combination of elastic and plastic behaviour exhibited by the material as it is loaded until failure is usually described by a stress-strain curve. The stress-strain curve can be represented in two ways: engineering stress-strain and true stress-strain, both shown in Figure 2.7. Engineering stress-strain values are calculated with respect to the original dimensions of the body, while true stress-strain values are calculated with respect to the deformed dimensions of the body, resulting from previous load increments. Engineering and true stress-strain values relate to each other according to Equations 2.12 and 2.13. They look similar until the peak in the engineering stress-strain curve then diverge significantly [5]. During conventional material testing engineering stress-strain curves are acquired, they have to be converted to true stress-strain curves in order to fit material models to them. This is because engineering stress-strain curves are dependent on the geometry of the specimen used, while material models describe geometry independent material behaviour.

$$\varepsilon_{true} = ln\left(1 + \varepsilon_{eng}\right) \tag{2.12}$$

$$\sigma_{true} = \sigma_{eng}\left(1 + \varepsilon_{eng}\right) \tag{2.13}$$

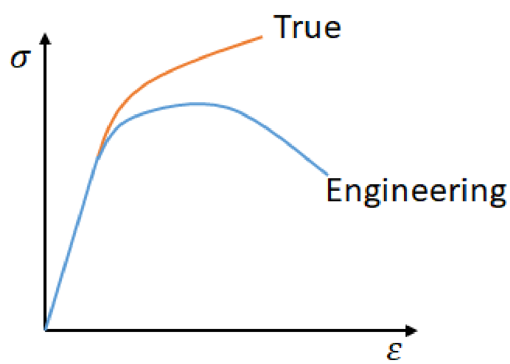

Figure 2.7: The difference between engineering and true stress-strain curves. Engineering values are in blue, true values are in orange.

The peak in the engineering stress-strain curve is the ultimate tensile strength (UTS). At that point necking, a localized reduction in area, starts to occur, which concentrates the stress at the neck causing a non-uniform stress state [5].

The end of the engineering stress-strain curve is where the material fails, the point characterized by fracture strength and fracture strain [5]. Some other tensile material properties are ductility (the area under the stress-strain curve), reduction in area and elongation to failure [5].

Ramberg-Osgood material model can be used to describe a true stress-strain curve. It is shown in Equation 2.14, where n and α are Ramberg-Osgood material model parameters. Parameter α is also known as the yield offset and the same stress-strain curve can be described by numerous sets of parameters. To describe the stress-strain curve with a unique equation one of the parameters of yield stress, n and α needs to be fixed.

$$\varepsilon = \frac{\sigma}{E} + \alpha \frac{\sigma}{E} \left(\frac{\sigma}{\sigma_y} \right)^{n-1} \tag{2.14}$$

2.3.2 Cyclic Behaviour

Fatigue is cumulative damage due to repeated cyclic loading. When describing the cycling program the maximum stress (σ_{MAX}), minimum stress (σ_{MIN}), mean stress (σ_{MEAN}) and stress amplitude (σ_a) are of interest. They are illustrated in Figure 2.8. The equations used to calculate them are Equations 2.15, 2.16, 2.17. Another factor used to describe the cycling is R ratio, calculated according to Equation 2.18 [5]. Fully reversed cyclic loading would have the same absolute values of maximum and minimum stress, zero mean stress and the R ratio of -1.

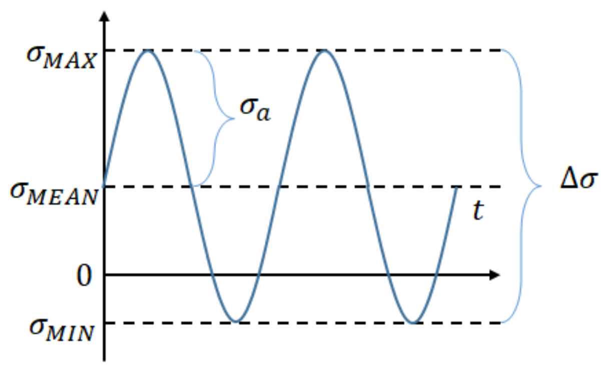

Figure 2.8: Illustration of the factors describing cyclic loading. t is time, σ_{MAX} is maximum stress, σ_{MIN} is minimum stress, σ_a is the stress amplitude, σ_{MEAN} is the mean stress and $\Delta\sigma$ is the stress range.

$$\Delta\sigma = \sigma_{MAX} - \sigma_{MIN} \tag{2.15}$$

$$\sigma_a = \frac{\sigma_{MAX} - \sigma_{MIN}}{2} \tag{2.16}$$

$$\sigma_{MEAN} = \frac{\sigma_{MAX} + \sigma_{MIN}}{2} \tag{2.17}$$

$$R = \frac{\sigma_{MIN}}{\sigma_{MAX}} \tag{2.18}$$

The phenomenon of stress increasing with increasing strain is called strain hardening, and decreasing stress with increasing strain is called strain softening. Both are illustrated in Figure 2.9. These terms can be used to describe both monotonic and cyclic behaviour and different parts of the monotonic or cyclic stress-strain curve can be described using different terms, for example, strain hardening up to UTS, then strain softening between UTS and failure.

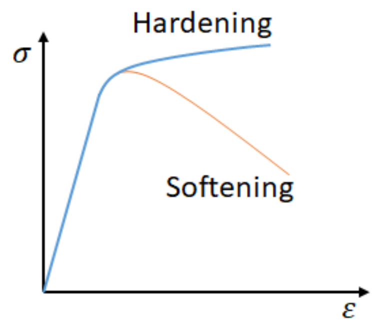

Figure 2.9: Illustration of strain hardening (blue) and strain softening (orange).

There are two main mechanisms used to describe hardening: isotropic hardening and kinematic hardening. Isotropic hardening manifests by the area enclosed by the yield surface increasing as shown in the Figure 2.10. Kinematic hardening manifests by the area enclosed by the yield surface not changing, but moving instead, as shown in Figure 2.11 [10]. Most materials exhibit a combination of these two behaviours, and it can described by a combined hardening model, shown in Equations 2.19 and 2.20 [11, 12]

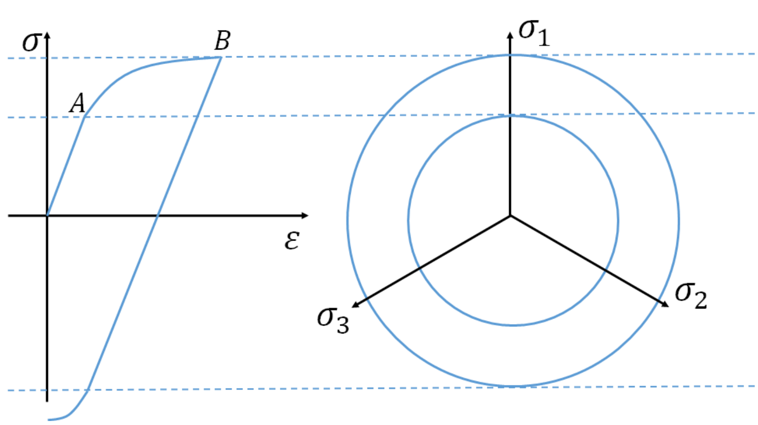

Figure 2.10: Illustration of isotropic hardening. The yield surface increases during plastic deformation (between A and B).

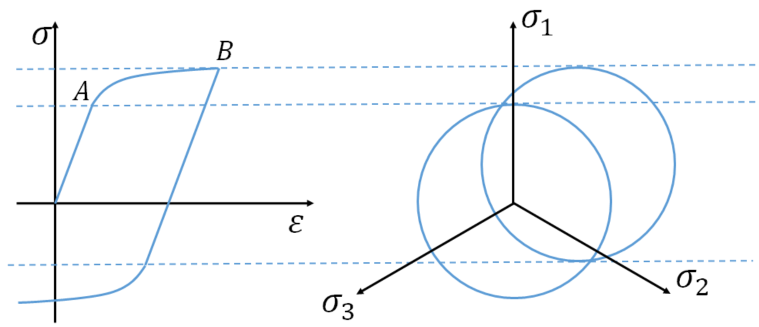

Figure 2.11: Illustration of kinematic hardening. The yield surface remains the same size, but moves by a distance that is equal to the stress difference between A and B.

$$\sigma_0 = \sigma|_0 + Q_\infty \left(1 - e^{-b_i \bar{\varepsilon}_{pl}}\right) \tag{2.19}$$

$$\dot{\boldsymbol{\alpha}} = C \dot{\bar{\varepsilon}}_{pl} \frac{1}{\sigma_0} \left(\boldsymbol{\sigma} - \boldsymbol{\alpha}\right) - \gamma \boldsymbol{\alpha} \dot{\bar{\varepsilon}}_{pl} \tag{2.20}$$

σ_0 is the size of the yield surface, $\sigma|_0$ is the size of the yield surface at zero plastic strain, b and Q_∞ are the isotropic hardening parameters, $\dot{\boldsymbol{\alpha}}$ is the rate of the backstress tensor, $\boldsymbol{\sigma}$ is the stress tensor, $\boldsymbol{\alpha}$ is the backstress tensor and C and γ are the kinematic hardening parameters. In order to represent the hardening behaviour more accurately several backstresses can be used.

Ratcheting is a phenomenon that happens when due to asymmetric stress cycles (non-zero mean stress) the hysteresis loop shifts along the strain axis, as shown in Figure 2.12. The main mechanism for it is nonlinear kinematic hardening and combined hardening model is suitable to describe it.

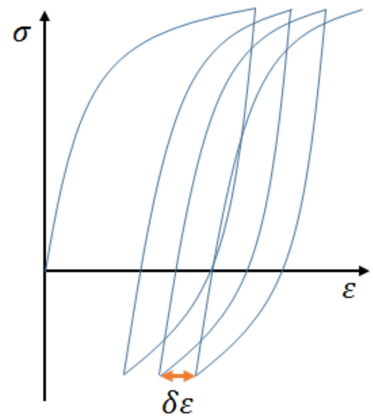

Figure 2.12: Illustration of ratcheting. $\delta\varepsilon$ is ratcheting strain.

Fatigue life describes for how many cycles the material can be loaded at a certain stress amplitude before it fails. It is usually shown as an S-N curve (Figure 2.13) with the number of cycles on the x-axis and the stress amplitude on the y-axis. Some materials, in particular ferrous alloys, exhibit an endurance limit, which is when the S-N curve goes horizontal. It appears that the material does not fail due to fatigue when loaded under that limit. Other materials, non-ferrous alloys, do not exhibit such behaviour and as the stress amplitude decreases the number of cycles to failure increases. Due to a random nature of defects in most materials, repeated fatigue life tests exhibit rather large scatter [5].

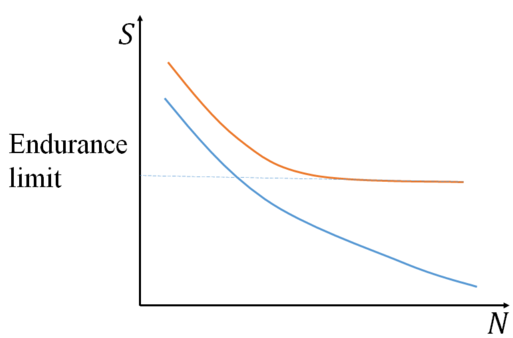

Figure 2.13: Illustration of S-N curve. S is stress amplitude, N is the number of cycles to failure. Some materials exhibit an endurance limit, under which the material can be loaded essentially indefinitely without failing (orange), some materials do not (blue).

The region with cycles to failure above 10^4 or 10^5 is called high cycle fatigue. Loading in that region is usually elastic-only, with tensile and compressive loading applied along the elastic part of the stress-strain curve [5].

The region with cycles to failure below 10^4 or 10^5 is called low cycle fatigue. Loading in that region is elastic-plastic, loading and unloading forms hysteresis loops on a stress-strain plot [5]. Coffin-Manson relationship, illustrated by Equation 2.21, where $\Delta\varepsilon_p$ is the plastic strain range, ε'_f is the fatigue ductility coefficient, $2N_f$ is the number of cycles to failure and c_f is the fatigue ductility exponent, can be used to describe low cycle fatigue by relating plastic strain range to the number of cycles to failure [13, 14].

$$\frac{\Delta\varepsilon_p}{2} = \varepsilon_f^{'} \left(2N_f\right)^{c_f} \tag{2.21}$$

Mean stress in cyclic loading affects the number of cycles to failure. The higher the mean stress the lower the stress amplitude required for failure. There are several different models used to explain the effect of mean stress, such as Gerber, modified Goodman and Soderberg. They are illustrated in Figure 2.14. Compressive mean stresses do not tend to affect the fatigue life negatively [5].

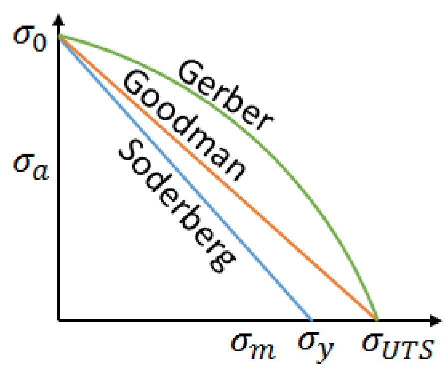

Figure 2.14: Illustration of mean stress effects, using Gerber, Goodman and Soderberg models. σ_0 is the endurance limit at completely reversed loading, σ_a is the endurance limit at a set σ_m, σ_m is mean stress.

2.3.3 Failure

After the material is loaded past its load carrying capacity it fails. Depending on the type of loading and the type of material failure can be either ductile or brittle. Ductile failure occurs by the material first experiencing significant plastic deformation, then localized reduction of cross-sectional area (necking). Voids nucleate, grow and link, then the surface shears and fractures, forming cup and cone shaped fracture. The fracture surface is rough and dimpled, due to voids [4].

In contrast, brittle failure occurs suddenly with no significant plastic deformation. Stress is concentrated at a defect, then a crack propagates either through grains (transgranular) or through grain boundaries (intergranular). The fracture surface is smoother than for ductile fracture, grainy and faceted [4].

Failure due to cyclic loading (fatigue failure) is incremental, with a crack growing incrementally with each cycle until the material cannot support any more loads and fractures completely. This results in characteristic "beach" marks on the fracture surface which can be used to count the number of cycles during which the crack was propagating [4].

2.3.4 Influence of Relevant Environmental and Process History on Material Behaviour

Temperature When temperature and/or composition of an alloy is varied, different equilibrium phases form and that results in different material behaviour. A phase diagram is a graphical representation of that phase change. An example of a phase diagram fragment can be seen in Figure 2.15. The phases represented in a phase diagram are only valid for slow change in temperature, as fast changes result in different phases due to there not being enough time for an equilibrium structure to be formed. The effects of temperature on material properties without phase change will be described in this section, while the effects of phase change will be described in the next section [15].

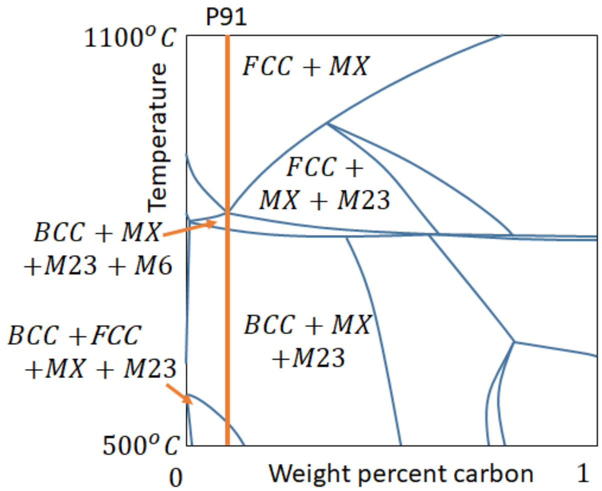

Figure 2.15: An example of a steel phase diagram including P91 steel [16]. *MX* is vanadium carbonitride, *M23* is $M_{23}C_6$, *M6* is M_6C, BCC is ferrite and FCC is austenite.

At elevated temperatures Young's modulus is reduced due to increased interatomic spacing, as that reduces the force that holds them together. The reverse is true for low temperatures. The specifics of this depend heavily on the material and the range of temperature of interest [17].

The effect of temperature on yield strength is much more material dependent than on Young's modulus. For some materials it increases with increasing temperature, then decreases, for some it decreases then increases then decreases again and for some it just decreases with increasing temperature [18].

Elevated temperature generally makes metallic alloys softer and moves the hardening curve lower than the room temperature curve. Low temperatures can make materials brittle, making the fracture strength close or coincident with yield strength and no hardening curve to speak of. Elevated temperature also tends to make materials more sensitive to different loading rates when testing [18].

The variation of Poisson's ratio with changing temperature is material dependent, however, generally it decreases with increasing temperature [19]. Fracture strength is also material dependent, low temperatures can make materials brittle and therefore significantly reduce the fracture strain [18].

Cyclic hardening and fatigue life are very material specific to begin with and adding temperature variation enhances that [18].

Heat Treatment Annealing is heating up the alloy to a recrystallization temperature and holding it there for a while, then slowly cooling. It generally softens the material by getting the microstructure closer to the equilibrium microstructure. Ductility is increased and hardness is decreased, residual stresses are removed. There are three stages: recovery, recrystallization and grain growth. Initially there is residual stress in the material due to cold work. If the material was rolled the grains are elongated (Figure 2.16 1). Then, when the temperature is raised above the recrystalization temperature, recovery occurs (Figure 2.16 2), dislocations and internal stresses disappear, resulting in the material softening. Afterwards recrystallization happens, when new grains are nucleating and growing (Figure 2.16 3). Then grain growth takes place, when grains that nucleated in the previous stage grow and coarsen (Figure 2.16 4) [2].

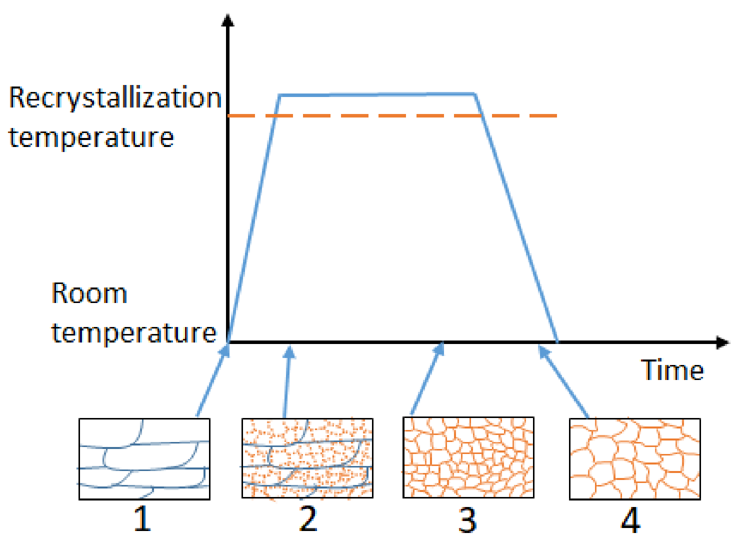

Figure 2.16: Annealing temperature pattern and change of microstructure.

Ageing (also called precipitation hardening) is a process during which particles precipitate from a supersaturated solid solution in the alloy. Ageing can be natural, when precipitation happens at room temperature, and artificial, when elevated temperature is used. As shown in Figure 2.17, initially there are no precipitates, then small precipitates form and the strength and hardness of the material being aged increase. However, if the ageing process continues, the material becomes overaged, the precipitates coarsen and the strength and hardness of the material goes down again [4].

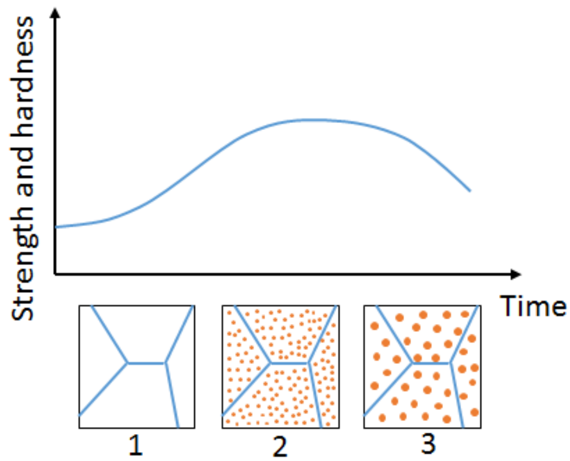

Figure 2.17: The effect of ageing on material properties and microstructure.

The mechanism by which precipitates improve material properties is either Orowan bowing (Figure 2.18 (a)) or particle shearing (Figure 2.18 (b)). In the case of Orowan bowing, the dislocation motion is impeded by the precipitates as dislocations bow around them. In the case of particle shearing, the dislocation motion is impeded by the fact that the particles need to be sheared before dislocations can move past them [4].

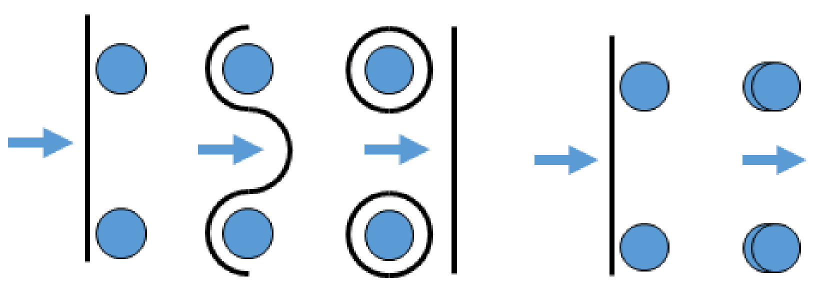

(a) (b)

Figure 2.18: Illustration of (a) Orowan bowing; (b) particle shearing.

When a steel is fully austenized (Figure 2.19 1) and quenched (Figure 2.19 2), martensite forms. It is a non-equilibrium microstructure, very hard, tough and brittle. In order to reduce toughness and improve machinability the material needs to be tempered, which means holding it at an elevated temperature to allow carbon to diffuse through the martensite matrix. This allows Fe_3C particles to form (Figure 2.19 3) on grain boundaries and plate boundaries [4].

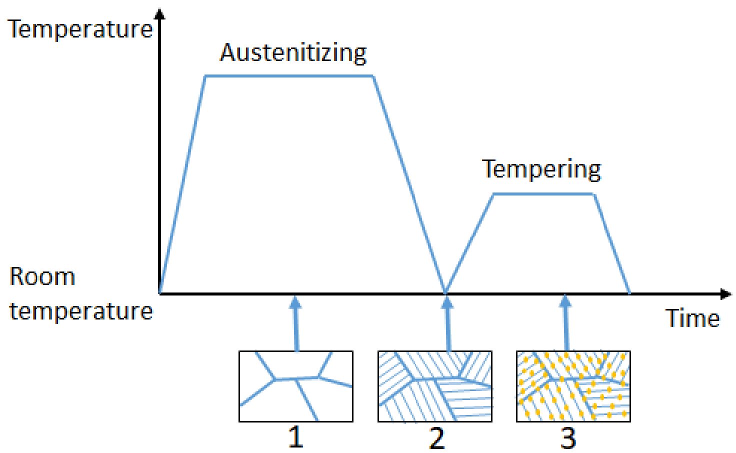

Figure 2.19: Tempering temperature pattern and change in microstructure.

Repeated Loading/Cold Work Cold work occurs when a material is shaped under its recrystallization temperature. It can be a consequence of rolling, which then results in elongated grains and potentially anisotropic material properties. It can also be a consequence of surface treatment or machining, which only affects the surface of the material and does not change the bulk material properties [18]. Repeated loading (cycling) can be considered as repeated cold work affecting bulk material properties.

Cold work and repeated loading generally do not affect Young's modulus, as shown in the section about monotonic material behaviour. The slope of the elastic unloading during cyclic loading changes due to damage in the cross-section not the alteration in material properties as it is sometimes used to determine failure under cyclic loading [20].

As cold work is a method to strengthen the material, it raises the yield strength. When only the surface is affected the effect might be small enough to not affect the overall test results significantly. If the cold work results in elongated grains and anisotropy, the yield strength could be increased in one direction and reduced (or stay the same) in others [21].

As for the hardening behaviour, the material follows the stress-strain curve after being reloaded, therefore it is affected by cold work. Similarly to yield strength, if only the surface is affected the overall test results might not be significantly affected and depending on the stress-strain behaviour anisotropy may or may not have a significant effect.

Assuming that the density of the material does not change when it is deformed and it is incompressible, the plastic behaviour Poisson's ratio can be assumed to be 0.5. For elastic deformation following plastic deformation and unloading, cold work does not affect Poisson's ratio, as it is related to elastic material behaviour constants, Young's modulus and shear modulus.

Cold work makes materials tougher, which reduces their ductility and therefore reduces the fracture strain. As for fatigue life, if only the surface is affected the fatigue life can be increased due to localized compressive stresses. If the whole material is affected, for example, it has been loaded cyclically already, then the fatigue life is reduced [18].

Surface Roughness There are two main ways surface roughness can affect material testing results: by reducing the effective load bearing cross-sectional area and by surface scratches acting as notches. This reduction of area has a more significant effect on specimens with smaller cross-section, as equivalent surface roughness removes a proportionally higher part of the load bearing cross-section. The resulting stresses in the specimen are higher than expected and the stress-strain curve calculated without accounting for surface roughness is lower than expected.

Notches concentrate stress and cause specimens to fail at lower than expected fracture strenght and lower number of cycles if loaded cyclically. Consequently, very smooth (polished) surface finish can also be unrepresentative as it would increase fatigue life and fracture strength.

2.4 Standard Testing

2.4.1 Tensile Testing

As mentioned before, there are several different tensile material properties that are commonly of interest in engineering applications. Standard tensile testing can be used to identify them. The general testing method is as follows: a specimen is gripped in a testing machine ensuring alignment, then a tensile load is applied until the specimen breaks. A stress-strain curve results from the test, from which material properties, such as Young's modulus, yield strength, UTS and fracture strength can be identified. Properties such as elongation to failure and reduction in area can be identified from measuring the specimen before the test and after failure.

Several different specimen geometries are used for tensile testing. Some are suitable for several types of tests, while some are specific to a particular test.

For general metallic material tensile testing at room temperature standard dog bone specimens (Figure 2.20), dog bone specimens with holes for loading (Figure 2.21 (a)), standard round bar specimens (Figure 2.21 (b)) and round bar specimens with collars (Figure 2.21 (c)) are used [22]. For metallic material testing for aerospace applications, the same specimens are used, except the dog bone specimens with holes for loading [23]. In both cases the specimens can also be pieces of unmachined material with constant cross-section or tubes. Thin specimens require special consideration and care has to be taken to ensure that the test results are representative of bulk material due to grain size effects [22, 23].

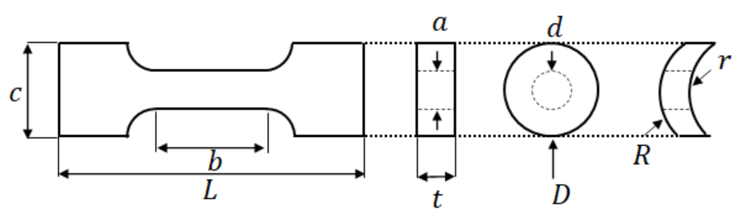

Figure 2.20: Standard dog-done specimen. b is at least 25 mm for circular cross-section and at least 50 mm for rectangular cross-section, other dimensions can vary in a wide range of values.

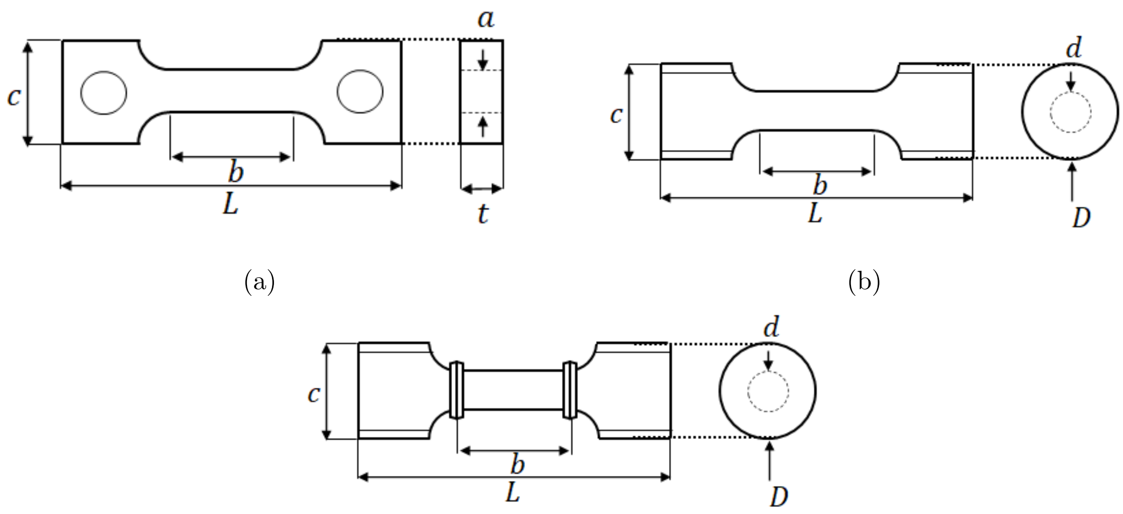

(c)

Figure 2.21: (a) Standard dog-bone specimen with holes for load application. b is at least 50 mm for t of 0.1 mm to 3 mm and at least 35 mm for t of 3 mm or more; (b) Standard round bar specimen used for tensile testing. Ends threaded for mounting into a testing machine. b is at least 20 mm for d of 4 mm, above that the dimensions increase proportionally; (c) Standard round bar specimen used for tensile testing with a collar. b is at least 30 mm and d of at least 6 mm.

The method to test transverse welds is broadly similar to standard tensile testing, the specimens used are standard dog bone specimens, standard round bar specimens and tubes. The weld has to be perpendicular to the length of the specimen and has to be located in the gauge length [24].

For testing metallic materials at elevated temperature for both general [25] and aerospace [26] applications, the same specimens as for room temperature testing can be used and conformance with temperature requirements has to be ensured to get representative results.

For testing general metallic materials at low temperature [27] and cryogenic [28] conditions, the same specimens can be used as the ones used for room temperature. It it preferable for the specimens to be as small as possible to ensure accurate temperature control. Also, for cryogenic testing, the use of smaller specimens would result in shorter exposure to the cooling medium which is beneficial as the cooling medium could potentially affect material properties.

When metallic materials are tested at high strain rates any specimen can be used, but standard high rate specimens A and B (Figures 2.22 (a) and 2.22 (b)) are recommended. The high rate loading can be applied by elastic-bar system, servo-hydraulic system or a split Hopkinson bar apparatus [29].

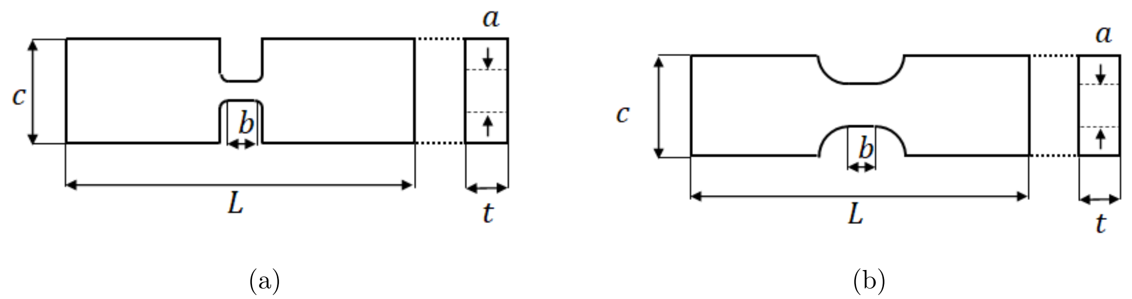

Figure 2.22: (a) Standard high rate specimen A. b is 10 mm or less and a is b divided by 2; (b) Standard high rate specimen B. Generally larger than specimen A.

For testing metallic materials under biaxial loading, cruciform specimens are used. Different ratios of force can be applied to the perpendicular arms of the specimen to investigate the effect of biaxiality [30]. The results are not as straightforward to interpret as uniaxial tensile test results, stress-strain behaviour and the plastic work have to be calculated.

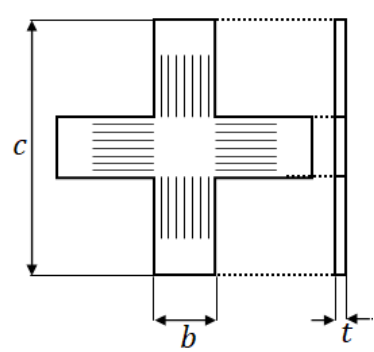

Figure 2.23: Standard cruciform specimen. b is at least 30 mm and t is at least 0.1 mm.

Ring ductility tests are used to inspect tubes for surface and internal defects, as well as to access ductility. The specimens used are shown in Figure 2.24. They are loaded by two pins that are pulled apart until the specimen breaks. Interpretation of the test result is left to relevant product standards [31].

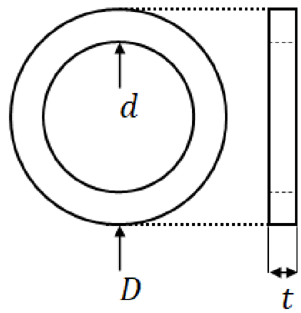

Figure 2.24: Standard ring specimen for evaluating ductility. D is more than 150 mm, d is more than 100 mm, D-d less or equal to 40 mm, t is about 15 mm. The pins used for testing have to have a diameter of at least $3\times(D\text{-}d)$.

2.4.2 Cyclic Testing

There are several different cyclic plasticity and fatigue properties that are commonly of interest in engineering applications. Standard cyclic testing can be used to identify them. The general testing method is as follows: a specimen is gripped in the testing machine ensuring alignment, then a cyclic load is applied until the test end condition is met. The test end condition can be specimen fully separating, a set percentage reduction in maximum force or any other agreed condition. A fatigue life under a certain load can be identified, an S-N curve can be found and, provided the test was for low cycle fatigue, cyclic plasticity behaviour can be identified.

There are several important factors which need to be controlled when making the specimens and testing them. Appropriate machining reduces the heating of the specimen, which can affect the material properties of the surface, also, appropriately smooth surface finish does not introduce stress concentrations. Keeping the temperature uniform during loading is important, as local heating can affect the results.

Several different specimen geometries are used for cyclic testing. Some are suitable for several tests, while some are specific to a particular test.

In general the fatigue tests can be axial force controlled [32], strain controlled [20, 33, 34] and stress controlled [33, 35]. The specimens used are standard hourglass (Figure 2.25 (a)), standard cylindrical (Figure 2.25 (b)), alternative cylinder (Figure 2.25 (c)) and standard flat sheet (Figure 2.25 (d)). Flat specimens are at particular risk of buckling, so anti-buckling constraints should be used, especially at lower specimen thickness. They can affect the test results due to friction between the specimen and the constraints.

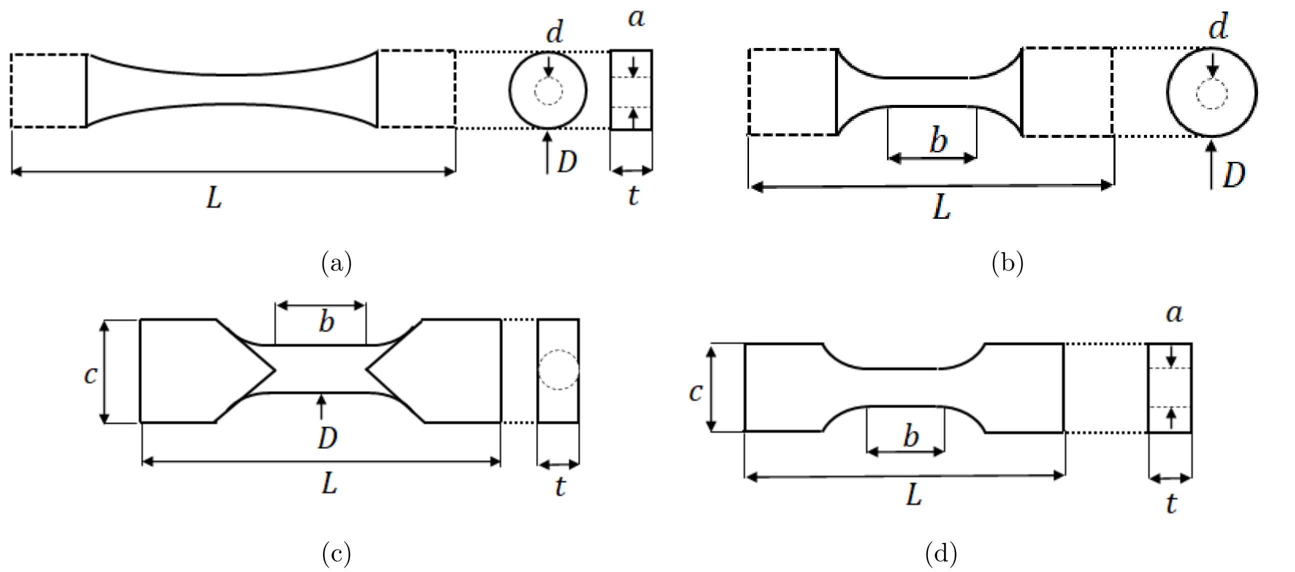

Figure 2.25: (a) Standard hourglass specimen. d is between 6 mm and 12.5 mm and cross-sectional area of rectangular cross-section is between 32 mm^2 and 640 mm^2; (b) Standard cylindrical specimen. d is between 6 mm and 12.5 mm. L is b is between 2 and 4 d, d is between 5 mm and 10 mm and D is more than 2 d. d more than 5 mm, b is between 1.5 and 3 d. d is between 5 mm and 12 mm, b is less than 5 d and D is more than 2 d. Some have different end attachments, some have a notch. L is more than 60 mm; (c) Alternative cylindrical specimen. L is at least 21.5 D, b is 1.5 to 3 D, c is 3 to 5 D, D is 5 mm to 10 mm (but less than (t-2 mm))and t is 7 mm to 14 mm; (d) Standard flat sheet specimen. Cross-sectional area between 32 mm^2 and 640 mm^2 for some. L is at least 50 mm, a is more or equal to t and more than 5 mm, b is between 1.5 and 3 t, c is between 3 and 5 t and t is 3 mm or more.

Thermomechanical fatigue (TMF) tests are usually performed in strain control mode. The specimens commonly used are smooth or threaded shank tube specimens (Figure 2.26 (a)), standard cylindrical specimens or standard rectangular specimens (Figure 2.26 (b)). Temperature control and compensating for thermal strain are important to get representative results [36].

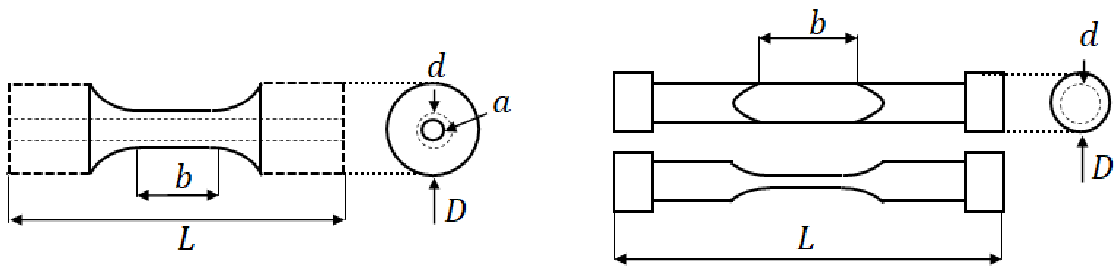

(a) (b)

Figure 2.26: (a) Standard tube specimen. a is between 0.8 and 0.9 d,b is between 1 and 3 d, d is between 5 mm and 12 mm and D is more than 1.5 d. Other variants have L between 87 mm and 140 mm, a is between 7 mm and 9 mm, b is between 19 mm and 51 mm, d is around 11 mm and D is between 13 mm and 15.8 mm; (b) Standard rectangular specimen. L is 125 mm, b is 22 mm D is 19 mm and d is 12 mm.

For aerospace applications cyclic tests are performed on standard cylindrical specimens, flat and round hourglass specimens, T-type specimens (Figure 2.27 (a)) and standard flat TMF specimens (Figure 2.27 (b)).

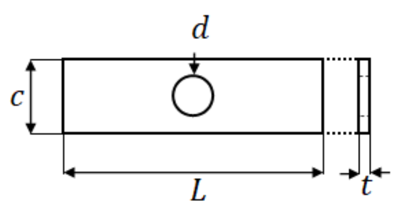

(a) (b)

Figure 2.27: (a) T-type specimen. L is 100 mm or 150 mm, c is 20 mm or 30 mm, d is 6.35 mm or 10 mm and t is between 1 mm and 3 mm, but higher values can be used in some cases; (b) Standard flat TMF specimen. L is 200 mm, c is 60 mm and t depends on the material and is between 10 mm and 20 mm.

In order to test sintered material, specimens can be die pressed and sintered, or sintered material can be machined. For the first type of test either notched (Figure 2.28 (a)) or plain specimens (Figure 2.28 (b)) should be used. For the second type of test hourglass or cylindrical specimens should be used, hourglass specimens are suitable for rotating bending tests while cylindrical specimens are suitable for axial loading tests [37].

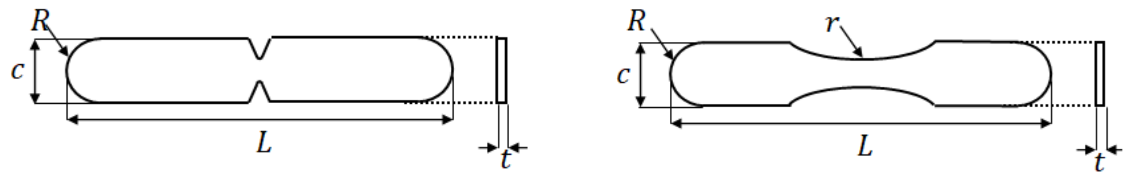

(a) (b)

Figure 2.28: (a) Notched standard specimen for fatigue testing of sintered material. L is 90 mm, R is 5.5 mm, c is 11 mm and t is 5 mm; (b) Standard specimen for fatigue testing of sintered material. L is 90 mm, R is 5.5 mm, c is 11 mm, r is 30 mm and t is 5 mm.

In order to do multiaxial fatigue testing a loading system or a specimen that allows multiaxial loading have to be used. Combinations of different loading methods can be used, such as bending and torsion, or specimens, such as the cruciform specimen (Figure 2.23) suitable for multiaxial loading can be used [38]. Variable amplitude testing is of interest when the effects of true service history is of interest, any standard specimen can be used [39].

For torque controlled fatigue testing a constant amplitude torsional load is applied to a specimen with a standard cylindrical or standard tube gauge section, the parts of the specimen not in the gauge section highly depend on the testing machine. This test is for high cycle fatigue, as loading is nominally elastic [40]. For rotating bar bending fatigue testing a load is applied to a rotating bar, there is a variety of different configurations with a different number of points for bending and different specimens, such as standard hourglass, standard cylinder or tapered [41].

2.5 Small Specimen Testing

2.5.1 Tensile Testing

Examples from all subcategories of specimens can be found when tensile properties are of interest. Sub-size standard specimens include various types of dog-bone specimens shown in Figure 2.29, button-head specimens shown in Figure 2.30 (a) and round bar specimens shown in Figure 2.30 (b). One sub-size standard fatigue specimen was also used, shown in Figure 2.30 (c).

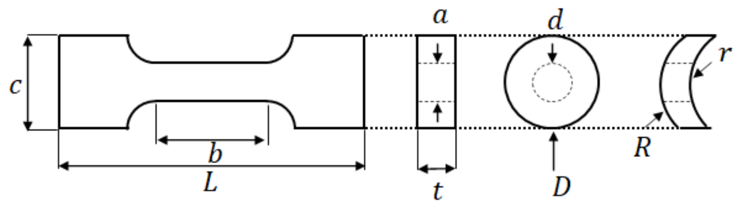

Figure 2.29: Dog-bone specimen. Can be flat, round or curved. L varies between 2.4 mm and 37 mm, a varies between 0.3 mm and 4 mm, b varies between 0.4 mm and 22 mm, c varies between 1.6 mm and 10 mm, d varies between 2 mm and 3 mm, t varies between 0.15 mm and 2 mm, D is mentioned once and is around 6 mm and R is 5.44 mm with r equal to 4.84 mm. In some cases the thickness is not uniform [42].

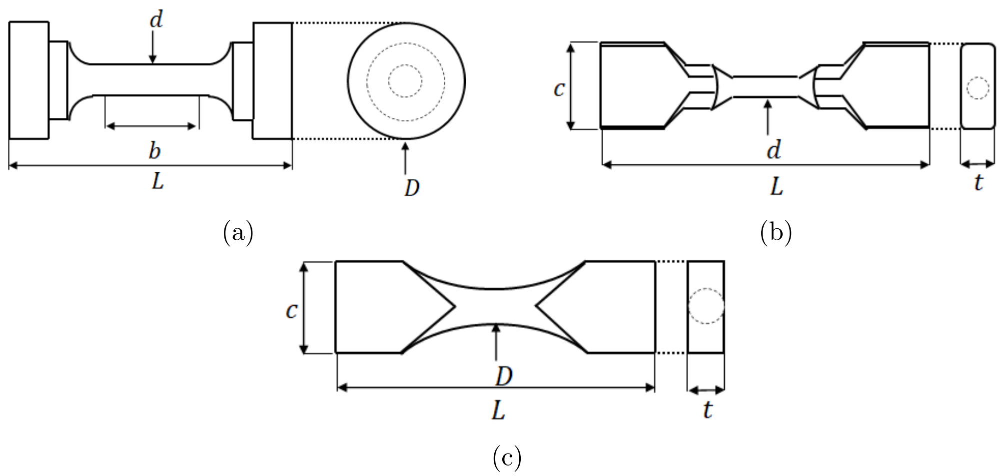

Figure 2.30: (a) Button head specimen. L varies between 34 mm and 35 mm, b varies between 4 mm and 18 mm, d varies between 2 and 3 mm and D varies between 8 mm and 10 mm; (b) Round bar specimen. L is 24 mm, c is 6 mm, D is 1 mm and t is 2 mm. (c) Small hourglass specimen. L is 25.4 mm, c is 4.96 mm, D is 1.25 mm and t is 1.52 mm.

Small punch specimens used were either round (Figure 2.31 (a), or square (Figure 2.31 (b)). The specimen during a small punch test (SPT) is usually loaded by clamping it between dies and pushing a hemi-spherical punch through it, as shown in Figure 2.31 (c).

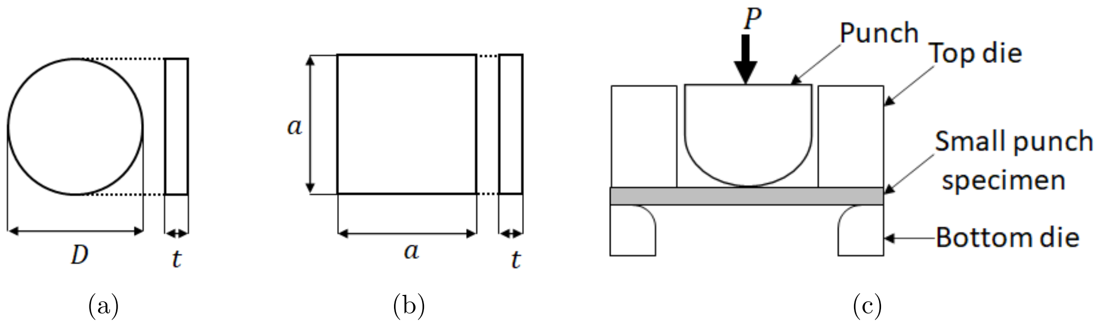

Figure 2.31: (a) Round small punch specimen. D varies between 3 mm and 10 mm and t varies between 0.1 mm and 1 mm; (b) Square small punch specimen. a is either 5 mm or 10 mm, t varies between 0.25 mm and 0.7 mm; (c) Small punch specimen testing diagram.

Indentation specimen geometry for automated ball indentation (ABI) testing was generally not specified, which makes sense as their geometry/ dimensions do not influence the results, provided a flat surface is available and the specimen is thick enough. The minimum thickness should be either 2 to 4 times the indentation diameter or more than 10 times the indentation depth, whichever one is smaller [43].

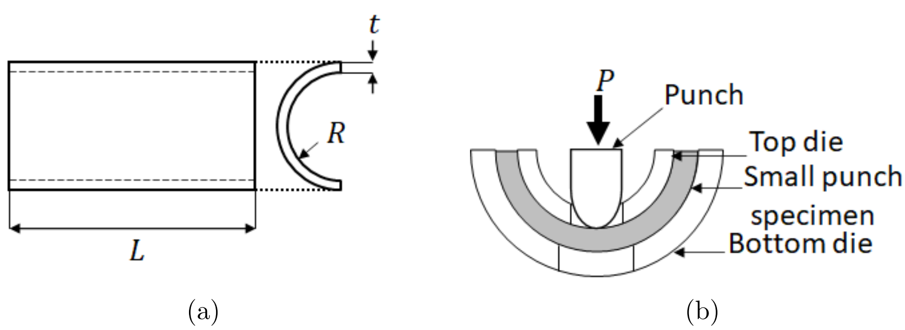

Figure 2.32: (a) Curved small punch specimen. L is 11 mm, R is 2.825 mm and t is 0.45 mm; (b) Curved small punch specimen testing diagram.

Bespoke specimens include octagonal specimens for hydraulic bulge testing, shown in Figure 2.33 (a). They were loaded by clamping them between dies and applying pressurized hydraulic oil under increasing pressure until they failed, as per Figure 2.33 (b).

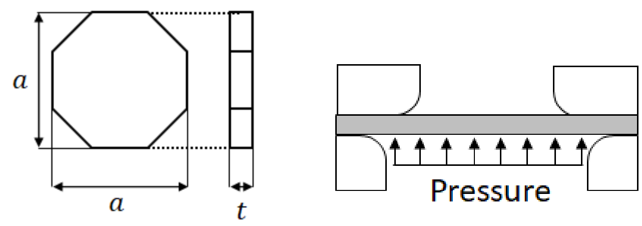

(a) (b)

Figure 2.33: (a) Octagonal hydraulic bulge specimen. a is 10 mm, t is 0.5 mm. L is 11 mm, R is 2.825 mm and t is 0.45 mm; (b) Hydraulic bulge test testing diagram.

Another geometry of specimen included were miniaturized tensile specimens, shown in Figure 2.34 (a). They were loaded by hooking the loading arms around the flats of the specimen, as shown in Figure 2.34 (b).

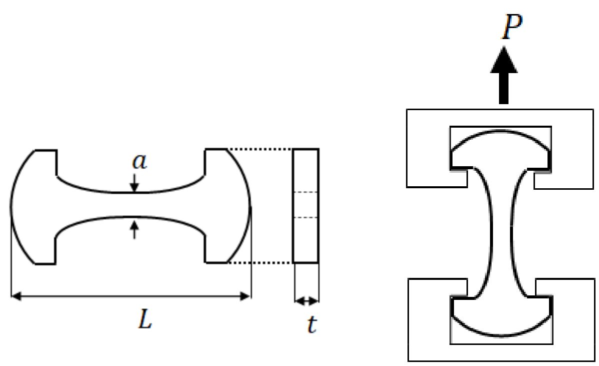

(a) (b)

Figure 2.34: (a) Miniaturized tensile specimen. L is 3 mm, a is 0.5 mm and t is unknown; (b) Miniaturized tensile specimen testing diagram.

Wire specimens shown in Figure 2.35 were also included. They were loaded in an unspecified way, but likely by wrapping the ends of the wire around the loading setup.

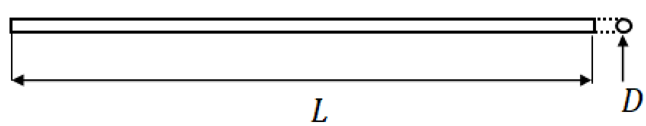

Figure 2.35: Wire specimen. L is 20 mm and D is 0.1 mm.

Another specimen type included was disc tensile specimens, shown in Figure 2.36 (a). They were tested by clamping them between two dies with a recess, to ensure full clamping, as per

Figure 2.36 (b).

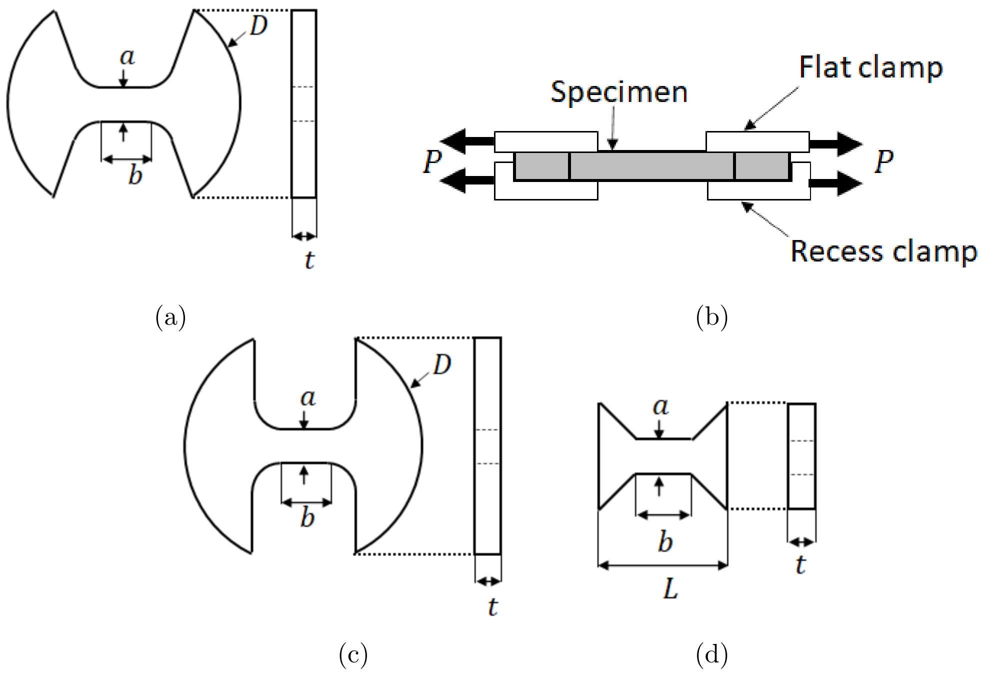

Figure 2.36: (a) Disc tensile specimen. D is 9.44 mm, a is 2 mm, b is 2.06 mm and t is 0.5 mm. (b) Testing diagram of a disc tensile specimen. (c) Ultra small size specimen, also known as micro tensile specimen. D is 8 mm or 10 mm, a is 1.5 mm, b is 2.6 mm or 3 mm and t is 0.5 mm. (d) Modified ultra-miniature specimen. L is 5.5 mm, a is 0.4 mm, b is 2.3 mm and t is 0.25 mm.

The other specimens included were made from a tube in a shape of a dog-bone shown in Figure 2.37. The loading method was not explained.

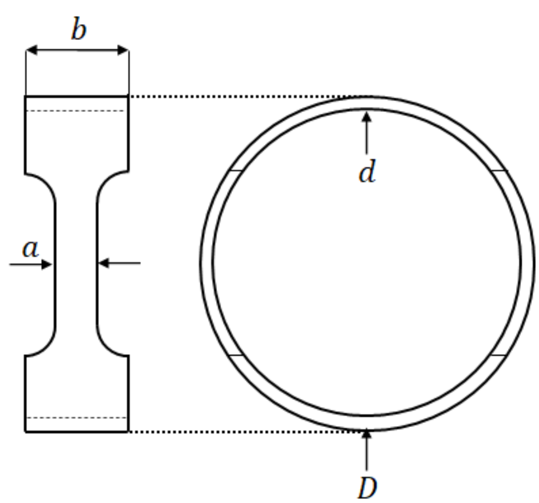

Figure 2.37: Dog-bone shaped specimen cut from a tube. a is 1 mm, b is 3 mm, d is 9.35 mm and D is 10.5 mm.

Young's Modulus Small specimen testing of Young's modulus was performed on a wide range of materials and specimens, shown in Table 2.1. The bespoke specimens used were disc tensile specimens (Figure 2.36 (c)) and specimens made from a tube in the shape of a dog-bone (Figure 2.37). When sub-size standard specimens were tested Young's modulus was determined directly from stress-strain curves and matched the results from standard uniaxial testing well when verified against standard uniaxial test results [44–47].

The SPT results are not as straightforward to interpret. In the example test results shown in Figure 2.38 the force-displacement curve is divided into five regions. The slope parameter of region I was found to relate to Young's modulus for aluminium alloys [52].

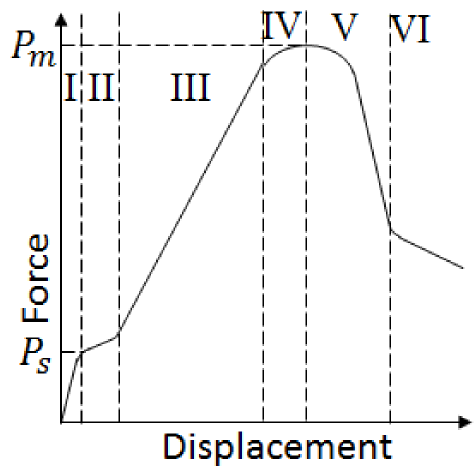

Figure 2.38: Example force-displacement curve from small punch testing. P_s is limit load, P_m is maximum load. Region I represents elastic bending, region II represents plastic bending, region III represents membrane-like behaviour due to the balance of work hardening and stretching, region IV is when necking and crack initiation happens, region V has fracture softening behaviour and region VI is when final fracture occurs.

Husain [53] developed an inverse finite element analysis (FEA) method which evaluated Young's

Table 2.1: Materials and specimens from which Young's modulus was acquired.

	Steels	Aluminium alloys	Nickel alloys
Sub-size standard specimens	[46–50]	[51]	[44, 45]
Small punch specimens	[52, 53]	[52]	
Bespoke specimens	[54, 55]		

modulus between 17 % lower and 11 % higher than the results from testing standard specimens, which is promising. The disc tensile specimens worked rather well, apart from finding about 6 % lower values for Young's modulus in comparison with uniaxial testing results, likely due to inelastic effects and micro-plasticity below proportional limit [54].

Results from all these studies suggest that Young's modulus can only be accurately determined from sub-size standard specimens, disc tensile specimens are good for an approximate estimate and SPT does not seem to be appropriate at all.

Yield Stress Small specimen testing of yield strength was performed on a wide variety of materials and specimens, shown in Table 2.2. The bespoke specimens used were an octagonal specimen for hydraulic bulge testing (Figure 2.33 (a)), miniaturized tensile specimen 2.34 (a)), disc tensile specimen (Figure 2.36 (a)), micro tensile specimen (Figure 2.36 (c)), modified ultra-miniature specimen (Figure 2.36 (d)) and a wire specimen (Figure 2.35).

When sub-size standard specimens were tested yield strength was determined from stress-strain curves directly [42, 44–47, 66] like when standard specimens were tested; consequently it matched well with yield strength from standard specimen tensile testing results. Several authors pointed out aspects which could influence the measurement of yield strength: there needed to be enough material in the gauge section to prevent brittle failure [62], microstructure and grain size needed to be taken into account [70] and surface roughness had a significant effect of reducing the effective gauge section [64]. Roughness was particularly relevant for smaller specimens as the surface layer was a larger part of the total cross-section, therefore it needed to be accounted for if the specimens were not polished. Ge [57] found that yield stress from small specimens was higher than standard, possibly because the specimen was not optimized like others were, just reduced in size. Good agreement was seen between sub-size standard specimen tensile test results and indirect yield strength measurements based on hardness correlations for welds and heat affected zone (HAZ) [49]. Yield strength determined from varied thickness (parameter t in Figure 2.29) sub-size standard specimen testing results is not affected by the variable thickness [42]. Vandermeulen found that

Table 2.2: Materials and specimens from which yield strength was acquired.

	Steels	Aluminium alloys	Nickel alloys	Titanium alloys	Copper alloys	Tungsten alloys	Magnesium alloys	Zirconium alloys
Sub-size standard specimens	[42, 46–50, 55–62]	[51, 63]	[44, 45, 64, 65]		[64, 66]	[63, 64]		
Small punch specimens	[53, 56, 58, 67–83]	[52, 71, 72, 84]	[85]	[71]			[86]	[87]
ABI specimens	[75, 77, 80, 88–100]	[101–103]		[104, 105]				[87]
Bespoke specimens	[54, 106–110]	[108, 110]	[108]	[108]	[110]			

the manufacturing method is more important when making small specimens than when making standard specimens, as turning a specimen creates a cold worked layer which then increases the yield strength in comparison to reference [65].

SPT specimens could not be used to determine yield strength directly as they only produce a force-displacement curve as opposed to a stress-strain curve. Therefore various correlations based on limit load (P_s in Figure 2.38) were used, with different ones being applicable to different materials [52, 76, 78, 84]. In general the results after applying the correlations matched standard testing results well, apart from when the material did not exhibit a limit load [73], sometimes the results were too scattered to be used for anything other than ranking [85] or when the thickness to grain size ratio was too low (less than 19), making the results not representative of bulk material [70]. Thickness has a significant effect, especially for thinner specimens, therefore additional corrections should be used [82]. Inverse FEA could also be used to acquire yield strength and could achieve good agreement with standard test results [53].

One of the other specimens and testing methods used to identify yield stress was hydraulic bulge test. An example force-displacement curve is shown in Figure 2.39 (a). The yield stress was calculated using a correlation between limit load (P_{lim} in Figure 2.39 (a)) from the force-displacement curve and yield strength from standard testing and achieved good agreement with standard test results [106]. Shear punch was another testing method used, illustrated by Figure 2.39 (b), it was also similar to SPT, but instead of a ball the punch was flat, there was a clearance of 0.02 mm between the punch (diameter 3 mm) and the die to ensure shear deformation, and both top and bottom dies had the same diameter. An example force-displacement curve is shown in Figure 2.39 (c). The yield strength was calculated using a correlation between the limit load (P_γ in Figure 2.39 (c)) and yield strength, good agreement with standard testing results was also achieved [75, 77, 90]. Varying the thickness was found to have an effect, however it was negligible between 0.29 mm and 0.4 mm [81]. Correlations were used to find yield strength from miniaturized tensile specimen test results [107], while inverse FEA was used to find it from the disc tensile specimen test results [54]. The use of correlations resulted in good agreement with standard testing results and inverse FEA results were within 2 % of standard testing results. Inverse FEA used the estimate of the proportional limit and calculated true stress-strain behaviour to determine the yield stress.

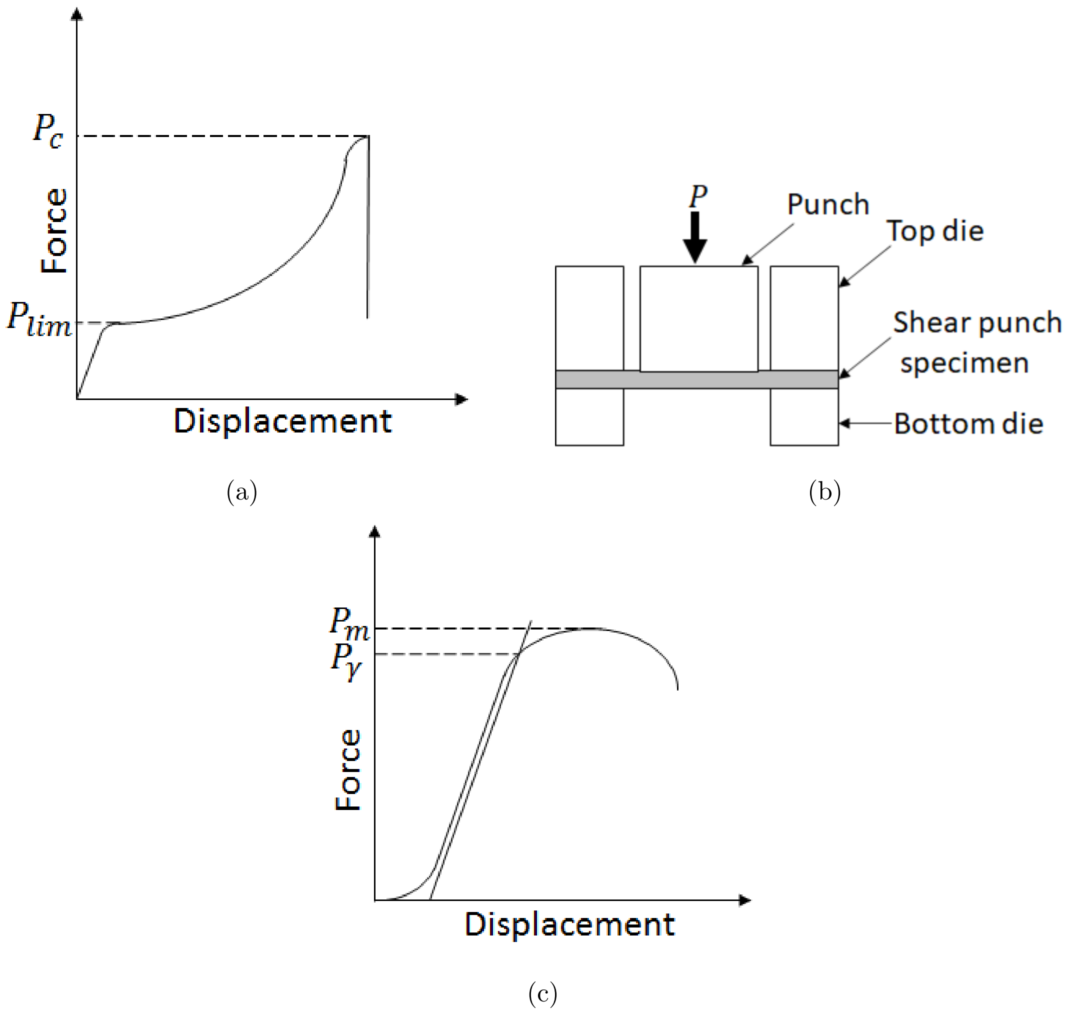

Figure 2.39: (a) Example pressure-displacement curve from hydraulic bulge test. P_{lim} is limit load, P_c is critical load; (b) Example force-displacement curve from shear punch test. P_γ is limit load, P_m is maximum load; (c) Shear punch testing diagram.

ABI (illustrated in Figure 2.40, the indenter is repeatedly pushed into the material, then partially unloaded, then reloaded) also relied on correlations and had good agreement with standard testing results, even better then SPT tests when compared directly [80]. It was also used to characterize the variation of yield stress across welds [91–94], the effect of high pressure torsion processing [103] and the effect of machining [98] due to being able to evaluate material properties locally. The effects of temperature [104], loading rate [105], effect of heat treatment [95, 102] and test setup parameters [99] were successfully investigated, good agreement was found with standard specimen test results. Alternative methods for calculating yield stress were investigated as well, such as neural networks [105], which result in better agreement between ABI and standard results than constitutive behaviour based correlations, and inverse analysis, which is shown to be a promising technique [96].

The wire specimen was an interesting case, as the yield strength was identified from a stress-strain curve, and it was significantly higher than of standard specimens, due to size effects [111]. Size effect in this case is the increase of material strength when small structures or small volumes of material are tested. In this case it is likely that the size effect was caused by a combination of both factors, as the microstructure is not specified.

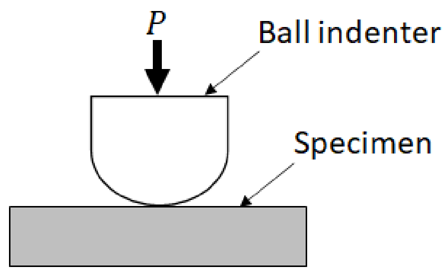

Figure 2.40: ABI loading diagram.

The effect of composition could be identified using sub-size standard specimens [59, 60]. For pressed and sintered material yield strength calculated from SPT results was very similar to calculated ultimate tensile strength (UTS) due to the brittleness of the material [69].

Overall, sub-size standard specimens seem to be the most suitable for yield strength, provided the geometry is appropriate. SPT is suitable in a lot of cases, but different correlations apply for different materials and sometimes it cannot be used. Shear punch and hydraulic bulge tests are similar to SPT as they both rely on correlations and the results agree with standard results well, however more studies should be done to investigate potential issues.

Ultimate Tensile Strength Small specimen testing of UTS was performed on a wide variety of materials and specimens, shown in Table 2.3. The bespoke specimens were octagonal hydraulic bulge specimens (Figure 2.33 (a)), disc tensile specimens (Figure 2.36 (c)), miniaturized tensile specimens (Figure 2.34 (a)), micro tensile specimens (Figure 2.36 (c)), modified ultra-miniature specimens (Figure 2.36 (d)) and wire specimens (Figure 2.35).

Table 2.3: Materials and specimens from which UTS was acquired.

	Steels	Aluminium alloys	Nickel alloys	Titanium alloys	Copper alloys	Tungsten alloys	Magnesium alloys	Zirconium alloys
Sub-size standard specimens	[42, 46–50, 55–60, 62, 63, 112–114]	[51, 63]	[44, 45, 64, 65]		[64, 66]	[63, 64]		
Small punch specimens	[53, 56, 58, 67–82, 115]	[52, 71, 72, 84]	[85]	[71]			[86]	[87]
ABI specimens	[75, 77, 80, 88–95, 98–100, 116]	[101–103]		[104]				[87]
Bespoke specimens	[54, 106–111]	[108, 110]	[108]	[108]	[110]		[117]	

If sub-size standard specimens were used UTS could be determined directly from stress-strain curves. The gauge section needed too have enough material to resist necking and not fail before UTS equivalent to UTS from standard specimen testing was reached [62]. For brittle materials the misalignment when manufacturing and loading could lead to significant differences between UTS acquired from small and standard specimens [63]. Surface roughness needed to be accounted for by subtracting the roughness from the specimen width and thickness to calculate the effective load-bearing cross-section, as that resulted in better agreement with standard testing results [64]. Similarly to yield strength, UTS is increased by cold working the surface when manufacturing the specimen, making it not representative of bulk material properties [65]. One of the sub-size standard specimen testing techniques relied on correlations instead of direct evaluation, in order to take the necking zone into account. It produced better results than without using the correlation [112]. The size effect was investigated for a sub-size hourglass specimen, it was discovered that UTS is mostly independent of specimen dimensions [114]. UTS is also mostly independent of varied thickness (parameter t in Figure 2.29) in sub-size standard specimens [42].

Determining UTS from SPT specimen results relied on correlations between UTS and maximum load (P_m in Figure 2.38), and, much like for yield strength, they were also material specific. Generally the results after applying the correlation agreed with the results from standard specimen testing well, but scatter was bigger than when standard specimens were used [56], sometimes making it impossible to use SPT as anything other than a ranking tool [85]. When developing a new correlation minimizing the scatter is important as scatter bands that are too wide make it difficult if not impossible to determine material properties [118]. The results from thinner specimens require additional corrections to be representative of bulk material [82]. If full size specimens were manufactured in a way that resulted in anisotropy between outer surface and the center of the specimen, testing SPT specimens cut as slices from the gauge section of the standard specimens did not result in the same material properties as standard specimens [86]. When a standard specimen is tested the difference in material properties is averaged out, but when a SPT specimen is tested only the central region is actually tested.

Bespoke specimens and testing methods included hydraulic bulge [106] (example result shown in Figure 2.39 (a)) and shear punch (example result shown in Figure 2.39 (c)) [75, 77, 90], both of which relied on correlations based on the critical or maximum load and had good agreement with standard tests. The thickness of the shear punch specimen has a significant effect on the results, but not when the thickness is between 0.29 and 0.4 mm [81]. Shear punch jump test, producing similar data to tensile jump test, also resulted in good agreement between calculated UTS and uniaxial UTS [117]. The more unusual specimens were the miniaturized tensile specimens and disc tensile specimens, one of which relied on correlations [107] and the other on inverse FEA [54]. ABI was also used, with a series of calculations applied in order to calculate UTS and it achieved reasonably good agreement with uniaxial results [77,80,116]. Similarly to yield stress, UTS was also evaluated across welds using ABI, due to its ability to measure material properties locally [91–94]. Similarly to determining yield stress, the effects of various parameters were investigated for determining UTS from ABI test results.

Wire specimens were not very good for representing bulk properties, as UTS was much higher than from standard specimens, due to size effects, however, bulk material properties were not of interest in this particular application [111].

Other observations regarding identifying UTS using small specimens were that small curved dog-bone specimens in combination with dog-bone tube can also identify anisotropy in steel tubes [55] and that for SPT there was a critical thickness to grain size ratio (25) over which correlations between maximum load and UTS applied [70].

Overall UTS can be identified from both sub-size standard and SPT specimens, however the results from SPT are less reliable and immediately usable as a suitable correlation needs to be identified or developed. ABI is also suitable for determining UTS, with good agreement to standard test results.

Plastic Behaviour Plastic behaviour is the shape of the uniaxial stress-strain curve beyond the yield stress. Materials and specimens from which plastic behaviour was investigated using small specimens are shown in Table 2.4. Disc tensile specimens (Figure 2.36 (a)) were the bespoke specimens used.

The objective here was to obtain the full stress-strain curve and subsequently parameters for plasticity models. Generally plastic behaviour was directly evaluated from stress-strain curves, especially in the case of sub-size standard specimens. In one case the stress-strain response of a small tensile specimen was significantly different from standard specimen testing results [57], thus showing that even when sub-size standard specimens are used the results might not necessarily agree with standard results. ABI is suitable for finding coefficients of a power law hardening

Table 2.4: Materials and specimens from which plastic behaviour was acquired.

	Steels	Aluminium alloys	Titanium alloys	Zirconium alloys
Sub-size standard specimens	[48, 50, 62]	[51]		
Small punch specimens	[53, 75, 119–121]			[87]
ABI specimens	[75, 89, 91–100, 116]	[101, 103]	[104, 105]	[87]
Bespoke specimens	[54]			

material model, by calculating a stress-strain curve from the indentation diameter, the indenter diameter, applied load and a correlation parameter, which is found iteratively. The strain hardening exponent can be found to be within 2% of the actual value [116]. There was a linear correlation between small punch strain hardening index (calculated from maximum load and limit load) and tensile test strain hardening index, which allowed to convert one into another. Shear punch method used a similar correlation between the shear punch hardening coefficient and the tensile hardening coefficient, it was less accurate than small punch for finding the strain hardening exponent due to larger scatter [75]. Inverse FEA was used as well, in both cases the results matched uniaxial tests well, at least up to UTS, then diverged due to necking [53, 54]. It also had a potential issue regarding the uniqueness of the solution as different stress-strain curves could potentially result in the same small punch response.

Neural networks were used for identifying plastic behaviour from SPT data after having been trained with FEA simulations, with good results [119, 120]. As the model is sensitive to stress triaxiality, at least two experiments at different triaxialities need to be done. Also split Hopkinson bar testing setup with a small tensile specimen was developed and used successfully [51]. Much like for other tensile properties, an appropriate amount of material in the gauge section was important to get data representative of bulk material [62].

Overall, it seems that plastic behaviour can be determined well using all small specimens, at least up to UTS. Necking, occurring after UTS, is very geometry dependent, causing difficulty in calculating standard-equivalent behaviour from test results acquired by using a different geometry.

Elongation at Break/Fracture Strain/Ductility Ductility was evaluated for materials and specimens shown in Table 2.5. Both specimen types were only suitable for ranking. Ductility directly depends on the dimensions of the specimen, as they are reduced, so is ductility [57]. The effect of stress triaxiality on ductility was investigated using small specimens. It was discovered that for both sub-size notched specimens and standard specimens more stress triaxiality lead to fracture at lower strain [122].

Table 2.5: Materials and specimens from which fracture strain and/or ductility parameters were acquired.

	Steels	Magnesium alloys
Sub-size standard specimens	[57, 122]	
Small punch specimens	[67]	[86]

Small Punch Load Line Behaviour Some research was conducted to investigate what influences small punch force-displacement results, without trying to correlate that to specific standard test results. This was done exclusively for steels, with varied SPT specimen dimensions [107, 115, 123–129]. The results showed that the yield load (P_s in Figure 2.38) did not depend on punch diameter, but varied as a square of sample thickness. Maximum load (P_m) increased with sample thickness [125] and punch diameter. Lower sample thickness and smaller punch diameter lead to more scatter [123].

Other observations were that the clamping force used to clamp the small punch specimen between the dies had a significant effect on the maximum load measured during SPT. Increasing the clamping force increases the maximum load measured, therefore an appropriate clamping force needs to be chosen to get material properties representative of bulk material [124]. Increasing cold work increased maximum force [107], which was also as expected, however maximum displacement did not depend on cold work. Orientation was found to be very significant, so if the material is anisotropic it should be tested in the appropriate direction [125]. Maximum force was observed to depend on deflection rate, which agreed well with standard testing results, when numerically the same deflection rate (in mm/s) and strain rate (in 1/s) were considered [115].

As heat treatment affects material properties, it also affects the results from small punch testing [126]. In the study where the response was compared to standard test results, good agreement was found [124]. The suitability of small punch specimen testing for evaluating thermal ageing embrittlement was investigated, however whether the results could be used as anything more than a ranking tool remains to be seen [127]. Liquid metal embrittlement was also investigated using small punch specimens without comparing the results to full-size specimens [130]. The effect of phase transformation due to deformation and loading rates was investigated, it was found that at room temperature the phase transformation enhances material performance [129]. At dynamic loading rates the heating caused by the deformation can cause thermal softening and therefore negative rate sensitivity.

Other Tensile Properties Elongation at maximum load was evaluated for two magnesium alloys using SPT data and a correlation between elongation under maximum load and displacement under maximum load, however the success of this test depended on microstructure of the material being tested [86].

Tensile elongation was also evaluated using SPT data for a sintered material, good agreement with uniaxial results was achived [69], however trying to evaluate it for a variety of unsintered steels via a correlation between it and displacement under maximum load was not successful [72]. It could be that SPT is only suitable for determining tensile elongation for brittle materials or perhaps different correlations are needed.

An analytical solution based on classical plate theory was developed in order to get material properties from SPT, however, it has not been verified [131]. Another investigation related to small punch testing was testing a piece of tube and comparing the response to a response from a flat SPT [132]. It was discovered that friction had a significant effect according to FEA and experimentally and the difference in force-displacement behaviour was due to geometry. Another investigation confirmed the effect of friction on small punch results and investigated the effect of friction on automated ball indentation test results [133]. One study found that surface roughness and the coefficient of friction do not have a significant effect on the results experimentally, which disagrees with other studies, but as there are many variables in small punch testing this could be a coincidence [128].

Sub-size standard specimens were also used for identifying other tensile properties. Uniform elongation was investigated, it was discovered that it was about the same for both standard and sub-size specimens, however total elongation was lower than for a standard specimen [57], which is as expected due to lower gauge volume being able to deform less before failing. Varied thickness (parameter t in Figure 2.29) and gauge length in sub-size standard specimens affects the uniform and total elongation non-linearly [42]. There was also a successful attempt to improve the calculation for UTS by identifying the necking zone using FEA [112]. Reduction in area is similar to standard specimens, however, that depends on specimen shape and size [65, 114].

Other tests that were performed were small punch jump test, which was capable of producing curves similar in shape to tensile jump test, making it suitable for evaluating deformation mechanisms and evaluating strain rate sensitivity [117]. Shear punch and ABI tests were used to find uniform elongation and a good linear correlation between it and strain hardening coefficient was found [77].

2.5.2 Cyclic Testing

Small cyclic plasticity and fatigue specimens come in all four categories as well. Sub-size standard specimens were dog-bone specimens described earlier, button-head specimens and hourglass specimens shown in Figure 2.41 and sub-size fatigue specimens described earlier.

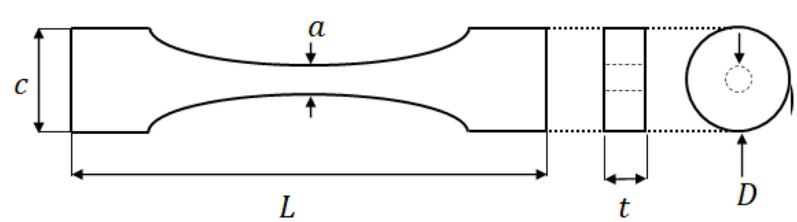

Figure 2.41: Different type of hourglass specimen. L is 45 or 30 mm, a is 3 or 4 mm, c is 6 or 7 mm, t is 0.5 mm and d is either 1 mm or 2.1 mm.

Small punch specimens, loaded according to the diagram in the Figure 2.42 (a), were used for fatigue testing with alternating deformation applied by the top and the bottom punches. Similar to the small punch, a hydraulic bulge specimen, shown in Figure 2.42 (b), was loaded with alternating pressure applied on the top and the bottom side of it, as per Figure 2.42 (c).

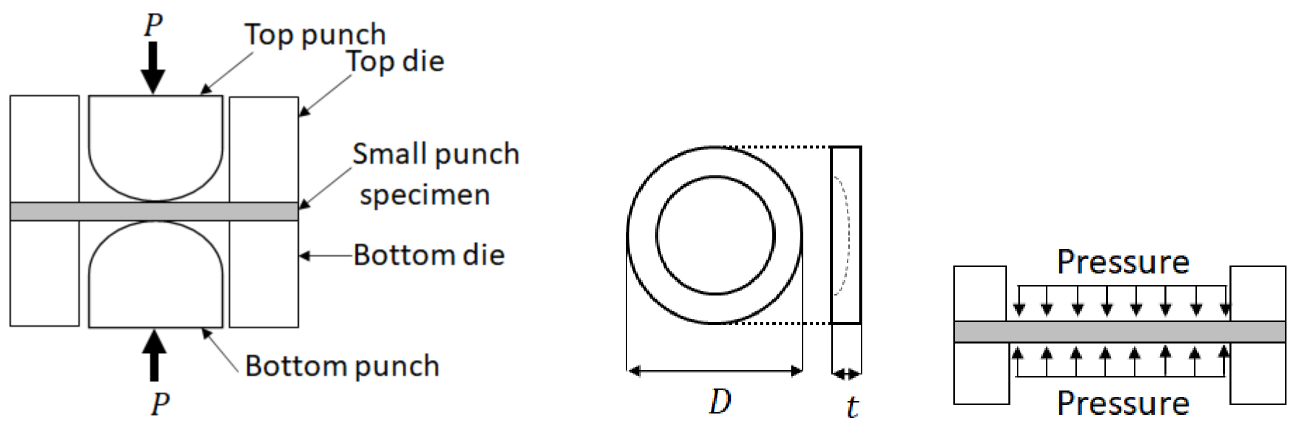

(a) (b) (c)

Figure 2.42: (a) Small punch specimen fatigue loading diagram; (b) Hydraulic bulge fatigue specimen. D is 8 mm and t is 0.4 mm; (c) Hydraulic bulge fatigue loading diagram.

ABI specimens are unspecified and bespoke specimens are small high cycle fatigue specimens shown in Figure 2.43 (a), modified Krouse type specimens shown in Figure 2.43 (b), small flat disc specimens shown in Figure 2.43 (c) (loaded similarly to the disc tensile specimens) and wire specimens. Small cruciform specimens (used to test material behaviour under biaxial loading) also exist, but due to their dimensions being bigger than the maximum size limit of this review they are not included.

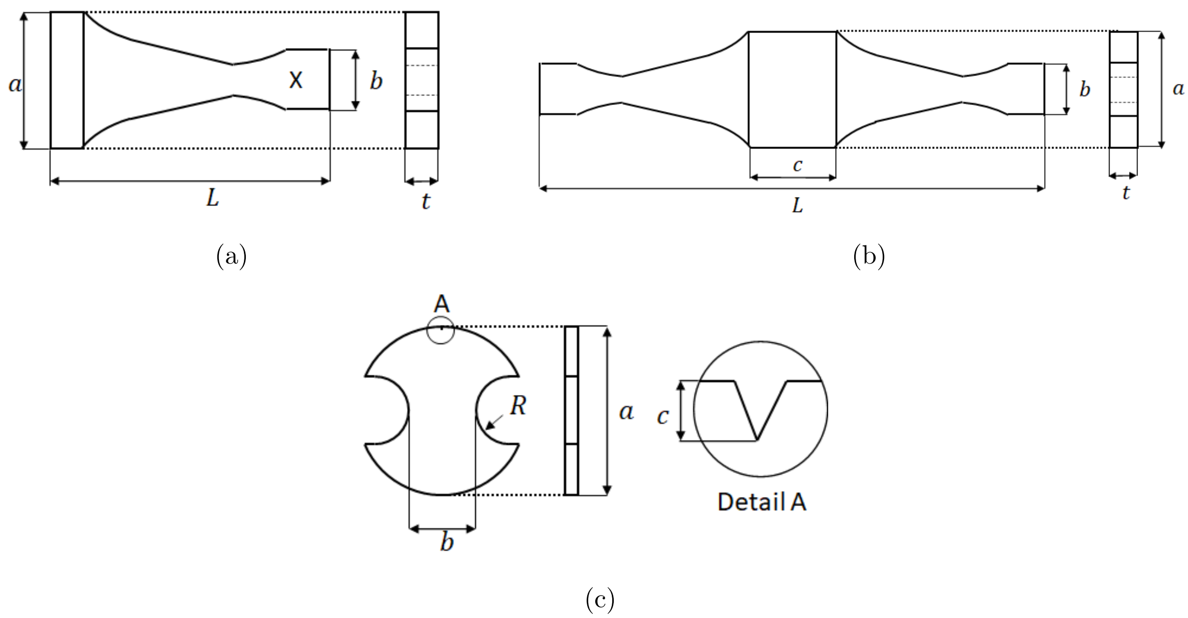

Figure 2.43: (a) Specimen designed for high cycle fatigue testing. Also referred to as high cycle specimen. L is 13.67 mm or 15.72 mm, a is 6.59 mm or 6.8 mm, b is 4.33 mm or 3.78 mm and t is 1.09 mm or 1 mm, loaded by applying an oscillating load near x. (b) Modified Krouse type specimen. L is 30 mm, a is 8 mm, b is 4 mm, c is 7 mm and t is 0.65 mm. (c) Small flat disc specimen. a is 15 mm, b is 6 mm and R is 3 mm, notch at the top.

Low Cycle Fatigue Life Sub-size standard specimens have been used to determine low cycle fatigue life for steels [134–137] and nickel alloys [44, 45]. All tests were done with fully reversible loading.

In general small specimen test results match standard specimen results well. Round bar specimens (Figure 2.30 (b)) were not sensitive to size effects, while hourglass specimens (Figure 2.30 (c)) were [134, 135]. Surface roughness was an important factor to control for [136], however useful recommendations are lacking in the literature. Overall small specimens seem to be suitable for determining low cycle fatigue life, however size effect needs to be considered when interpreting the results.

High Cycle Fatigue Life High cycle fatigue testing of small specimens was investigated for an aluminium alloy using a specially designed high cycle specimen (Figure 2.43 (a)) [138, 139], and for a steel using a sub-size hourglass specimen [47]. Tests were performed with fully reversible loading.

The conclusions from both papers about the high cycle specimens were that microstructure had a significant influence on fatigue life as small grains without dislocations resulted in higher fatigue life. The fatigue life identified could only be used for ranking due to being lower than textbook values [138, 139]. It may be the case that grain size relative to the specimen size should be considered in order to get data that is suitable for more than ranking. Sub-size hourglass is particularly suitable for determining high cycle fatigue life, the results being within the scatter band of standard testing results [47].

General Fatigue Life Estimation Materials and specimens used to determine general fatigue life are shown in Table 2.6. Some of the tests were done without fully reversible loading, due to the specifics of the testing technique, such as ABI [140] or testing a wire specimen (Figure 2.35) as it would buckle [111]. Another interesting observation regarding fatigue life was that it can be predicted well when a single crystal of pure iron was tested as a representative sample of an extra-low carbon steel [141]. Small flat disc specimens (Figure 2.43 (c)) were determined to not be suitable as their results depended too much on stress concentrations making them unreliable [142]. Small round bar specimens (Figure 2.30 (b)), like their full-sized counterparts, experienced buckling with reversed loading. Small hourglass specimens (Figure 2.30 (c)) had a longer fatigue life than determined from a standard round bar specimen when a larger strain range was applied and shorter fatigue life when a smaller strain range was applied [143]. This makes it not suitable to consistently characterize the full fatigue life.

The effect of irradiation on fatigue life was investigated, the in-beam material had fatigue life extended by a factor of 2, while the post-irradiation material had fatigue life extended by a factor of 2.5 [147]. The effect of notches was investigated from two different angles. First one was the effect of surface roughness, where the roughness was considered to introduce notches. It was discovered that small polished specimens had a fatigue life closer to that of standard specimens than rougher specimens with roughness adjusted for [64]. The other angle was investigating the effect

Table 2.6: Materials and specimens from which general fatigue life estimation was acquired.

	Steels	Aluminium alloys	Nickel alloys	Titanium alloys
Sub-size standard specimens	[64, 113, 114, 140, 143–145]	[140]	[64]	[64]
Sub-size standard specimens (notched)	[141, 146, 147]			
Other specimens	[111, 140–142, 148–151]	[140, 152]	[153, 154]	[153, 155]

of nitriding on steel using small specimens. It was discovered that for smooth specimens nitriding increases fatigue life unless load amplitude was increased, but a notch significantly reduced fatigue life [146]. Also the fatigue life of the wire specimen was determined to be significantly longer than of a standard specimen, which meant that there was a significant size effect [111]. The high cycle specimen and the modified Krouse specimen both can be used to characterize the whole fatigue life curve, by applying a different stress range calculated according to beam deflection formula. As the stress values are calculated according to the deflection and applied load, it is very important for those to be measured accurately [149, 150]. Modified Krouse specimen was designed for testing additively manufactured material, the dual gauge providing a higher area and sensitivity to manufacturing defects [149].

Small punch fatigue testing looks like a promising technique for determining cyclic plasticity and fatigue life evaluation, however currently there are no correlations developed to actually calculate them [153, 155]. Cyclic ABI (constant load amplitude) testing is a promising technique for evaluating fatigue life, but, similarly to small punch fatigue testing, there currently is no way to convert the cyclic ABI life data to standard life data [151, 154]. Evaluating when exactly failure occurs is difficult in post-processing, therefore acoustic emission should be used instead [154].

Overall small specimens are capable of determining fatigue life. The main challenges with small specimen fatigue testing are the inconsistent size effects for some specimens, certain specimens only being suitable to be loaded in tension-tension as opposed to tension-compression due to buckling and complicated methods required to interpret data, especially when the results from a multiaxial stress state in a small specimen need to be correlated to results from a uniaxial stress state in a standard specimen.

Other Properties Evaluated from Fatigue Testing Other properties evaluated from small specimen fatigue testing include residual fatigue life, which has been evaluated for a nickel superalloy using sub-size standard specimens, however, due to low amounts of material available it was not directly verified by using standard specimens [44]. An ABI test was determined to be suitable to indicate fatigue damage for a set of various metallic materials, but not to quantify it [140]. Ratcheting was investigated using a wire specimen (Figure 2.35) made from stainless steel, and it was determined that ratcheting strain rate decreased when the number of cycles increased and the wire specimen had a strong memory of previous loading history [111].

2.5.3 Modelling

Small specimen modelling is important in order to understand the stress state and deformation behaviour as the specimens are being loaded, as well as to develop methods to interpret their test results. The behaviour of small punch specimen under tensile loading has been investigated the most [53, 72, 76, 82, 112, 119, 120, 126, 129, 132, 151, 156]. The main decisions to be made when modelling small punch specimens are whether to include damage in the model, whether to use a deformable or rigid clamping setup and whether to use an axisymmetric or 3D model. As small punch specimens experience high levels of deformation and early yield, including damage allows for more accurate modelling of the force-displacement curve up to the maximum load, while not including damage requires additional correlations for accurate maximum load [156]. Deformable clamping setup (punch and plates clamping the specimen in place) is more representative of reality even if the punch and clamping plates are significantly stiffer than the specimen [82, 132], but it is also more computationally expensive, as significantly more elements have to be used, while offering inconsistent benefits, therefore the majority of small punch models used rigid setup [53, 72, 112, 119, 120, 126, 129, 151]. Flat small punch specimen loaded with a vertically displaced punch is axisymmetric, allowing for the use of axisymmetric model [72, 82, 112, 119, 120, 126, 129, 151], but if the specimen is curved [132] a 3D model has to be used.

In some cases FEA modelling results were used to train neural networks to replicate the FEA in order to speed up calculations [119,120]. Some other uses of modelling were to investigate things difficult to investigate experimentally, such as the effect of the coefficient of friction and tracking the change of thickness as the specimen deforms [82].

ABI loading was also relatively frequently modelled, deciding whether to use a rigid [96, 151] or a deformable [80, 116] ball is important. As with SPT, rigid ball is not realistic, but it also increases the computational cost of the model. The primary use of these models was to understand the stress state as the loading progresses.

Subsize standard specimens and similar were also modelled, using symmetry where possible to reduce the computational cost [42, 54, 62, 66, 141]. As grips on such specimens are usually far from the gauge section, deciding whether to model them as rigid or deformable is not important. These models were used for investigating stress distribution [42, 62, 66, 141] as well as to calculate the material properties using inverse analysis [54].

Modelling fatigue behaviour is usually computationally expensive, as a large number of cycles have to be modelled. Small specimens under cyclic loading that were modelled were specimens similar to standard [135], spot welded specimens [48], SPT [151, 155], ABI [151] and hydraulic bulge [148, 151], however, some of these did not model actual cyclic behaviour, only a snapshot of stress state. Similarly to other small specimens, the main interest was in the stress state as the loading progresses, as well as the effects of factors difficult to investigate experimentally, such as the optimal geometry of specimen [148].

2.5.4 Fracture Morphology

As fracture morphology enables the identification of the mechanism of failure, it can be used to identify if small specimen failure behaviour is representative of standard specimen failure behaviour and whether small specimen testing can then be used to predict it.

Fracture morphology of small specimens was investigated for specimens tested under tension [62, 67, 68, 72, 80, 85, 118, 122, 124, 125, 127–130, 133], fatigue [66, 135, 138, 139, 141, 145–147, 150, 153, 155] and fracture testing [59, 60] conditions. The majority of investigations focused on small punch specimens [67, 68, 72, 80, 85, 118, 124, 125, 127–130, 133, 153, 155], much like the majority of recent investigations in the field of small specimens in general. Others were on small hourglass [135, 136, 145], dogbone [62, 66, 122, 141, 147], round bar [135], small Charpy [59, 60] and high cycle [138, 139, 150] specimens.

Fractography was used to identify the mechanism of failure (ductile or brittle, examples shown in Figure 2.44), where exactly the crack initiated (weakened grain boundary, surface defects, or inclusions) and how it propagated (microvoid coalescence, integranular or transgranular). Images of fracture surface were taken using SEM as it allows to observe the uneven fracture surface due to having a depth of focus as opposed to a point of focus, like optical microscopes.

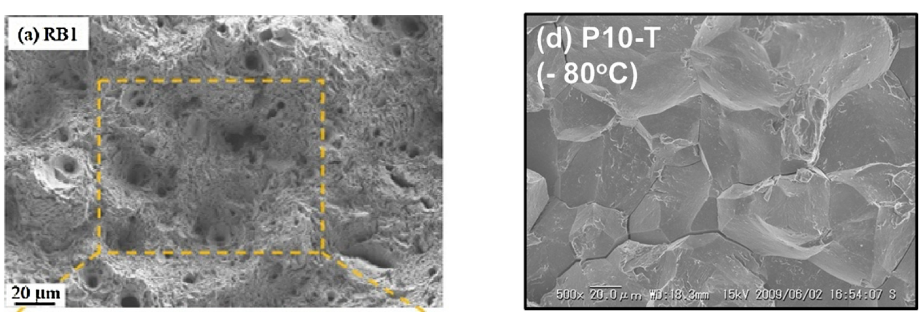

(a) (b)

Figure 2.44: Example of (a) ductile fracture surface (as adapted from [122]); (b) brittle fracture surface (as adapted from [60]).

For specimens loaded under fatigue conditions, fractography allows to identify whether fatigue damage took place, as it results in characteristic striations (example shown in Figure 2.45) or beach marks on the fracture surface (stage 2 crack propagation) [66, 135, 138, 139, 141, 145–147, 150]. For small punch specimens loaded with fully reversed fatigue loading the striations were abraded and could not be seen [153, 155]. As cracks initiate in areas with stress concentration, that location can be used to calculate the stress ratio the specimen experienced (using FEA) as opposed to trying to relate the applied load ratio to uniaxial fatigue test results [141].

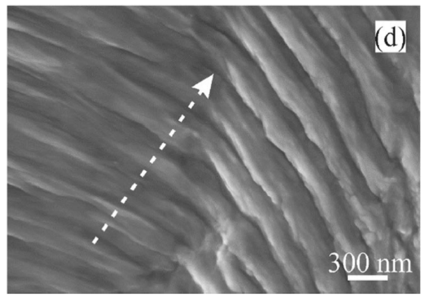

Figure 2.45: Example of fatigue fracture surface. As adapted from [66].

2.5.5 Creep Testing

As creep is the material property recently investigated using small specimens the most it is useful to include a short overview of small creep testing here. The small specimens for creep testing come from all subcategories, as per [157]. Sub-size standard creep specimens used are shown in Figure 2.46. They are loaded the same way as regularly sized specimens are and the data interpretation is also the same.

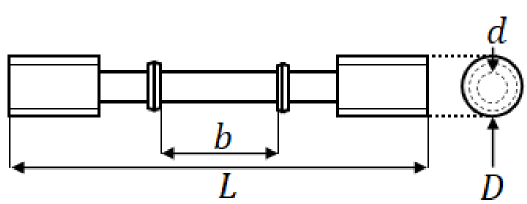

Figure 2.46: Sub-size standard creep specimen. L is around 30 mm, b is around 10 mm, d is around 2 mm and D is around 10 mm.

Small punch specimens used for creep testing are round, as shown in Figure 2.31 (a), with a diameter of around 8 mm and thickness of 0.5 mm.

Indentation specimens used are rectangular plates for instrumented indentation, as shown in Figure 2.47 (a). Indenters of a variety of geometries are used, the indenter is pushed into the specimen and the load/displacement response is recorded, as per Figure 2.47 (b).

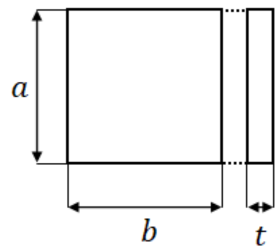

(a)

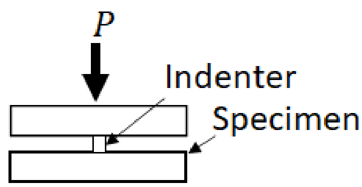

(b)

Figure 2.47: (a) Indentation specimen. a is around 10 mm, b is around 10 mm and t is around 1 mm; (b) Indentation specimen testing diagram.

Bespoke specimens include two-bar specimens shown in Figure 2.48 (a) loaded by a constant load between pins, as per the diagram in Figure 2.48 (b), as well as small ring specimens, which will be described in more detail, as the small ring specimen tensile and cyclic testing techniques are based on them.

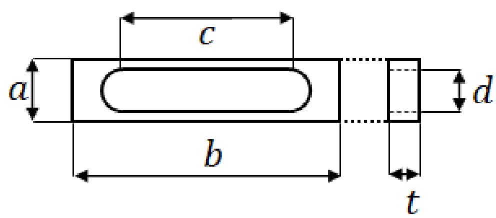

(a)

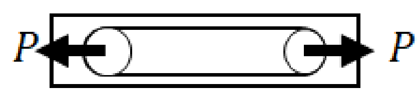

(b)

Figure 2.48: (a) Two-bar specimen. a is around 9 mm, b is around 26 mm, c is around 13 mm, d is around 5 mm and t is around 1 mm; (b) Two-bar specimen testing diagram.

Small Ring Specimen Creep Testing The small ring specimen creep testing setup was developed by Hyde and Sun [1]. It was based on a standard creep specimen, adapted to load a small ring specimen as shown in Figure 2.49.

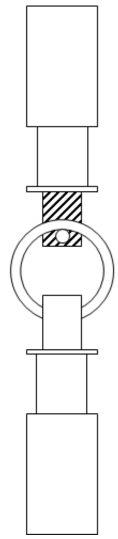

Figure 2.49: Small ring creep loading setup. The pin diameter is 2.5 mm, the inner ring diameter is 9 mm and the overall length of the setup and other dimensions are the same as shown in Figure 3.1.

The small ring specimens were tested by first keeping the ring slack to provide space for the setup to expand during heating. Then heating was applied in the form of a furnace, when stable temperature was achieved, a small pre-load of around 10 % of the applied load was applied, then the load was applied and the specimen was allowed to creep [158].

Regarding the data interpretation, force-displacement data was collected from a load cell and an LVDT, with the LVDT setup described in [1]. Then the force-displacement data was transformed into creep data by using an analytical solution based on thin beam theory [159].

2.6 Summary

To summarize, metallic materials are generally crystalline and their crystal structures and grain size influence their properties. Monotonic material behaviour is usually characterized by a stress-strain curve, which can be described using several different material models, the one most of interest in this work is the Ramberg-Osgood material model.

There are two aspects to cyclic behaviour: fatigue life and cyclic plasticity. Fatigue life is characterized by an S-N curve and cyclic plasticity is characterized by the evolution of hysteresis loops during cyclic loading and can be described using several different material models, the one most of interest in this work is the combined hardening model.

Environmental and processing factors influence material behaviour. The main influences are temperature, heat treatment and cold work. Most of those effects are heavily material dependent.

There are standardised methods to evaluate those material properties, using specific loading setups, specimens and loading rates. For tensile testing, dog-bone specimens are commonly used, but other specimen geometries are used for specific applications. For cyclic testing, round bar or hourglass specimens are commonly used, but similarly to tensile testing, other specimen geometries are used for specific applications.

In the cases when there is not enough material for full size standardised tests to be done, small specimen testing is used. There are two most commonly used types of small specimens, sub-size standard specimens and small punch specimens, as well as a number of bespoke specimen geometries. The data interpretation of sub-size specimens is similar to the interpretation of standard specimen results. As for other specimen geometries, the majority of data interpretation is based on correlations that are material specific and therefore not always applicable.

Sub-size standard specimen testing for both tensile and cyclic properties is well understood, as well as various factors which affect the various small specimen test results. For non-standard specimens, material-independent test result interpretation methods are lacking, as well as detailed investigations into effects of surface roughness, grain size and repeatability.

Literature is lacking regarding evaluating Young's modulus from non-standard specimens and the specifics of the plastic behaviour under tensile loading. There also is a lack of non-standard specimen research for low-cycle fatigue applications and cyclic plasticity properties. Current non-standard specimens provide issues with applying fully reversible loading and identifying when exactly failure occurred.

Developing a small ring specimen cyclic testing method would result in a simple way to apply fully reversible loading, identifying failure and evaluating cyclic plasticity and low cycle fatigue properties.

2.7 Objectives of the Project

The main overall objective of the project was to develop a small ring specimen cyclic testing technique. There were several objectives that needed to be achieved before this main objective could be achieved. To begin with, the suitability of small ring specimens for tensile testing had to be evaluated, as if they could not be used for tensile testing it would be extremely unlikely that they could be used for cyclic testing, especially as the first quarter cycle of a cyclic stress-strain curve is functionally a tensile stress-strain curve. This means that the first step towards developing a small ring specimen cyclic testing technique was developing a small ring specimen tensile testing technique.

The development of a small ring specimen tensile testing technique had several objectives of its own. First of all, a method to test the small ring specimens under tensile loading had to be developed. Then a representative model had to be developed to understand the stress-state in the small ring as it deforms, which would then lead to developing a method to calculate standard-equivalent stress-strain behaviour from the force-displacement results. Afterwards the suitability of the small ring specimen for tensile loading had to be evaluated.

Following that, the small ring specimen cyclic testing technique had to be developed, with certain aspects of it based on the tensile testing technique. A novel fixture had to be developed, as the creep testing setup, which was used for tensile testing, was not suitable for applying reversible cyclic loading. Then a methodology for using the fixtures effectively had to be developed. Similarly to the tensile testing technique, a representative FEA model had to be developed, in order to understand the stress evolution in the ring during loading and evaluate the effects of material and geometry parameters. Having understood the stress evolution, a method to interpret the small ring specimen cyclic testing data to get standard-equivalent cyclic plasticity data and potentially fatigue data would be derived.

3 Methodology

3.1 Introduction

This chapter contains the description of the materials used during this project, the specimens used and how they were manufactured. As grain size and failure mechanism are important to know when using small specimens, the methods for specimen preparation and microscopy are also included.

Standard testing techniques for materials under tension and cyclic loading, which were used to acquire data for comparison with small ring specimen test results, are described.

As the conventional test results were used for modelling, material models needed to be fitted to them and the fitting procedures are also included in this chapter, as well as the models used to model the small ring specimens under tensile and cyclic loading.

3.2 Materials

3.2.1 7175-T7153 Aluminium

One of the materials tested was aluminium alloy 7175-T7153, with the composition shown in Table 3.1. This material was chosen as it is being considered for aircraft gearbox housing applications and some tensile testing data at room temperature and elevated temperatures was available [160]. As mentioned in the Literature review, small specimens are used in situations when not enough material is available for standard specimens and aerospace components under high loads and high temperature operating conditions are too small for standard specimens to be made. It was supplied by Amari-Aerospace Ltd. in the form of 1.5 m x 1.0 m x 0.03 m hot rolled plate. This material is a heat treated wrought alloy. The T7351 heat treatment is solution heat treatment with artificial ageing for improved stress corrosion resistance, performed by heating it to above the solid solution temperature, quenching, then stretching in a controlled way to relieve stress, then artificially overaging to achieve corrosion resistance. The effects of overaging are described in Section 2.3.4. The grain size of the material is around 250 nm^2, found from TEM images of the material [160]. The grain size is small enough that this material can be used for small ring specimen testing, as there is a sufficient number of grains through each dimension of the cross-section [161].

Table 3.1: Aluminium 7175-T7153 composition [160].

Name	Zn	Mg	Cu	Cr	Ti	Fe	Mn	Si	Other	Al
wt %	5.7	2.5	1.6	0.2	0.04	0.06	0.02	0.03	0.02	Bal

3.2.2 2014A-T6 Aluminium

Another material tested was aluminium alloy 2014A-T6, with the composition shown in Table 3.2. This material was chosen due to it being an aerospace alloy, used for high strength structural components in the aerospace industry, and the availability of uniaxial tensile data from undergraduate tensile labs. It is a heat treated wrought alloy. The T6 heat treatment is a solution heat treatment with artificial ageing, performed by heating the casting above the solid solution temperature, quenching it, then heating it to lower temperature to allow precipitates to form, then cooling in air. The presence of precipitates increases the strength and hardness of the material, as described in Section 2.3.4. The material for the small ring specimens was supplied by Nigel Smith Alloys Ltd. in the form of a rod with a diameter around 1/2".

Table 3.2: Aluminium 2014A-T6 composition [162].

Name	Si	Fe	Cu	Zn	Mn	Mg	Ti	Other	Al
wt %	0.50-2.10	0-0.70	3.9-5.00	0-0.25	0.40-1.00	0.20-0.80	0-0.15	0-0.15	Bal

3.2.3 6082-T6 Aluminium

The last aluminium alloy tested under tensile loading was 6082-T6, with the composition shown in Table 3.3. It was also chosen due to being a structural aerospace alloy and the availability of uniaxial tensile data from undergraduate tensile labs. It is a heat treated wrought alloy and was supplied by Nigel Smith Alloys Ltd. in the form of a rod with a diameter around 1/2".

Table 3.3: Aluminium 6082-T6 composition [163].

Name	Mn	Fe	Mg	Si	Cu	Zn	Ti	Cr	Al
wt %	0.40-1.00	0-0.50	0.60-1.20	0.70-1.30	0-0.10	0-0.20	0-0.10	0-0.25	Bal

3.2.4 P91 Steel

Another material tested was P91 steel supplied in the form of a pipe with a 298.5 mm outer diameter and 55 mm wall thickness [164], austenized at 1060^{o}C for 45 minutes, then tempered at 760^{o}C for 2 hours, the composition is shown in Table 3.4. As described in Section 2.3.4, this heat treatment is intended to produce tempered martensite, which improves the toughness and machinability of the material. This material was chosen due to availability of tensile data and being used in power plant pipes, which is a potential application for small ring specimens [165]. Due to the heat treatment the microstructure of the material is martensitic therefore the grain size was not investigated.

Table 3.4: P91 steel composition [165].

Name	C	Mn	P	S	Si	Cr	Mo	V	N	Ni	Al	Cb	Ti	Zr	Fe
wt %	0.08-0.12	0.3-0.6	$\leq$0.02	$\leq$0.01	0.2-0.5	8-9.5	0.85-1.05	0.18-0.25	0.03-0.07	$\leq$0.04	$\leq$0.02	0.06-0.1	$\leq$0.01	$\leq$0.01	Bal

3.2.5 Oxygen Free High Conductivity Copper

The last material tested was oxygen free high conductivity (OFHC) copper (grade C110), with the composition shown in Table 3.5. It was supplied by Nigel Smith Alloys Ltd. in the form of a rod with a diameter of around 19 mm. This material was chosen due to the availability of a wide range of low cycle fatigue test data [166], being soft and easy to machine. This material is a wrought copper alloy. Material was annealed at 600^{o}C for 1 hour or at 700^{o}C for 1 hour in order to compare the experimental results with the results found in literature [167, 168].

Table 3.5: Copper 110 composition [169].

Name	Cu	P	S	Pb	Other (including As, Ab, Bi, Cd, Mn, Se, Te, Zn)
wt %	99.99	0-0.0003	0-0.002	0-0.001	Bal

3.3 Specimens

3.3.1 Tensile Specimens

Standard creep specimens (shown in Figure 3.1) were used for tensile testing and data collected from testing standard tensile specimens (shown in Figure 3.2) was used as well [160]. Standard creep specimens were used for testing 7175-T7153 aluminium and P91 steel, because the rings are loaded using a modified creep specimen. They were manufactured using a lathe.

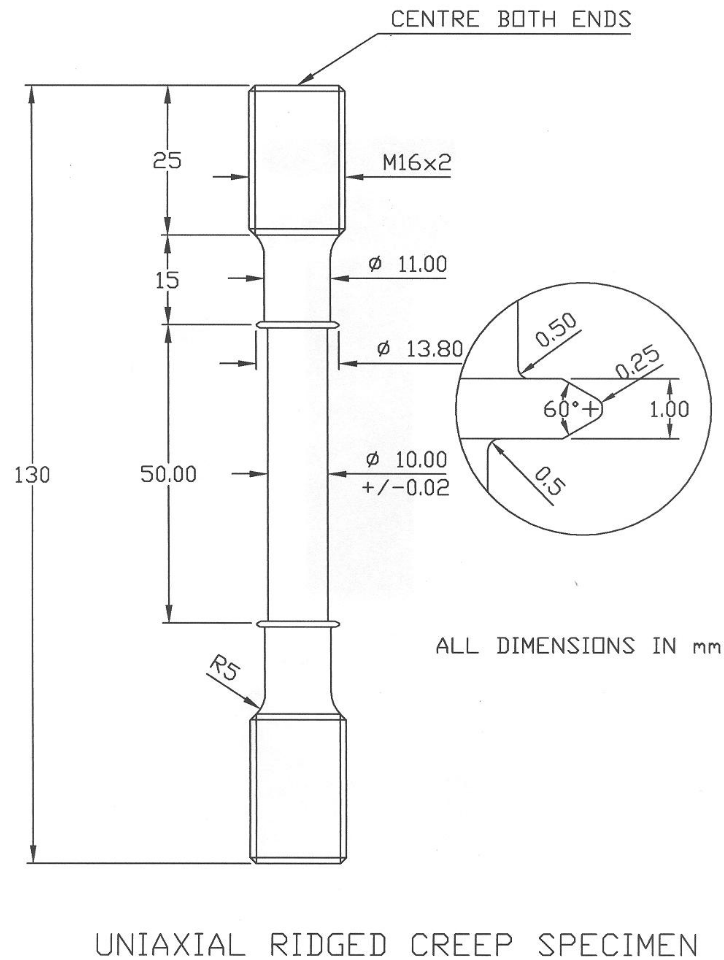

Figure 3.1: Standard creep specimen (as adapted from [170]).

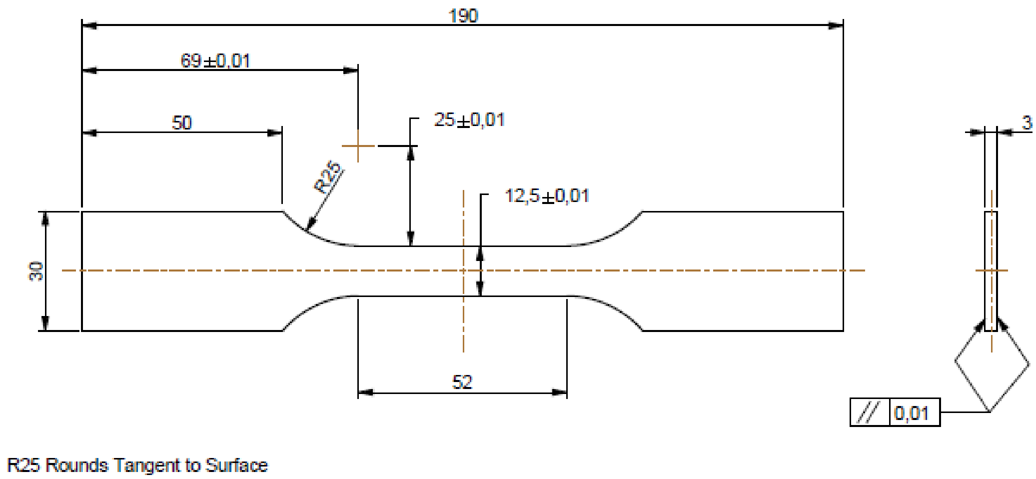

Figure 3.2: Standard tensile specimen (as adapted from [160]).

Standard specimens of different geometry than described previously (Figure 3.3 (a)) were used in undergraduate labs for tensile testing 2014A-T6 and 6082-T6 aluminium. These specimens were stamped, with the edge shown in Figure 3.3 (b).

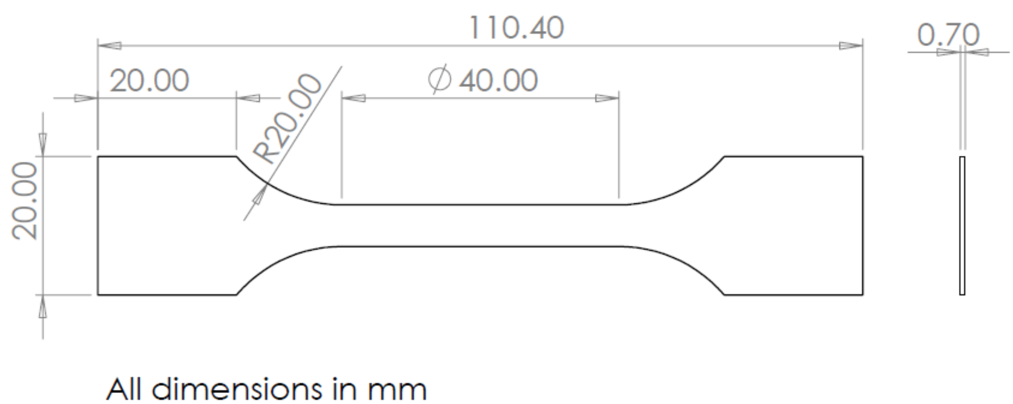

(a)

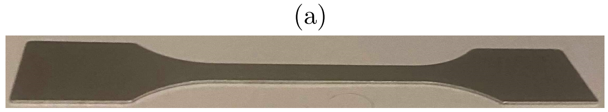

(b)

Figure 3.3: Standard tensile specimen used in undergraduate labs (as adapted from (M. Mason, personal communication, May 2, 2019)).

3.3.2 Cyclically Loaded Specimens

Standard fatigue specimens suitable to be tested on a Tinius Olsen machine were used, shown in Figure 3.4. They were manufactured by turning a rod on a lathe, then cutting threads on the ends. The expected surface roughness on the gauge length due to manufacture is between 0.8 μm and 0.1 μm.

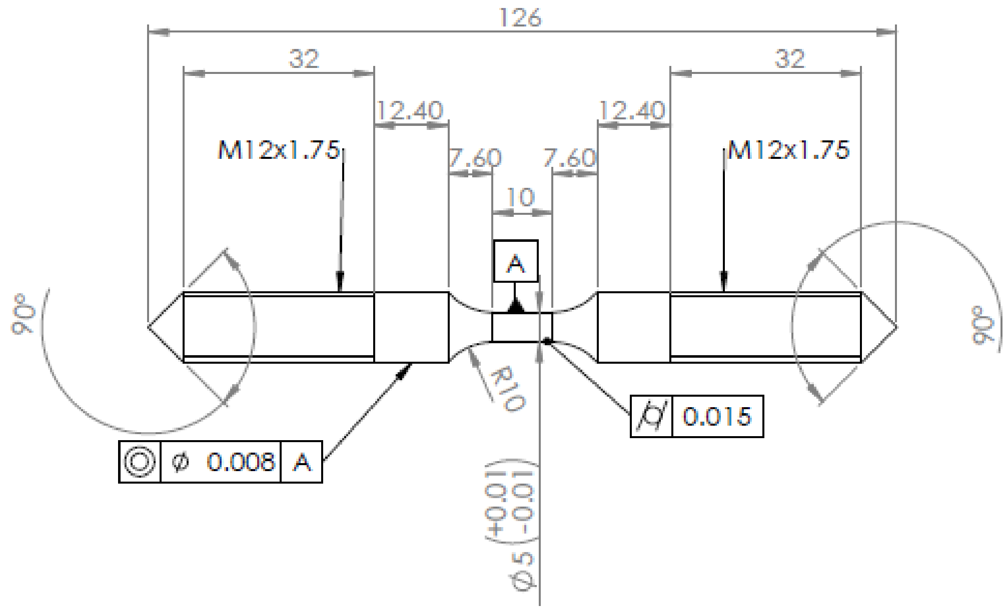

Figure 3.4: Standard fatigue specimen for a Tinius Olsen machine (as adapted from (S. Maskill, personal communication, June 4, 2019)).

3.3.3 Small Ring Specimens

A small ring specimen has an outer diameter of 11 mm, inner diameter of 9 mm (radial thickness of 1 mm) and lateral thickness of 2 mm, as shown in Figure 3.5 (a). These specimens were first developed as small creep testing specimens by Hyde and Sun [1]. In order to make the descriptions of specimen clearer, lateral thickness and radial thickness are defined in Figure 3.5 (b).

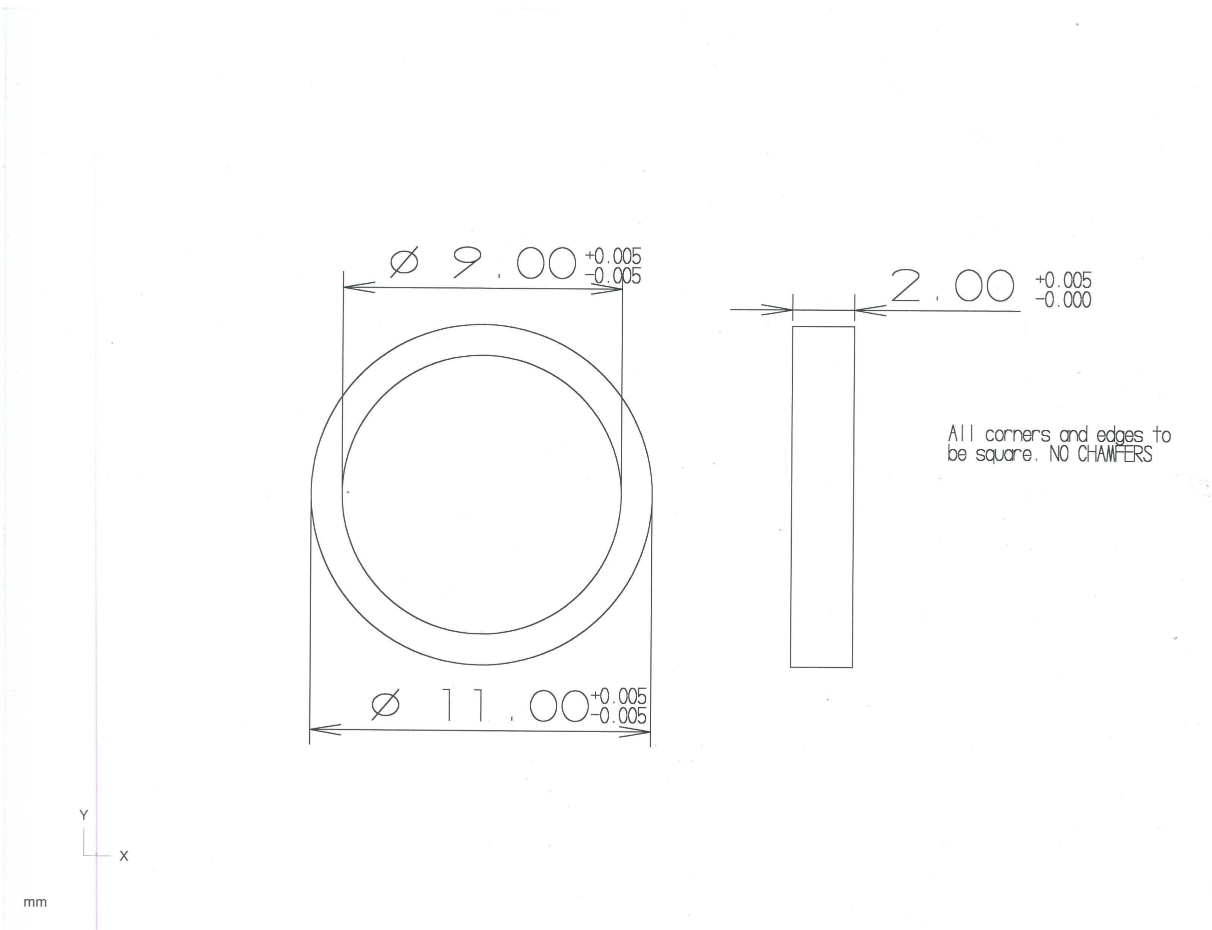

(a)

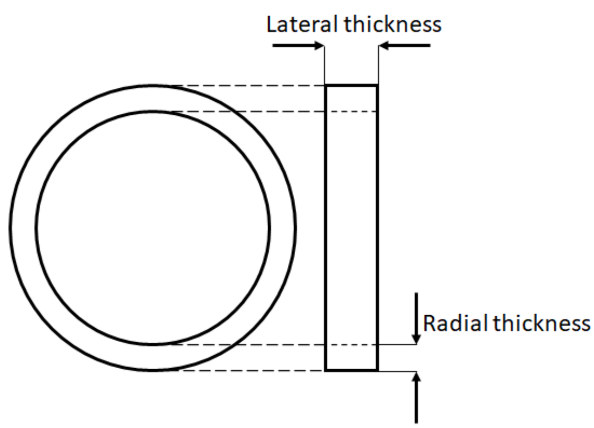

(b)

Figure 3.5: (a) Small ring specimen (as adapted from [1]). (b) Radial and lateral thickness on the small ring specimen.

To manufacture the specimens the material stock was held in the collet chuck, faced across, then the outside diameter was machined down to about 0.5 mm over the finished size by using small cuts. The hole was center drilled to around 8.5 mm diameter, then reamed to 9 mm diameter using a taper shank machine reamer. The outside diameter was cut to the finished size and sharp edges were deburred. The rings were cut off using a part off tool, then deburred again using fine wet and dry abrasive paper.

3.4 Standard Testing Methods

3.4.1 Tensile Testing

All standard tensile tests for 7175-T7153 were done on a Mayes 250 testing machine with a 25 kN load cell. Loading rates were selected to accompany previous studies of this material [160] to check for rate dependency, 10 mm/min and 0.1 mm/min. LVDT displacement control mode was used. Tests were done at room temperature, 160^{o}C and 200^{o}C using standard creep specimens described in Section 2.5.5.

Tensile data for P91 was taken from previous investigations into this material [171] and unpublished test results (J. P. Rouse, PhD, University of Nottingham, document, April 16, 2016).

Tensile test data for 2014A-T6 and 6082-T6 aluminium was taken from undergraduate lab results carried out at the University of Nottingham. Tests were done at room temperature, 5 mm/min loading rate on an Instron 3369 testing machine with cross-head displacement control.

The initial results were in the form of force-displacement, with force readings taken from the load cell of the machine and displacement readings taken from an LVDT (apart from undergraduate test results, where the displacement readings were taken from the cross-head). The force measurements were transformed into stress by dividing the force by the cross-sectional area of the gauge section, while the displacement measurements were transformed into strain by dividing the displacement by the original length of the gauge length between where the LVDT was attached. As for the undergraduate test results there was no LVDT data, it was assumed that all of the deformation occurred in the gauge section, which makes the results less accurate than the ones where LVDT results were available.

3.4.2 Cyclic Testing

All standard fatigue tests were done on a Tinius Olsen H25KS testing machine with a 25 kN load cell in LVDT displacement control mode, with R ratio of -1. Material used was OFHC copper annealed at 600^{o}C and 700^{o}C. Loading rates were selected to get the same strain rate as in literature [167, 168], for 700^{o}C anneal it was 0.002 mm/s, then 0.02 mm/s to check for rate sensitivity in order to see if the small ring specimen tests could be sped up, for the 600^{o}C anneal it was 0.02 mm/s. The test for the 700^{o}C anneal was run for 55 cycles, the 600^{o}C anneal was run to failure and then for 50 number of cycles to get more detail about the shape of the hysteresis loop and to be able to fit a combined hardening model to the data. All of the tests were done at room temperature. Horizon software was used to control the tests.

Similarly to standard tensile tests, standard cyclic tests had force and displacement as outputs. Force was transformed into stress by dividing the force values by the cross-sectional area, while displacement was transformed into strain by dividing it by the original gauge length between the LVDT attachment locations.

3.5 Specimen Characterization

3.5.1 Grain Structure

In order to find out the grain size of the materials and see if they are suitable for small ring testing (have enough grains in the cross-section), specimens were prepared for microscopy by using the conventional sequence of actions: the specimens were cut, mounted, ground, polished and etched to reveal the grain boundaries.

Cutting was done by clamping the specimen in a vice, then cutting it in half with a cutting disc. The untested specimens were cut in half without taking account of direction, as specimens were made from rods and direction was not relevant. The tested specimens were cut in half at a halfway point between where contact with the pins occurred, as some specimens thinned and failed at the point of contact, making that area not suitable for grain size estimation.

The specimens were then mounted in resin, Conductmount Black. Stainless steel stands had to be used in order to keep the specimens upright during the mounting process. The mounting was done by putting the specimen in the stand, making sure that the cut surfaces were flat on the mounting machine surface in order to minimize the grinding required, then resin granules were poured, and pressure applied. The mounting machine then heated the resin with the pressure still applied in order to cure the resin, then cooled the resin to make sure it solidified and kept the specimen in place. The mounted specimen was then taken out of the machine and left to cool to room temperature.

Afterwards the specimens were ground by using a machine with rotating discs of sandpaper, lubricated with water. The rotation speed was around 300 rpm. The sandpaper used was of increasing grit, from 240 to 400, to 800, to 1200. At first the sharp edge caused by the mounting had to be removed, then the surface was ground until all the scratches on the surface were in the same direction. Then the specimen was rotated 90^o and ground until all the scratches were in the opposite direction. For the subsequent grits, the specimen was ground only once, until all the scratches were in the same direction. Due to the small size of the visible cross-section, it was difficult to evaluate the quality of grinding, especially at higher grits, and a microscope had to be used to evaluate if the specimen needed to be reground. Between the different grits used, the specimen was cleaned.

Then the specimens were polished, initially with Planocloth (roughness of 6 μm) lubricated with white spirit, then with Alphacloth (roughness of 1 μm) lubricated with white spirit. While during grinding the specimens were kept in place, during polishing they were moved in the opposite direction of the rotation of the polishing device to speed up the process. The duration of polishing was around 45 s per specimen. Between the different polishes the specimen was cleaned.

After an appropriately smooth surface was achieved (without significant scratches remaining), the specimens were etched. Copper specimens were etched using aqueous ferric chloride solution (100 ml distilled water, 5-50 ml hydrochloric acid and 5-25 g ferric chloride) by immersing for a few minutes then washing. Specimens made from 2014A-T6 aluminium were etched using Keller's etch (190 ml distilled water, 5 ml nitric acid, 3 ml hydrochloric acid, 2 ml hydrofluoric acid). The specimen was immersed for 10 s, washed, then inspected with a microscope to see whether grain boundaries were visible, if they were not visible the process was repeated. Specimens made from 6082-T6 aluminium were etched using ASTM No.2 etchant (1 g NaOH and 100 ml deionized water) by swabbing for 10 s, then washing.

Grain size was evaluated by taking images of polished specimen surfaces, drawing lines across, counting the number of grains along the lines and dividing the length of the line by the number of grains. In order to achieve more accurate results, several lines were drawn across several images for each material and average grain size was noted. The images were taken using a Nikon Eclipse LV100ND optical microscope, between 10 times and 100 times magnification.

3.5.2 Fractography

Fracture surfaces of small ring specimens tested under tensile and cyclic conditions were inspected in order to evaluate the failure mechanism. The images of fracture surfaces were taken using an Olympus Infinity 2 optical microscope with 10 times magnification using Infinity Capture software due to a lack of SEM availability, which did not allow for full characterization of the fracture surface due to lack of depth of focus.

3.5.3 Surface Roughness

As described in Section 3.3.3, the outer surface of the small ring specimen was achieved by turning in a lathe, the inner surface was reamed and the sides were created by the part off tool then deburred using fine wet and dry abrasive paper. The common surface roughness for these operations are as follows [172]:

- Turning - 6.3 - 0.4 μm
- Reaming - 3.2 - 0.8 μm
- Parting off and fine wet and dry abrasive paper - 1.32 -0.38 μm [173]

3.6 Curve Fitting

3.6.1 Tensile Curve Fitting

Ramberg-Osgood material model (deformation plasticity model in ABAQUS, described in Equation 2.14) was fitted to conventional specimen tensile test results in order to evaluate the distribution of the the results, repeatability and to validate the model created in ABAQUS. In some cases the test results were not zeroed properly, beginning not at zero force or displacement, or the specimen appears to have slipped, with several different slopes in the elastic region. Those results had to be pre-processed in order to get a clear stress-strain curve. If the initial slope was clear and the test did not start at zero the first point of the test was moved to zero, shifting the whole force-displacement curve. In the cases where, instead of one clear slope going to the yield point, there were several slopes transitioning into one another, the last slope before yield was evaluated and projected down to zero force, then the point of zero force was assumed to be the point of zero displacement. Then the processing would begin.

First, the engineering stress-strain curves were transformed into true stress-true strain curves according to Equations 2.12 and 2.13. Then, as the model is suitable to describe material behaviour with increasing stress, the peak stress was found and the data after it was discarded. In the cases where strain softening was present from close to the yield point a large number of points had to be discarded and if next to no strain hardening after yield was present the Ramberg-Osgood material model could not be fitted, but Young's modulus and yield stress could still be evaluated.

MatLab Curvefitting Toolbox was used to fit the model, with Nonlinear Least Squares. Bisquare fitting method was chosen as it produced the best fitting models and Trust Region algorithm was used because it allows for limits to be used when fitting coefficients, to ensure that the fitted parameters are realistic. Maximum function evaluations and maximum iterations were increased to 1000 and other settings were left to be the default values.

Young's modulus was fitted first, to the initial linear region of the stress-strain curve. The end of the straight region was identified by fitting a line to the data from the beginning, adding points one by one and noting the values of the correlation coefficient. The peak value of the correlation coefficient was taken to be the end of the initial linear region. In cases where the full model could not be fitted, the end of the initial straight region was taken to be the yield stress.

Other three parameters were fitted together, by defining appropriate boundaries and using the previously fitted Young's modulus as a constant. If all parameters, including Young's modulus were fitted together the model usually fitted the plastic part of the stress-strain curve better, but did not fit the elastic region due to the low number of points there.

3.6.2 Cyclic Curve Fitting

A combined hardening model (described in Equations 2.19 and 2.20) was fitted to cyclic stress-strain data in order to use the data in an ABAQUS model. The method of fitting was taken from literature [174] and can be summarized as follows:

1. Fit Ramberg-Osgood material model to the first quarter cycle
2. Fit the isotropic component after processing the experimental results and fitting Equation 2.19 to them
3. Fit the kinematic components to the first quarter cycle by finding $ln\left(\frac{\partial\sigma}{\partial\varepsilon_p} - \frac{\partial R}{\partial\varepsilon_p}\right)$ and plotting it against plastic strain

Ramberg-Osgood material model coefficients were fitted to the first quarter cycle of the results by using the method described in Section 3.6.1, finding Young's modulus and yield stress.

Then, in order to fit the isotropic hardening component to the model (Equation 2.19), accumulated plastic strain and values of R had to be calculated from the experimental results. Values of R were calculated by finding the peak tensile and compressive stresses, calculating the absolute values, then subtracting the initial yield stress from them. Plastic strain in each cycle was evaluated by following the line of elastic unloading for each load reversal to zero stress, then absolute plastic strain was evaluated and accumulated plastic strain values were calculated by adding all the previous values to each new value. Equation 2.19 was fitted to the resulting dataset, using the same settings as described in Section 3.6.1, finding parameters Q_∞.

Then, in order to fit the kinematic hardening parameters, the data from the first quarter cycle was used again. Plastic strain was calculated by finding the yield strain from yield stress and Young's modulus, then subtracting it from the total strain. All resulting negative values were equated to zero. The $\frac{\partial R}{\partial \varepsilon_p}$ is found by using the previously fitted Q and b_i and Equation 3.1. The equation for finding $\frac{\partial \sigma}{\partial \varepsilon_p}$ is derived according to literature [174]. Equation 3.2, taken from literature, shows the relationship between the derivative of stress with respect to plastic strain, the derivative of stress with respect to total strain and total and plastic strain rates. As the plastic strain rate can be expressed in terms of total strain rate, Young's modulus and the derivative of stress with respect to plastic strain, as shown in Equation 3.3, it can be substituted into Equation 3.2 to get Equation 3.4.

$$\frac{\partial R}{\partial \varepsilon_p} = b_i Q e^{-b\varepsilon_p} \tag{3.1}$$

$$\frac{d\sigma}{d\varepsilon_p} = \frac{d\sigma}{d\varepsilon_t} \cdot \frac{1}{\dot{\varepsilon_p}} \cdot \dot{\varepsilon_t} \tag{3.2}$$

$$\dot{\varepsilon_p} = \dot{\varepsilon_t} \left(1 - \frac{1}{E} \cdot \frac{d\sigma}{d\varepsilon_t}\right) \tag{3.3}$$

$$\frac{d\sigma}{d\varepsilon_p} = \frac{d\sigma}{d\varepsilon_t} \cdot \frac{E}{E - \frac{d\sigma}{d\varepsilon_t}} \tag{3.4}$$

Now, as per literature, the derivative of stress with respect to total strain could be found by differentiating the Ramberg-Osgood material model and rearranging, to get Equation 3.5, which could be calculated by using the parameters fitted to the first quarter cycle before. Then $ln\left(\frac{\partial\sigma}{\partial\varepsilon_p} - \frac{\partial R}{\partial\varepsilon_p}\right)$ was plotted against plastic strain and a line fitted to the result, as per Equation 3.6 and parameters C and γ found. To fit two backstresses a line was first fitted to the latter points then the fitted coefficients were used to calculate the coefficients for the backstress explaining the initial hardening behaviour.

$$\frac{d\sigma}{d\varepsilon_t} = \frac{E\sigma_y^{n-1}}{\sigma_y^{n-1} + \alpha\left(n-1\right)} \tag{3.5}$$

$$ln\left(\frac{\partial\sigma}{\partial\varepsilon_p} - \frac{\partial R}{\partial\varepsilon_p}\right) = -\gamma\varepsilon_p + ln\left(C\right) \tag{3.6}$$

4 Small Ring Specimen Tensile Modelling

4.1 Introduction

The deformation of the small ring specimen needs to be accurately modelled and for that three models were developed: a semi-analytical model based on Euler-Bernoulli beam bending theory, an FEA model of 1/8th of the small ring specimen (due to symmetry) and a full 3D FEA model used to investigate misalignment. Initial modelling studies were done in order to calculate loading rates for small ring specimens and to validate the FEA model, then modelling work was carried out to investigate how varying material and geometry parameters affects the force-displacement results.

4.2 Models

The models used to model the small ring specimen under tensile loading are described in this section. Several FEA models were created in ABAQUS (2D, 3D of 1/8th of the ring and full 3D) is order to evaluate which model was the most appropriate and to investigate the stress state in the small ring specimens used tensile loading. The semi-analytical solution was derived, implemented in MatLab and the results compared to experimental and FEA results.

4.2.1 FEA Models

2D Model A 2D model was initially investigated to see if it would be suitable for modelling the deformation of the small ring specimen. Plane stress and plane strain elements were the ones considered, however, neither was immediately suitable as the plane stress approximation is suitable for thin plates and plane strain is suitable for thick plates. The ratio of lateral thickness to radial thickness (thickness to width) of the small ring specimen is 2 mm to 1 mm, (2:1), which does not fit either definition. However, one of them could potentially offer a sufficiently accurate approximation, which is why they where investigated.

The FEA model is based on the experimental setup for small ring creep testing, as it was also used for small ring tensile testing. The model itself consists of a ring and a pin. Due to the setup being symmetrical 1/4th of the setup is modelled. The ring has an inner radius of 4.5 mm and the outer radius of 5.5 mm, it is modelled as a deformable body. The pin has a radius of 1.25 mm and is modelled as a discrete rigid body due to being significantly stiffer than the ring. As the model was 2D thickness was not specified.

In order to define the material, a Ramberg-Osgood material model (deformation plasticity in ABAQUS, Equation 2.14) was used.

The step used was static general, with non-linear geometry enabled, due to large deformations occurring during the analysis. Time period was arbitrarily set, due to assumed rate in-dependency in the material. Static general step neglects inertia effects and time dependent effects, but takes rate dependent effects into account. As the small ring specimen is light, making inertia effects appropriate to ignore, and creep is not being taken into account, this step is suitable.

Surface-to-surface contact was set up between the ring and the pin, with the pin being the master surface as it is rigid and the ring being the slave surface due to being deformable. Sliding formulation was finite sliding, as it continuously tracks which parts of the master surface are in contact with which parts of the slave surface. Discretization method was surface to surface, as two smooth surfaces are in contact with each other. Surface smoothing was enabled due to surfaces being circular. Tangential behaviour was set up as frictionless for the initial investigation of the suitability of the models. Normal behaviour was set up as "Hard" contact, which does not allow the penetration of the contact surfaces, with contact occurring until the contact pressure becomes zero and surfaces coming into contact when the clearance between them becomes zero. As this is what occurs during the small ring test this type of normal behaviour is appropriate.

There were symmetry boundary conditions set up on all planes of symmetry. The pin was displaced and therefore the ring was deformed by applying a displacement boundary condition onto the reference point of the pin, which was only permitted to be displaced vertically. The displacement applied was 2 mm, which was equivalent to 4 mm experimentally and was past the point where rings generally fail.

For the initial investigations element size chosen for the ring was about 0.2 mm x 0.2 mm x 0.2 mm, resulting in 5 elements across the radial thickness of the ring. Mesh controls were set up to a structured mesh with hex elements. The elements used to model the ring were Standard quadratic 2D plane stress or plane strain elements (CPS 4R or CPE4R), with reduced integration (C3D20R), due to them being suitable for modelling curved surfaces and the elements used to model the pin were R3D4.

1/8th 3D Model This FEA model is based on the same experimental setup as the 2D models. The model itself consists of a pin and the ring. Due to the setup being symmetrical 1/8th of the setup is modelled. The ring has an inner radius of 4.5 mm and outer radius of 5.5 mm, half thickness of 1 mm and is modelled as a deformable body. The pin has a radius of 1.25 mm and an arbitrary length of 3 mm and is modelled as a discrete rigid body due to being significantly stiffer than the ring. The model is shown in Figure 4.1.

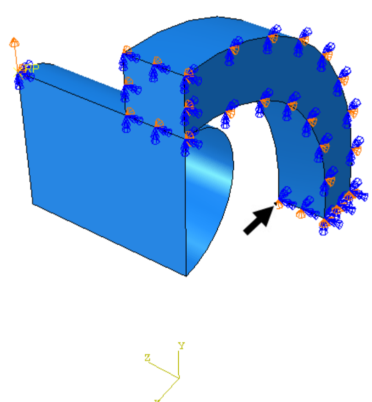

Figure 4.1: The model used for tensile FEA analysis.

In order to define the material, a Ramberg-Osgood material model (deformation plasticity in ABAQUS, Equation 2.14) was used.

The step used was static general, with non-linear geometry enabled, due to large deformations occurring during the analysis. Time period was arbitrarily set, due to assumed rate in-dependency in the material.

Surface-to-surface contact was set up between the ring and the pin, with the pin being the master surface as it is rigid and the ring being the slave surface due to being deformable. Sliding formulation was finite sliding. Discretization method was surface to surface. Surface smoothing was enabled. Tangential behaviour was set up as frictionless, as according to a coefficient of friction sensitivity study, which is shown in Figure 4.28, there was no significant effect on the force-displacement curve when the coefficient of friction was varied between realistic values. Normal behaviour was set up as “Hard” contact.

There were symmetry boundary conditions set up on all planes of symmetry. The pin was displaced and therefore the ring was deformed by applying a displacement boundary condition onto the reference point of the pin, which was only permitted to be displaced vertically. The displacement applied was 2 mm.

Element size chosen for the ring was about 0.2 mm x 0.2 mm x 0.2 mm, resulting in 5 elements across the thickness of the ring. This size was determined to be appropriate according to a mesh density study shown in Figure 4.2 (a), as the force-displacement curve for 5 elements was smooth and did not differ from the smaller number of elements, showing convergence. This number of elements also showed a clear variation in stress in the ring as the loading progressed, especially the movement of the neutral axis from it’s initial position towards the outer surface of the small ring, as shown in Figure 4.2 (b). The uneven behaviour, in particular seen in the force-displacement curve of 1 x 1 element plot, was likely caused by the interactions between the mesh of the pin and the mesh of the ring, with nodes coming into contact causing the uneven behaviour. Mesh controls were set up to a structured mesh with hex elements. The elements used to model the ring were Standard quadratic 3D stress elements, with reduced integration (C3D20R), due to them being suitable for modelling curved surfaces and the elements used to model the pin were R3D4. An example mesh can be seen in Figure 4.2 (c).

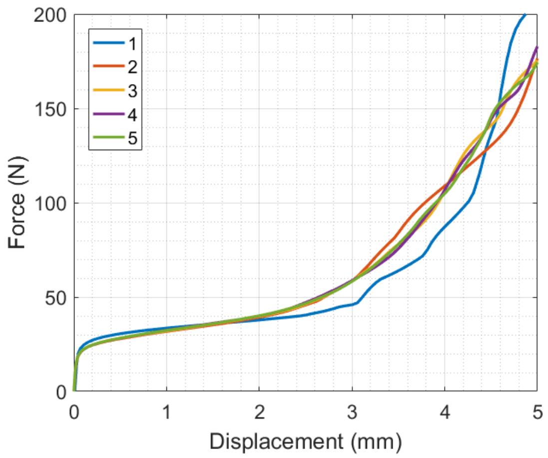

(a)

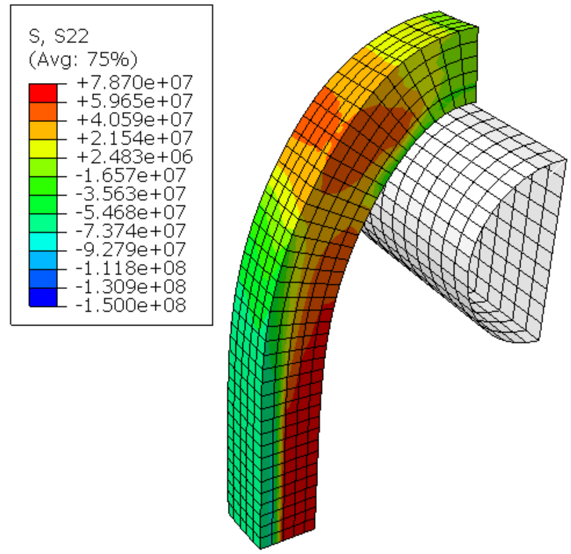

(b)

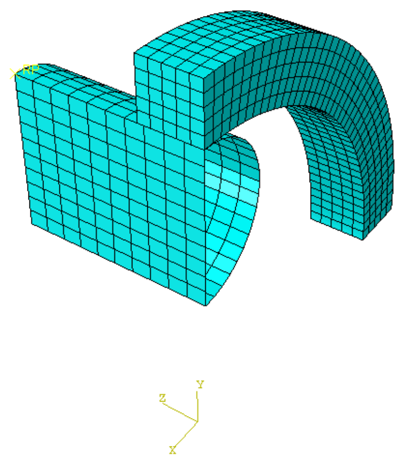

(c)

Figure 4.2: (a) Tensile small ring FEA model mesh convergence study, showing the change in response with the change in the number of elements across the cross-section of the small ring specimen; (b) An example of the stress state in the small ring specimen, stress in the y direction; (c) Meshed tensile small ring FEA model.

Full Ring 3D Model The full ring model was developed in order to investigate the effect of misalignment. When the pins are misaligned with respect to the ring the whole setup becomes asymmetrical and makes the 1/8th model not suitable.

The model consists of two pins and a ring. The ring has an inner radius of 4.5 mm, outer radius of 5.5 mm and thickness of 2 mm, the same as the small ring specimen used for testing. The pins have a radius of 1.25 mm and a length of 4 mm, with flat surfaces at the ends to prevent the ring from slipping off due to misalignment. The ring is a deformable body, while the pins are discrete rigid bodies, same as in the 1/8th model. The model itself can be seen in Figure 4.3.

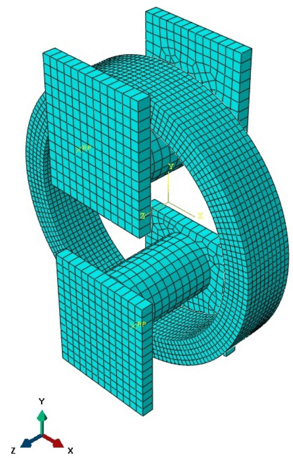

Figure 4.3: Full 3D model used to investigate the effects of misalignment.

The material model used was the Ramberg-Osgood material model (deformation plasticity in ABAQUS). Static general step with non-linear geometry enabled was used, with an arbitrarily set time period due to assumed rate in-dependency in the material. The contact between the pins and the ring was set up as surface-to-surface contact, with pin surfaces as master surfaces and ring surfaces as slave surfaces. The sliding formulation was finite sliding, discretization method was surface to surface. Due to the ring and the pins being circular, surface smoothing was enabled. Tangential behaviour was set to penalty, with 0.4 coefficient of friction, as friction would have an effect when the pins are misaligned and 0.4 is a realistic coefficient of friction. Normal behaviour was set up as “Hard” contact.

The boundary condition for the bottom pin was encastre, as it stays stationary during testing, while the top pin was vertically displaced up to about 4 mm during the analysis. The element size and type was the same as for the 1/8th model, about 0.2 mm x 0.2 mm x 0.2 mm, with 5 elements across the radial thickness and 10 along the lateral thickness, which is double the number of elements along lateral thickness in the 1/8th model. This element size was chosen because it was appropriate for the 1/8th model and was further verified as shown in Section 4.2.3. The elements used to model the ring were C3D20R, while the pin elements were R3D4.

4.2.2 Semi-analytical Solution

A semi-analytical solution based on the strain energy approach was developed in order to calculate the force-displacement response of the small ring specimens. This was motivated by the need for rapid approximation of linear behaviours prior to expensive inverse FEA. The assumptions used were that the cross-section remains constant, the stress through the lateral thickness is constant, the ring deforms into an ellipse, the material behaviour is isotropic and homogeneous, the ring and the loading setup are symmetric and the applied load is a point load. The cross-section remains close to constant until the ring starts to thin at high deformations. The assumption about the elliptical shape is correct up to a certain displacement, around 2 mm, which is due to the width of the pin impinging on the ring as it bends, further detail on this is shown in Section 4.2.3. The ring is symmetrical and deforms symmetrically provided that there is no misalignment, the load applied is not a point load, however it is approximated as such.

The schematic loading diagram and the free body diagram can be seen in Figures 4.4 (a) and (b). P is the applied load, Q is a dummy load, M_0 is the reaction moment keeping the section vertical, a_{el} is the semi-minor radius of the ellipse, b_{el} is the semi-major radius of the ellipse. Dummy load Q was added in order to be able to calculate the horizontal displacement using Castigliano's theorem, which requires an applied load in the direction of the displacement which is being calculated. The strain energy can be differentiated with respect to that load to find the displacement [5].

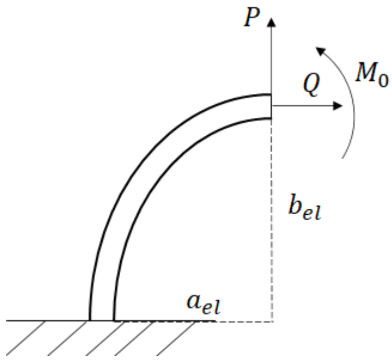

(a)

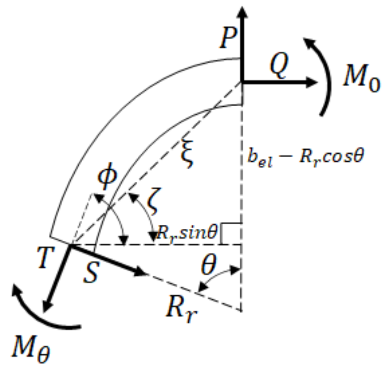

(b)

Figure 4.4: (a) Schematic loading diagram for the semi-analytical solution; (b) Free-body diagram for the semi-analytical solution.

As the ring is symmetric, only 1/4th of it is analysed in this solution. Initially it is circular, with a_{el} equal to b_{el}, as the load is applied it deforms into a vertical ellipse, with a_{el} reducing and b_{el} increasing. The end of the quarter of the ring on the x-axis is assumed to be built-in, while the end on the y-axis is assumed to be on rollers, to keep it vertical, but allow it to move both vertically and horizontally. These boundary conditions were selected to simplify the solution and make it easier to follow. The deformation of the ring with these boundary conditions is equivalent to the deformation with rollers applied to both ends, as the relative displacement of one end to the other would be the same.

Expressions based on the definition of ellipse and basic geometry are Equations 4.1 to 4.4. R_r is the radius of the ellipse, which is different at every angle θ when semi-major and semi-minor radii are kept constant. When θ is 0^o, the radius is the same as the semi-major radius b_{el} and when it is 90^o it is the same as the semi-minor radius a_{el}. ξ is the distance between the load application point and the end of the arc at angle θ as shown in Figure 4.4, which is the moment arm for forces P and Q around the end of the arc at angle θ. Angle ζ is the angle between line ξ and the x-axis, while angle ϕ is the angle of the tangent to the ellipse at angle θ.

$$R_r(\theta) = \frac{a_{el} b_{el}}{\sqrt{b_{el}^2 cos^2\theta + a_{el}^2 sin^2\theta}} \tag{4.1}$$

$$\xi(\theta) = \sqrt{b_{el}^2 - 2b_{el} R_r cos\theta + R_r^2} \tag{4.2}$$

$$\zeta = arctan \frac{b_{el} - R_r cos\theta}{R_r sin\theta} \tag{4.3}$$

$$\phi = arctan\left(\frac{b_{el}^2}{a_{el}^2} tan\theta\right) \tag{4.4}$$

The balance of moments for the free body diagram in Figure 4.4 at angle θ is shown in Equation 4.5. The moments acting clockwise are M_θ and the moment resulting from dummy load Q and moment arm ξ at angle ζ, while the moments acting counter-clockwise are M_0 and the moment resulting from applied load P and moment arm ξ at angle ζ. This moment arm and angle were chosen as opposed to $R_r sin\theta$ for P and $b_{el} - R_r cos\theta$ for Q in order to make the solution less complicated to follow.

$$M_\theta = M_0 + P\xi cos\zeta - Q\xi sin\zeta \tag{4.5}$$

For an Euler-Bernoulli beam, the internal bending strain energy is shown in Equation 4.6 [5]. The assumptions for an Euler-Bernoulli beam are that plane sections remain plane and that the deformations are small. As the beam in this case was curved and the expression for the moment depends on angle θ the equation was rewritten in terms of it.

$$U_b = \int_0^L \frac{M_\theta^2}{2EI} dx = \int_0^{\frac{\pi}{2}} \frac{M_\theta^2}{2EI} R_r d\theta \tag{4.6}$$

The expression for reaction moment M_0 is unknown and it can be found by applying Castigliano's theorem. As moment M_0 is a reaction moment, it does not cause any rotation, but resists rotation to keep the section of the ring at the vertical plane of symmetry vertical. This results in Equation 4.7, which is then rearranged to Equation 4.8. Three integrals which will be numerically integrated were identified as Equations 4.9 to 4.11. The equation for the moment M_0

can be rewritten in terms of these integrals into Equation 4.12 to make the further solution easier to follow.

$$\frac{\partial U_b}{\partial M_0} = 0 = \frac{1}{2EI}\int_0^{\frac{\pi}{2}} \left(M_0 + P\xi cos\zeta - Q\xi sin\zeta\right) R_r d\theta \tag{4.7}$$

$$M_0 \int_0^{\frac{\pi}{2}} R_r d\theta = Q\int_0^{\frac{\pi}{2}} R_r \xi sin\zeta d\theta - P\int_0^{\frac{\pi}{2}} R_r \xi cos\zeta d\theta \tag{4.8}$$

$$A_1 = \int_0^{\frac{\pi}{2}} R_r d\theta \tag{4.9}$$

$$A_2 = \int_0^{\frac{\pi}{2}} R_r \xi sin\zeta d\theta \tag{4.10}$$

$$A_3 = \int_0^{\frac{\pi}{2}} R_r \xi cos\zeta d\theta \tag{4.11}$$

$$M_0 = \frac{QA_2 - PA_3}{A_1} \tag{4.12}$$

Applied load P causes the vertical displacement, therefore the partial differential of bending strain energy with respect to that load is equal to the bending contribution to the vertical displacement as per Equation 4.13. Another integral which will need numerical integration is identified as Equation 4.14, which then allows to rewrite the vertical displacement due to bending as Equation 4.15.

$$\frac{\partial U_b}{\partial P} = u_{vb} = \frac{P}{2EI}\left(\frac{2A_3^2}{A_1^2}\int_0^{\frac{\pi}{2}} R_r d\theta + 2\int_0^{\frac{\pi}{2}} R_r \xi^2 cos^2\zeta d\theta - 4\frac{A_3}{A_1}\int_0^{\frac{\pi}{2}} R_r \xi cos\zeta d\theta\right) \tag{4.13}$$

$$A_4 = \int_0^{\frac{\pi}{2}} R_r \xi^2 cos^2\zeta d\theta \tag{4.14}$$

$$u_{vb} = \frac{P}{EI}\left(A_4 - \frac{A_3^2}{A_1}\right) \tag{4.15}$$

Applied load P also causes the horizontal displacement, however, as it is not in the direction of the horizontal displacement, dummy load Q has to be used for the partial differentiation of bending strain energy to evaluate the bending contribution to horizontal displacement as per Equation 4.16. Another integral which needs numerical integration is shown in Equation 4.17, which then allows the bending contribution to horizontal displacement to be rewritten as Equation 4.18.

$$\frac{\partial U_b}{\partial Q} = u_{hb} = \frac{1}{2EI}\int_0^{\frac{\pi}{2}} \left(\frac{-2PA_2A_3}{A_1^2} + 2\frac{A_2}{A_1}P\xi cos\zeta + 2\frac{PA_3}{A_1}\xi sin\zeta - 2P\xi^2 sin\zeta cos\zeta \right) R_r d\theta \quad (4.16)$$

$$A_5 = \int_0^{\frac{\pi}{2}} R_r\xi^2 sin\zeta cos\zeta d\theta \quad (4.17)$$

$$u_{hb} = \frac{P}{EI}\left(\frac{A_2A_3}{A_1} - A_5\right) \quad (4.18)$$

The expressions for the internal reaction tensile (T) and shear (S) forces in terms of applied load P and dummy load Q are shown in Equations 4.19 and 4.20.

$$T = Qcos\phi + Psin\phi \quad (4.19)$$

$$S = Pcos\phi - Qsin\phi \quad (4.20)$$

Strain energy due to a tensile load can be derived from the definition of strain energy, as per Equation 4.21 [5]. Similarly, strain energy due to a shear load can be derived as per Equation 4.23, into which the relationship between the shear modulus and the Young's modulus (Equation 4.22) can be substituted.

$$U_t = \int_V \frac{1}{2}\frac{\sigma^2}{E}dV = \int_0^L \frac{T^2}{2A^2E}Adx = \int_0^L \frac{T^2}{2AE}dx = \int_0^{\frac{\pi}{2}} \frac{T^2}{2AE}R_r d\theta \quad (4.21)$$

$$G = \frac{E}{2\left(1+\nu\right)} \quad (4.22)$$

$$U_s = \int_V \frac{1}{2}\frac{\tau^2}{G}dV = \int_0^L \frac{S^2}{2A^2G}Adx = \int_0^L \frac{S^2}{2AG}dx = \int_0^{\frac{\pi}{2}} \frac{S^2\left(1+\nu\right)}{AE}R_r d\theta \quad (4.23)$$

As applied load P also causes the tensile internal reaction force, it can be used to differentiate the tensile strain energy to get the tensile contribution towards the vertical displacement, as per Equation 4.24. Integral B_1 is defined in Equation 4.25 in order to rewrite the tensile contribution to vertical displacement as Equation 4.26.

$$\frac{\partial U_t}{\partial P} = u_{vt} = \frac{1}{2AE}\int_0^{\frac{\pi}{2}} 2PR_r sin^2\phi d\theta \tag{4.24}$$

$$B_1 = \int_0^{\frac{\pi}{2}} R_r sin^2\phi d\theta \tag{4.25}$$

$$u_{vt} = \frac{PB_1}{AE} \tag{4.26}$$

Tensile strain energy is differentiated with respect to dummy load Q in order to get the tensile contribution to horizontal displacement, shown in Equation 4.27. Integral B_2 is defined as Equation 4.28 which allows the rewriting of the tensile contribution to horizontal displacement as Equation 4.29.

$$\frac{\partial U_t}{\partial Q} = u_{ht} = \frac{1}{2AE}\int_0^{\frac{\pi}{2}} 2PR_r sin\phi cos\phi d\theta \tag{4.27}$$

$$B_2 = \int_0^{\frac{\pi}{2}} R_r sin\phi cos\phi d\theta \tag{4.28}$$

$$u_{ht} = \frac{PB_2}{AE} \tag{4.29}$$

Shear strain energy can be differentiated with respect to applied load P to get the shear contribution to vertical displacement, as shown in Equation 4.30. Equation 4.31 defines integral B_3, and the shear contribution to vertical displacement can be rewritten into Equation 4.32.

$$\frac{\partial U_s}{\partial P} = u_{vs} = \frac{1+\nu}{AE}\int_0^{\frac{\pi}{2}} 2PR_r cos^2\phi d\theta \tag{4.30}$$

$$B_3 = \int_0^{\frac{\pi}{2}} R_r cos^2\phi d\theta \tag{4.31}$$

$$u_{vs} = \frac{2P\left(1+\nu\right)B_3}{AE} \tag{4.32}$$

In order to get the shear contribution to horizontal displacement, shear strain energy has to be differentiated with respect to dummy load Q, as per Equation 4.33, which is rewritten into

Equation 4.34 by substituting the expression for integral B_2.

$$\frac{\partial U_s}{\partial Q} = u_{hs} = \frac{1+\nu}{AE}\int_0^{\frac{\pi}{2}} -PR_r sin\phi cos\phi d\theta \tag{4.33}$$

$$u_{hs} = \frac{-2P\left(1+\nu\right)B_2}{AE} \tag{4.34}$$

Adding the bending, tensile and shear contributions to vertical and horizontal displacements results in the final expressions for the total vertical and horizontal displacements shown in Equations 4.35 and 4.36.

$$u_{vtot} = \frac{P}{EI}\left(A_4 - \frac{A_3^2}{A_1}\right) + \frac{PB_1}{AE} + \frac{2P\left(1+\nu\right)B_3}{AE} \tag{4.35}$$

$$u_{htot} = \frac{P}{EI}\left(\frac{A_2A_3}{A_1} - A_5\right) - \frac{P\left(1+2\nu\right)B_2}{AE} \tag{4.36}$$

The deformation of the ring is calculated by applying a load increment, calculating vertical and horizontal displacements, then adding the vertical displacement to the semi-major radius and subtracting the horizontal displacement from the semi-minor radius to update the shape of the ellipse. This is done for every load increment until the maximum prescribed load is reached.

The solution is elastic-only up to this point. In order to include plasticity into this solution, the change in material properties throughout the ring has to be tracked, due to different strain values resulting in different stresses and therefore different contributions towards deformations. As a continuous solution cannot be developed, a semi-analytical solution, with material properties being tracked at discrete points is developed. A number of points are defined circumferentially and radially in the ring, as shown in Figure 4.5, which has 4 points radially and 11 points circumferentially. The material behaviour is described by the Ramberg-Osgood material model (Equation 2.14).

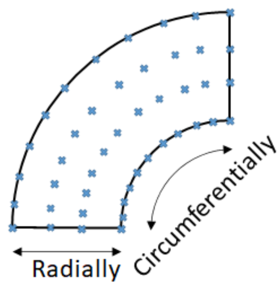

Figure 4.5: Discretized points at which the variation of effective Young's modulus is tracked.

The flowchart explaining how the analytical solution in implemented in MatLab is shown in Figure 4.6. Part B shows how the change in shape of the small ring under tensile loading is calculated, part C shows the calculation of strain due to the change is shape. Part D shows how the effective Young's modulus for each point is calculated, then part E shows how the effective Young's modulus and effective flexural rigidity (EI) are calculated for the next load increment.

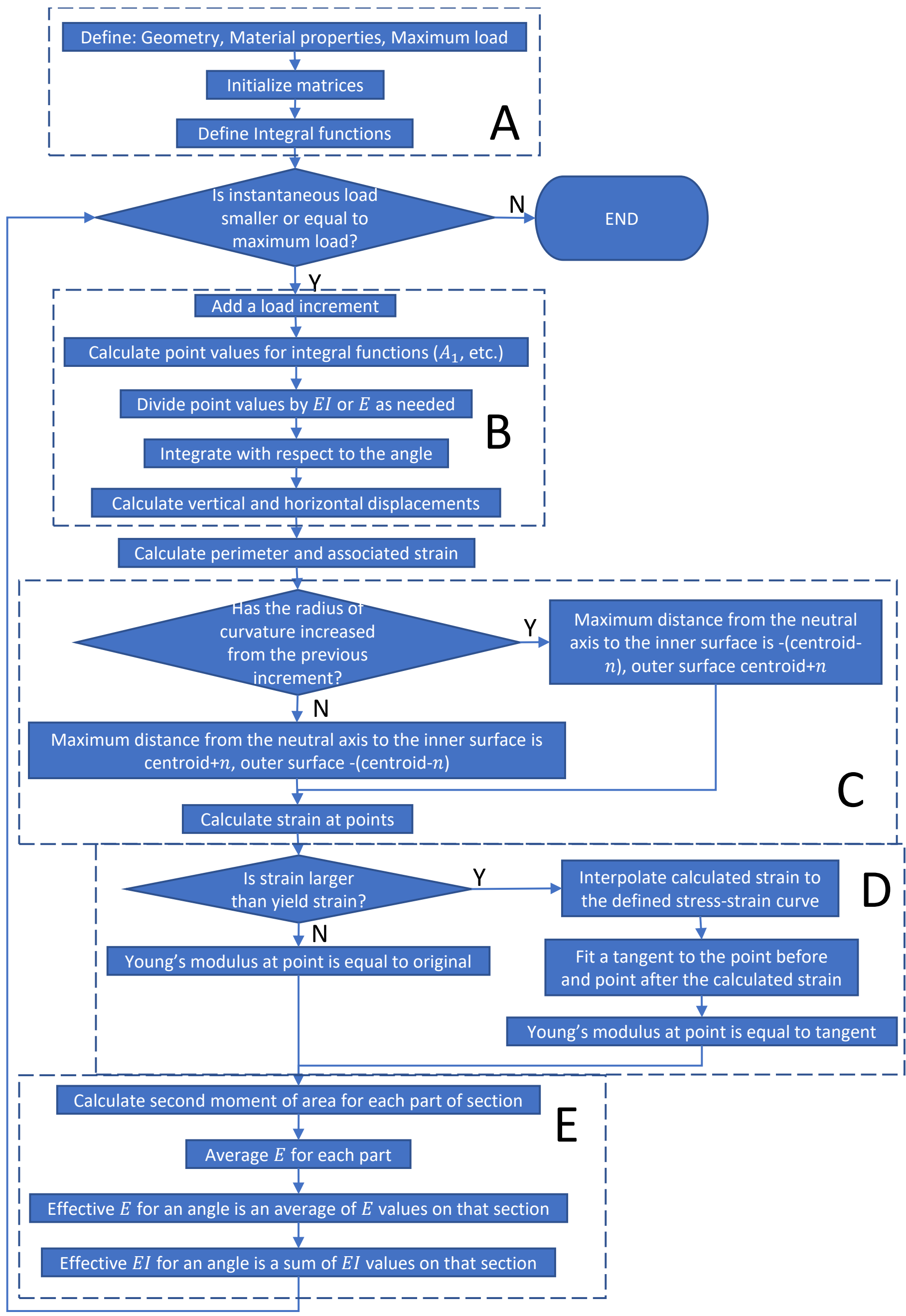

Figure 4.6: The flowchart showing the implementation of the analytical solution in Matlab.

Part B of Figure 4.6 begins with a load increment, which is then used to calculate the values of the integral functions along the neutral axis (based on Equations 4.9, 4.10, 4.11, 4.14, 4.17, 4.25, 4.28 and 4.31), then integral functions A are divided by effective EI for that angle as both Young's modulus and second moment of area around the neutral axis change as the loading progresses. The values of integral functions B are divided by the effective Young's modulus only, as the cross-sectional area is assumed to remain constant. The resulting equations are Equations 4.37 to 4.44.

$$A_1 = \frac{R_r}{EI} \tag{4.37}$$

$$A_2 = \frac{R_r \xi sin\zeta}{EI} \tag{4.38}$$

$$A_3 = \frac{R_r \xi cos\zeta}{EI} \tag{4.39}$$

$$A_4 = \frac{R_r \xi^2 cos^2\zeta}{EI} \tag{4.40}$$

$$A_5 = \frac{R_r \xi^2 sin\zeta cos\zeta}{EI} \tag{4.41}$$

$$B_1 = \frac{R_r sin^2\phi}{E} \tag{4.42}$$

$$B_2 = \frac{R_r sin\phi cos\phi}{E} \tag{4.43}$$

$$B_3 = \frac{R_r cos^2\phi}{E} \tag{4.44}$$

The resulting values are integrated using the trapezium rule and the vertical and horizontal displacements are calculated using Equations 4.45 and 4.46 which are adapted from Equations 4.35 and 4.36 to take into account the changing material properties. The shape of the ring is updated, by adding the vertical displacement to the vertical radius and subtracting the horizontal displacement from the horizontal radius, then the change in the perimeter of the ring and the strain associated with it is calculated.

$$u_{vtot} = P\left(\int_0^{\frac{\pi}{2}} A_4 d\theta - \frac{\left(\int_0^{\frac{\pi}{2}} A_3 d\theta\right)^2}{\int_0^{\frac{\pi}{2}} A_1 d\theta}\right) + \frac{P}{A}\int_0^{\frac{\pi}{2}} B_1 d\theta + \frac{2P\,(1+\nu)}{A}\int_0^{\frac{\pi}{2}} B_3 d\theta \tag{4.45}$$

$$u_{htot} = P\left(\frac{\int_0^{\frac{\pi}{2}} A_2 d\theta \int_0^{\frac{\pi}{2}} A_3 d\theta}{\int_0^{\frac{\pi}{2}} A_1 d\theta} - \int_0^{\frac{\pi}{2}} A_5 d\theta\right) - \frac{P\,(1+2\nu)}{A}\int_0^{\frac{\pi}{2}} B_2 d\theta \tag{4.46}$$

In part C, the radius of curvature (R_{curve}) is calculated along the neutral axis using Equation 4.47, which is acquired by differentiating the equation of the ellipse twice [175].

$$R_{curve} = \left|\frac{(a_{el}^4 - (a_{el}^2 - b_{el}^2) \times (R_r sin^2\theta))^{\frac{3}{2}}}{-a_{el}^4 b_{el}}\right| \tag{4.47}$$

For thick and initially curved rings, the neutral axis does not coincide with the centroid, instead, they are related by parameter n_r as shown in Equation 4.48 [5]. Figure 4.7 illustrates the location of the various radii on a curved beam.

$$n_r = -R_n + \frac{d_r}{2} \times \frac{e^{\frac{d_r}{R_n}} + 1}{e^{\frac{d_r}{R_n}} - 1} = -R_{curve} + \frac{d_r}{2} \times \frac{e^{\frac{d_r}{R_{curve}}} + 1}{e^{\frac{d_r}{R_{curve}}} - 1} \tag{4.48}$$

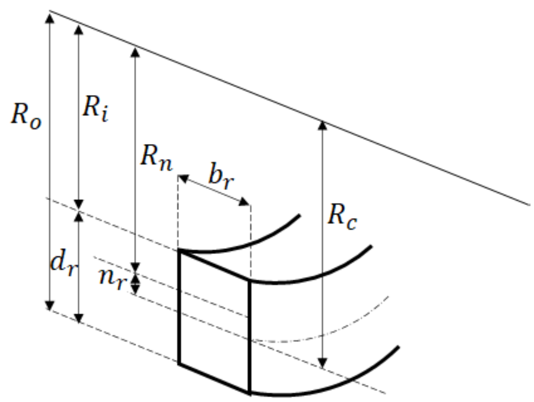

Figure 4.7: Illustration of the location of various radii on a curved beam. R_o is the outer radius, R_i is the inner radius, d_r is the radial thickness, the difference between outer and inner radii. R_c is the radius of the centroid, which is the average of the inner and outer radii, R_n is the radius of the neutral axis, while n_r is the distance between the centroid and the neutral axis. b_r is the lateral thickness of the beam.

The distance from the neutral axis to the inner and outer radius of the ring depends on the change in radius of curvature and distance n_r as stated in the flowchart. The strain at points shown in Figure 4.5 is calculated using Equation 4.49, where R_1 is the initial radius, R_2 is the final radius and y is the distance from the neutral axis.

Then in part D the stress-strain curve is differentiated with respect to strain to get the effective Young's modulus at that point. Following that, in part E the second moment of area associated with each point is calculated. Flexural rigidity is calculated by multiplying the effective E and associated second moment of area for each point and effective flexural rigidity is calculated by adding up the flexural rigidity at the same angle. Effective Young's modulus for each angle is calculated by averaging the Young's modulus of the points at the same angle.

$$\varepsilon = \frac{y\,(R_1 - R_2)}{R_2\,(R_1 + y)} \tag{4.49}$$

There are three discretization parameters in this model: number of points along the neutral axis, number of points across the radial thickness and the load increment. Convergence studies for all these were performed, as shown in Figure 4.8. The load convergence study (Figure 4.8 (a)) shows convergence as the response of the 1 N load increment and 0.1 N load increment is very similar. The convergence study for the radial number of points (Figure 4.8 (b)) shows convergence as the response from 20 and 25 elements is the same, while the convergence study for the circumferential number of points (Figure 4.8 (c)) shows convergence as the response from 20 and 25 elements is also the same.

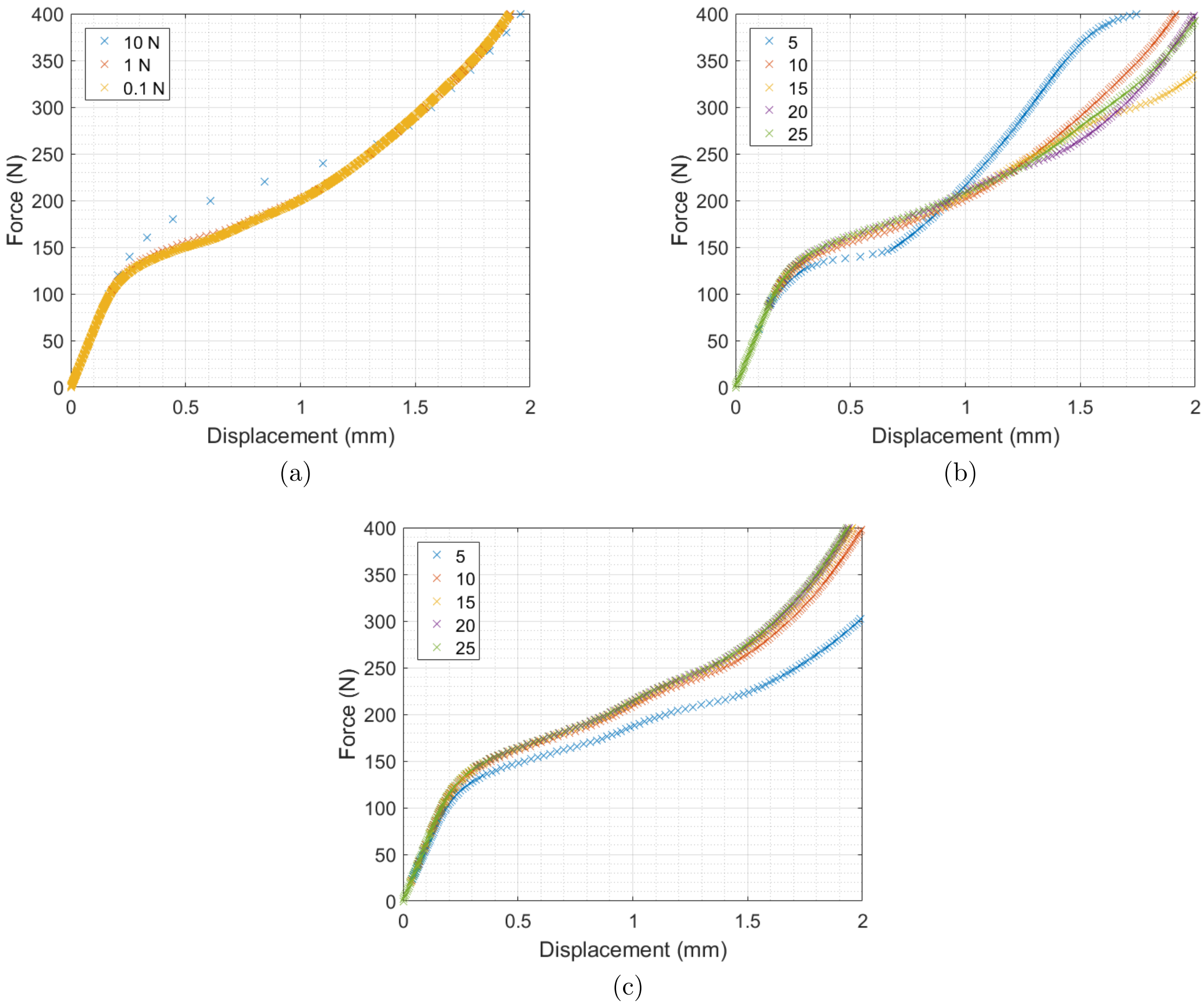

Figure 4.8: Convergence studies for the semi-analytical solution with plasticity included for the (a) applied load; (b) number of points radially; (c) number of points circumferentially.

Non converged values, with the discretization parameters being 10, 10 and 10 respectively do agree with experimental results well up to a certain point (around 1.2 mm for vertical displacement and 0.3 mm for horizontal displacement), as shown in Figure 4.9. These test results were chosen because they had the highest displacement to failure and therefore could be used to evaluate the accuracy of the semi-analytical model for the largest range of displacements. The poor agreement between the converged solution and the experimental results shows that the model with plasticity included is not stable and cannot be reliably used, as changing material properties would require new convergence studies. Also the agreement of the experimental results and the analytical solution results would not necessarily mean that the material properties in both are the same.

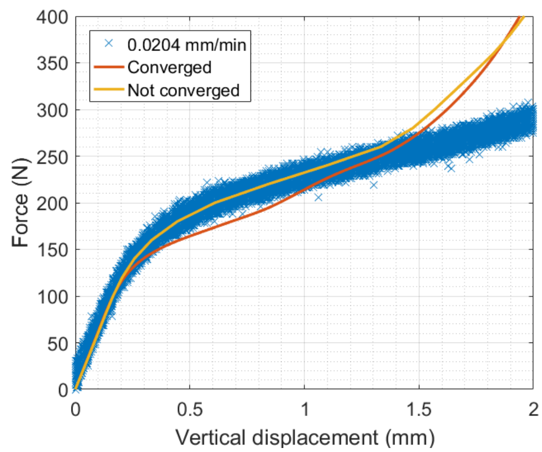

(a)

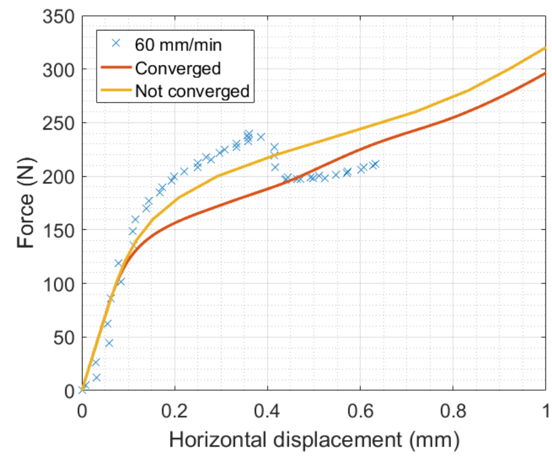

(b)

Figure 4.9: Comparison of experimental results and semi-analytical solution for (a) vertical displacement-force relationship; (b) horizontal displacement-force relationship.

The main reason why the force-displacement results from the converged model do not agree with the experimental results is because the model does not accurately represent the stress state that develops in the small ring specimen during loading. If the stress field is not accurately represented the strain energy approach, which depends on an accurate stress field, cannot deliver accurate results. The main limitation of Euler-Bernoulli beam theory is that due to the assumptions of plane sections remaining plane and small deformations it does not take shear deformation into account. Timoshenko beams do take shear into account and could be used to improve this model as a part of future work.

4.2.3 Preliminary Modelling Analysis

Material constants were determined by fitting the model to stress-strain curves obtained from standard testing. The curves were fitted using Matlab Optimization toolbox, with the square error being minimized to get a good fit, as described in Section 3.6.1. An example fit can be seen in Figure 4.10. The model fits well everywhere apart from around the yield point. The material model constants fitted can be seen in Table 4.1. Poisson's ratio used was 0.3, as it was identified during a previous investigation into this material [160]. A sensitivity study was done in order to investigate the effects of Poisson's ratio, it will be presented in Section 4.3.

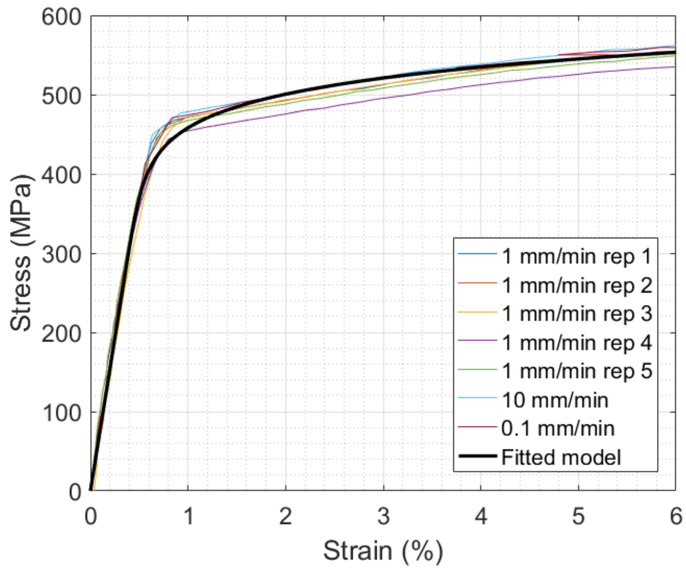

Figure 4.10: Example fit of a Ramberg-Osgood material model on experimental stress-strain data.

Table 4.1: Ramberg-Osgood material model parameters fitted to room temperature aluminium experimental data.

E (GPa)	σ_y (MPa)	n	α
77.2	435.6	13.57	0.364

The comparison of the FEA model results and experimental results can be seen in Figure 4.11. These test results were chosen because they had the highest displacement to failure and therefore could be used to evaluate the accuracy of the FEA models for the largest range of displacements. For vertical displacement, shown in Figure 4.11 (a), the plane strain assumption results in the force values being consistently higher than experimental results after the initial straight region, plane stress assumption results in the force values being consistently lower than experimental results after the initial straight region. 1/8th model and full ring model results overlap exactly, which was expected because of symmetry. Both of them are also slightly higher than experimental results, but closer than the results from other models. The results start to diverge more at higher displacements (above 3.2 mm displacement), which could be explained by the model not having damage included. 1/8th model is sufficient for modelling small ring specimens under tensile loading.

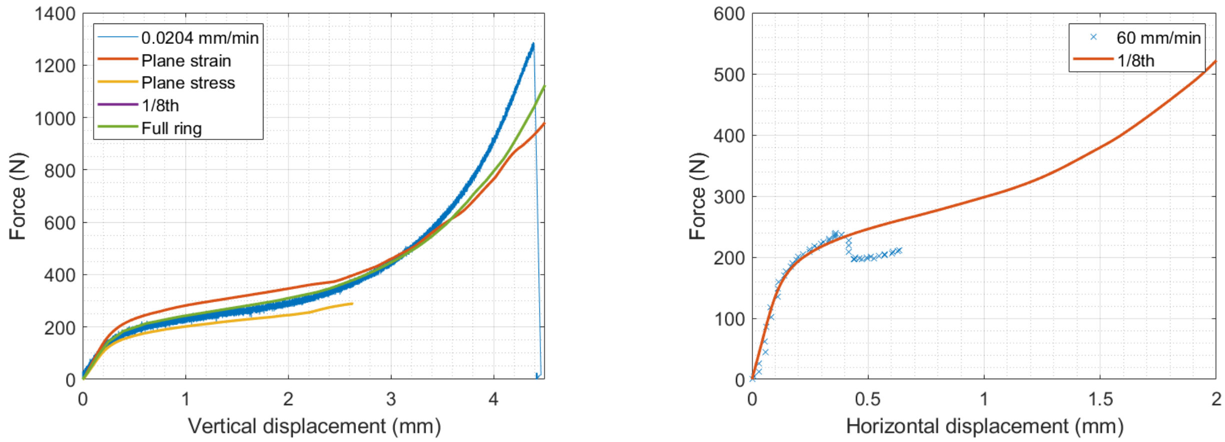

(a) (b)

Figure 4.11: The comparison of the experimental results and the FEA solution for (a) force-vertical displacement response; (b) force-horizontal displacement response.

For horizontal displacement the 3D 1/8th FEA solution agrees with the experimental results well until the specimen begins to fail. This confirms that the 1/8th FEA model is representative of experimental results enough and then can be used to develop a method to interpret other experimental data.

Regarding the shape that the ring deforms into as it is being loaded, it is elliptical or very close to elliptical up to an experimental deformation of around 2 mm as shown in Figure 4.12. The displacement of three points along the ring was tracked and the ellipse equation based on the semi-major and semi-minor axis measurements was plotted over those points. It was decided that the maximum error between the location of the tracked point and the location calculated according to the equation of the ellipse to still consider the shape of the ring elliptical was 5 %.

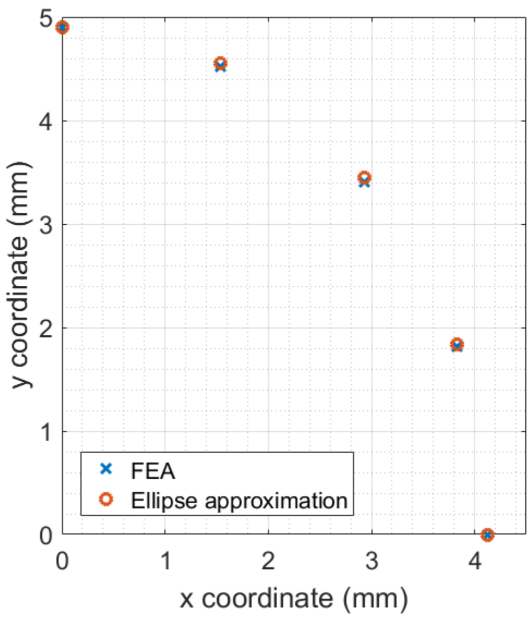

(a)

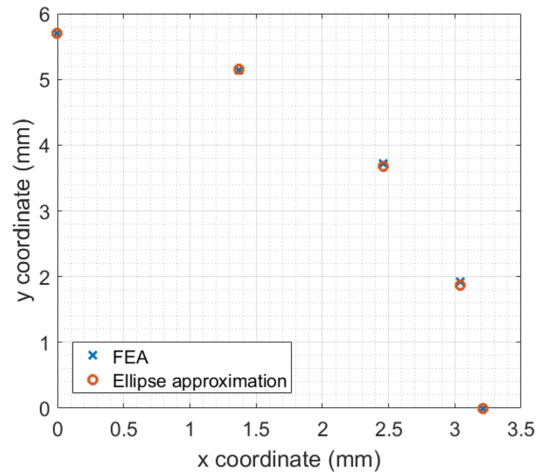

(b)

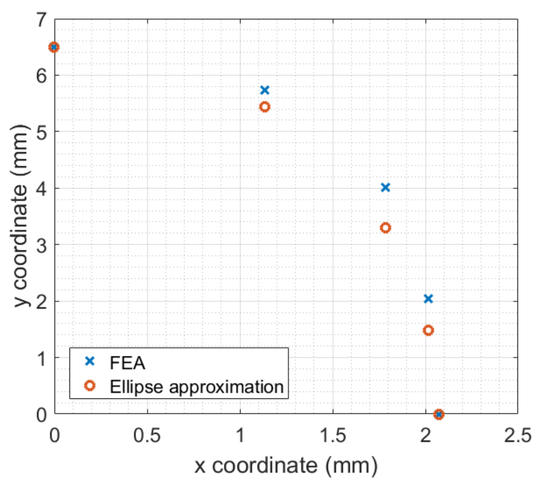

(c)

Figure 4.12: The comparison of the shape in the FEA analysis and the ellipse approximation at displacement of (a) 0.4 mm (0.8 mm experimentally, all errors under 1.5 %); (b) 1.2 mm (2.4 mm experimentally, all errors under 5 %); (c) 2 mm (4 mm experimentally, all errors under 30 %).

Stress and strain state in the small ring specimen was inspected throughout the loading process. At the initial loading stage, shown in Figure 4.13, the highest principal strain can be seen on the outside surface of the ring above the loading pin. Stress and strain through the thickness of the ring appears to be near constant. The middle of the ring has lower stress than the inner and ouiter surfaces, as expected from the analytical analysis. Compressive stress can be seen where the ring is in contact with the pin.

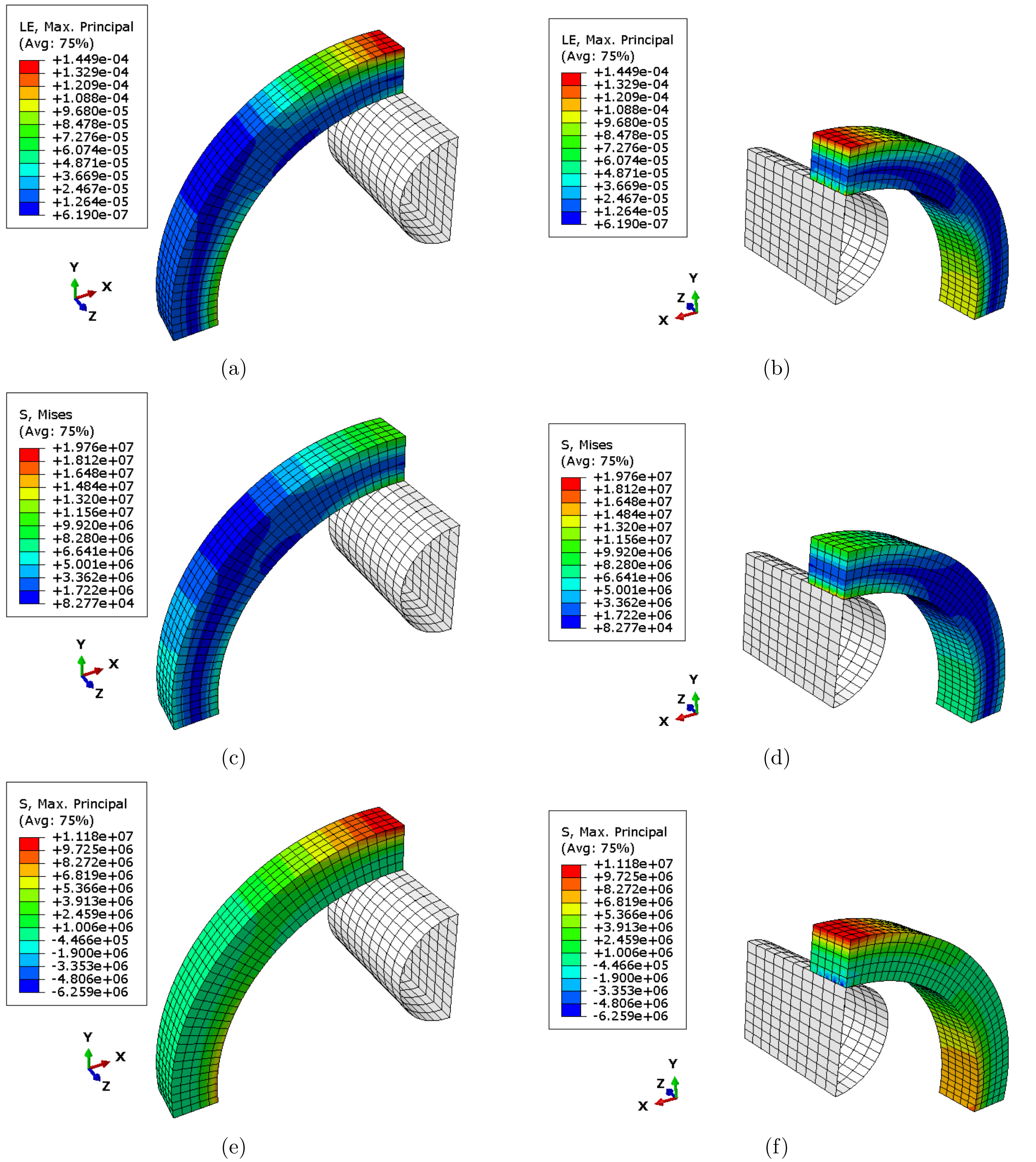

Figure 4.13: (a, b) Strain state (maximum principal strain); (c, d) stress state (von Mises stress); (e, f) stress state (maximum principal stress) at the beginning of loading.

As the loading progresses, towards the highest deformation when the ring can still be considered elliptical, the highest principal strain continues to be on the outer surface of the ring above the pin, as shown in Figure 4.14. The variation of stress and strain through the thickness of the ring increases, seen particularly well in Figure 4.14 (f), where compressive stress remains only close to the plane of symmetry as due to anticlastic curvature the outer surface of the ring loses contact with the pin.

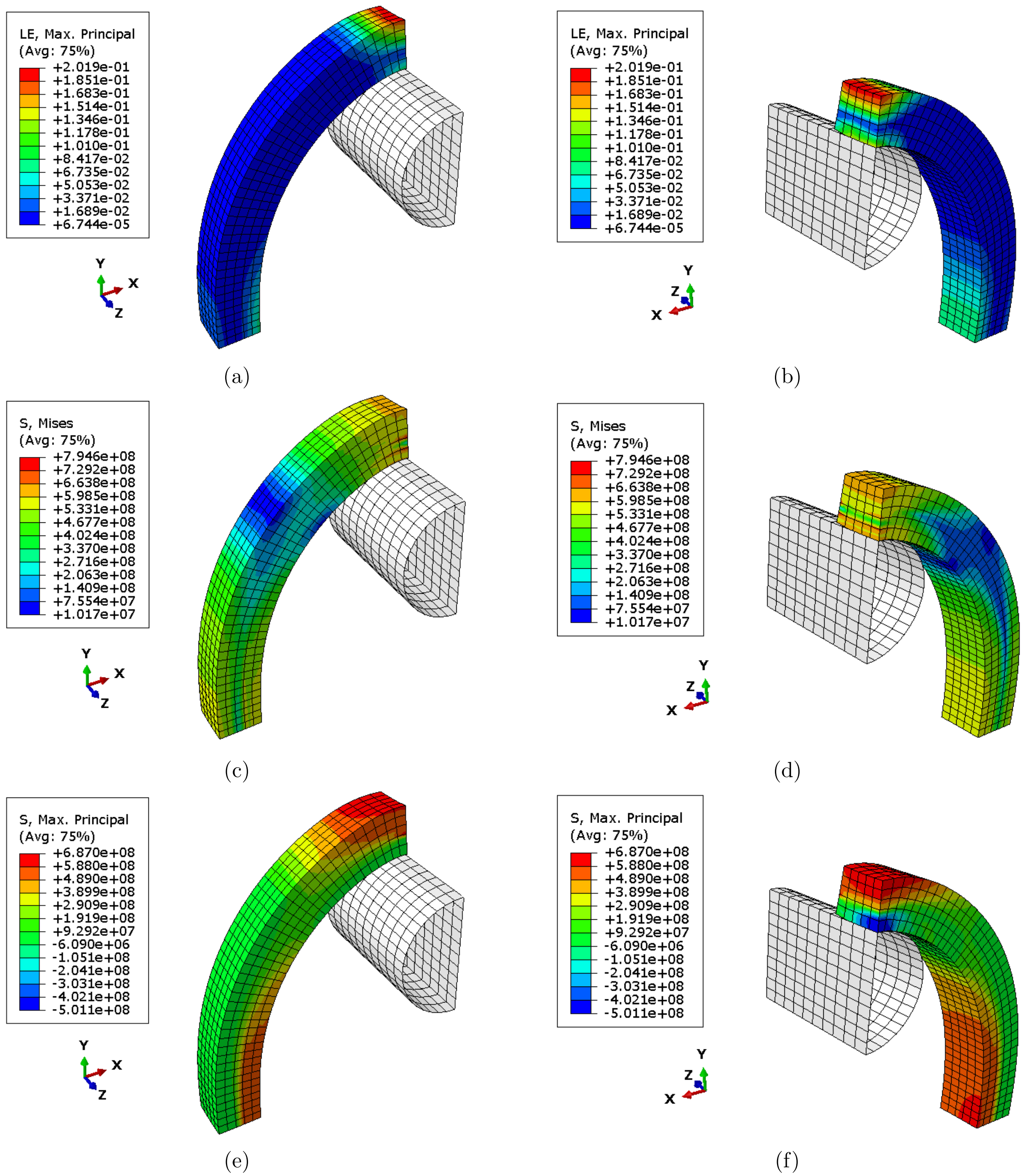

Figure 4.14: (a, b) Strain state (maximum principal strain); (c, d) stress state (von Mises stress); (e, f) stress state (maximum principal stress) at approximately the middle of loading.

When the ring is loaded past the point at which the elliptical assumption is correct, it deforms into a shape shown in Figure 4.15. The area above the pin conforms to the shape of the pin, next section retains an outwards curve and the middle portion of the ring curves inwards due to anticlastic curvature. Highest strain remains on the outside surface above the pin, variation of stress through thickness increases.

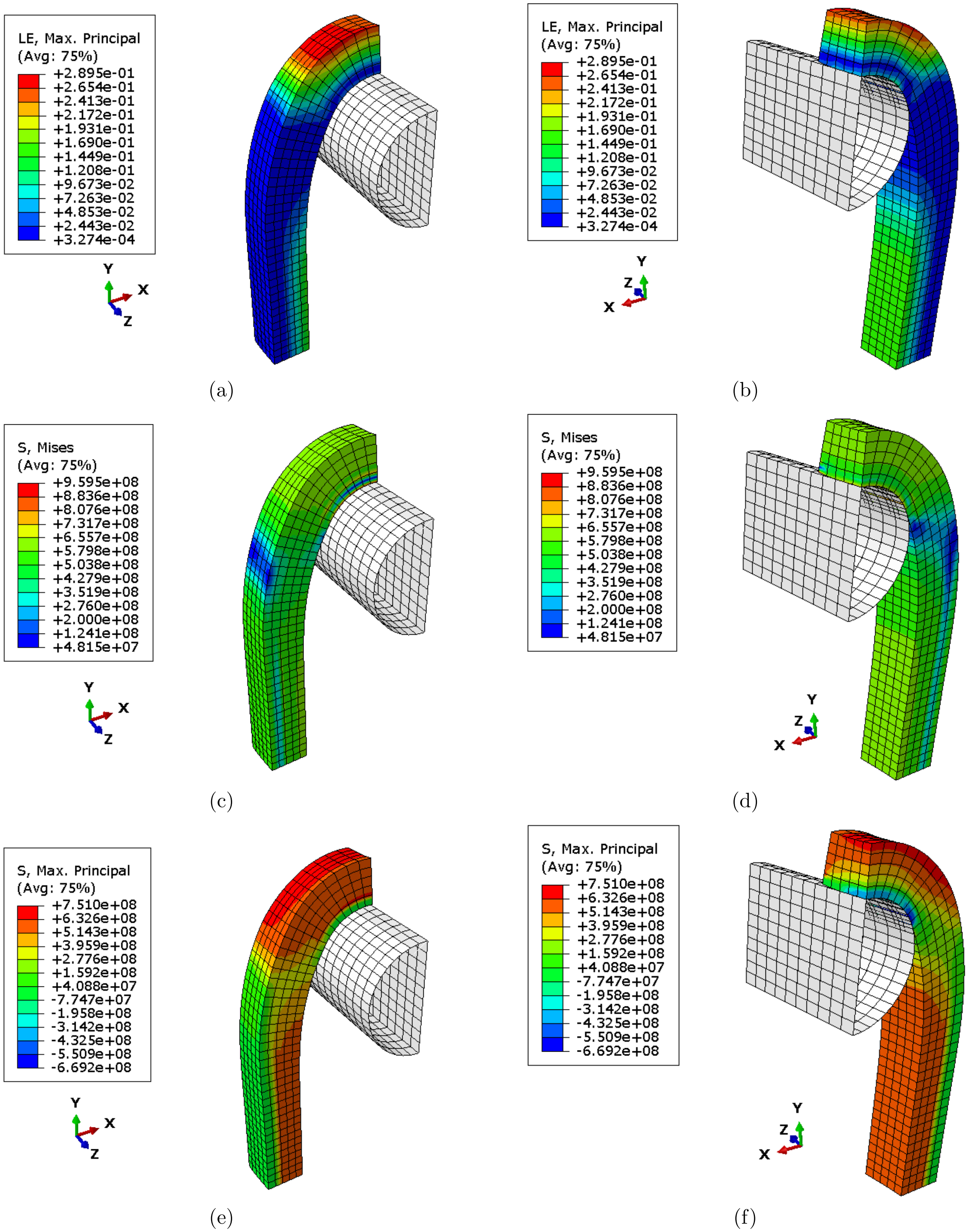

Figure 4.15: (a, b) Strain state (maximum principal strain); (c, d) stress state (von Mises stress); (e, f) stress state (maximum principal stress) towards the maximum loading.

To inspect the stress state in more detail stresses in 11 (x) direction and 22 (y) direction at later stages of loading are shown in Figure 4.16. Above the pin the outside surface of the ring is in tension due to it elongating as loading progresses while the inside surface is in compression due to contact with the pin and shortening as it conforms to the pin's curvature. The middle of the ring has the opposite stress state, with the outside surface being in compression due to the ring bending inwards and the inner surface being in tension.

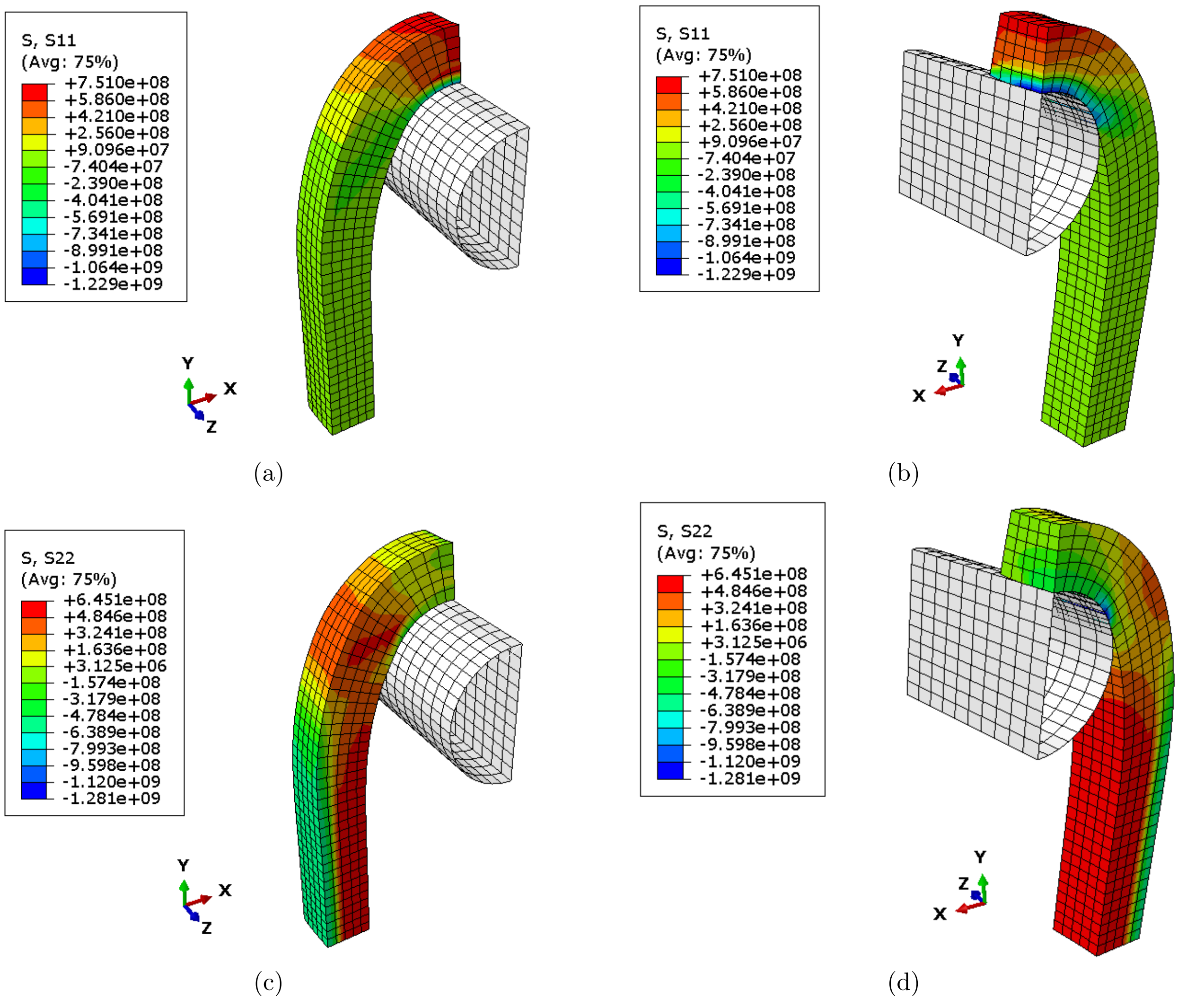

Figure 4.16: (a, b) Stress state in 11 (x) direction; (c, d) stress state in 22 (y) direction towards maximum loading.

Generally, small ring specimen tensile test results form a force-displacement curve which is shown in Figure 4.17. This is described in more detail in Chapter 5. Region I is the first slope, region II is the first transition, region III is the second slope, region IV is the second transition, it is followed by the third slope in region V, then the peak load in region VI and failure in region

VII. As damage is not included in the FEA model to keep it simpler, regions Vi and VII are not seen in FEA results.

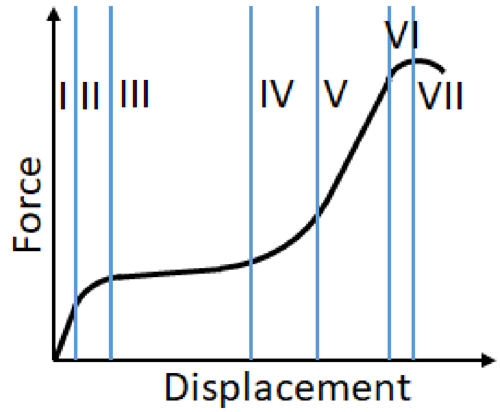

Figure 4.17: Example force-displacement curve with different regions labelled.

As the stress-strain state in the small ring specimen is not uniform the small ring specimen does not have a constant gauge length and section. Instead equivalent gauge section and equivalent gauge length were defined, showing the progression of the stress-strain state as the loading progresses.

The process was as follows: stress and strain in the vertical direction were extracted from the corner of the ring model (highlighted in Figure 4.1). The maximum principal stress in this location is aligned with the vertical direction, which can be seen in Figure 4.18, and other principal stresses were small in comparison, suggesting a uniaxial stress state. It is also the location of the onset of plasticity due to bending and tensile stress distributions. Reaction force and displacement in the y direction were extracted from the reference point of the pin. The equivalent gauge section A_{gauge} and the equivalent gauge length L_{gauge} were defined using Equations 4.50 and 4.51, respectively [1]:

$$L_{gauge} = \frac{\Delta L}{\varepsilon} \tag{4.50}$$

$$A_{gauge} = \frac{P}{\sigma} \tag{4.51}$$

where ΔL is the increment in length acquired from the reference point of the loading pin, ε is strain in the vertical direction, P is the applied load acquired from the reference point of the pin and σ is stress in the vertical direction.

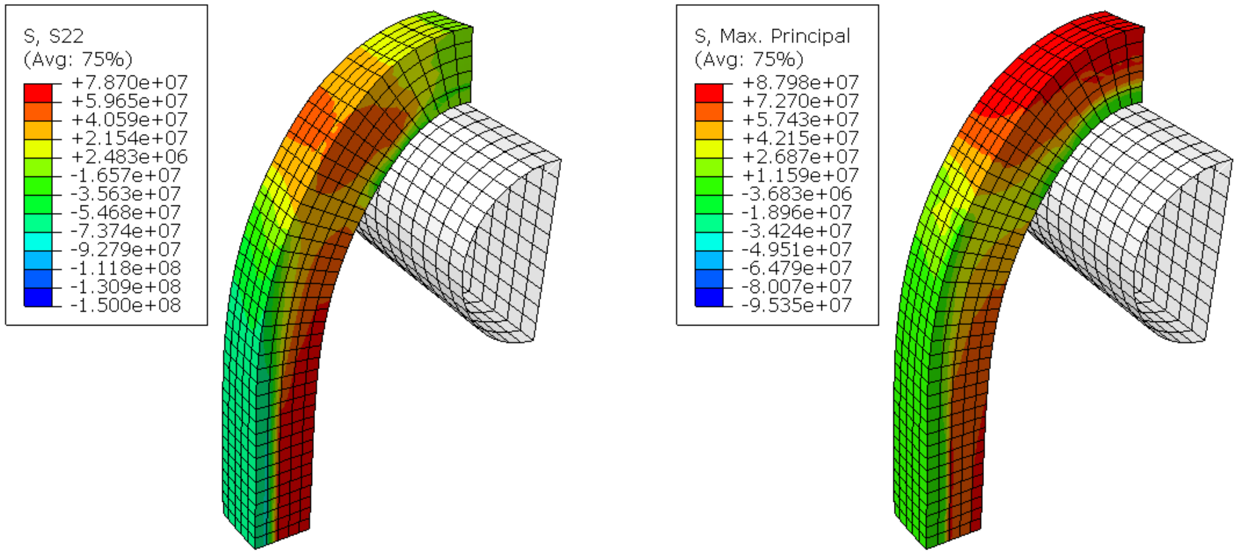

(a) (b)

Figure 4.18: Maximum stress in the small ring model (a) in the y-direction; (b) principal stress.

The resulting equivalent gauge length and section can be seen in Figure 4.19. The equivalent gauge section begins with a flat region, then transitions into a constant upwards slope. The flat region coincides with mostly elastic deformation while the slope coincides with hardening behaviour. The equivalent gauge length varies significantly during the loading, in this case between about 45 mm and about 23 mm, being higher at the beginning and then reducing. As the loading rate cannot be adjusted according to the change in gauge length during the testing, the initial value is used to calculate the appropriate loading rate, as per Equation 4.52, where $\Delta \dot{L}_{ring}$ is the loading rate for the small ring specimen, $\Delta \dot{L}_{standard}$ is the loading rate of the standard specimen, L_{gauge} is the equivalent gauge length of the small ring specimen and $L_{standard}$ is the gauge length of the standard specimen. For example, if the standard specimen has a gauge length of 50 mm and is loaded at the rate of 1 mm/min, for a small ring specimen with an equivalent gauge length of 45 mm the equivalent loading rate is $\frac{45\times 1}{50} = 0.9$ mm/min.

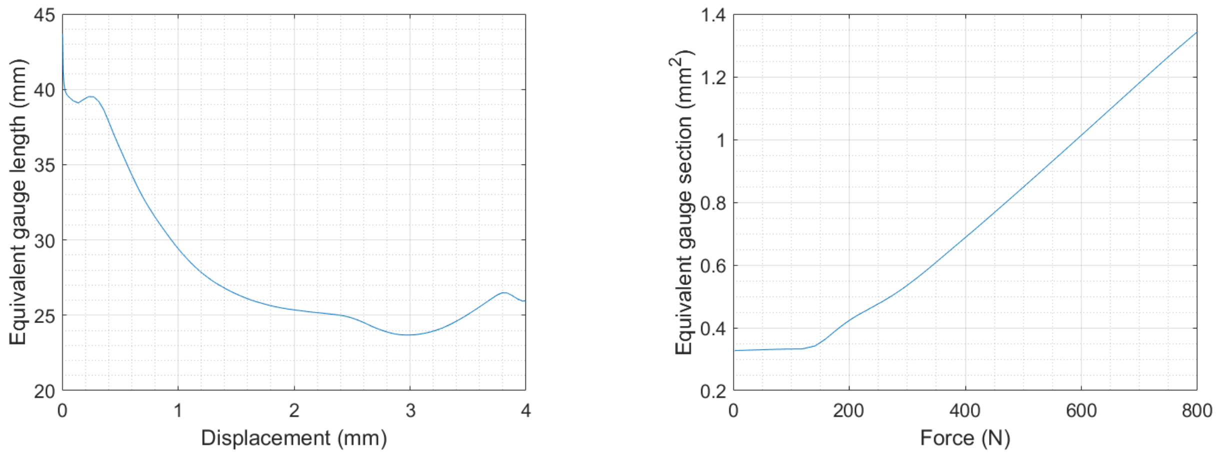

(a) (b)

Figure 4.19: Resulting equivalent gauge (a) length; (b) section.

$$\Delta \dot{L}_{ring} = \frac{\Delta \dot{L}_{standard} L_{gauge}}{L_{standard}} \tag{4.52}$$

4.3 Effects of Varied Material and Model Parameters

It is important to evaluate how varying material parameters and geometry parameters influences the small ring specimen test results. The effects of constitutive behaviour are important for developing a method to calculate bulk material stress-strain behaviour, while the effect of coefficient of friction shows if it is a significant contributor to the deformation and therefore a potentially significant source of error in test results. While geometry parameters were not varied experimentally, it is important to know how they would affect the test results, as changing them could affect the sensitivity to certain material model parameters, making the calculation of bulk material behaviour easier and more reliable.

4.3.1 Material

The Ramberg-Osgood material model parameters and the coefficient of friction were varied in order to see how they would affect the results of the small ring specimen tensile FE analysis and to provide a direction for developing a method to interpret the experimental data. The parameters varied were Young's modulus, yield stress, parameter n, parameter α and the coefficient of friction. They were varied one at a time, while keeping the other parameters constant to evaluate the magnitude of the effect of each parameter. When parameters were kept constant, Young's modulus was set to 50 GPa, yield stress was set to 400 MPa, parameter n was set to 10, parameter α was set to 1 and friction behaviour was set to frictionless.

Young's modulus was varied between 50 GPa (applicable to tin) and 250 GPa (applicable to certain nickel chrome alloys), the effects of this variation on the stress-strain curve and force-displacement curve can be seen in Figure 4.20. The variation in the stress-strain curve does not only result in a change in slope but also in a longer transition and the stress being higher after the transition with higher Young's modulus. This is expected as Equation 2.14 showing the Ramberg-Osgood material model used to describe the materials accounts for Young's modulus in both elastic and plastic parts of the stress-strain curve. A similar trend can be seen in the force-displacement curve, however there the first transition becomes shorter when Young's modulus increases. The shape of the remaining part of the curves does not seem to be affected. This indicates that the first slope of the force-displacement curve is governed by Young's modulus.

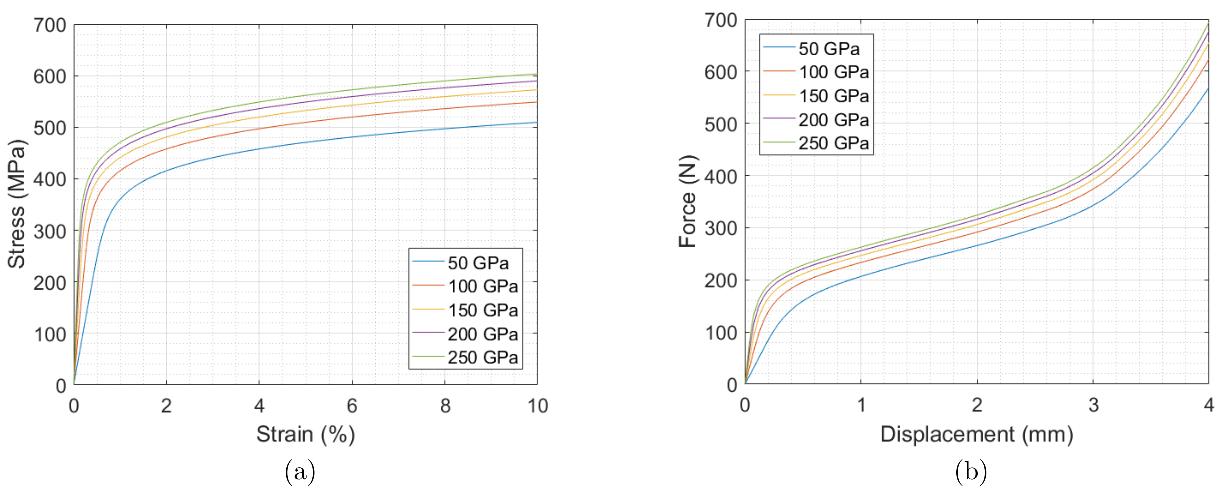

Figure 4.20: The effect of varied Young's modulus on the (a) stress-strain curves; (b) force-displacement curves.

Figure 4.21 shows the effect of varied Young's modulus on the equivalent gauge length. The initial part of the equivalent gauge length (up to about 0.1 mm) is not affected at all, then the curves diverge and converge again at around 4 mm displacement. Young's modulus of 50 GPa corresponds with higher equivalent gauge length, varying between 50 mm at the point of divergence and 35 mm at the lowest point, while Young's modulus of 250 GPa corresponds with lower equivalent gauge length, with the lowest value being around 30 mm. Higher Young's modulus also results in sharper drop of the equivalent gauge length. This can be explained by the fact that higher Young's modulus results in lower strain to yield stress and, while keeping the displacement the same, it results in the equivalent gauge length curves with higher Young's modulus diverging at lower displacement. Lower Young's modulus also results in lower strain when displacements are the same.

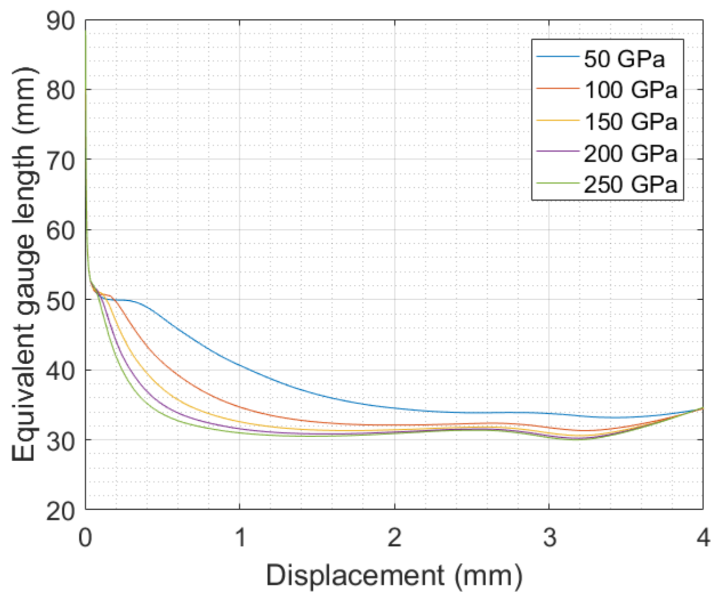

Figure 4.21: The effect of varied Young's modulus on the equivalent gauge lengths.

The yield strength was varied between 200 MPa (applicable to brass) and 600 MPa (applicable to certain steels), the effects of this variation on the stress-strain curve and force-displacement curve can be seen in Figure 4.22. In a stress-strain curve the variation of yield strength affects the divergence from the elastic region. As parameter α (yield offset) was set to 1 yield stress appears to be lower than specified. In the force-displacement curves it affects the length of the first slope and the second slope, as well as the second transition. The increase in resulting forces in the second slope appears to be linear, with a linear increase in yield strength resulting in linear increase in force, seen particularly well in Figure 4.22 (b) at 2 mm displacement, as the difference between the adjacent curves is around 50 N. Therefore it can be stated that the divergence from the initial slope and the second slope in the force-displacement curves are governed by yield stress.

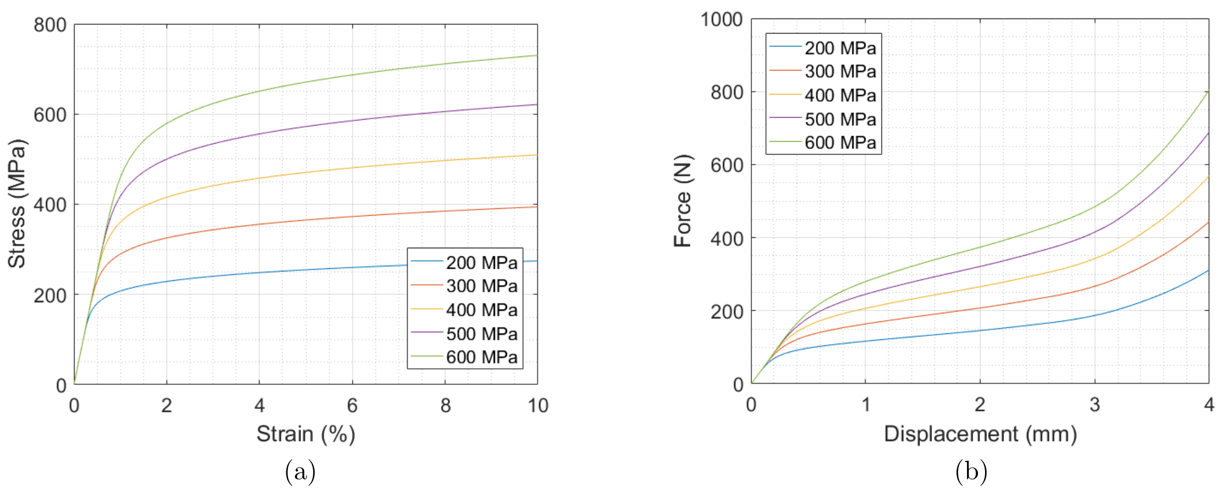

Figure 4.22: The effect of varied yield strength on the (a) stress-strain curves; (b) force-displacement curves.

The effect of varied yield strength on the equivalent gauge length is shown in Figure 4.23. The initial part of the equivalent gauge length is also not affected by this variation, with the curves diverging at around 0.1 mm, then converging again at around 4 mm. Higher yield strength results in higher equivalent gauge sections, 200 MPa corresponding to a variation of 50 mm at the point of divergence and 31 mm at the lowest point, while 600 MPa results in the lowest value of 35 mm. Lower yield strength also results in sharper transition to the lowest value, similarly to high values of Young's modulus. As lower yield stress results in a lower strain at yield, it would result in a higher equivalent gauge length.

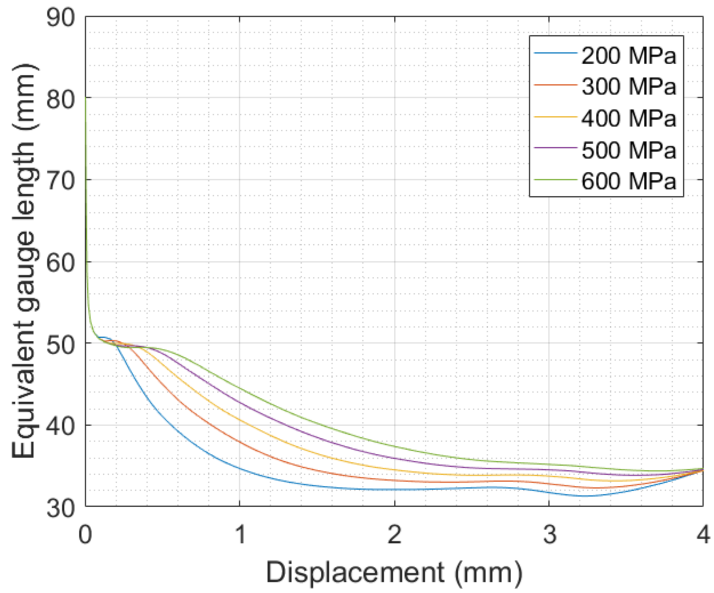

Figure 4.23: The effect of varied yield strength on the equivalent gauge lengths.

Parameter α was varied between 0.5 and 1.5, the effects of this variation on the stress-strain curve and force-displacement curve can be seen in Figure 4.24. This range was chosen as it was wide enough to clearly show the effect of varying this parameter. Decreasing parameter α elongates the transition in the stress-strain curve, similar to the effect of increasing Young's modulus on the transition. In the force-displacement curves the first transition is also elongated by decreasing α, which then also increases the steepness of the second slope. According to the Ramberg-Osgood equation, while keeping the stress the same higher α results in higher strain, as well as higher displacements at the same force.

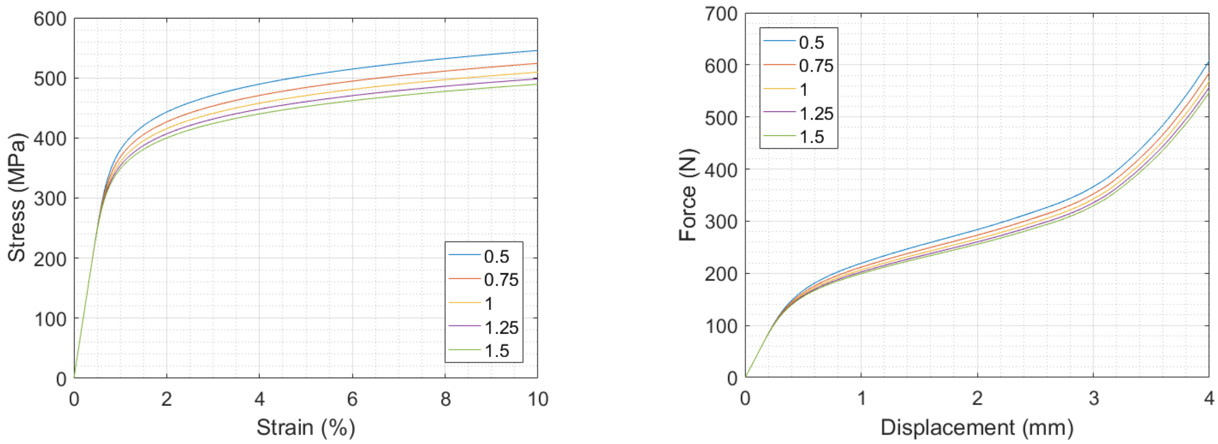

(a) (b)

Figure 4.24: The effect of varied parameter α on the (a) stress-strain curves; (b) force-displacement curves.

Equivalent gauge length is barely affected by the change in parameter α as shown in Figure 4.25. Higher parameter α results in lower equivalent gauge length. The explanation for why the higher values of α result in lower equivalent gauge length is the same as for varied Young's modulus and yield stress.

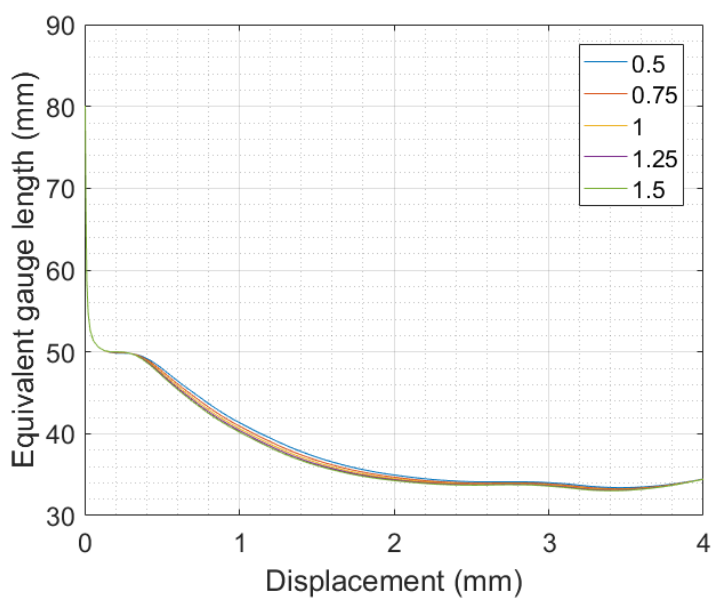

Figure 4.25: The effect of varied parameter α on the equivalent gauge lengths.

As for parameter n, it was varied between 10 and 26, the effects of this variation on the stress-strain curve and force-displacement curve can be seen in Figure 4.26. This range was chosen as it was wide enough to clearly show the effect of varying this parameter. Increasing parameter n results in a sharper transition and lower stresses after it. The effect on the force-displacement curves is similar, with lower values of n resulting in higher forces after the first transition and smoother second transition. The effect on the first transition is negligible.

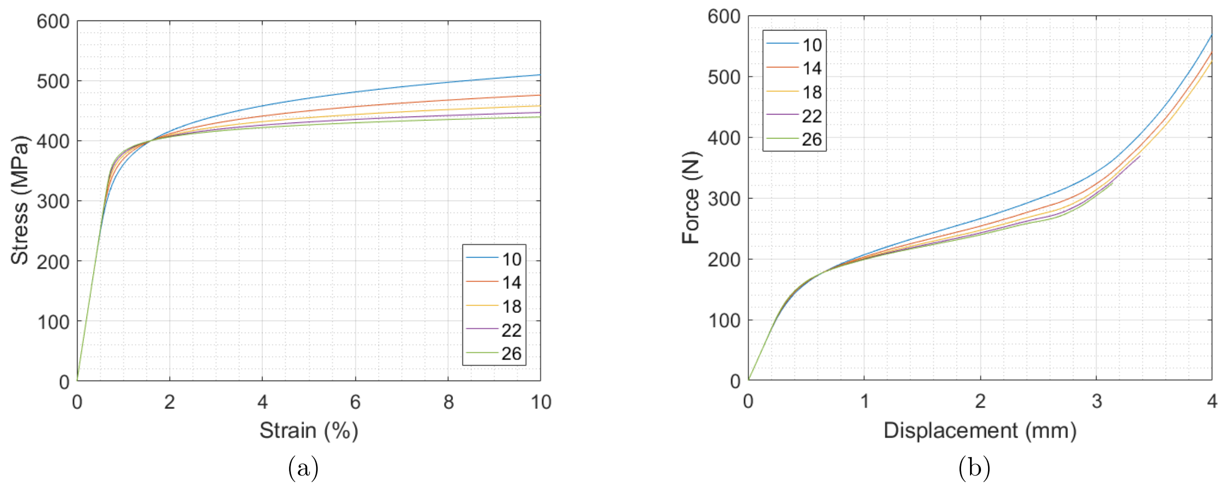

Figure 4.26: The effect of varied parameter n on the (a) stress-strain curves; (b) force-displacement curves.

The effect on equivalent gauge length is also small, but more significant than parameter α, as shown in Figure 4.27. Lower values of n result in higher equivalent gauge length and smaller variation of it as the loading progresses, between 50 mm at divergence and 34 mm for 10 and 50 mm and 29 mm for 26. The explanation for why the higher values of n result in lower equivalent gauge length is the same as for varied Young's modulus and yield stress.

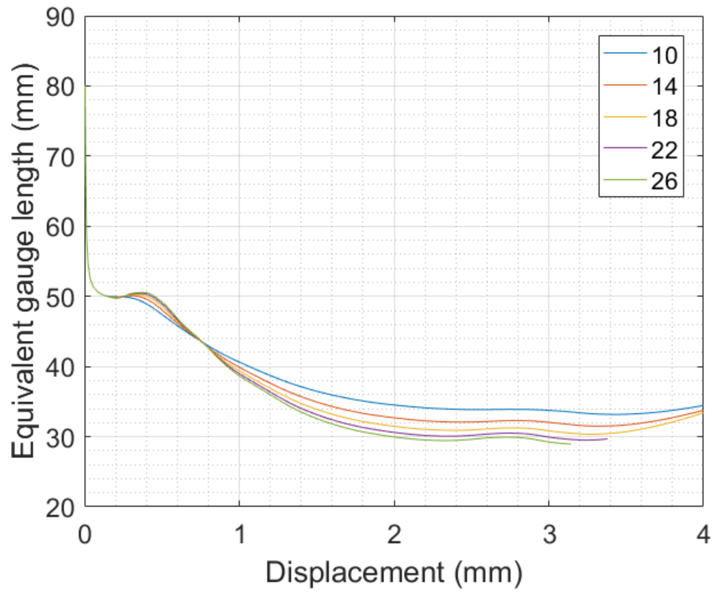

(a)

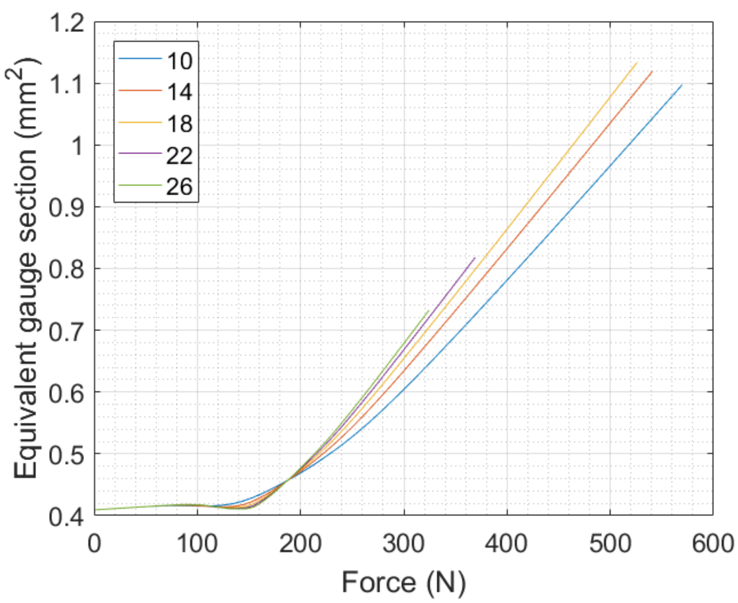

(b)

Figure 4.27: The effect of varied parameter n on the (a) equivalent gauge lengths; (b) equivalent gauge sections.

Overall, it can be concluded that the first slope is governed by elastic behaviour only, as varying other parameters does not change it. The first transition is governed by all parameters, with yield strength having the most significant effect. The second slope is governed by all parameters apart from Young's modulus, with yield stress having the most significant effect. The second transition is governed by all parameters, with n having the most significant effect. The initial gauge length and gauge section are not affected by material parameters at all. All variations investigated result in an equivalent gauge length between 30 mm and 40 mm for a significant part of the deformation, with the initial length sharply dropping from around 80 mm to 50 mm. Equivalent gauge section is affected by all parameters after the initial region with yield strength having the most significant effect on the shape. This means that, for an initial estimate of material behaviour, the loading rate for small ring tensile tests and the relationship between displacement and strain can be reasonably estimated without knowing any material properties, but the relationship between force and stress cannot, and a more sophisticated interpretation method needs to be developed.

As for coefficient of friction, it was varied between 0 (frictionless behaviour) and 1 as this is a realistic range of coefficients of friction for metal on metal contact. The effects of this variation on the force-displacement behaviour can be seen in Figure 4.28. There is no significant effect, therefore the contact is modelled as frictionless for small ring specimen tensile FEA and no additional measures have to be taken when setting up the tests.

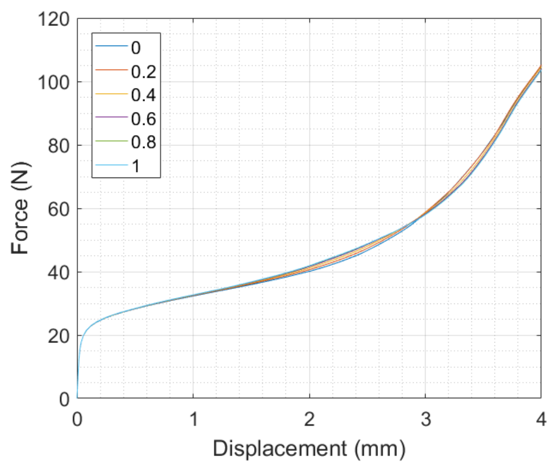

Figure 4.28: The effect of varied coefficient of friction on the force-displacement curve.

4.3.2 Geometry

The geometry parameters of the small ring tensile testing setup were varied in order to see how it would affect the sensitivity of the test and to provide a direction for improvements to the setup for future testing depending on what specific part of the response is of interest. The ring parameters varied were the radius at load application making the ring either elliptical vertically or horizontally before it is deformed, also the radial thickness (the difference between the outer and inner radius of the ring) and lateral thickness making the cross-section differently proportioned. The effects of making the pin elliptical were also investigated, however that would be difficult to implement practically. The parameters were varied one at a time, while keeping the other parameters constant to evaluate the magnitude of the effect of each parameter.

The radius of the ring at load application (parameter b in Figure 4.4 (a)) was varied between 5 mm and 7 mm making the ring into a vertical ellipse before loading begins. This range was chosen because the lower radius of the range makes the ring only slightly elliptical and the upper radius of the range still allows the ring to bend freely before impinging onto the pins. The effects of that variation on the resulting force-displacement curves, the equivalent gauge section and length can be seen in Figure 4.29. There is a significant effect on the whole force-displacement curve, with larger radius corresponding with lower forces and longer second slope, while smaller radius corresponds with longer first slope. Equivalent gauge section plot begins with a flat region, then transitions into a converging slope. Higher values of radius correspond with lower equivalent gauge section and this reduction appears to be proportional to the increase in radius. Equivalent gauge length increases as the radius increases, with the magnitude of the increase also increasing at higher values of the radius. For example, at 1 mm of displacement the increase in equivalent gauge length between 5 mm and 5.5 mm radius is around 10 N, but between 6.5 mm and 7 mm it is around 20 N. Overall, this change in geometry would make it easy to keep the ring in alignment as it would naturally align while hanging on a pin. Longer equivalent gauge section is an advantage, however the more elongated the ellipse is, the closer it becomes to a two-bar specimen, which would likely behave differently due to a different geometry around the pins. The effect of the pins on the small ring specimen deformation would also become relevant at lower deformations.

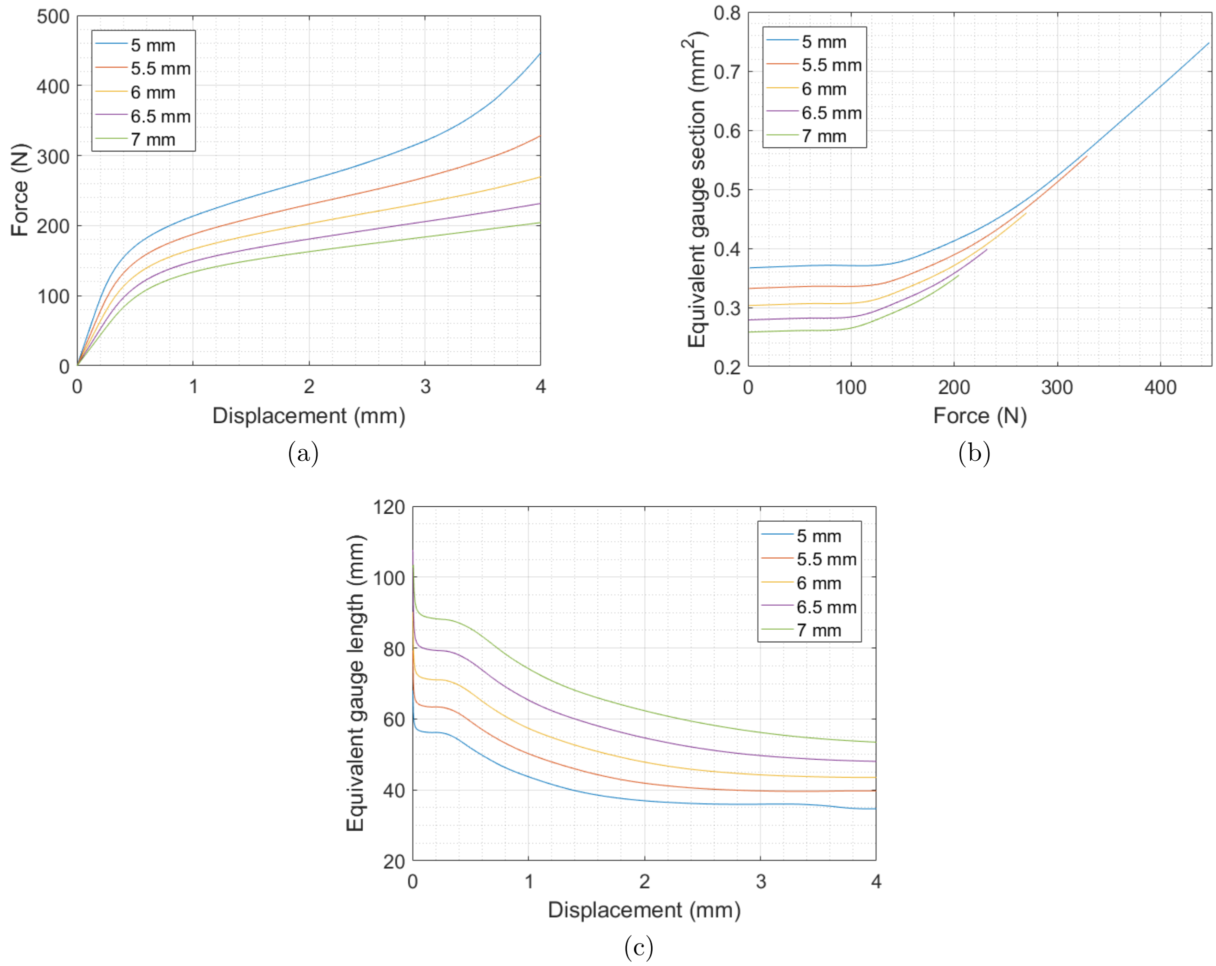

Figure 4.29: The effect of changing the ring into a vertical ellipse on (a) force-displacement curves; (b) the equivalent gauge section; (c) the equivalent gauge length.

Then, the radius of the ring at load application (parameter b in Figure 4.4 (a)) was varied between 2.5 mm and 4 mm making the ring into a horizontal ellipse before loading begins. This range was chosen because the lower radius is the absolute minimum radius which still allows to use the same pins and the upper radius makes the ring slightly elliptical. The effects of that variation on the resulting force-displacement curves, the equivalent gauge section and length can be seen in Figure 4.30. Force-displacement curves are only significantly affected after the displacement of around 1.5 mm, with lower values corresponding to higher forces and shorter second slope. The equivalent gauge section plot begins with a flat region, then transitions into a slope, with all slopes being separate, unlike when the ring was changed into a vertical ellipse. Higher radius corresponds to higher equivalent gauge section, which is the opposite of what was found by making the ring into a vertical ellipse. As for equivalent gauge length, higher values of radius correspond with higher equivalent gauge length, which is the same as what was found when making the ring into a vertical ellipse. As longer equivalent gauge length is advantageous, a circular ring is preferable to a horizontal ellipse. This change in geometry would make appropriate ring positioning difficult to achieve in practice, making this potential improvement not viable.

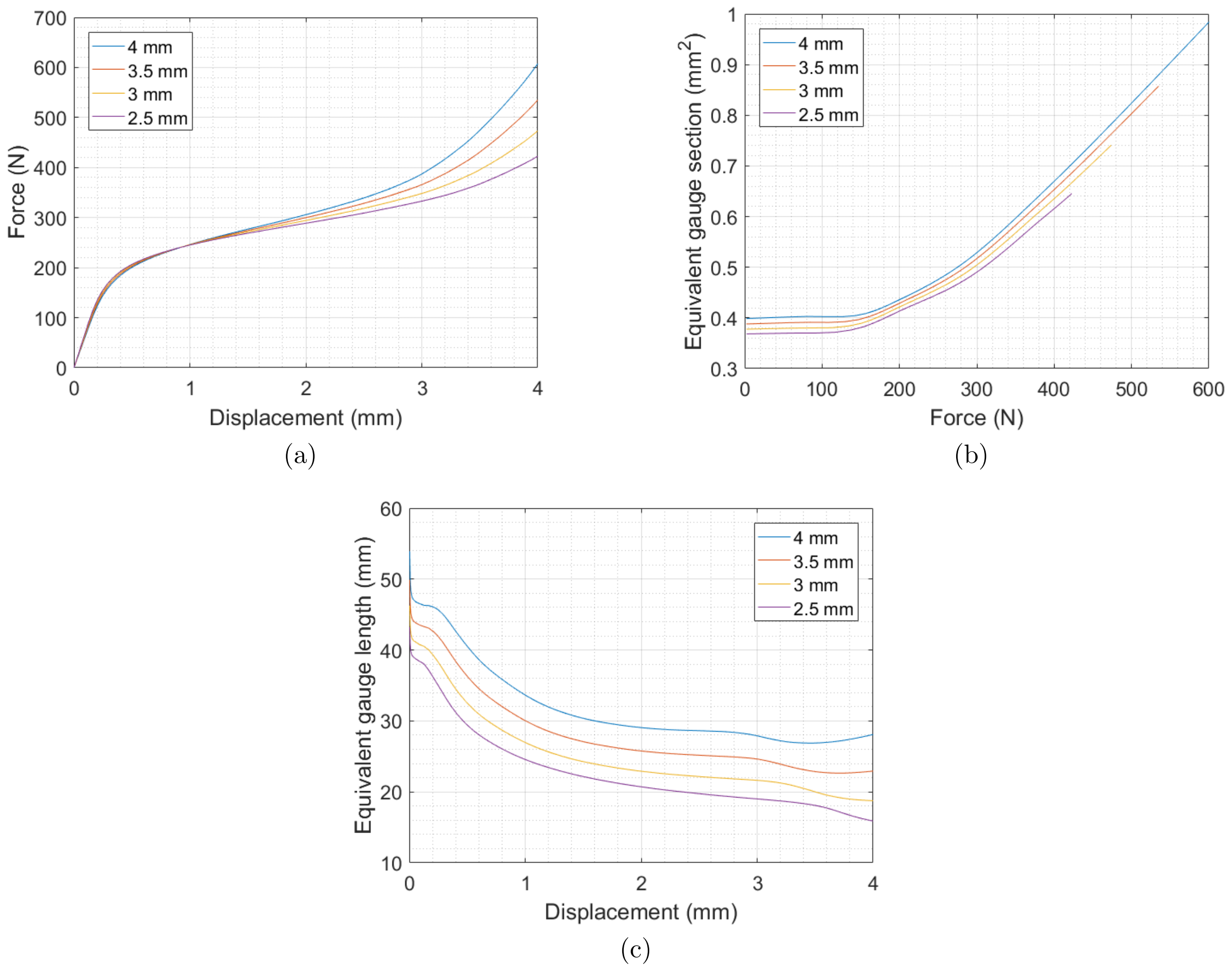

Figure 4.30: The effect of changing the ring into a horizontal ellipse on (a) force-displacement curves; (b) the equivalent gauge section; (c) the equivalent gauge length.

Figure 4.31 shows the effect of varied radial thickness (the difference between inner and outer radius) on the resulting force-displacement curve, equivalent gauge length and section. The radial thickness was varied between 0.5 mm and 1.25 mm. This range was chosen because it was wide enough to clearly show the effect of varying this parameter. The whole force-displacement curve is affected, with higher thickness corresponding to longer first slope, and steeper first and second slopes. As for equivalent gauge section, it starts with a flat region, the length of which increases as the thickness increases, then transitioning into a slope, which does not depend on the thickness. Higher thickness also corresponds with higher initial equivalent gauge section. As for equivalent gauge length, higher thickness corresponds to lower equivalent gauge length values. This reduction is very non-linear, as at 1 mm displacement the change of thickness between 0.5 mm and 0.75 mm results in a reduction of about 32 mm, while the change between 1 mm and 1.25 mm results in a reduction of 7 mm. As longer equivalent gauge length is preferable, a thinner ring would be beneficial, however, that could cause early failure. On the other hand, keeping in mind that some of the small ring tensile results had a very short first slope, using a thicker ring would make it clearer.

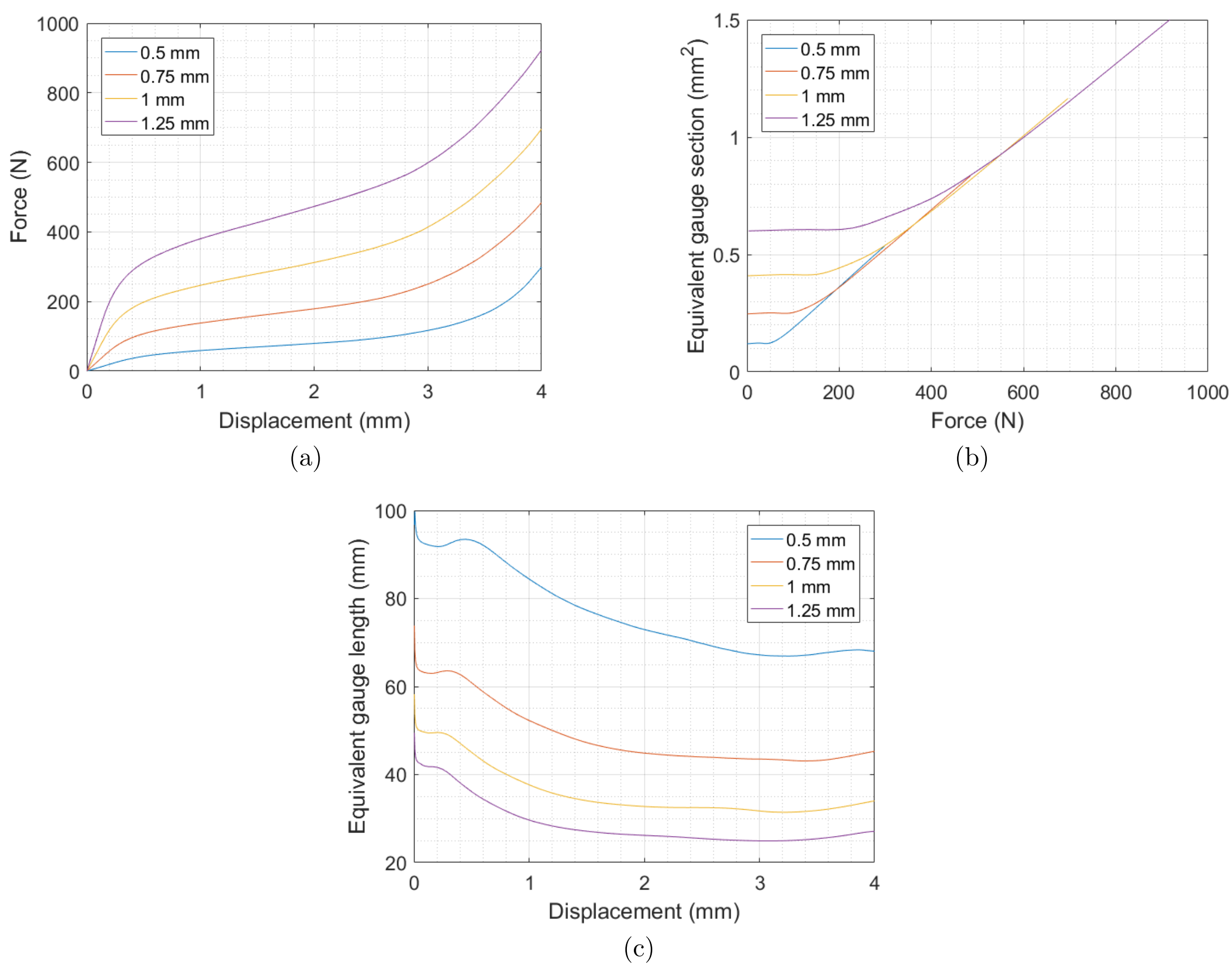

Figure 4.31: The effect of varied radial thickness on (a) force-displacement curves; (b) the equivalent gauge section; (c) the equivalent gauge length.

Lateral half-thickness (the distance between the plane of symmetry and a flat surface of the ring) was varied between 0.5 mm and 2 mm. For a full ring that is equivalent to a variation between 1 mm and 4 mm. This range was chosen because the lower limit would make the ring very thin laterally in comparison to the radial thickness and the upper limit is the maximum lateral thickness of a ring which can be tested in the existing setup. The effects of that variation on the resulting force-displacement curve, equivalent gauge length and section can be seen in Figure 4.32. For the force-displacement curve and equivalent gauge section, the effect is very similar to the effect of changing radial thickness. Equivalent gauge length is affected significantly less, with a change in thickness of 1.5 mm resulting in a difference of around 3 mm at 1 mm displacement, while the change of 0.75 mm resulted in a difference of 55 mm when radial thickness was varied. Using both a thicker and thinner ring has potential advantages and disadvantages. A thinner ring would use less material, however it could experience early failure, while a thicker ring would use more material, but the equivalent gauge length would also be marginally increased and the first slope would be longer and clearer. Overall, if the first slope is of interest and needs to be elongated without sacrificing the equivalent gauge length, lateral thickness, as opposed to radial thickness should be increased.

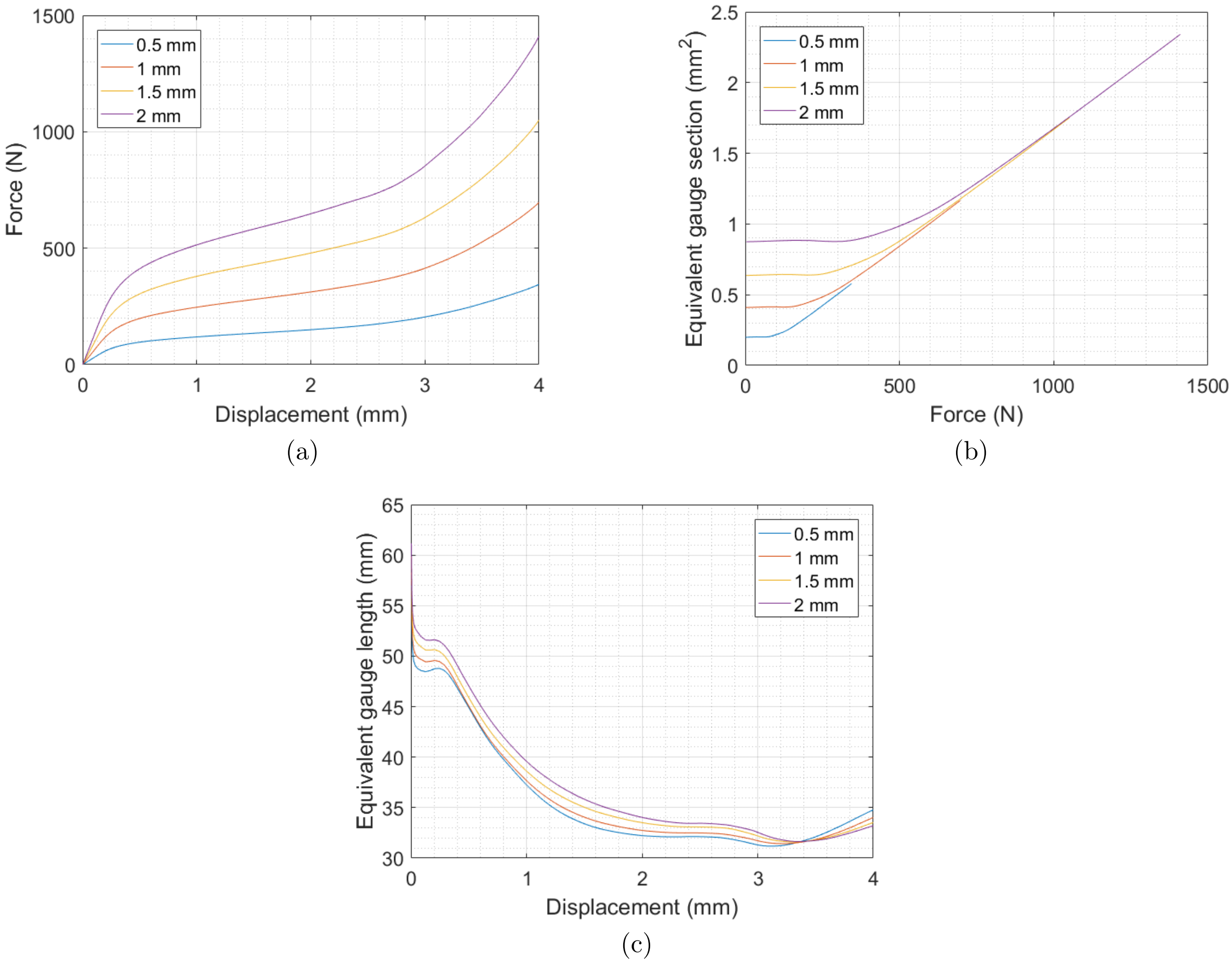

Figure 4.32: The effect of varied lateral thickness on (a) force-displacement curves; (b) the equivalent gauge section; (c) the equivalent gauge length.

Moving on to geometry changes, which would be difficult to implement practically, using elliptical pins. Keeping the radius of the pin 90^o from the radius in contact with the ring 1.25 mm and varying the radius in contact with the ring between 0.75 mm and 1.5 mm has a significant effect on the force-displacement curves after a displacement of 1.5 mm and no significant effect on the equivalent gauge section and length, as shown in Figure 4.33. This range was chosen because it was wide enough to clearly show the effect of varying this parameter. Higher radius results in shorter second slope and earlier second transition. Some wobbles can be seen in Figure 4.33 (c), specifically with the vertical pin radius of 1.5 mm between 2.5 mm and 3.5 mm displacement. They are likely caused by the interactions between the mesh of the pin and the mesh of the ring and could be avoided by using analytical rigid surface as opposed to discrete rigid surface definition, however that would increase the time needed to run the analysis.

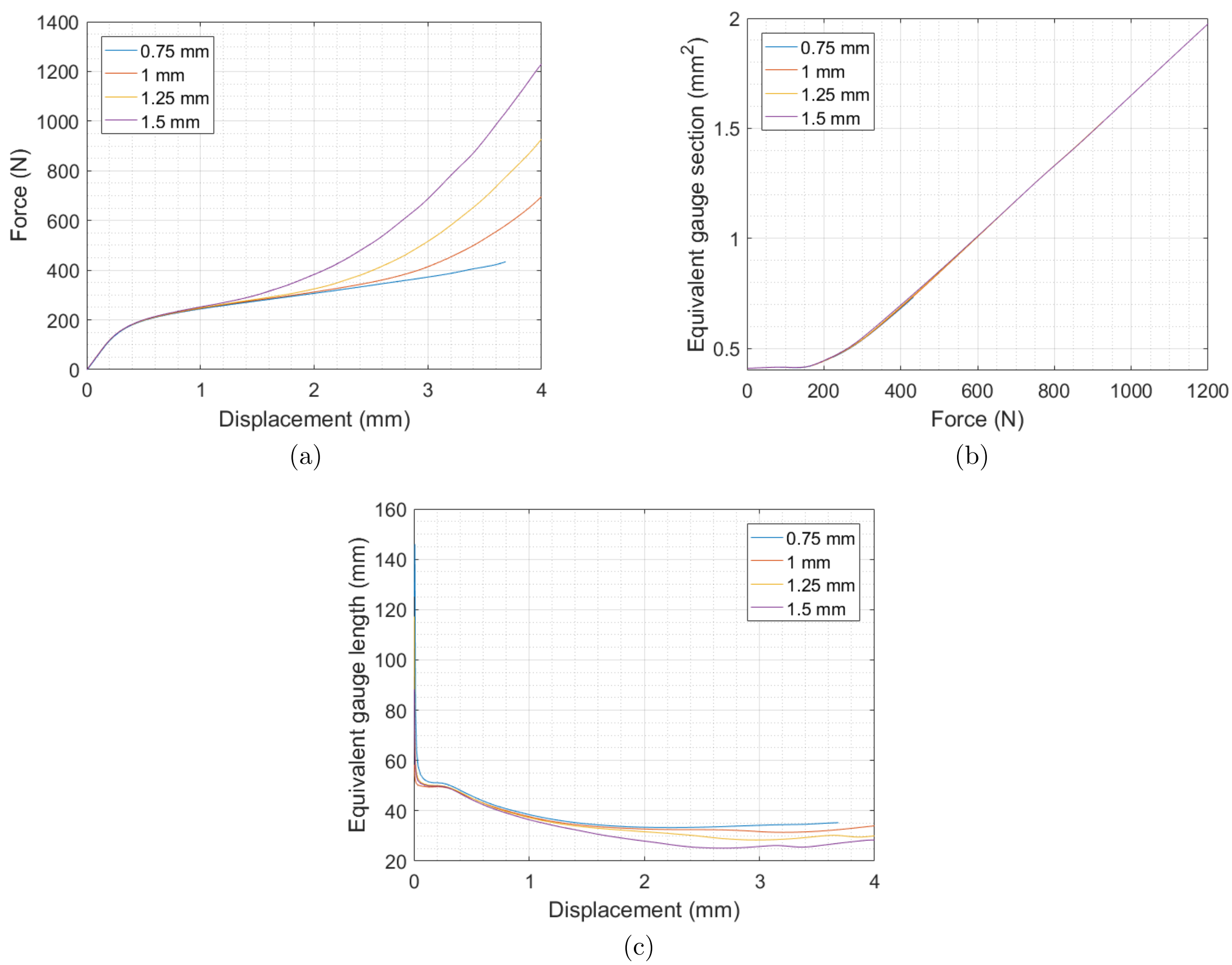

Figure 4.33: The effect of varied vertical radius of the pin on (a) force-displacement curves; (b) the equivalent gauge section; (c) the equivalent gauge length.

Then, keeping the radius in contact with the ring 1.25 mm and varying the radius 90^o from the contact between 0.75 mm and 1.5 mm has a significant effect after the displacement of around 2 mm and virtually no effect on equivalent gauge section and length, as shown in Figure 4.34. This range was chosen because it was wide enough to clearly show the effect of varying this parameter. Higher radius corresponds with longer second slope.

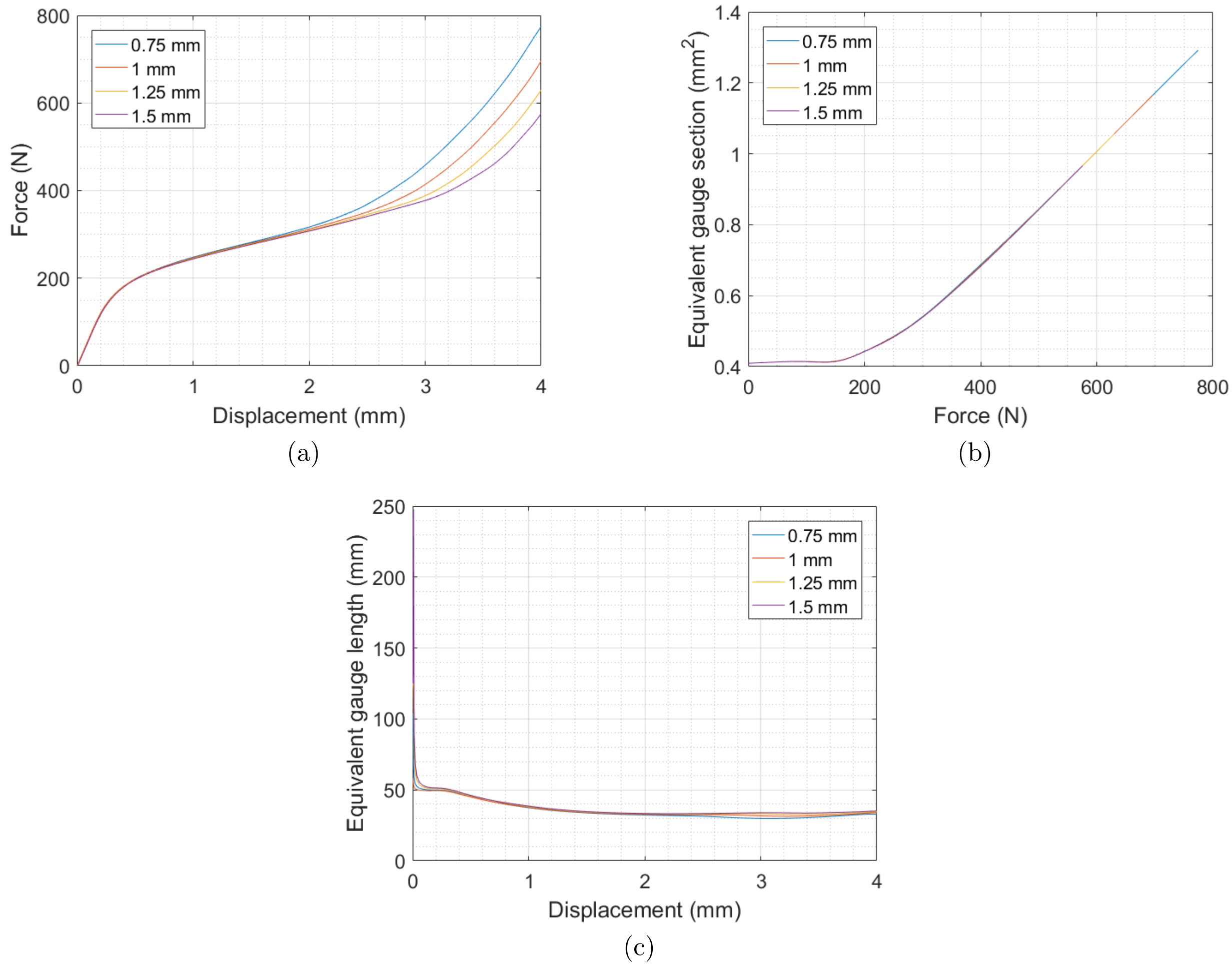

Figure 4.34: The effect of varied horizontal radius of the pin on (a) force-displacement curves; (b) the equivalent gauge section; (c) the equivalent gauge length.

Overall, making the ring into an ellipse before loading removes the advantage of it being simple to manufacture and does not give any significant advantages. Making a thicker ring increases the length of the first slope, which is potentially useful for evaluating the Young's modulus of material with low yield stress, and lateral thickness is more suitable for this than radial thickness, as the effect on equivalent gauge length is smaller. Using elliptical pins would require the loading setup to be redesigned and the benefits would be marginal at best.

4.4 Discussion

The FEA model was deemed to be representative of small ring specimen tensile results, even though it diverges from experimental results at higher deformations. The divergence is caused by the fact that the model does not take damage into account, as a lot of materials (especially aluminium alloys) fail before it becomes relevant. This model is applicable only to materials which can be described using the Ramberg-Osgood material model. A different material model would need to be used to describe those materials and that was not investigated in this work.

In comparison to the FEA model, the analytical model is promising for calculating full force-displacement behaviour, showing good agreement with experimental behaviour and FEA up to 1.2 mm for vertical displacement and 0.6 mm horizontal displacement. However, it is currently only suitable for elastic behaviour due to the accurate plastic behaviour being very dependent on appropriate load increment. The advantage of this model is that it would be less computationally expensive to generate a large number of force-displacement curves than when using the FEA model when the model is completed. The elastic-only version of this model could be used to calculate Young's modulus using inverse analysis, or, if it was simplified to not take the change of shape into account, by applying a formula.

FEA investigation of the small ring deformation shows that the shape of the ring can be approximated to an ellipse at the initial stages of deformation but diverges from it at displacement higher than 2 mm, which is caused by the ring conforming to the shape of the pins as it deforms. The stress state in the ring indicates that it behaves like a beam under bending apart from areas in contact with the pin. A generalized force-displacement curve for a small ring specimen under tensile loads was identified, with seven distinct regions, but due to the specifics of the FEA model setup the last two regions are not visible on the FEA curves.

Varying material model parameters and observing the changes which occur in the force-displacement curves, shows that the first slope is suitable for determining Young's modulus as changing the other parameters does not affect it. It is further proven by a lack of variation in the first slope between repeats of the tests of the same material, shown in Chapter 5. The remaining part of the curve is governed by a combination of all parameters, with yield stress being a particularly significant contributor to the second slope. This means that, provided the parameters n and α do not vary significantly, the second slope (parameter d) can be used to determine yield stress. Also, significant changes in material properties do not change the equivalent gauge length significantly, therefore loading rates for rate independent materials can be calculated easily. As the coefficient of friction does not have a significant effect on the force-displacement results is does not have to be accounted for when interpreting them.

Varying geometry parameters is not particularly relevant for interpreting the experimental results, instead, it is useful for planning future testing. The parameters most practical to change are radial and lateral thickness and varying them could make the first slope longer in cases of low yield stress and make Young's modulus easier to evaluate. Regarding misalignment, the misalignments investigated do not affect the testing results due to small allowable maximum magnitudes.

4.5 Summary and Conclusions

This chapter described the work done on modelling the small ring specimen under tensile loading. A semi-analytical model was developed and the FEA models were validated. Initial investigations into the shape of deforming ring and the stress state in it were made. Using the validated models, geometry and material model parameters were varied to establish trends and direct the development of an interpretation method.

The main conclusions from this chapter are as follows:

- An FEA model representative of experimental setup was developed using a Ramberg-Osgood material model.
- The current version of the analytical solution is suitable for evaluating Young's modulus using inverse analysis, additional work is needed for it to be suitable for the stress-strain

behaviour.

- Seven stages of the small ring specimen force-displacement curves were identified.
- Misalignment and coefficient of friction were found to have no significant effect on force-displacement curves.

5 Small Ring Specimen Tensile Testing and Data Interpretation

5.1 Introduction

Tensile testing results from conventional and small ring tests are presented and discussed in this chapter. An overview of tensile material behaviour is described in Section 2.3.1. As the aim of the whole project is to develop a small ring specimen cyclic testing technique, first the suitability of small ring specimens for tensile testing had to be evaluated as that is a good stepping stone towards cyclic testing, as shown by several testing techniques that were first applied to tensile testing then adapted to cyclic or fatigue testing, such as the hydraulic bulge test [106, 148] or the small punch test [155, 176]. In order to evaluate the suitability, a method to test the small ring specimens under tensile load and a method to interpret the data had to be developed and a sufficient number of tests had to be done. It is described in this chapter.

Specifically, a range of temperatures and rates are used during testing to investigate the effects of ageing and rate dependency on the results. Repeatability is investigated for both conventional testing and small ring testing, as well as fracture behaviour, failure patterns and characteristic force-displacement curves for small ring specimen tensile results.

A dataset of virtual test FEA results was created and then used to investigate the suitability of several different methods for calculating bulk material tensile properties: direct correlations between parameters fitted to the force displacement curves and the material model parameters, ordinary least squares, principal component regression, neural networks and inverse analysis. Real small ring tensile test data was then used to test the methods, by using them to calculate stress-strain behaviour and comparing this to the stress-strain behaviour acquired from conventional specimen testing.

5.2 Testing Methodology

The small ring specimen creep loading setup [1] was used for tensile testing without additional adaptations. Small ring tensile tests of 2014A-T6 and 6082-T6 aluminium were done on the small ring specimen cyclic testing setup (shown in Figure 7.9) without using a clamping rod, which was unnecessary as it was used to clamp cyclically loaded small ring specimens in order to apply a fully reversed displacement. Some rates (4.08 mm/min, 2.04 mm/min, 0.204 mm/min and 0.0204 mm/min) were chosen according to preliminary FEA analysis (described in detail in Section 4.2.3) and other ones (5 mm/min) were chosen according to finalized FEA analysis. In order to evaluate vertical displacement LVDT extensometer readings from knife edges were used [1]. Data used to calculate the horizontal displacement was collected by an undergraduate project student using a FLIR SC7200 infrared camera, the rates there (600 mm/min, 60 mm/min and 6 mm/min) were chosen according to the work on small ring specimen creep testing [177].

The small ring specimen tensile testing programme is described in Table 5.1. Both Tinius Olsen H25Ks and Mayes 250 testing machines were fitted with a 25 kN load cell. The loading rates for P91 steel were chosen according to finalized FEA analysis, while the loading rates for 2014A-T6 aluminium and 6082-T6 aluminium were chosen to be the same as for standard specimens (5 mm/min), as the gauge length of the conventional specimens used and the equivalent gauge length of the small ring specimen was similar. Both testing machines were LVDT displacement controlled and force-displacement data was collected with Horizon software.

Table 5.1: Small ring specimen tensile testing programme. V+H means vertical and horizontal displacement was measured.

Material	Test temperature (^oC)	Testing machine	Loading rate (mm/min)	Number of repeats	Additional comments
7175-T7153 aluminium	RT	Mayes 250	2.04	1	
			0.204	1	
			0.0204	1	
		Tinius Olsen H25KS	600	1	V+H
			60	1	V+H
			6	1	V+H
	160	Mayes 250	4.08	1	
			2.04	1	
			0.204	2	
			0.0204	2	
	200	Mayes 250	4.08	1	
			2.04	1	
			0.204	2	
			0.0204	2	
P91 steel	400	Tinius Olsen H25K	2.6	1	
			0.36	1	
			0.12		
	600	Tinius Olsen H25K	2.6	1	
			0.36	1	
			0.12	1	
2014A-T6 aluminium	RT	Tinius Olsen H25K	5	20	
6082-T6 aluminium	RT	Tinius Olsen H25K	5	20	

The loading rates were kept constant during the test and the tests were stopped when specimen failure was observed by noting a sharp drop in force.

5.2.1 Compliance

Compliance in experimental setup is necessary to investigate as it cannot be accounted for experimentally. When a small ring is loaded in tension the extensometer cannot measure only the deformation of the ring. Instead it measures the deformation of the ring, the bending of the pin and the deformation of the part of the loading setup between the extensometer locations. These contributions were investigated analytically, assuming elastic-only behaviour.

In order to simplify the analysis, the compliance error contributors can be split into the pin bending, deformation of the uniform cross-section of the loading setup and deformation of the section with the cutouts. Most of the tensile tests were done on the fatigue setup, so the error contributions are slightly different due to differences in material (the creep setup is made from Nimonic, while the fatigue setup is made from EN24 steel), however they are in the same order of magnitude due to the Young's modulus of both being similar (200 GPa and 207 GPa). In order to simplify the calculations only the errors due to the fatigue setup will be calculated.

Deformation of the uniform cross-section will be addressed first. The cross-section can be seen in Figure 5.1, and the parameters describing the geometry are: $R_{out} = 7$ mm, $R_{in} = 2$ mm, $w_d = 11$ mm and $b_d = 14$ mm. The assumption is that the force is applied uniformly.

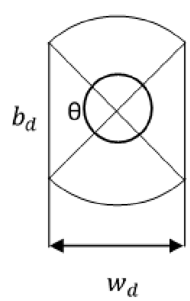

Figure 5.1: Uniform cross-section of the loading setup.

The total area of the cross-section consists of 2 triangles, 2 circle segments and 1 circle subtracted from that, as per Equation 5.1.

$$A_{tot} = 2 \times \frac{1}{2} \times R_{out}^2 \times sin\left(2arccos\frac{w_d}{2R_{out}}\right) + 2 \times \frac{\pi R_{out}^2}{2\pi} \times \left(\pi - 2arccos\frac{w_d}{2R_{out}}\right) - \pi R_{in}^2 = 123.61\text{mm}^2 \tag{5.1}$$

The length of the uniform cross-section depends on where the extensometer is clipped on, due to the geometry of the setup the maximum possible length is 20 mm. The maximum value will be used in the deformation calculation, as it represents the maximum compliance error and as the material the setup is made from is EN24 the Young's modulus is 207 GPa [178]. The calculation of the maximum compliance error can be seen in Equation 5.2.

$$\Delta L = \frac{FL}{AE} = 161.8\frac{F}{E} = 0.782F \times 10^{-9}\text{m} = 0.782F \times 10^{-6}\text{mm} \tag{5.2}$$

The deformation of the cross-section with the cutouts is very complicated to investigate analytically, therefore the real geometry and loading are simplified to the loading shown in Figure 5.2 (b). The length of the build in beam is assumed to be 2.5 mm, and the cross-section of the beam is 3.5 mm by 1.5 mm.

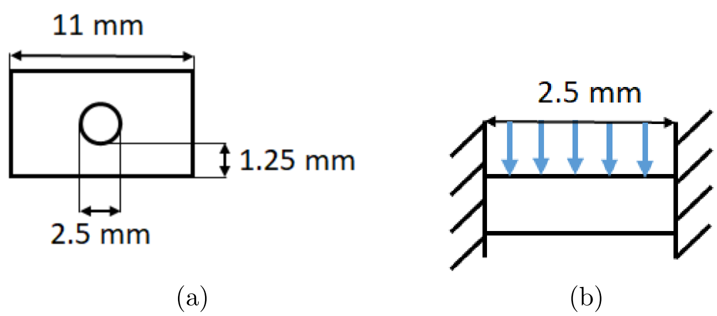

Figure 5.2: (a) Geometry of the lower fork; (b) Simplified lower fork.

The second moment of area of that beam is $I = \frac{b_I h^3}{12} = 3.5 \times \frac{1.5^3}{12} = 0.98\text{mm}^4$, resulting in the maximum deflection being $\frac{FL^3}{384EI} = 41.5\frac{F}{E}\text{m} = 0.2F \times 10^{-9}\text{m} = 0.2F \times 10^{-6}\text{mm}$.

As for the bending of the pin, there are two potential assumptions for the end conditions, shown in Figure 5.3, built-in ends and simply supported ends. The fit between the hole and the pin is a clearance fit, meaning that initially the pin acts as if it was simply supported, until the end of the pin in the hole bends up enough to touch the edge of the hole, which restricts the further bending, making it act built-in.

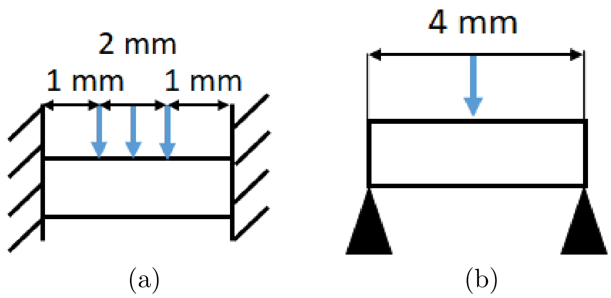

Figure 5.3: (a) Built-in assumption for the pin; (b) Simply supported assumption for the pin.

The length of the pin is 4 mm, the diameter is 2.5 mm and the length of the applied load is 2 mm. The pins are made of Nimonic, with a Young's modulus of around 200 GPa [179]. The deformation in the case of the simply supported beam is $\frac{FL^3}{48EI} = \frac{64F\times10^{-9}}{48EI} = 3.47F \times 10^{-9}\text{m} = 3.47F \times 10^{-6}$ mm. The load that changes the boundary condition depends on the precise measurements of the pins and the holes the pins interact with.

The deformation in the case of a built in beam is calculated as follows: the reaction force at both ends is equal to $\frac{F}{2}$, due to the symmetry of the loading only a half of the beam will be considered. Moments are taken away from the built in end, as per Equation 5.3, where M_1 is the reaction moment at the support, F is the applied load, b_{di} is the length over which the load is applied and a_d is the distance between the support and the load application. When the expression for an Euler-Bernoulli beam (Equation 5.4) is substituted into it, the relationship between the curvature of the beam and the applied loads becomes Equation 5.5. When the values of a_d and b_{di} are substituted as 1 mm and 2 mm respectively, the result is Equation 5.6.

$$M(x) = M_1 + \frac{F}{2}x - \frac{F}{2b_{di}}(x - a_d)^2 + \frac{F}{2b_{di}}(x - a_d - b_{di})^2 \tag{5.3}$$

$$-M = EI\frac{d^2w}{dx^2} \tag{5.4}$$

$$EI\frac{d^2w}{dx^2} = -M_1 - \frac{F}{2}x + \frac{F}{2b_{di}}(x - a_d)^2 - \frac{F}{2b_{di}}(x - a_d - b_{di})^2 \tag{5.5}$$

$$EI\frac{d^2w}{dx^2} = -M_1 - \frac{F}{2}x + \frac{F}{4}(x - 1)^2 - \frac{F}{4}(x - 3)^2 \tag{5.6}$$

Then Equation 5.6 is integrated once to find the relationship between applied load and the slope, to get Equation 5.7, which is integrated again to get the relationship between applied load and displacement, as per Equation 5.8.

$$EI\frac{dw}{dx} = -M_1x - \frac{Fx^2}{4} + \frac{F}{12}(x-1)^3 - \frac{F}{12}(x-3)^3 + D \tag{5.7}$$
$$EIw = -\frac{M_1x^2}{2} - \frac{Fx^3}{12} + \frac{F}{48}(x-1)^4 - \frac{F}{48}(x-3)^4 + Dx + B \tag{5.8}$$

In order to find integration constant B, a boundary condition of $w = 0$ at $x = 0$ is used, which results in $B = 0$. Then to find integration constant D, a boundary condition of $\frac{dw}{dx} = 0$ at $x = 0$ is used, which results in $D = 0$. To find the reaction moment M_1, a boundary condition of $\frac{dw}{dx} = 0$ at $x = L = 4$ mm is used, resulting in Equation 5.9, with reaction moment being equal to Equation 5.10. After substituting this into Equation 5.8, the deflection equation becomes Equation 5.11. The maximum deflection, which is the pin contribution to the compliance is at $x = 2$ mm, can be calculated according to Equation 5.12.

$$0 = -M_1L - \frac{FL^2}{4} + \frac{F}{12}(L-1)^3 - \frac{F}{12}(L-3)^3 \tag{5.9}$$
$$M_1 = -\frac{22F}{48} \tag{5.10}$$
$$EIw = \frac{11Fx^2}{48} - \frac{Fx^2}{12} + \frac{F}{48}(x-1)^4 - \frac{F}{48}(x-3)^4 \tag{5.11}$$
$$w = \frac{29F}{48EI} = 1.57F \times 10^{-9}\ m = 1.57F \times 10^{-6}\text{mm} \tag{5.12}$$

All of the compliance contributions to the errors in force-displacement measurements can be seen summarized in Table 5.2, with the errors at the same magnitude of applied load calculated for easy comparison. It can be seen that the largest error contributor is the pin bending, however it is still very small in comparison with the deformations seen by the small ring itself.

Table 5.2: Summary of tensile error contributions.

Contributor	Equation	Comparative deformation at 100 N
Uniform cross-section	$\frac{40F}{123.61E}$	$1.564 \times 10^{-4}\ mm$
Cut outs cross-section	$\frac{41.5F}{E}$	$0.4 \times 10^{-4}\ mm$
Pin (simply supported)	$\frac{128F}{48EI}$	$6.94 \times 10^{-4}\ mm$
Pin (built-in)	$\frac{58F}{48EI}$	$3.14 \times 10^{-4}\ mm$

In case of P91 results, the deformation of the whole setup needs to be accounted for, as there was an issue with LVDT measurements during testing. Assuming that the Young's modulus remains constant and that the total deformation of the pins is the average of the deformations with built-in and simply supported conditions, the deformations of the setup at 2000 N load is around 0.017 mm, which is small enough that it does not need to be accounted for.

5.3 Grain Structures

Figure 5.4 shows the grain structure of 2014A-T6 aluminium, as received. The grains are very long, a significant number of them spanning the entire lateral thickness of the small ring specimen (2 mm), however, they are thin, around 30 μm. The material was wrought, which caused the grains to elongate, and then heat treated, which in this case does not appear to have caused recrystallization and grain nucleation and growth. On one hand, there are not enough grains across the cross-section laterally, potentially making the test results not representative, on the other hand, there are enough grains radially and loading is applied radially as well. The black artefacts could indicate overetching or precipitates formed by the heat treatment process.

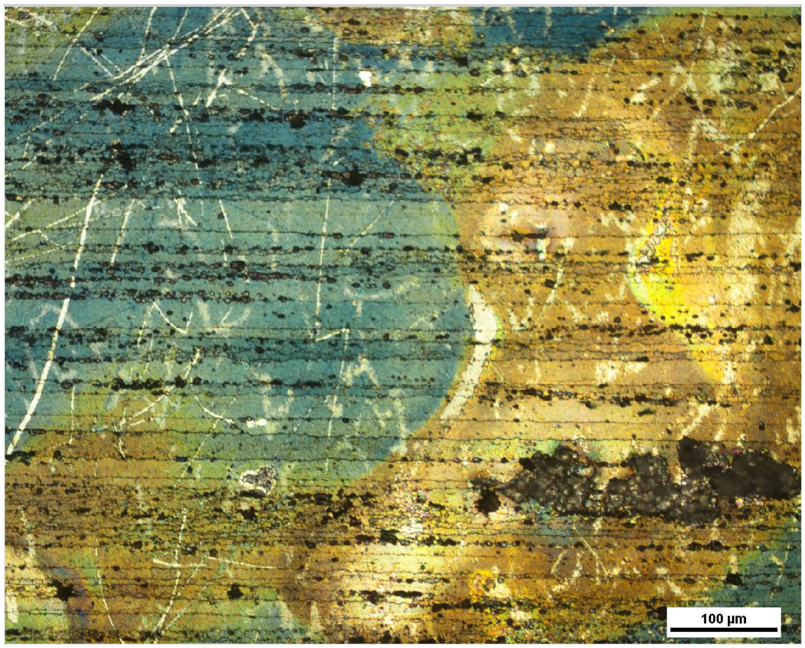

(a)

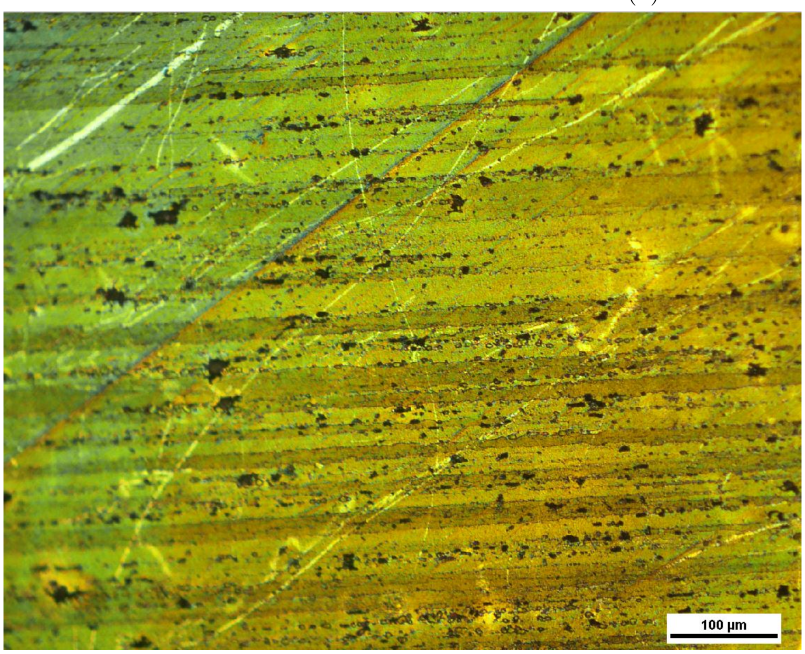

(b)

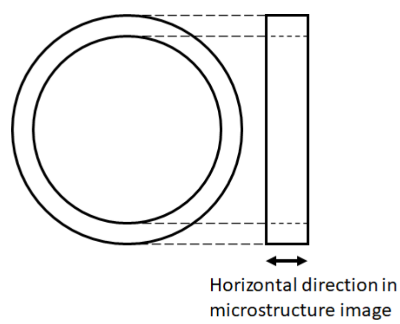

(c)

Figure 5.4: Grain structure of 2014A-T6 aluminium.

As for the grain structure of 6082-T6 aluminium, as received, it is shown in Figure 5.5. The grains are small, around 10 μm across, they appear to be of regular shape. There are definitely enough grains in the cross-section for this material to be suitable to be tested while using small ring specimens. For this material the heat treatment appears to have caused recrystallization, grain nucleation and growth. Similar to 2014A-T6 aluminium grain structure images, the black artefacts could indicate overetching or precipitates formed by the heat treatment process.

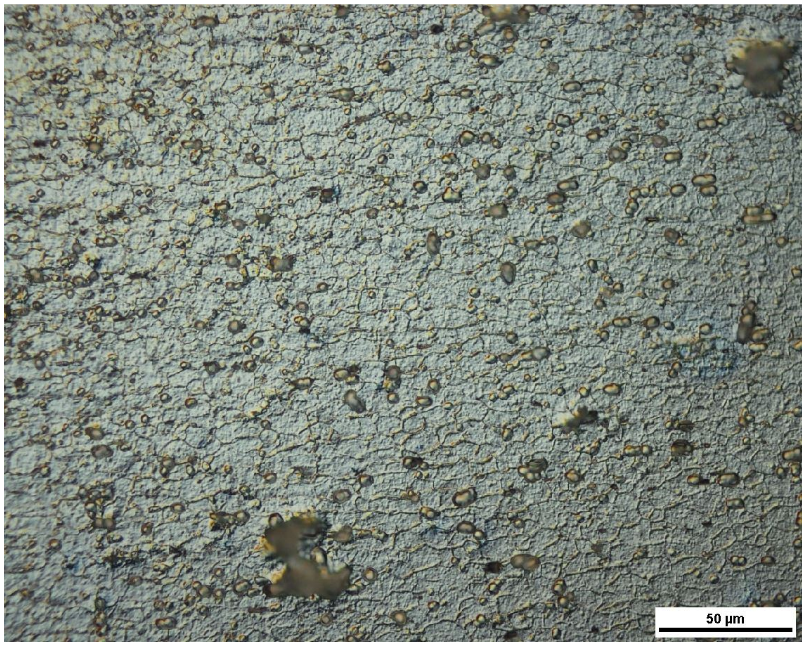

(a)

(b)

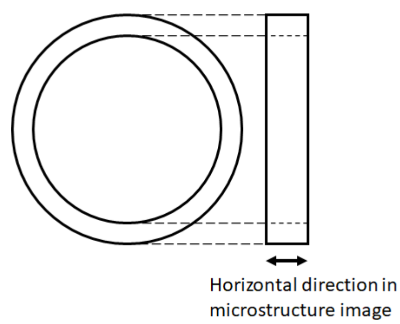

(c)

Figure 5.5: Grain structure of 6082-T6 aluminium.

5.4 Testing Results

Small ring specimens made from 7175-T7153 aluminium were tested at varied temperatures and loading rates. The results from testing at room temperature can be seen in Figure 5.6 (a). All three results overlap before failure. Two experienced progressive failure and failed in region III. The lowest loading rate test failed in sudden failure at region V at a significantly higher displacement than the other two.

160^{o}C test results can be seen in Figure 5.6 (b). All of the curves show all regions shown in Figure 4.17, the results exhibit some rate sensitivity. The region III in the 4.08 mm/min test result is significantly shorter than in all other test results. 2.04 mm/min R1 and 0.204 mm/min R1 test results are similar to each other, and both 0.204 mm/min test results are very similar to each other as well, with all loading rates apart from 4.08 mm/min forming a group. The peak load decreases and displacement to failure increases as loading rate decreases.

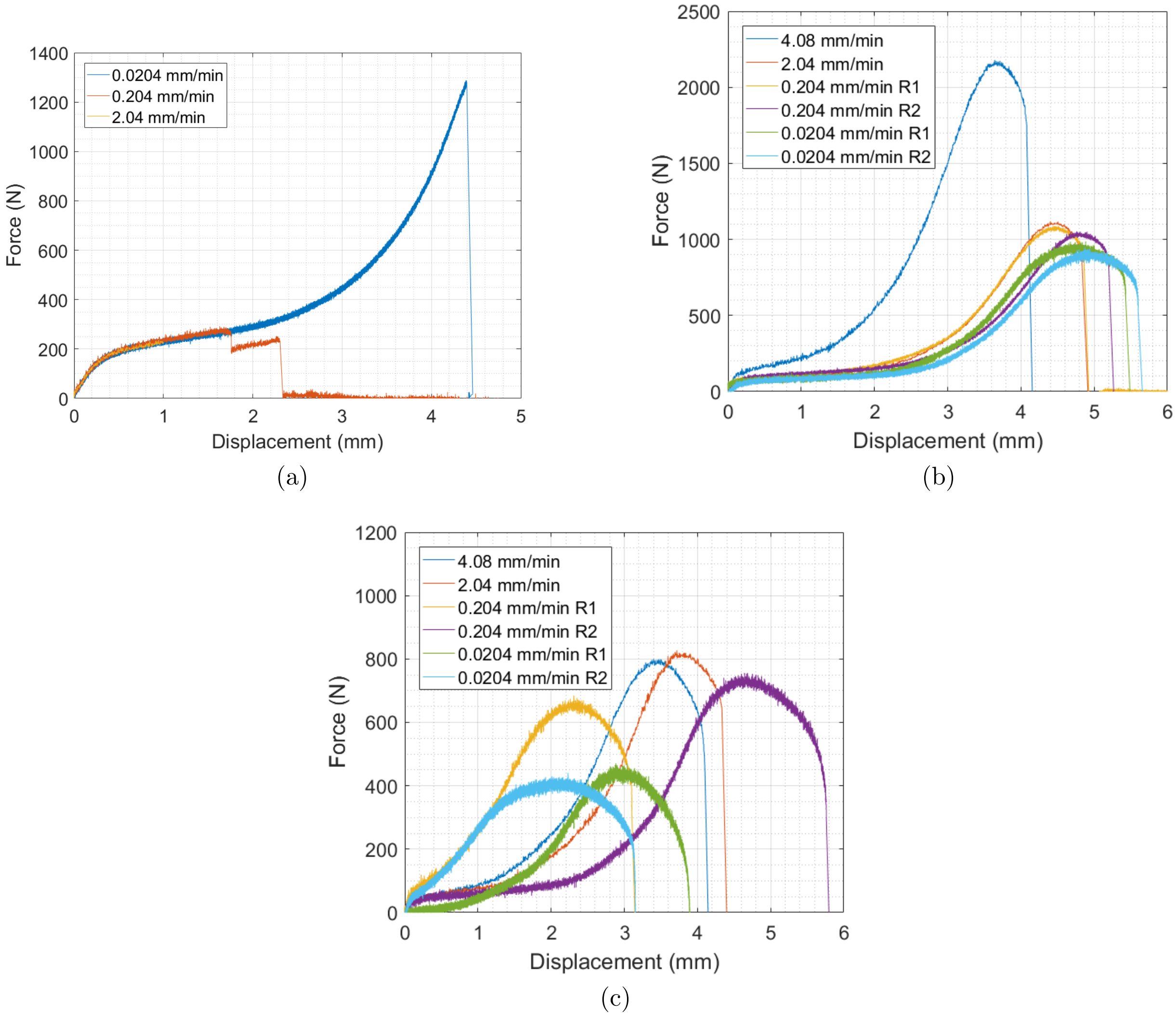

Figure 5.6: 7175-T7153 aluminium alloy ring tensile testing results at varied loading rates (in mm/min) and (a) room temperature; (b) 160^{o}C; (c) 200^{o}C.

Figure 5.6 (c) shows the 200^{o}C test results, which have a noticeable rate sensitivity. Test results from 4.08 mm/min, 2.04 mm/min and 0.204 mm/min R2 show all regions of the generalized force-displacement curve and overlap initially, diverging at around 0.5 mm, with the length of region II increasing as the loading rate decreased. 0.204 mm/min R1 and 0.0204 mm/min R2 do not show region III, overlap initially and diverge at around 1.2 mm, with the faster loading rate corresponding with a longer region V. 0.0204 mm/min does not show regions I and II, starting at region II. The peak loads are similar when the same loading rate is used, apart from 0.204 mm/min test results, which are around 75 N apart. Overall, higher loading rates correspond with higher peak loads and no consistent observation about displacement to failure can be made.

In order to show the effect of varied temperature at fast loading rates, instead of plotting the test results done at the same temperature as was done previously, the test results done at the same loading rate were plotted instead, as shown in Figure 5.7. For the 4.08 mm/min test results the higher temperature results in lower forces throughout the test, region V in particular becoming significantly shorter, the displacement to failure is not affected. For the 2.04 mm/min all results initially overlap, the results at elevated temperatures diverge at around 0.1 mm. Increasing temperature reduces the length of region I for all tests and both region III and region V at elevated temperatures, as the specimen tested at room temperature failed before the length of region III could be evaluated. No consistent observations can be made about the relationships between test temperature, peak load and displacement to failure.

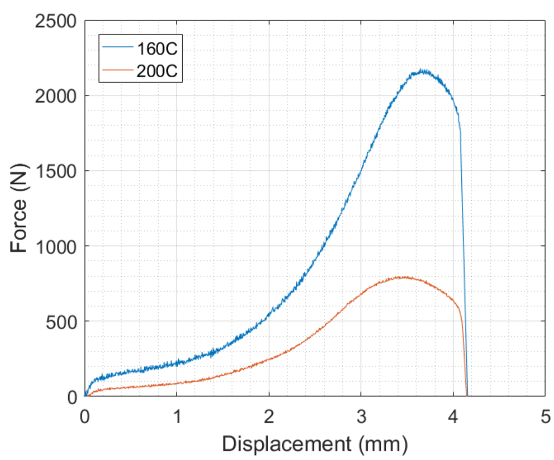

(a)

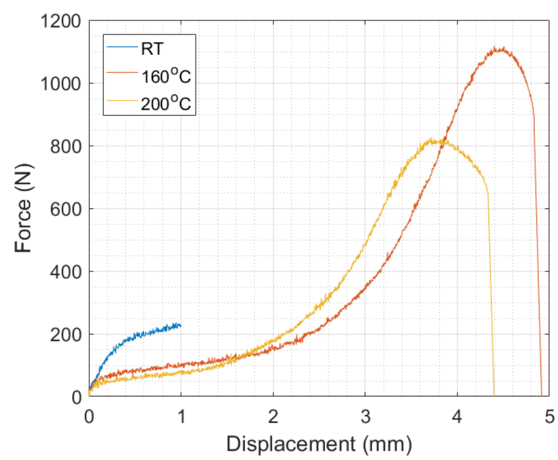

(b)

Figure 5.7: 7175-T7153 aluminium alloy ring tensile testing results at varied temperatures and (a) 4.08 mm/min; (b) 2.04 mm/min.

For the 0.204 mm/min loading rate, the replotted results can be seen in Figure 5.8 (a). All tests apart from 200^{o}C R2 initially overlap, they diverge at around 0.1 mm. At elevated temperatures higher temperature results in lower peak loads and peak loads for repeats at the same temperature are similar. The 0.0204 mm/min test results are shown in Figure 5.8 (b), all tests apart from 200^{o}C R2 overlap initially. The peak loads of the repeats at the same temperature are similar, higher temperature results in lower peak loads and no consistent observations can be made about displacement to failure.

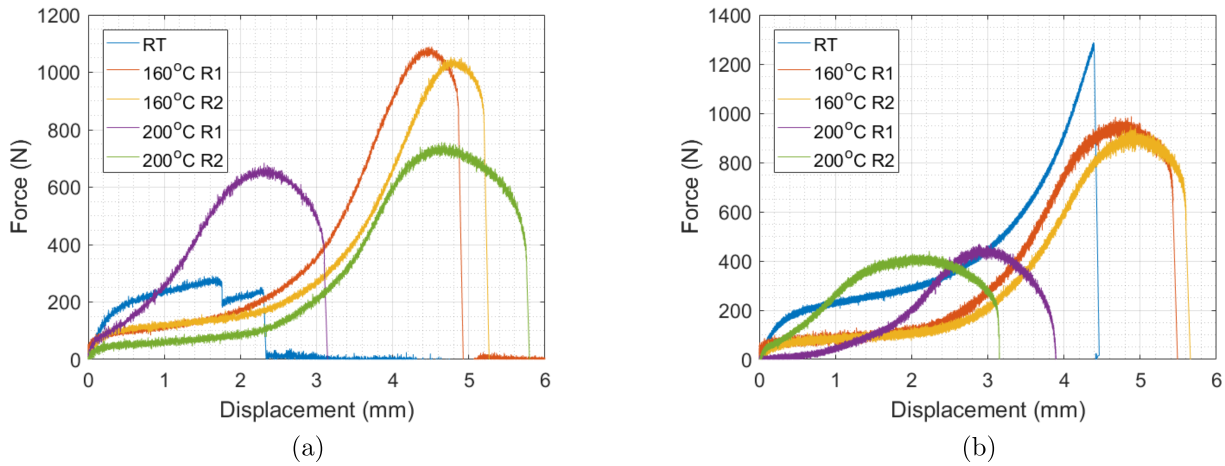

Figure 5.8: 7175-T7153 aluminium alloy ring tensile testing results at varied temperatures and (a) 0.204 mm/min; (b) 0.0204 mm/min.

The results from small ring tensile tests of P91 steel at elevated temperatures and varied loading rates can be seen in Figure 5.9. All test results show all regions shown in the generalized force-displacement curve. The test results at 400^{o}C are very similar, with the largest difference in region III. Between around 1 mm and 8 mm displacement, the results from 2.6 mm/min and 0.36 mm/min are around 100 N higher than the result from 0.12 mm/min. The failure displacements are similar as well. The tests done at 600^{o}C overlap initially, higher loading rate results in longer region I, steeper slope in region III and higher peak load. No consistent observations can be made about the displacement to failure.

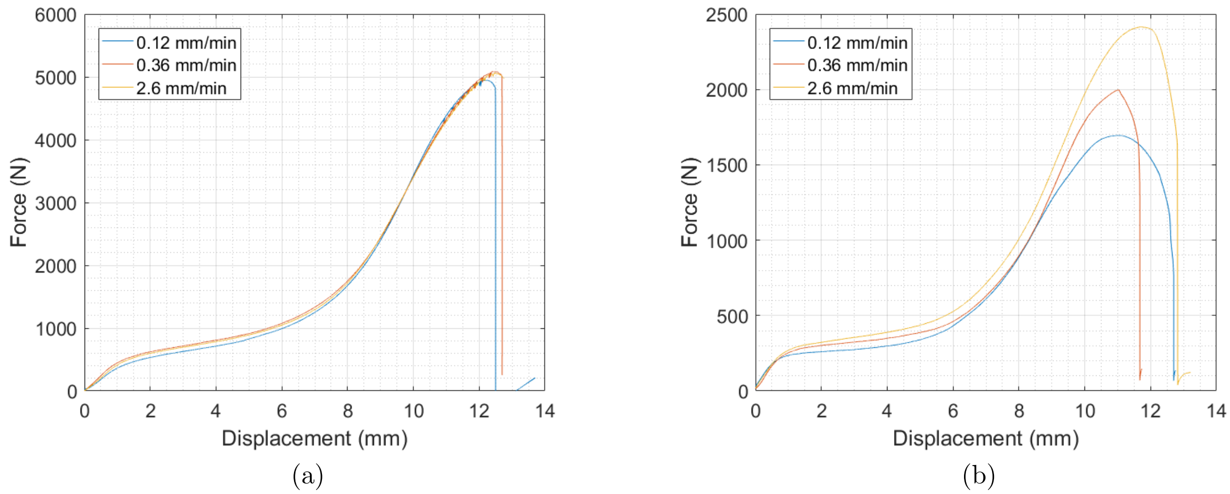

Figure 5.9: Small ring tests of P91 steel at varied loading rates and (a) 400^{o}C; (b) 600^{o}C.

In order to clearly show the effect of varied temperature at the same loading rates, the P91 results were replotted in Figure 5.10. The initial parts of the force-displacement curves overlap, but, after about 0.5 mm displacement, the higher temperature results in lower force at the same displacement. The displacement to fracture does not appear to be affected by temperature or loading rate in the range investigated.

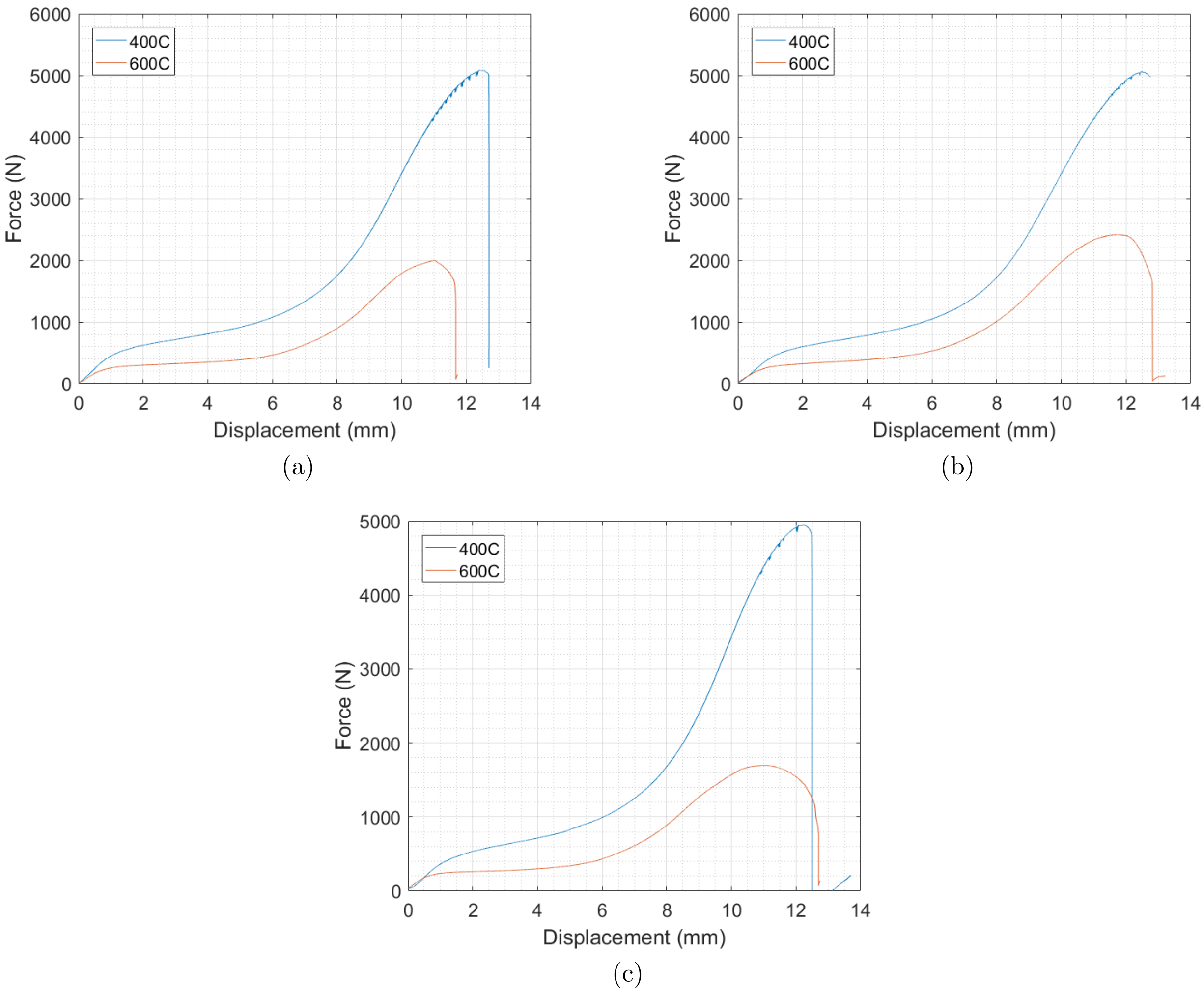

Figure 5.10: Small ring tests of P91 steel at varied temperatures and (a) 2.6 mm/min; (b) 0.36 mm/min; (c) 0.12 mm/min.

The results from 20 repeats of small ring tensile tests of 2014A-T6 and 6082-T6 aluminium alloys at room temperature can be seen in Figure 5.11. The majority of the tests of 2014A-T6 fail in region III, with a few failing in region IV, as they diverge from a straight line. The length of region I varies between 0.3 mm and 0.7 mm, with the force in that region varying between 150 N and 170 N, then the region III begins at around 0.7 mm to 1 mm, with initial force values between around 200 N and 210 N. The tests of the 6082-T6 all fail in regions IV to VI. The results are very similar up to around 1.5 mm, the length of region I is around 0.2 mm to 0.4 mm, with the forces between 100 N and 110 N, the second region began at around 0.5 mm, with the forces varying between 160 N and 150 N.

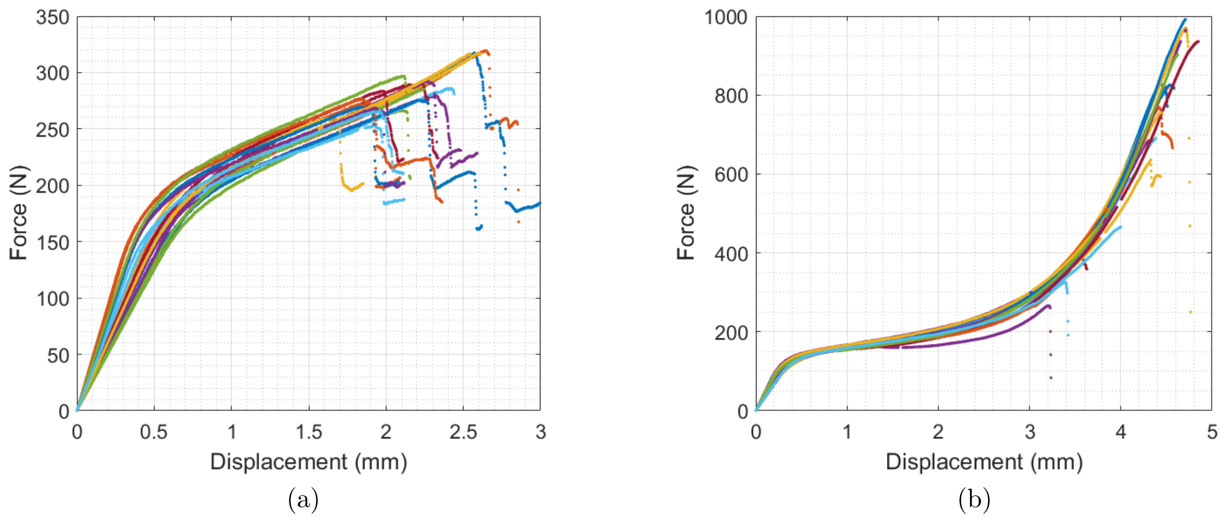

Figure 5.11: 20 repeats of tensile small ring tests of aluminium alloy (a) 2014A-T6; (b) 6082-T6.

Figure 5.12 illustrates common failure types and locations. The ring (a) cracked at the middle of the pin and is close to elliptical in shape. The ring (b) cracked at the side by the pin, has thinning at the bottom, opposite of the crack and straight sides without bending inwards. The ring (c) cracked on the side, with a crack on the other side. The ring (d) cracked at the middle of the pin and there is clear bending inwards on the sides, especially when compared to ring (b).

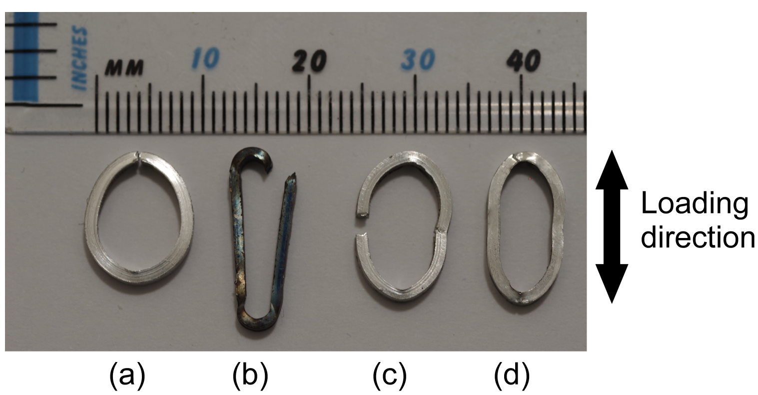

Figure 5.12: Examples of failed rings. (a) 7175-T7153 aluminium tested at room temperature at 2.04 mm/min; (b) P91 steel tested at 600^{o}C at 0.36 mm/min; (c) 2014A-T6 aluminium tested at room temperature at 5 mm/min; (d) 6082-T6 aluminium tested at room temperature at 5 mm/min.

The failure locations are shown on a schematic diagram of a loaded small ring specimen in Figure 5.13. Middle of the pin is also shown in Figures 5.12 (a) and (d). Middle of the ring is similar to Figure 5.12 (c), however, middle of the ring only has one through crack as opposed to multiple. Side of the pin is also shown in Figure 5.12 (b), with thinning noticeable at the other pin on the opposite side of the crack.

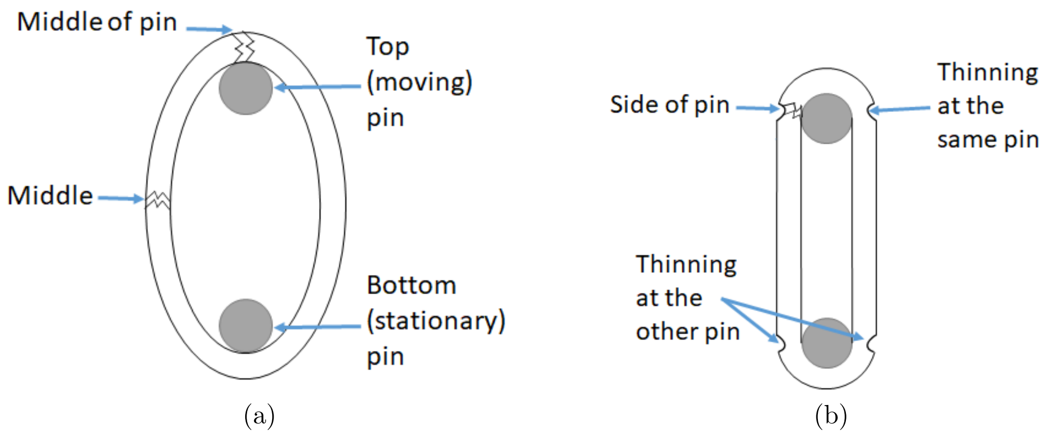

Figure 5.13: Schematic illustrations of failure locations in a small ring specimen: (a) middle of the pin, middle (of the ring), (b) side of the pin and thinning.

The failure locations for 7175-T7153 aluminium are summarized in Table 5.3. At room temperature the rings failed at the middle of the pin and between the pins, while all rings at elevated temperatures failed at the side of the pin. Thinning by a pin was observed, in some cases it occurred at the same pin where the ring cracked, in other cases it occurred at the other pin. Thinning occurred more frequently at higher temperature. There was visible bending inwards in the specimens after all tests.

As for P91 steel, the failure locations are described in Table 5.4. The rings failed at the side by the pin in the majority of tests, apart from one failure in the middle between the pins, at higher temperature the rings showed thinning by the pin, either the same pin where the failure occurred or the other pin, similarly to the observation about the failure of the 7175-T7153 aluminium rings tested at elevated temperature. The rings showed no noticeable bending inwards after failure.

Table 5.3: Failure of aluminium 7175-T7153 small rings.

Temperature ^oC	Rate (mm/min)	Failure location	Other observations
RT	2.04	Middle of pin	Close to elliptical
RT	0.204	Middle of pin	Close to elliptical
RT	0.0204	Upper middle side	
160	8.08	Side by the pin	
160	2.04	Side by the pin	Thinning by a pin
160	0.808	Side by the pin	
160	0.204	Side by the pin	Thinning by a pin
160	0.0808	Side by the pin	
160	0.0204	Side by the pin	Thinning by a pin
200	8.08	Side by the pin	Thinning by a pin
200	2.04	Side by the pin	
200	0.808	Side by the pin	Thinning by a pin
200	0.204	Side by the pin	
200	0.0808	Side by the pin	Thinning by a pin
200	0.0204	Side by the pin	Thinning by a pin

Table 5.4: Failure of P91 steel small rings.

Temperature ^oC	Rate (mm/min)	Failure location	Other observations
400	2.6	Side by the pin	
400	0.36	Side by the pin	
400	0.12	Side by the pin	
600	2.6	Middle	Thinning by a pin
600	0.36	Side by the pin	Thinning by a pin
600	0.12	Side by the pin	Thinning by a pin

Table 5.5 describes the failure of 2014A-T6 aluminium small rings. The majority of the rings failed in the middle of the pin, two rings failed on the side (ring (c) from Figure 5.12), with a crack on the opposite side, no cracks at the pins. Two rings had multiple fractures, one broke in half, while a quarter broke out from the other. The rings that failed at the pin remained close to elliptical. All of the rings exhibited bending inwards.

Table 5.5: Failure of 2014A-T6 aluminium alloy small rings.

Failure location	Number of failures	Other observations
Middle bottom pin	4	Close to elliptical
Middle top pin	4	Close to elliptical
Middle pin	8	Close to elliptical
Middle side	2	Failure on one side, crack on the other
Split in half	1	
Quarter out	1	

The failure locations for 6082-T6 aluminium are described in Table 5.6. About the same number of rings failed at the top pin and at the bottom. More rings failed after larger deformation having deformed past the ellipse shape. All of them exhibited bending inwards.

Table 5.6: Failure of 6082-T6 aluminium alloy small rings.

Failure location	Number of failures	Other observations
Middle bottom pin	4	Close to elliptical
Side bottom pin	7	
Middle top pin	2	Close to elliptical
Side bottom pin	7	

5.5 Fractography Results

Figure 5.14 shows the fracture surface of small ring specimen made from 7175-T7153 aluminium alloy tested under tensile loading. It is difficult to tell exactly due to lack of depth of focus, but the surfaces in all cases look to be ductile. Dimples indicating ductile fracture can be seen best in Figure 5.14 (d). Overall the surfaces are rough, as shown by the microscope being not able to be in focus for the whole fracture surface.

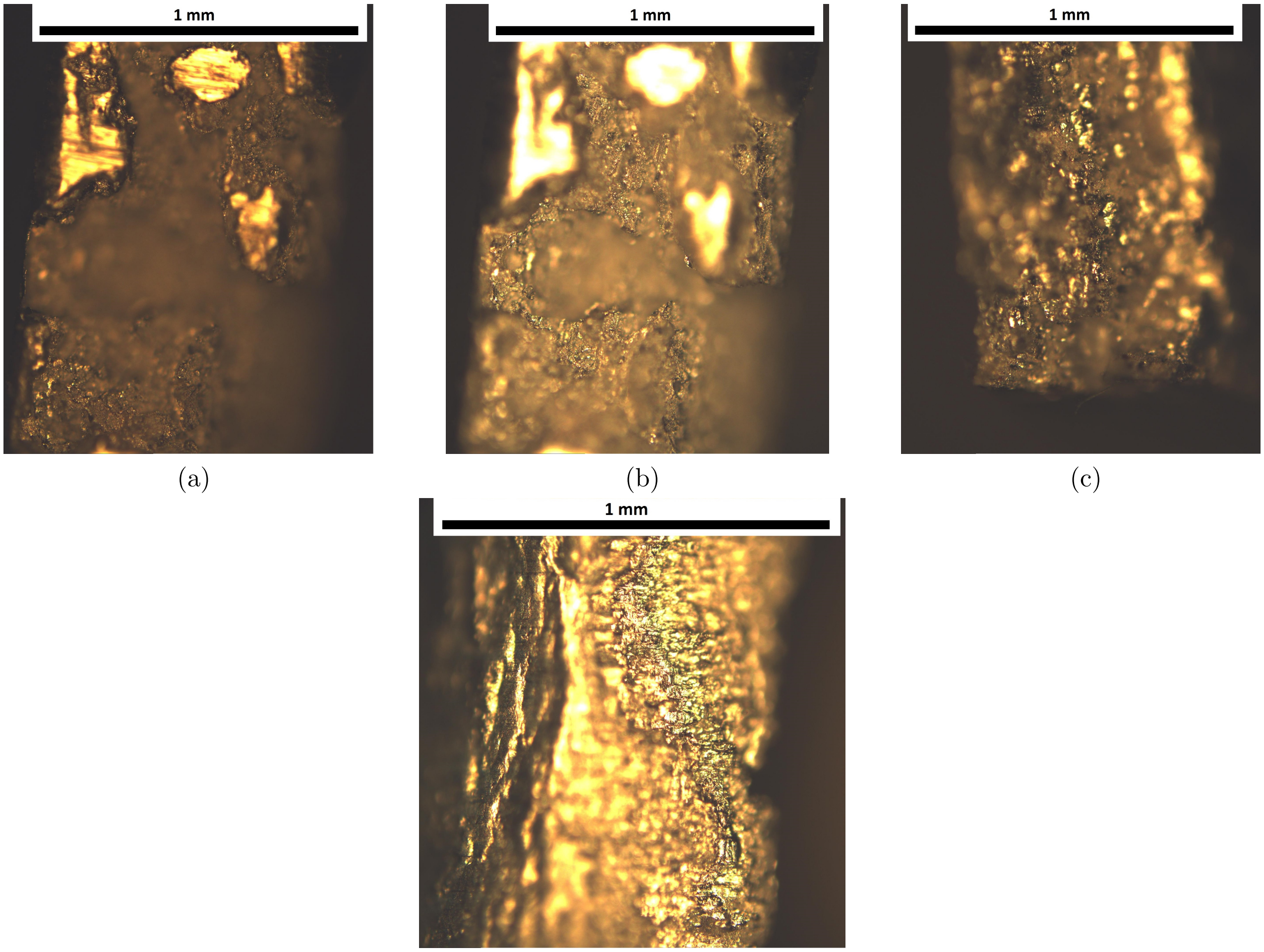

(a) (b) (c) (d)

Figure 5.14: Fracture surface of 7175-T7153 aluminium tested under tensile conditions at (a) room temperature; (b) room temperature; (c) 160^{o}C; (d) 200^{o}C.

Figure 5.15 shows the fracture surface of small ring specimen made from 2014A-T6 aluminium alloy tested under tensile loading. Fracture surfaces are also rough, but dimples cannot be seen. It could be mixed mode fracture (ductile and brittle). Regions in focus are oriented the same way as long grains identified from grain structure investigation, potentially indicating some degree of brittle fracture, but due to lack of depth of focus it is difficult to say for certain.

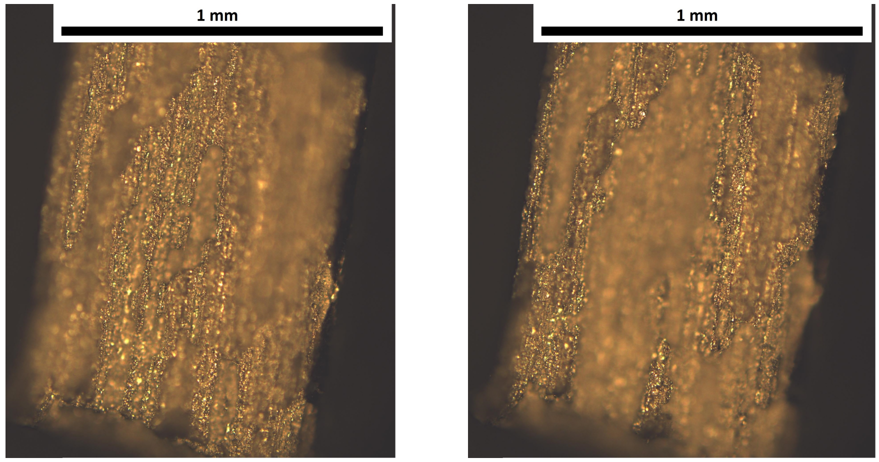

(a) (b)

Figure 5.15: Fracture surface of 2014A-T6 aluminium tested under tensile conditions.

Figure 5.16 shows the fracture surface of small ring specimen made from 6082-T6 aluminium alloy tested under tensile loading. Fracture surface appears to be very rough, with a very small proportion of it being in focus at any one time, indicating ductile fracture. Dimples cannot be seen, but this material was identified to have a fine grain structure, so the dimples could be too small to see well through an optical microscope. Using SEM would allow to evaluate the fracture surface better.

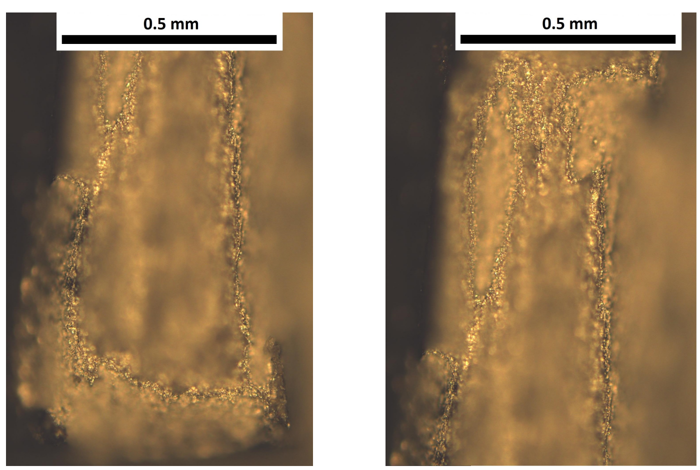

(a) (b)

Figure 5.16: Fracture surface of 6082-T6 aluminium tested under tensile conditions.

Figure 5.17 shows the fracture surface of small ring specimen made from P91 steel tested under tensile loading. Both surfaces look quite smooth, however, the magnification used was not very high so it is entirely possible that details of the fracture surface are not visible. As tests were done at elevated temperatures and fracture surface was observed at room temperature it is possible that the microstructure changed between testing and surface investigation, potentially affecting the fracture surface as well.

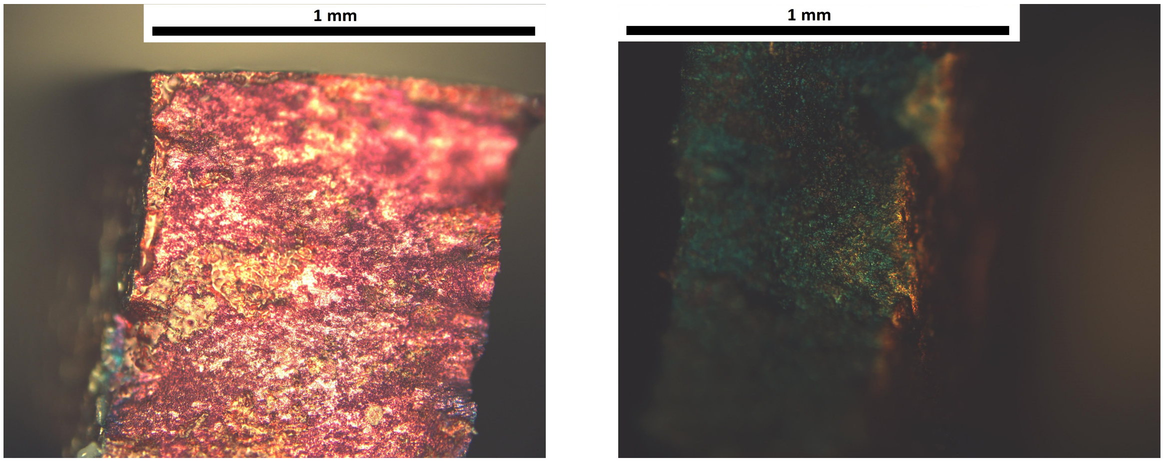

(a) (b)

Figure 5.17: Fracture surface of P91 steel tested under tensile conditions at (a) 400^{o}C; (b) 600^oC.

5.6 Development of Interpretation Methods

A virtual small ring tensile test result database was generated using the 1/8th model and varied Ramberg-Osgood material model parameters. It was then used to develop several different methods of calculating bulk material stress-strain behaviour. The performance of those methods was then evaluated using this dataset and well performing methods were used to calculate bulk material properties according to small ring tensile test results acquired experimentally.

5.6.1 Methodology

In order to develop a method to calculate the stress-strain behaviour from force-displacement behaviour that would work for a variety of materials, a representative set of stress-strain curves had to be acquired. To make the process more efficient a set of 100 virtual test stress-strain curves were generated by performing a uniformly distributed random selection of Ramberg-Osgood material model parameter ranges shown in Table 5.7. Those ranges were selected as representative of ranges found in real metallic materials and producing a selection of stable stress-strain curves. The virtual set of materials was then used to run 100 FEA analyses using the 1/8th FEA model and the resulting force-displacement behaviour was noted.

Table 5.7: Parameter ranges for virtual test stress-strain curves.

	E (GPa)	σ_y (MPa)	n	α
Minimum	1	5	10	0.5
Maximum	200	400	26	1.5

Then Equation 5.13 was fitted to the force-displacement curves. This form of equation was chosen because it fit the shape of the force-displacement curves well and the parameters have a meaning that shows potential for relating them to the Ramberg-Osgood material model parameters. Parameter a is the transition offset (the end of the first slope), parameter b is the speed of transition (the curve of the first transition), parameter c is the initial slope (first slope) and parameter d is the final slope (second slope). The maximum displacement for curve fitting was selected so that the second transition was not accounted for, as some materials fail before it.

$$P = u_{vtot}\left(c + (d-c)\left(\frac{arctan\left(\frac{u_{vtot}-a}{b}\right)+\frac{\pi}{2}}{\pi}\right)\right) \tag{5.13}$$

The equation was fitted to the data using MatLab Curvefitting Toolbox using the method described below.

1. FEA displacement was scaled to full-size displacement by multiplying by 2
2. FEA force was scaled to full-size force by multiplying by 4
3. Maximum displacement was set to 2.4 mm as that avoided the second transition in all cases
4. First guess for parameter c was

(a) A slope was fitted to the force-displacement results from the beginning adding 1 point at a time

(b) Correlation coefficient corresponding to each slope was calculated

(c) The slope corresponding to the maximum correlation coefficient was selected and multiplied by 2 and scaled down by 1000 for better fitting results

5. First guess for parameter d was

   (a) Minimum correlation coefficient from fitting a slope was found

   (b) A slope was fitted to the points after the minimum correlation coefficient point, scaled down by 100 for better fitting results

6. First guess for parameter a was the u_{vtot} value corresponding to the end of slope c scaled up by 10

7. First guess for parameter b was the u_{vtot} value corresponding to the end of slope c scaled up by 10

8. Method used to fit the curves was Nonlinear Least Squares

9. Lower boundaries for the coefficients were set to be $[0.7 \times a \quad 0 \quad 0.9 \times c \quad 0.9 \times d]$ and upper boundaries were set to be $[1.5 \times a \quad \infty \quad 1.1 \times c \quad 1.1 \times d]$ so that the coefficients fitted were meaningful

The scaling (1000 times for parameter c, 100 for parameter d, 10 times for parameters a and b) was done for the parameters to have similar magnitudes in order to improve the fitting results. Otherwise the lower magnitude parameters would be treated as less important by the fitting algorithm.

The fitted curves were plotted against real data and residuals were plotted as well to investigate the goodness of fit. An example of a fitted cure and residuals can be seen in Figure 5.18. This example fit was chosen because it shows that the Equation 5.13 fits the virtual force-displacement curve data, as the residuals and the actual fits look similar in all cases. The residuals are not evenly distributed around the fitted curve, however, as the curve is being fitted to simulated data without scatter as opposed to experimental data with scatter, with a goal to fit a simple equation, this was deemed acceptable.

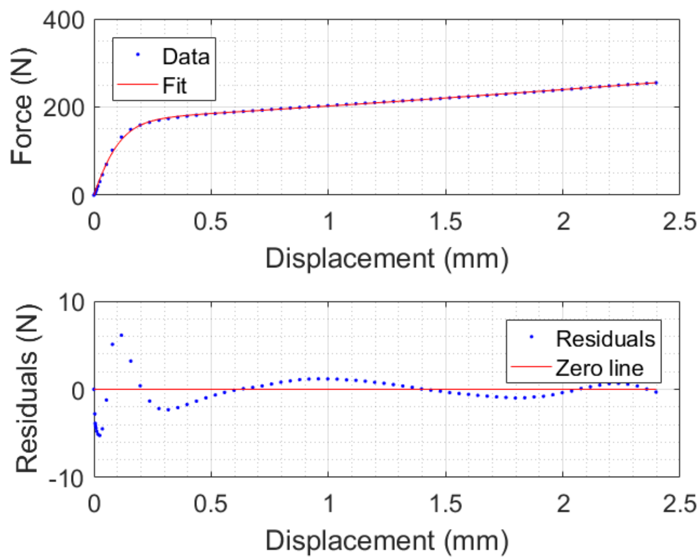

Figure 5.18: Example fit of the equation to the force-displacement curve and residuals.

The resulting ranges of fitted parameters can be seen in Table 5.8. As the goal is to develop a method to calculate a stress-strain curve from parameters fitted to experimental data, several methods were considered. The simplest method considered was to find direct correlations between one of the fitted parameters and one of the Ramberg-Osgood material model parameters. When the parameters were plotted against each other, the only visible correlations were the linear relationships seen in Figure 5.19. Other plots showed no significant correlations.

Table 5.8: Parameter ranges for virtual stress-strain curves.

	a	b	c	d
Minimum	0.0025	0.0135	9.666×10^{-8}	1.2586
Maximum	1.1140	6.7338×10^{4}	3.0469×10^{3}	72.86

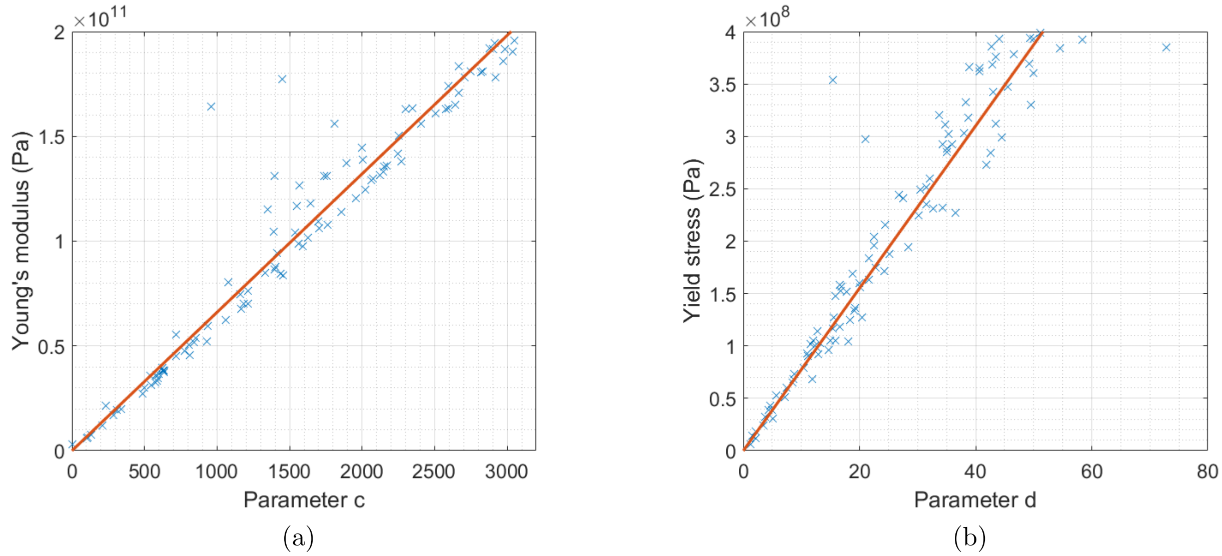

Figure 5.19: Actual and predicted values of (a) Young's modulus; (b) yield strength.

The relationship between Young's modulus and parameter c was identified to be $E = 6.6063 \times 10^7 c$, with a mean absolute percentage error (MAPE) of 10.2532 %. The formula for it is $MAPE = \frac{1}{100} \times sum \left| \frac{Actual - Predicted}{Actual} \right| \times 100\%$. The relationship between yield stress and parameter d was identified to be $\sigma_y = 7.7489 \times 10^6 d$, with a MAPE of 12.3414 %. These relationships were then used to process experimental results as a part of the combined processing method, which used direct correlations to find Young's modulus and yield stress and ordinary least squares to find n and α.

The main limitation of this method is that it is only applicable if other Ramberg-Osgood material model parameters do not affect these fitted parameters significantly and there are no interactions between the Ramberg-Osgood material model parameters that would affect the fitted parameters. These limitations apply to all models that rely on linear relationships, in this case ordinary least squares and principal component regression. Overall, these correlations are good, but other methods are needed to evaluate the other parameters and potentially achieve better correlations.

Ordinary Least Squares Ordinary least squares (OLS) is a method that can be used to fit a linear model with multiple parameters [180]. It is applicable when the system of equations of interest is overdetermined, which applies to this system of equations as there are more equations than there are coefficients being fitted. The following is an example of how the Ramberg-Osgood material model coefficients were calculated from parameters fitted to the force-displacement curves:

1. Take $[E]$ as the outcome vector and $[a\,b\,c\,d]$ as the data matrix to be used for fitting
2. Fit the coefficients by minimizing the sum of squared residuals $\beta_{OLS} = \left([a\,b\,c\,d]^T\,[a\,b\,c\,d]\right)^{-1}$ $[a\,b\,c\,d]^T\,[E]$
3. Calculate the new values of E, $[E_{new}] = [a\,b\,c\,d]\,\beta_{OLS}$
4. Calculate the MAPE to evaluate the goodness of fit $MAPE = \frac{1}{100} \times sum\left|\frac{E-E_{new}}{E}\right| \times 100\%$
5. Plot the actual values $[E]$ against the new values $[E_{new}]$

The resulting equations for all Ramberg-Osgood material model parameters are Equations 5.14 to 5.17. These equations were then used to process experimental data as the OLS method and Equations 5.16 and 5.17 were used as a part of the combined method.

$$E = 4.4889 \times 10^{10}a + 6.7850 \times 10^{4}b + 7.2979 \times 10^{7}c - 5.8131 \times 10^{8}d \tag{5.14}$$

$$\sigma_y = -1.0187 \times 10^{8}a + 2.1341 \times 10^{3}b - 226.6987c + 8.0253 \times 10^{6}d \tag{5.15}$$

$$n = 38.5135a + 1.6148 \times 10^{-4}b + 0.0074c + 0.0293d \tag{5.16}$$

$$\alpha = 1.4279a + 1.0380 \times 10^{-4}b + 4.2802 \times 10^{-4}c + 0.0027d \tag{5.17}$$

The MAPEs for all Ramberg-Osgood material model parameters are shown in Table 5.9.

Table 5.9: MAPE calculated using OLS.

E	σ_y	n	α
18.6039 %	12.4386 %	37.2546 %	42.5584 %

The figures showing the actual values of the coefficients plotted against the calculated values of the coefficients are Figures 5.20 (a) to (d). The errors for E and σ_y are of similar magnitude to the errors from the direct correlations between them and fitted coefficients. The figures show that the correlation is worse than the direct correlations as well. Regarding coefficients n and α, there does not appear to be an appropriate correlation, but the order of magnitude is correct, and as was seen from the investigation into how the variation of material model parameters affects the stress-strain and force-displacement results, the variation in that range does not affect the stress-strain behaviour significantly. The results from the fitting suggest that there are no linear relationships between parameters n and α and any of the parameters fitted to the force-displacement curves. This method seems suitable for a rough estimate of the stress strain behaviour in terms of parameters n and α, or as a first guess for an inverse analysis method.

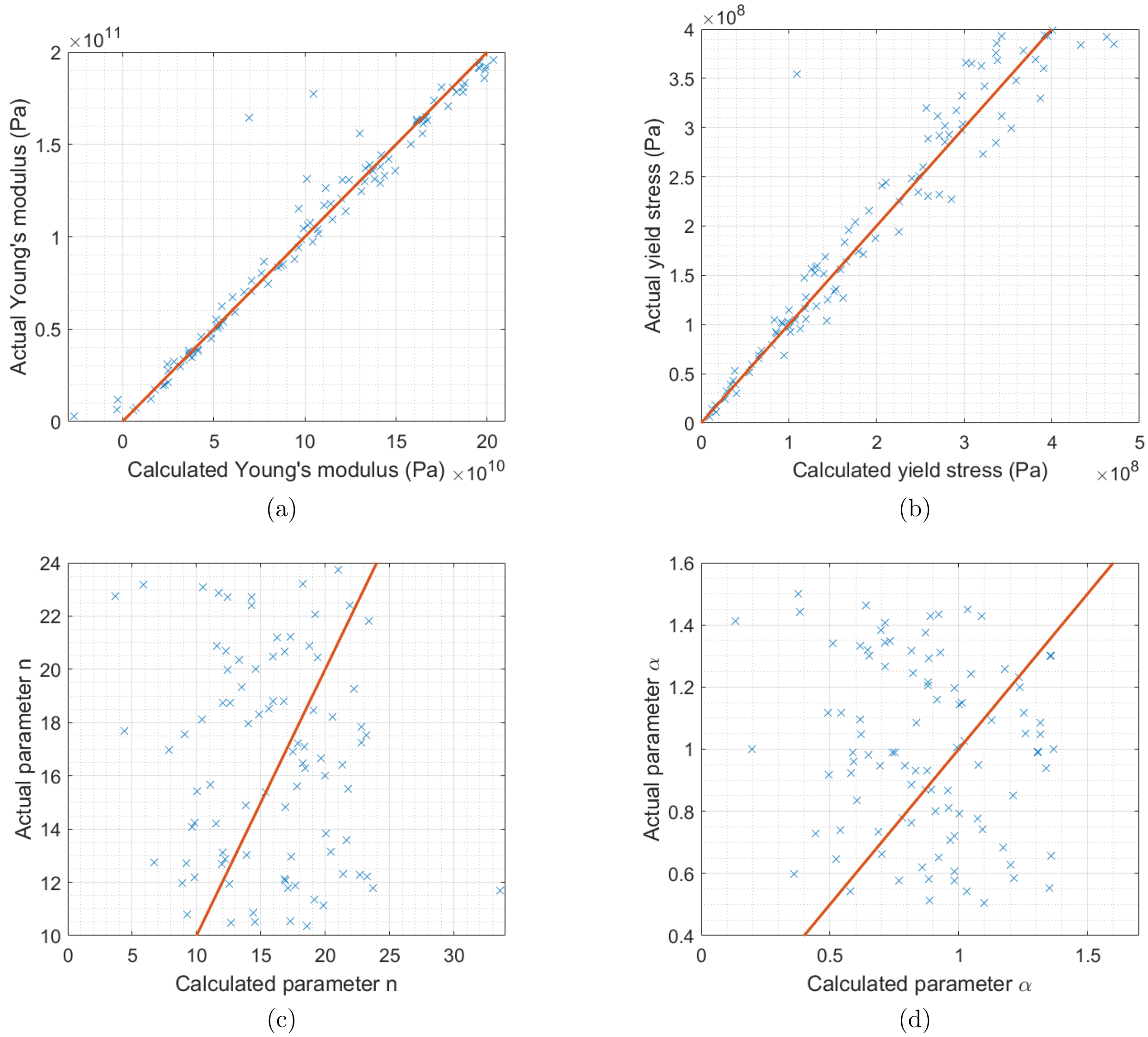

Figure 5.20: Actual and predicted values of (a) Young's modulus; (b) yield strength; (c) parameter n; (d) parameter α.

Principal Component Regression Principal component regression (PCR) is a regression method that uses principal component analysis (PCA) to fit a linear model with multiple parameters [181]. This model is different from OLS as it projects the data onto the principal components. If the coefficients in the data matrix were not independent, this projection makes them independent. The principal components are arranged in order of how much variation in data they explain, not all of them have to be used. The following is an example of how the Ramberg-Osgood material model coefficients were calculated from the parameters fitted to the force-displacement curves.

1. Take $[E]$ as the outcome vector and $[a\,b\,c\,d\,]$ as the data matrix to be used for fitting
2. Center the outcome vector to get $[E_c]$ and the data matrix to get $[a_c\,b_c\,c_c\,d_c]$
3. Perform PCA on the centered data matrix $[a_c\,b_c\,c_c\,d_c\,] = [U]\,[\Delta]\,[V]^T$
4. Decide how many principal components will be used, between 1 and 4
5. Project the data matrix onto the principal components $[W] = [a_c\,b_c\,c_c\,d_c]\,[V]$
6. Using OLS fit an intermediate set of coefficients $\gamma_{PCA} = \left([W]^T\,[W]\right)^{-1}[W]^T\,[E_c]$
7. Project the intermediate coefficients back to the original centered data $\beta_{PCA} = [V]\,\gamma_{PCA}$
8. Calculate the new values of E, $[E_{new}] = [a\,b\,c\,d]\,\beta_{PCA}$
9. Calculate the MAPE to evaluate the goodness of fit $MAPE = \frac{1}{100} \times sum\left|\frac{E-E_{new}}{E}\right| \times 100\%$
10. Plot the actual values $[E]$ against the new values $[E_{new}]$

The MAPEs for all Ramberg-Osgood coefficients are shown in Table 5.10. It shows the variation of error with a different number of principal components used for calculating the new values so that the lowest error option could be chosen to evaluate how suitable this method is. The number is how many components were used, they were removed in order of explaining variance, with the one explaining the lowest amount of variance being removed first.

Table 5.10: MAPE variation with a different number of principal components used.

	E	σ_y	n	α
4	30.2693 %	20.7059 %	100.3290 %	113.2564 %
3	33.3023 %	13.1889 %	105.9710 %	112.3139 %
2	9.5364 %	76.0826 %	101.9873 %	99.4519 %
1	116.0255 %	99.7243 %	99.9881 %	99.9965 %

The results with the lowest error were then selected to make a note of the equations, which are Equations 5.18 to 5.21, using 2 principal components, 3 principal components, 1 principal component and 2 principal component respectively.

$$E = -3.5028 \times 10^3 a - 5.418 \times 10^4 b + 6.4462 \times 10^7 c + 2.4836 \times 10^5 d \tag{5.18}$$

$$\sigma_y = 3.0647 \times 10^4 a + 1.9158 \times 10^3 b - 176.9243c + 7.2577 \times 10^6 d \tag{5.19}$$

$$n = 3.5652 \times 10^{-12} a + 3.2882 \times 10^{-6} b - 7.1564 \times 10^{-8} c - 2.2673 \times 10^{-10} d \tag{5.20}$$

$$\alpha = -1.7673 \times 10^{-10} a + 1.2632 \times 10^{-7} b + 3.2522 \times 10^{-6} c + 1.2532 \times 10^{-8} d \tag{5.21}$$

The figures showing the actual values of the coefficients plotted against the calculated values of the coefficients are Figures 5.21 (a) to (d). It can be seen that while the fits for E and σ_y are about as good as the ones acquired by OLS, the other two fits have nothing in common with actual data, therefore this method was not pursued further.

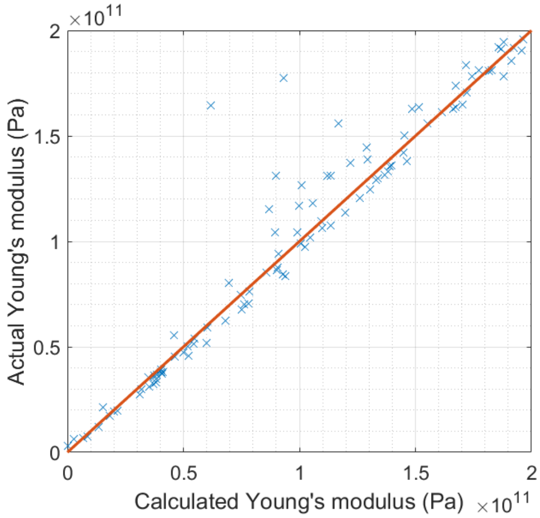

(a)

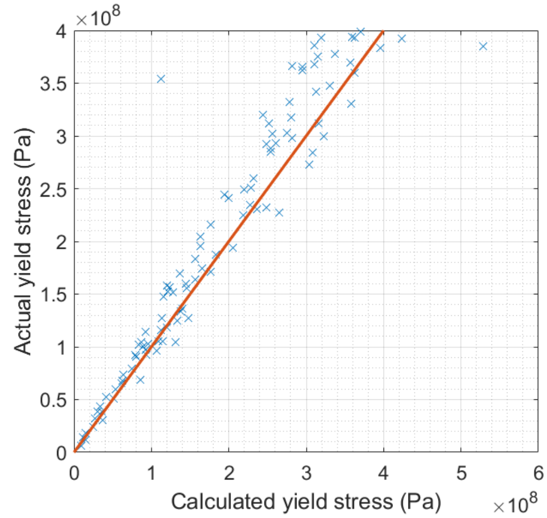

(b)

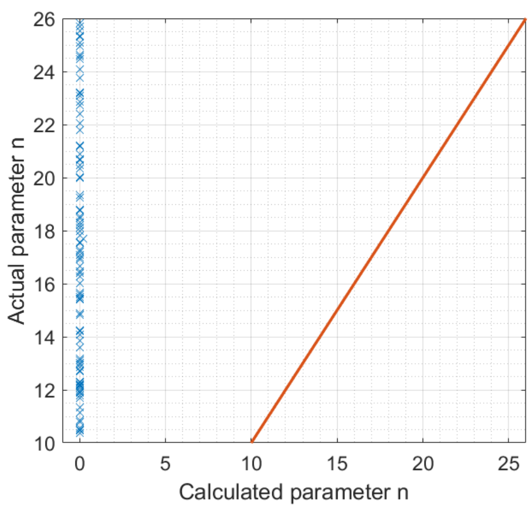

(c)

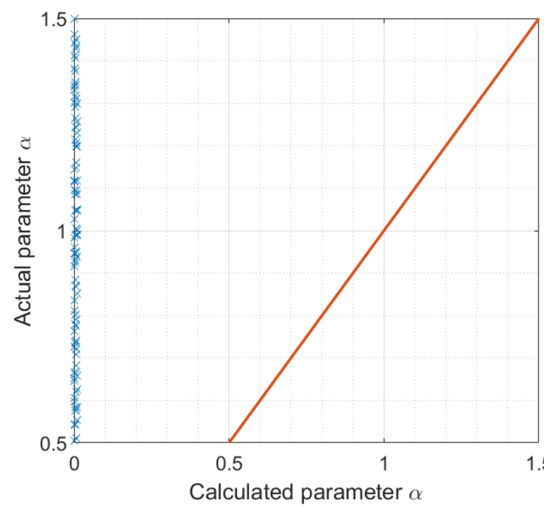

(d)

Figure 5.21: Actual and predicted values of (a) Young's modulus; (b) yield strength; (c) parameter n; (d) parameter alpha.

Neural Networks Neural networks are systems of artificial nodes (neurons), which can learn underlying patterns in data [182]. They are particularly suitable for finding non-linear patterns in data, which OLS and PCR are not suitable for due to their built-in linearity. This method is also likely to be faster to run than inverse analysis after the pattern is found. In this case the networks were trained on the virtual FEA results in order to find underlying relationships between parameters fitted to force-displacement curves and Ramberg-Osgood material model parameters. MatLab Neural Network Fitting toolbox was used to construct the neural networks. Initially it was attempted to construct a network which was capable of finding all Ramberg-Osgood material model parameters, but it was not successful. Instead, separate neural networks for finding only Young's modulus, only yield stress and both parameters n and α were constructed.

The diagrams of the networks which resulted in the lowest MAPE error between actual and predicted values of Ramberg-Osgood material model parameters can be seen in Figure 5.22. The networks for finding Young's modulus and yield stress use only a single layer of neurons, while the network used to find parameters n and α uses two layers. All hidden neurons were sigmoid and the training method used was Bayesian regularization. The error function used to train the networks was sum squared error. It was selected because it gave better correlations between actual and calculated values than mean squared error. These networks were then used to calculate stress-strain behaviour from small ring tensile test data.

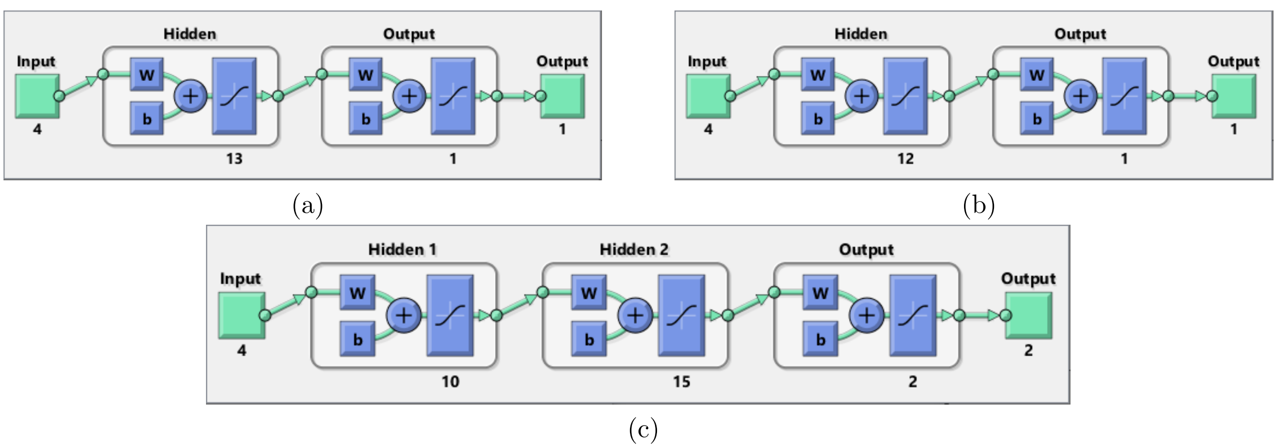

Figure 5.22: Neural networks used to calculate (a) Young's modulus; (b) yield strength; (c) parameters n and α.

The errors resulting from the networks shown in Figure 5.22 between actual and calculated values can be seen in Table 5.11.

Table 5.11: MAPEs calculated using neural networks.

E	σ_y	n	α
2.6150 %	6.1422 %	3.3170 %	10.8002 %

When the actual Ramberg-Osgood material model parameters are compared with the parameters calculated using neural networks (shown in Figure 5.23), it can be seen that all correlations are good, the correlation for parameter n has more outliers than the previous correlations and parameter α correlation has a wider scatter band than the other three correlations.

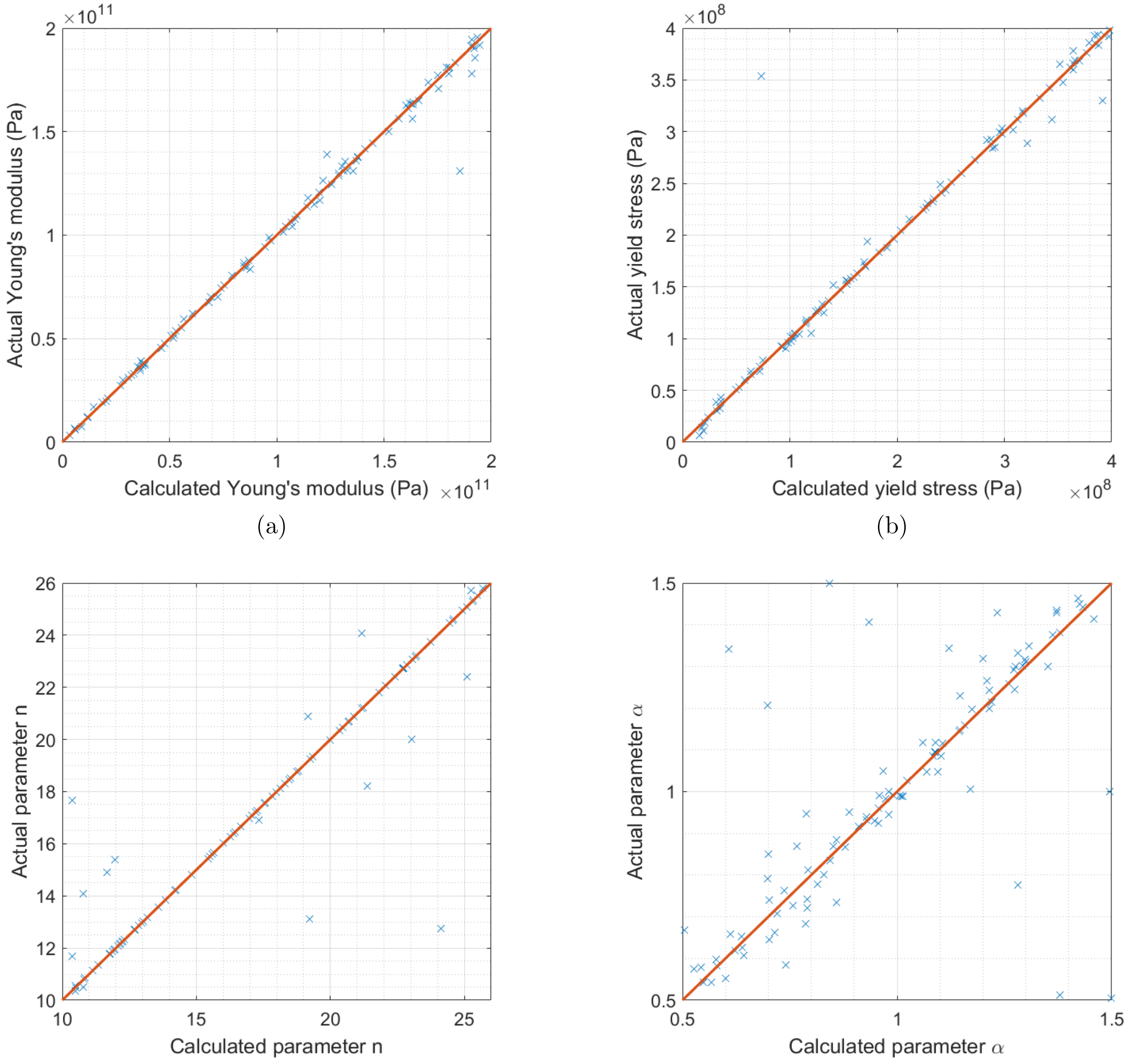

Figure 5.23: Actual and predicted values of (a) Young's modulus; (b) yield strength; (c) parameter n; (d) parameter α.

The main limitation of this method is that the accuracy of the model depends significantly on how representative the dataset used to train it is of the real data it is meant to interpret. In this case, the selection of ranges for Ramberg-Osgood material model parameters has to be appropriate, considering the range of parameters seen in real test results, the equation fitted to the resulting force-displacement curves has to be suitable and the fitting method has to be reliable. Another issue is that if the set of parameters it needs to process is outside the boundaries of the training set, the results will not be accurate as this method is not suitable for extrapolating.

FEA-based Inverse Analysis Inverse analysis is a method to calculate the material behaviour by varying the material properties in an FEA model in order to minimize the difference between the experimental results and FEA results. This is a computationally expensive method as a very large number of simulations has to be performed to calculate the stress-strain behaviour according to one experimental result. A representative FEA model is essential for this method to succeed. Due to that only a couple of example stress-strain curves were calculated from virtual results as a proof of concept before implementing this method to calculate the stress-strain behaviour according to experimental results.

The inverse analysis was done using a 1/8th FEA model to reduce the computation time. This model was identified to be appropriately representative according to the investigation described at the beginning of this chapter. The objective function selected was the sum of squared differences between the scaled FEA force displacement curve and the experimental force-displacement curve at the same displacement. Currently the method is limited to materials that can be described using a Ramberg-Osgood material model and do not experience any significant rate dependence, ageing or other viscoelastic effects. It is also prone to getting stuck in local minimums. The procedure is described below.

1. OLS results were used as the first guess, in case one of the signs was negative it was changed to positive. This occured occasionally due to the random selection of material properties not necessarily being representative of real materials.

2. The simulation was run once, the resulting force-displacement curve was compared with experimental results and and an educated improvement of the initial values was made according to the results from investigating the effects of varied material model parameters on

the force-displacement curve.

3. The simulation was run again to see if further large improvements were needed, this was repeated until the FEA and experimental curves looked reasonably close together. This took up to 3 runs usually.

4. Maximum displacement for data matching was evaluated. If the ring failed before 2 mm maximum displacement the displacement at failure was taken as the maximum value. If the second transition occurred before 2 mm the maximum value was taken to be 1 mm as such early transitions did not occur with a Ramberg-Osgood material model used in FEA. In all other cases the maximum displacement was taken to be 2 mm, as the FEA solution started to diverge from the experimental results due to not having damage accounted for.

5. The optimization study was run with the initial parameters scaled to themselves to eliminate the possibility of their relative magnitudes affecting the optimization.

6. The change in current function value was observed, if marginal improvements were seen for 2 or more iterations or if the magnitudes of the parameters have changed significantly the optimization was stopped.

7. The results were inspected, if they agreed with experimental results less well than before the analysis was started, the initial parameters had to be adjusted and the optimization rerun, if they looked better than the initial results the parameters were rescaled and the optimization restarted, if they looked sufficiently good the final values were noted for calculating the final Ramberg-Osgood material model parameters. The error in the sufficiently good cases was usually in the low thousands.

Evaluating the exact stopping condition quantitatively is difficult as the error depends on the maximum displacement selected, the number of points in the experimental data and scatter in experimental data. A rigorous method for inverse analysis would require the use of a potentially different error function and likely experimental data smoothing. Also, instead of inverse analysis based on varying material model parameters, it could be based on reconstructing the constitutive behaviour by segments, as in [54].

5.7 Interpretation Results

5.7.1 Conventional tensile testing results

In order to evaluate the quality of small ring specimen test result interpretation, standard specimen tensile test results were collected. To begin with, Ramberg-Osgood material model was fitted to the standard specimen tensile testing results, according to the method described in Section 3.6.1. Ramberg-Osgood material model is only suitable to describe continuously strain hardening materials, while some of the test results in this chapter exhibited strain softening. The resulting fits can be seen in Table 5.12. When all Ramberg-Osgood material model parameters could not be fitted due to strain softening, Young's modulus and yield stress could still be evaluated.

Table 5.12: The ranges of Ramberg-Osgood material model parameters fitted to conventional experimental data.

Material	Temperature (^{o}C)	Rate	E (GPa)	σ_y (MPa)	n	α
7175-T7153	RT	All	69.06-77.47	417.1-475.7	11.18-13.55	0.2911-1.349
	160	10 mm/min	68.78	387.5	45.87	0.148
		1 mm/min	46.8-51.68	322.4-329.3	53.23-64.11	0.01002-0.03263
		0.1 mm/min	67.62	341.2	100	0.1239
	200	10 mm/min	71.49	307.4	N/A	N/A
		1 mm/min	42.57-55.11	256.2-286.2	34.46-331.5	0.03446-2.272
		0.1 mm/min	62.6	260	N/A	N/A
P91	400	All	180.6-188.2	383.6-399.6	11.31-19.53	0.1071-0.6142
	600	0.001 1/s	132.6	304.5	14.66	0.5995
		0.00015 1/s	122.6	321.3	17.44	1.24
		0.00005 1/s	121	262.5	25.71	0.07756
2014A-T6	RT	5 mm/min	11.37-37	370-474.9	1.589-13.6	0.09272-0.9767
6082-T6	RT	5 mm/min	12.84-33.73	244.9-279.7	9.249-9.766	0.2834-1.32

Moving on to the actual results, aluminium 7175-T7153 was tested under tensile loading, using the specimens described in Section 3.3.1 at different loading rates (10 mm/min, 1 mm/min and 0.1 mm/min) and temperatures (room temperature, 160^{o}C and 200^{o}C) in order to investigate rate sensitivity. The results at 1 mm/min for all temperatures were taken from previous investigations into this material [160]. The results at room temperature can be seen in Figure 5.24 (a). The elastic response varies between 69 and 78 GPa and the plastic behaviour up to UTS is appropriately similar for all rates investigated. The fracture strength varies between 460 MPa and 520 MPa, fracture strain between 6.7 % and 15.5 %.

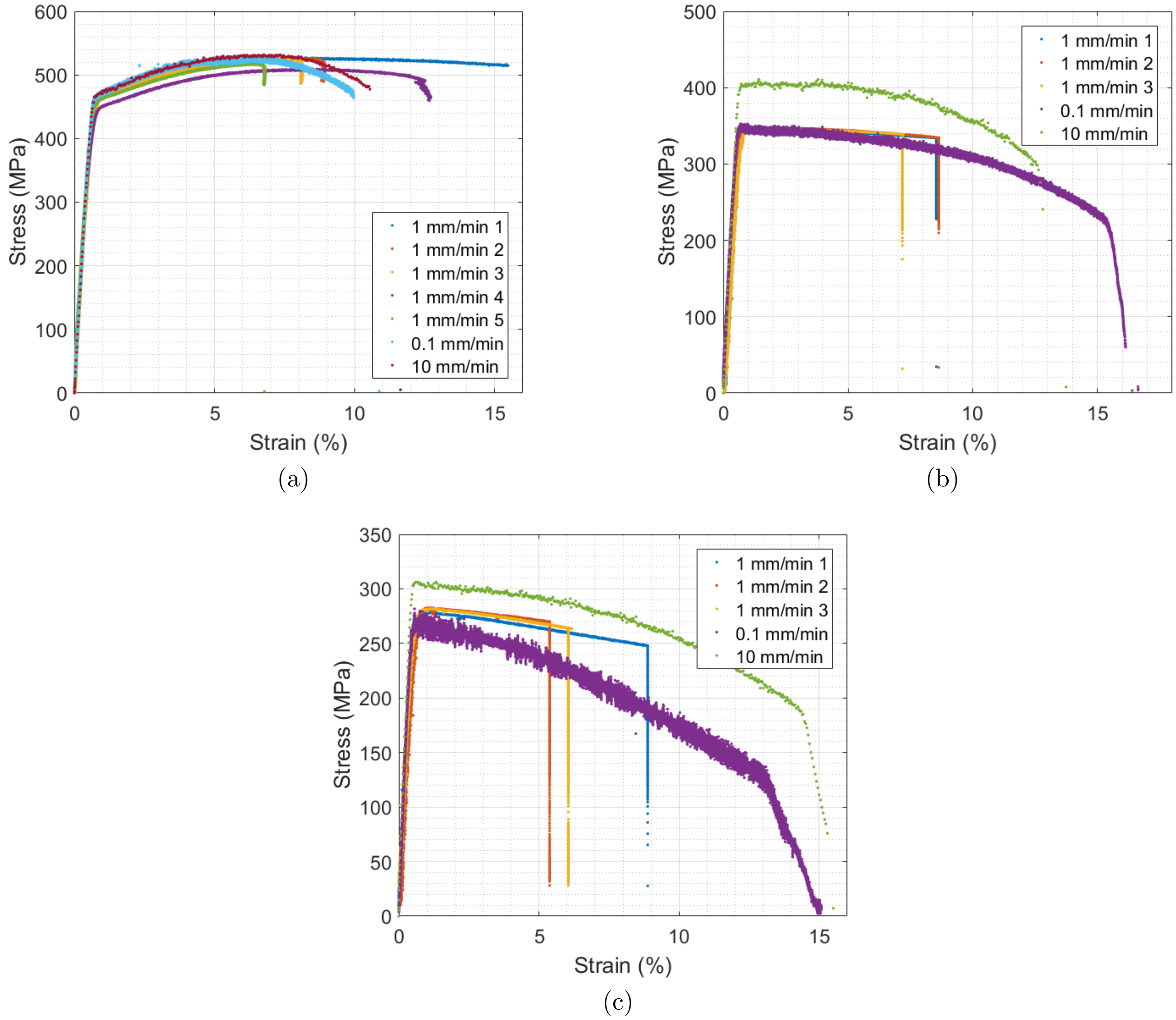

Figure 5.24: 7175-T7153 aluminium alloy standard tensile testing results at varied loading rates and (a) room temperature; (b) 160^{o}C; (c) 200^{o}C.

The elastic response of all the tests at 160^{o}C (Figure 5.24 (b)) varies between 47 and 68 GPa, the initial plastic response of the lower rates is similar, all yielding close to 330 MPa, with the 10 mm/min specimen yielding at 388 MPa. The response of that test is about 50 MPa higher that the response from the other rates throughout the test. The UTS is close to the yield strength.

Finally, the results of 7175-T7153 aluminium tested at 200^{o}C can be seen in Figure 5.24 (c). The elastic response of all the tests varies between 43 and 71 GPa. The results diverge at yield, which appears to coincide with UTS in this case, and the stress tends to go up as the loading rate goes up (from 257 MPa to 307 MPa). The fracture strain is similar for 10 mm/min and 0.1

mm/min (around 14 %), but much lower for 1 mm/min (between 5 % and 9 %).

Data for P91 steel collected from [171] and previous experimental studies (J. P. Rouse, PhD, University of Nottingham, document, April 16, 2016) was collated to investigate the rate dependence as shown in Figure 5.25. The data for 0.001 1/s was taken from the first cycle of a fatigue test, resulting in low maximum strain. There appears to be a small rate sensitivity at 400^{o}C, with the faster loading rate resulting in higher stress. For the 600^{o}C, there is no visible rate sensitivity between 0.001 1/s and 0.00015 1/s and both of them have higher stresses than the 0.00005 1/s test [183]. Perhaps there would be a difference between 0.001 1/s and 0.00015 1/s at higher strains, but that data was not available.

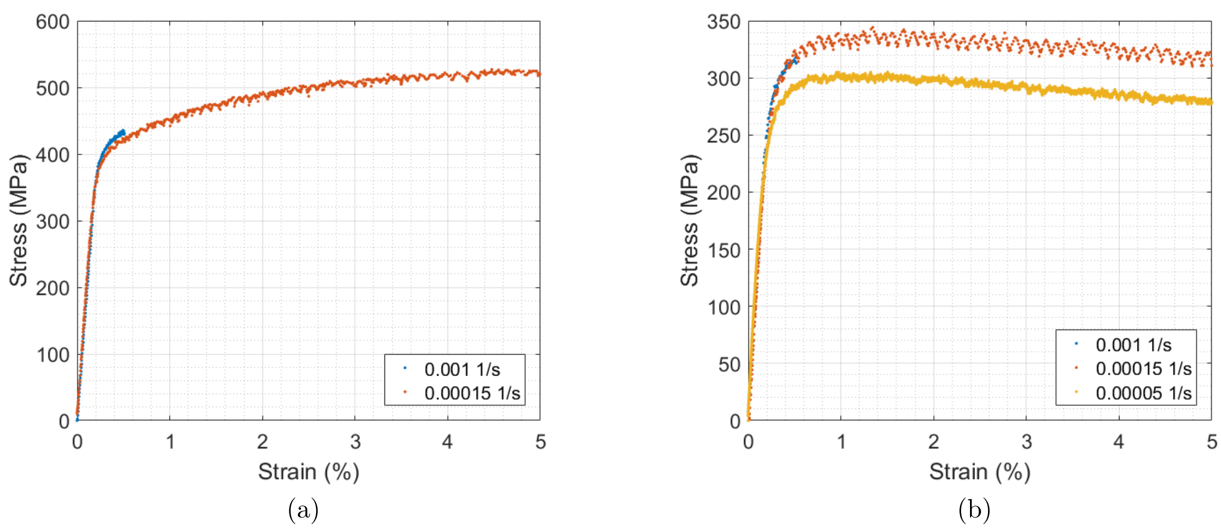

Figure 5.25: P91 steel experimental results at (a) 400^{o}C and (b) 600^{o}C.

Regarding fracture of P91 specimens, at 400^{o}C the 0.00015 1/s specimen failed at around 525 MPa and 10.5 % strain, at 600^{o}C the 0.00015 1/s specimen failed at 280 MPa and 11 % strain, while the 0.00005 1/s specimen failed at 225 MPa and 16.5 % strain.

Two large datasets from undergraduate tensile lab tests were available. They were collated, edited to zero appropriately and processed to get a distribution of stress-strain behaviour. The results for 2014A-T6 aluminium are shown in Figure 5.26. There is a lot of scatter in the elastic behaviour between the repeated tests, with the range of Young's modulus of 12 to 38 GPa, mean of 26 GPa and 8.9 GPa standard deviation, while the plastic behaviour is reasonably consistent, the stresses after yield falling within around 40 MPa.

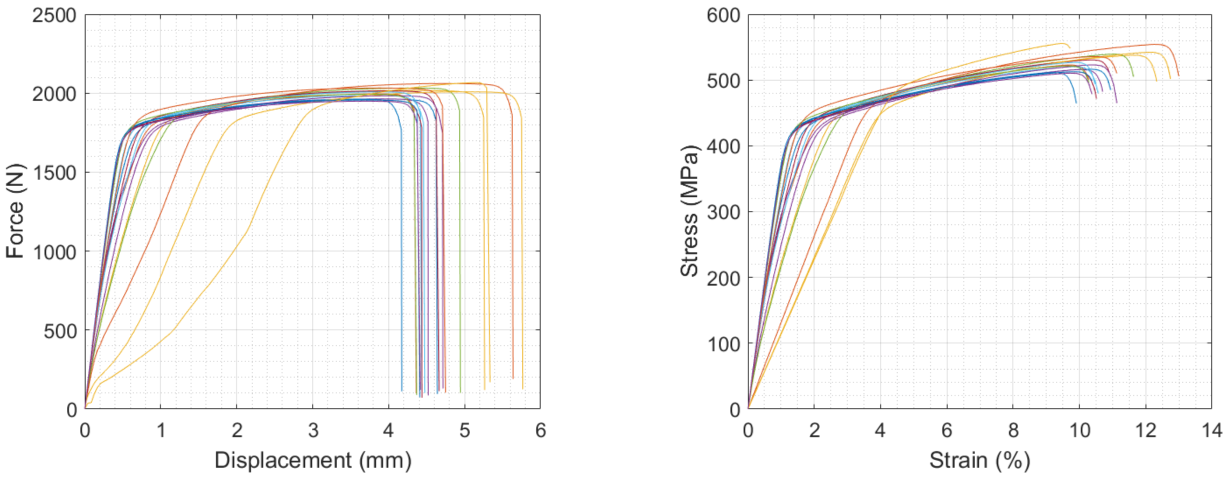

(a) (b)

Figure 5.26: 18 repeats of aluminium alloy 2014A-T6 tensile tests in the form of (a) force-displacement and (b) stress-strain.

As for 6082-T6 aluminium, the distribution of stress-strain is shown in Figure 5.27. The elastic behaviour falls in the range of 13 and 34 GPa, with a mean of 26.8 GPa and standard deviation of 7 GPa and plastic behaviour is also consistent between the repeats, within 30 MPa of each other, apart from one outlier, which is 20 MPa higher than the others.

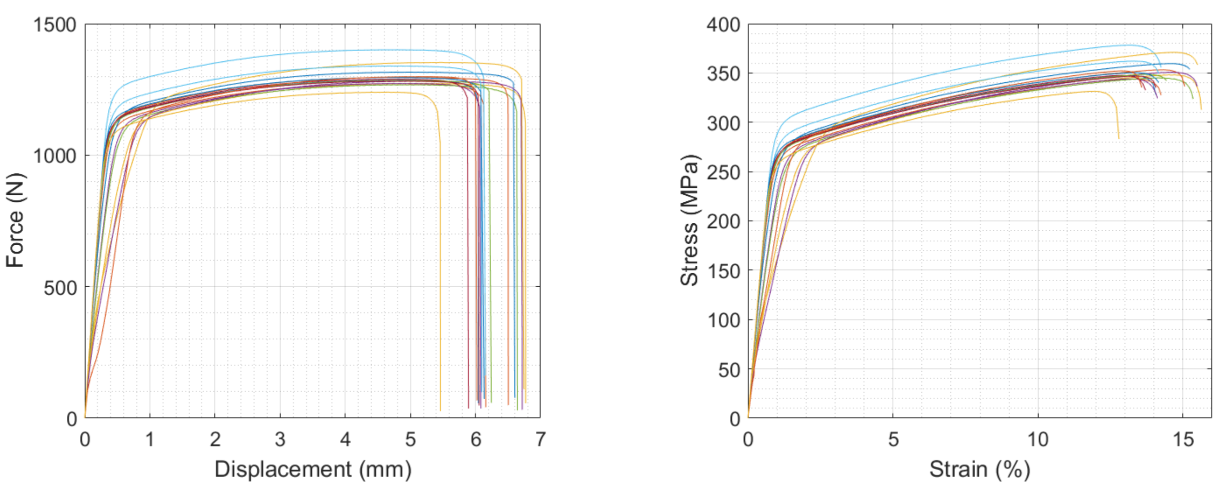

(a) (b)

Figure 5.27: 18 repeats of aluminium alloy 6082-T6 tensile tests in the form of (a) force-displacement and (b) stress-strain.

As the standard tests on 2014A-T6 and 6082-T6 aluminium alloys were done by a lot of different users with limited experience, there is a lot of scatter in the results. The possible causes for that are the specimen being misaligned when the test is being set up and the specimen slipping due to insufficient clamping as the test is being performed. The evidence for the first cause is that the scatter for the elastic behaviour of both materials is high and the evidence for the second cause is that there are noticeable changes in slope in the force-displacement curves, in particular seen in Figure 5.26 (a). The variation of Young's modulus for 2014A-T6 is between -47.05 % and +55.91 % of the mean, while yield stress varies between -13.38 % and +10.47 %. For 6082-T6 the Young's modulus varies between -25.93 % and +52.06 % of the mean, while yield stress is between -5.51 % and +7.61 %.

Table 5.13: Material properties of experimentally investigated materials.

Material	E (GPa)	σ_y (MPa)	$\sigma_U TS$ (MPa)	μ
7175-T7153	72	435	505	0.33
P91	200	415	585	0.29
2014A-T6	73.1	380	450	0.33
6082-T6	72	250	290	0.33

In comparison to the Young's modulus values from the datasheets, which are 71 GPa and 72 GPa for 2014A-T6 aluminium alloy and 6082-T6 aluminium alloy, the standard test results are significantly lower. This could be caused by the experimental error, the grain size of this material not being suitable for flat dog-bone specimens or by damage to the cross-section due to stamping. As this data is being used to evaluate the spread of values from real test results this inaccuracy is not relevant.

Equation 5.13 was fitted to small ring specimen tensile results, the fitted parameters can be seen in Table 5.14. The values of parameter a were out of the virtual result boundaries for 400^{o}C at 2.6 mm/min and 0.36 mm/min. All of the values of parameters b and c were within the virtual result boundaries. A significant proportion of parameter d values are above the maximum virtual result boundary (72.86). This could cause issues for the OLS method, as the equations to calculate the Ramberg-Osgood material model parameters were derived with significantly lower values of parameter d and this combination of values could result in inaccuracies. Neural networks are very likely to have issues with these experimental results, because they cannot extrapolate.

Table 5.14: Parameters fitted to small ring tensile testing experimental results.

Material	Temperature (°C)	Rate (mm/min)	a	b	c	d
7175-T7351	RT	2.04	0.1	0.3546	1408	67.46
		0.204	0.149	0.4225	1129	65.57
		0.0204	0.1955	0.3926	1110.6	74.964
	160	4.08	0.1312	0.1486	1543	150.3
		2.04	0.1535	0.206	675.9	45.77
		0.204	0.069	0.2465	1097	30.28
		0.0204	0.1345	0.3042	555.4	24.43
	200	4.08	0.082	0.1462	1016	59.14
		2.04	0.0566	0.1198	970.3	38.84
		0.204	0.0695	0.0744	1467	200
			0.051	0.1462	757.1	23.68
		0.0204	0.1128	0.07	632.9	215.7
P91	400	2.6	1.4638	0.7712	527.82	197.9321
		0.36	1.2477	0.9551	652.60	173.4922
		0.12	1.0404	1.097	594.89	135.0914
	600	2.6	1.0370	0.8433	419.12	70.9786
		0.36	0.6985	0.9444	545.36	43.5382
		0.12	0.6024	0.8344	521.91	31.1995
2014A-T6	RT	5	0.4157-1.0294	0.5096-0.6911	728.48-728.48	74.1996-104.344
6082-T6	RT	5	0.2467-0.5393	0.3797-0.5461	456.55-821.79	20.1237-57.2628

5.7.2 Ordinary Least Squares and Combined Methods

Starting from OLS, the recalculated Ramberg-Osgood material model parameters can be seen in Table 5.15. Some of the results for Young's modulus are negative, which occurred due to the parameter d being higher than appropriate for this model.

Table 5.15: Ramberg-Osgood material model parameters recalculated using OLS method.

Material	Temperature (^{o}C)	E (GPa)	σ_y (MPa)	n	α
7175-T7351	RT	46.52-68.03	526.83-581.44	16.06-17.93	0.88-0.96
	160	29.61-65.55	182.23-1192.5	10.01-20.85	0.50-1.25
	200	-74.14-50.77	184.67-1719.4	8.26-19.37	0.60-1.27
P91	400	-10.83-11.59	978.03-1439.2	48.42-66.08	2.10-2.85
	600	35.88-47.00	188.90-463.89	27.97-45.42	1.17-1.85
2014A-T6	RT	5.28-26.45	542.85-760.29	23.68-44.80	1.12-1.86
6082-T6	RT	25.45-59.35	136.18-426.49	16.16-25.73	0.76-1.11

Then the Young's modulus and yield stress were calculated using direct correlations and shown in Table 5.16. No negative values were found, which is expected as all the values for parameters c and d are positive and the relationships used to calculate them only have positive coefficients.

Table 5.16: Ramberg-Osgood material model parameters recalculated from direct correlations.

Material	Temperature (^{o}C)	E (GPa)	σ_y (MPa)
7175-T7351	RT	73.37-93.02	522.74-580.89
	160	36.69-101.94	189.3-1164.7
	200	41.81-96.91	183.49-1671.4
P91	400	34.87-43.11	1046.8-1533.8
	600	27.69-36.03	241.76-550.01
2014A-T6	RT	21.06-48.13	574.96-808.55
6082-T6	RT	30.16-54.29	155.94-443.72

Both methods can be easily compared by plotting the recalculated stress-strain curves side by side, for 7175-T7351 aluminium this can be seen in Figure 5.28. The yield stress results are similar for both methods, while Young's modulus is higher using direct correlations when room temperature results and 160^{o}C results are processed, but lower when 200^{o}C results are processed.

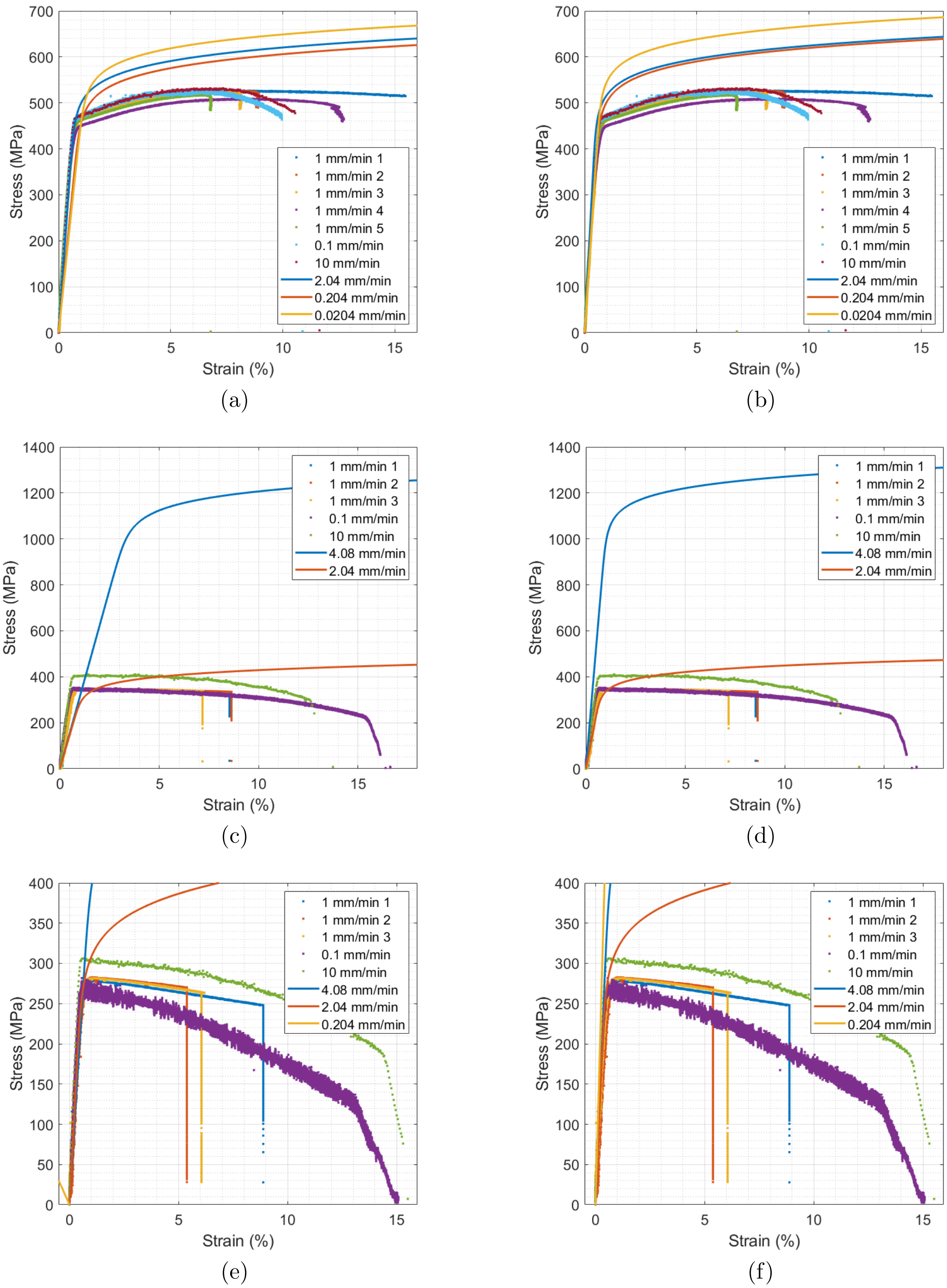

Figure 5.28: Recalculated stress-strain curves of aluminium 7175-T7351 (a) using OLS at room temperature; (b) using a combined method at room temperature; (c) using OLS at 160^{o}C; (d) using a combined method at 160^{o}C; (e) using OLS at 200^{o}C; (f) using a combined method at 200^{o}C.

The recalculated results for P91 steel can be seen in Figure 5.29. The combination of fitted coefficients for P91 steel at 400^{o}C resulted in a negative Young's modulus in one case and a significantly lower Young's modulus in another. Yield stress was similar in all other cases, while Young's modulus was lower for the OLS at 400^{o}C and for the direct correlations at 600^{o}C.

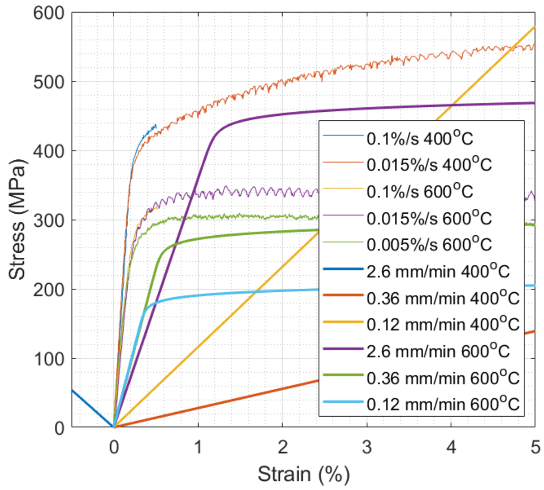

(a)

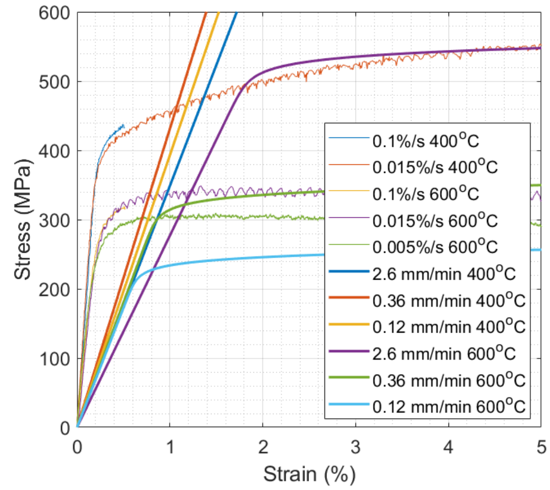

(b)

Figure 5.29: Recalculated stress-strain curves of P91 (a) using OLS; (b) using a combined method.

In the case of larger datasets, the results from 2014A-T6 aluminium and 6082-T6 aluminium can be seen in Figure 5.30. Overall, the Young's modulus is lower when direct correlations are used. There is one outlier in both plots for 2014A-T6 aluminium, in the case of OLS, the Young's modulus is significantly lower than others, while in the case of direct correlations, the yield stress is significantly higher than others. As for the 6082-T6 aluminium, the yield stress is consistently slightly higher when direct correlations are used than when OLS is used.

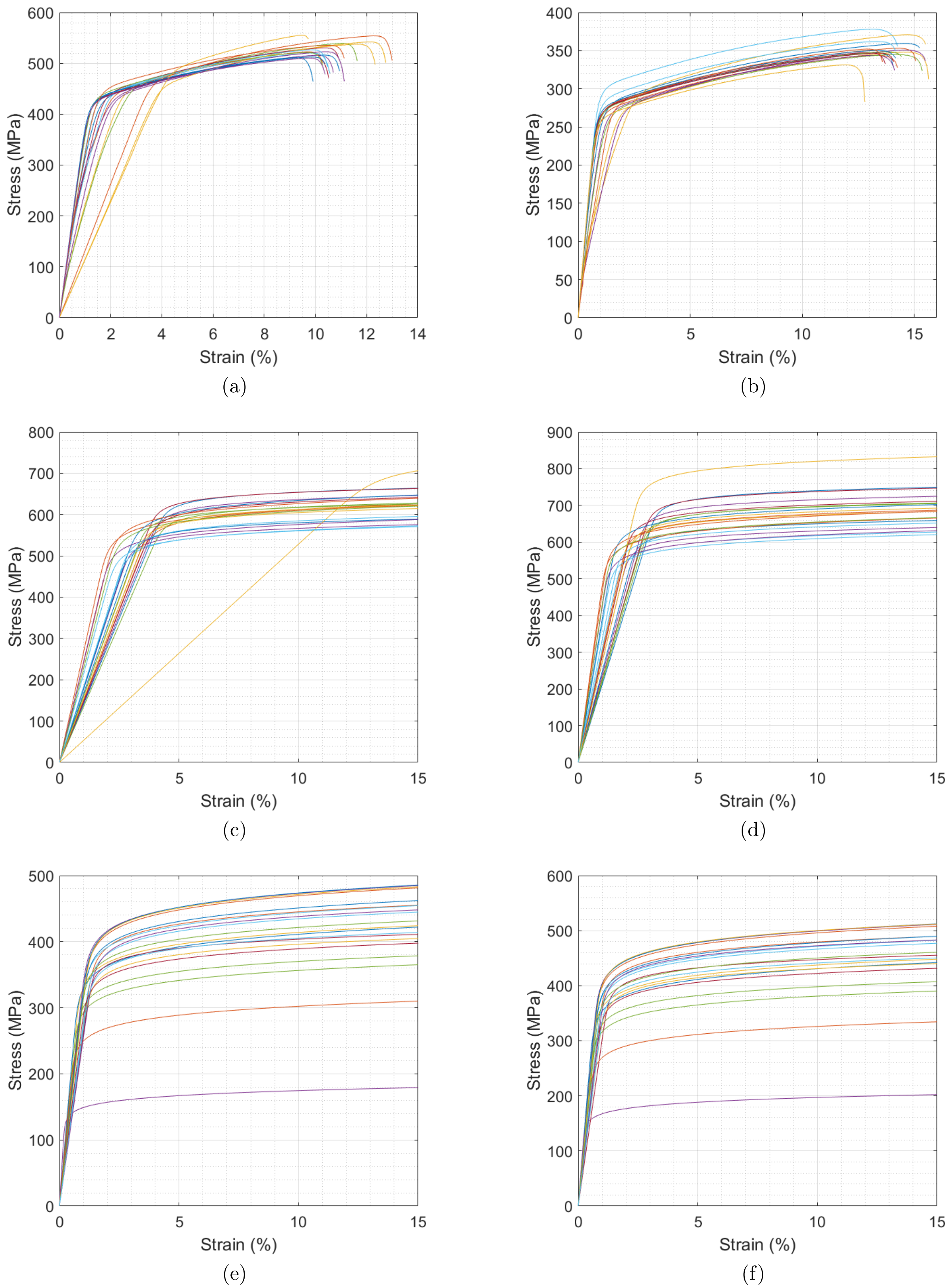

Figure 5.30: Standard tensile test stress strain curves for (a) 2014A-T6; (b) 6082-T6. Recalculated stress-strain curves from 20 repeats of (c) 2014A-T6 using OLS; (d) 2014A-T6 using a combined method; (e) 6082-T6 using OLS; (f) 6082-T6 using a combined method.

5.7.3 Neural Networks

Next the neural network approach was used, as while the selection and training of networks was time consuming, the recalculation of stress-strain behaviour was very quick. The recalculated Ramberg-Osgood material model parameters can be seen in Table 5.17. Considering that neither Young's modulus nor the slope of the initial region of the force-displacement curves vary significantly the large ranges of Young's modulus calculated for all materials are unexpected. The repetition of yield stress values of 395 MPa makes it seem like that number is related to a limitation of neural networks, so does the repetition of 1.4991 in the values of parameter α.

Table 5.17: Ramberg-Osgood material model parameters recalculated using neural networks.

Material	Temperature (^{o}C)	E (GPa)	σ_y (MPa)	n	α
7175-T7351	RT	22.55-54.52	393.98-395.73	10.38-10.50	0.5521-1.0837
	160	32.22-92.86	197.97-398.45	10.40-19.22	0.5332-0.8960
	200	3.10-73.29	47.23-398.45	10.38-10.42	0.5219-1.4524
P91	400	5.38-8.05	398.26-398.45	16.55-16.66	1.4991
	600	22.21-51.62	371.40-398.45	24.60-25.79	0.7577-1.4991
2014A-T6	RT	6.31-13.71	359.58-397.7	14.22-23.03	1.4991
6082-T6	RT	18.85-44.96	200.79-395.24	13.55-25.81	0.5378-1.4991

The recalculated stress-strain curves using neural networks from 7175-T7351 aluminium test results can be seen in Figure 5.31. The range of stress past the yield point for the room temperature data is around 70 N, for the 160^{o}C it is around 350 N and for 200^{o}C it is over 400 N. One of the results at 200^{o}C has a significantly different Young's modulus, which could be caused by the initial slope in the corresponding small ring tensile test result being too short or the data too scattered.

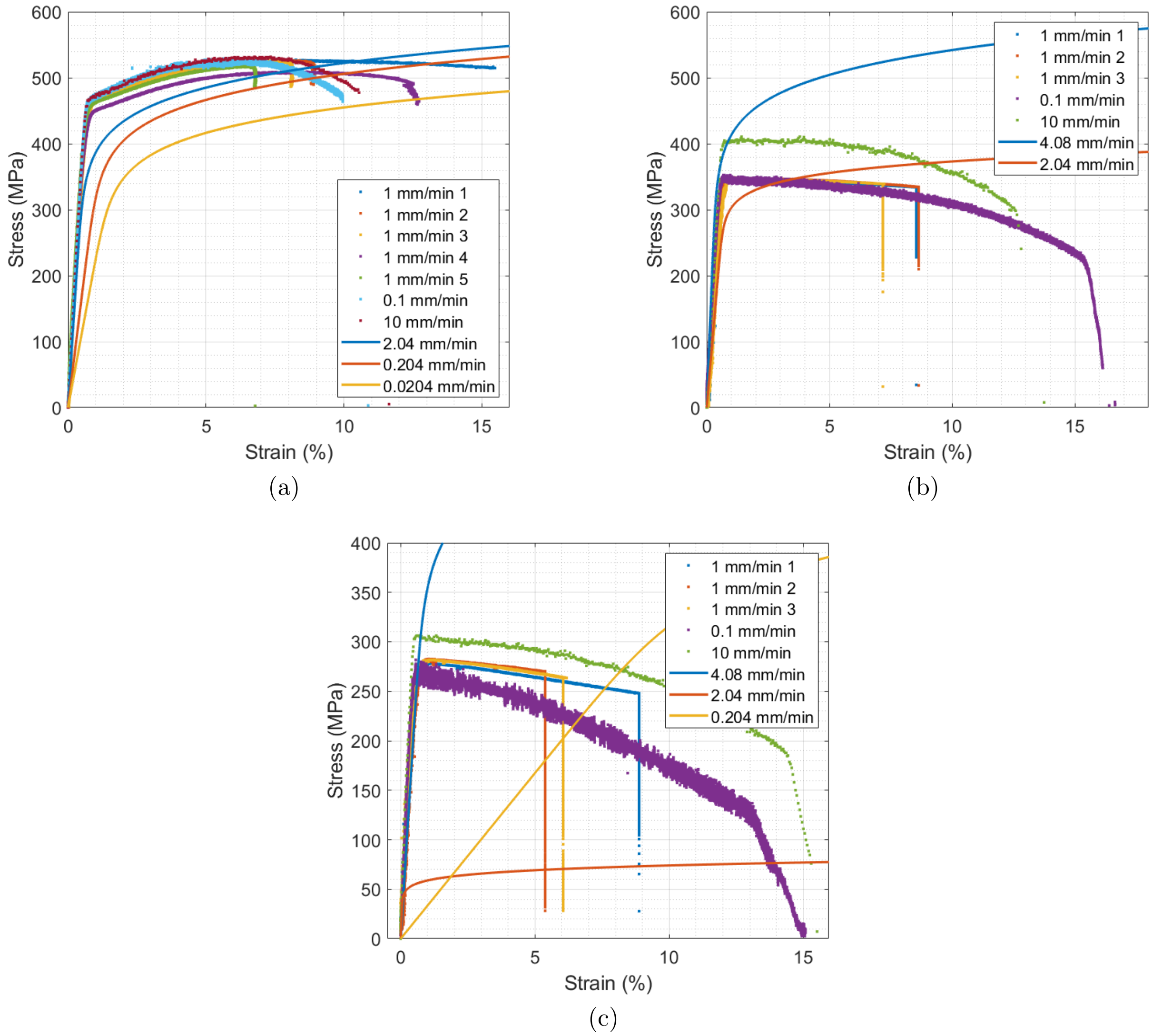

Figure 5.31: Recalculated stress-strain curves of aluminium 7175-T7351 using neural networks at (a) room temperature; (b) 160^{o}C; (c) 200^{o}C.

The stress-strain behaviour past the yield point, recalculated from P91 steel test results at 400^{o}C is in a narrow range, shown in Figure 5.32, alongside with the results from 600^{o}C tests, which have a wider range, similar to the range in standard test results.

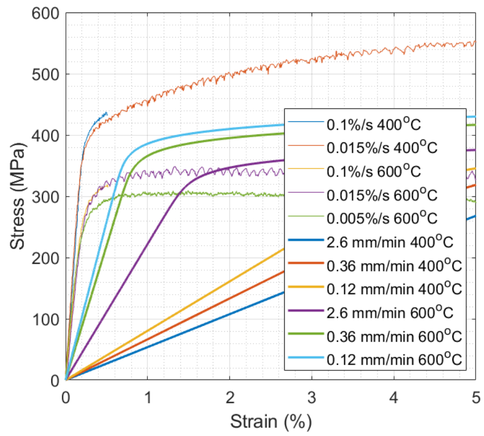

Figure 5.32: Recalculated stress-strain curves of P91 using neural networks.

As for the results from a wide range of experimental results of 2014A-T6 aluminium and 6082-T6 aluminium, they can be seen in Figure 5.33. The majority of the 2014A-T6 aluminium results are in a narrow band of about 50 N, apart from one result with a significantly lower Young's modulus. The majority of the 6082-T6 aluminium results are in a wider band of about 100 N, with one outlier with a significantly lower yield stress.

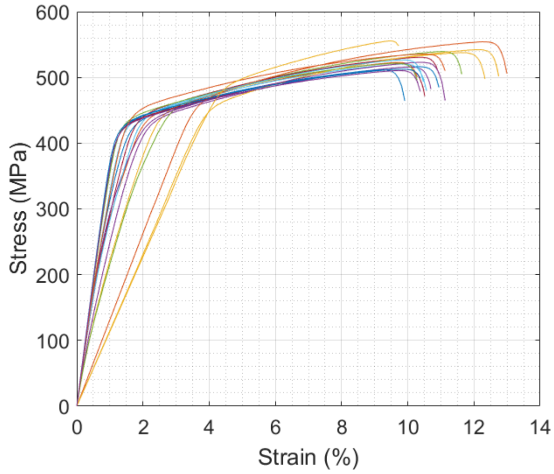

(a)

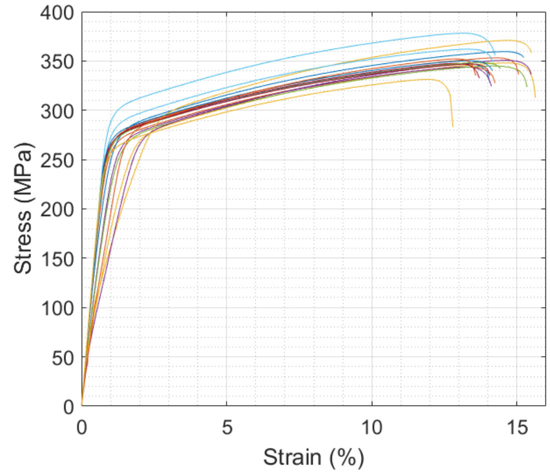

(b)

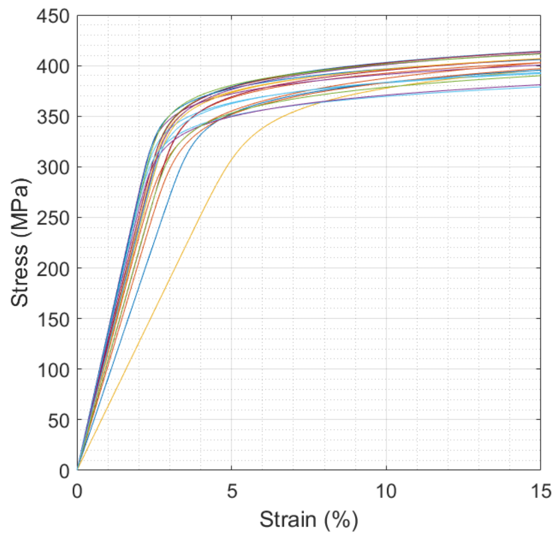

(c)

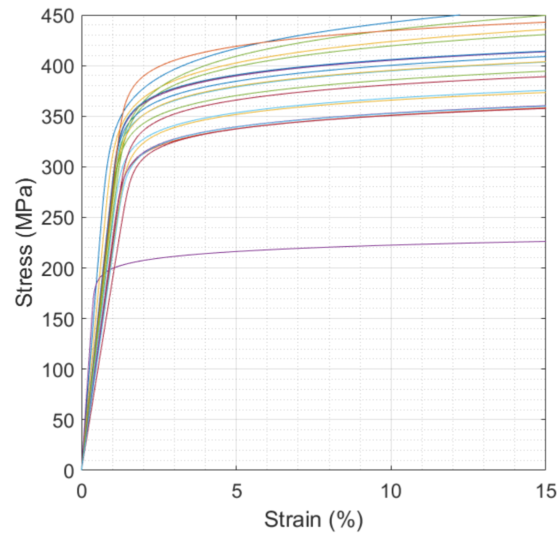

(d)

Figure 5.33: Standard tensile test stress strain curves for (a) 2014A-T6; (b) 6082-T6. Recalculated stress-strain curves using neural networks from 20 repeats of (a) 2014A-T6; (b) 6082-T6.

5.7.4 Inverse Analysis

Moving on to the inverse analysis results, Ramberg-Osgood material model coefficients calculated from small ring tensile testing results can be seen in Table 5.18. Due to the method being computationally expensive, only one example of each material was calculated, apart from 2014A-T6 and 6082-T6 aluminium alloys, which had two examples calculated to provide a range of values. The examples chosen for the other materials were from the fastest loading rates as these were the least likely to be influenced by ageing (in the case of 7175-T7351 aluminium at elevated temperatures). In the case of 7175-T7351 aluminium at room temperature and P91 steel small ring specimen testing results, they were similar when the loading rates were varied, making the evaluation of stress-strain behaviour from all of them not needed.

Table 5.18: Ramberg-Osgood material model parameters recalculated using inverse analysis.

Material	Temperature (^{o}C)	E (GPa)	σ_y (MPa)	n	α
7175-T7351	RT	80.84	403.02	47.57	0.0543
	160	152.6	227.6	5.1550	0.6290
	200	35.11	134.46	5.27	1.8064
P91	400	48.81	1155.6	221.08	111.1051
	600	37.38	607.55	21.90	12.6117
2014A-T6	RT	29.45-39.66	482.91-523.63	15.46-46.67	8.8878-90.765
6082-T6	RT	38.62-72.50	343.57-698.42	18.94-24.81	5.1144-7.1442

The stress-strain curves resulting from inverse analysis of 7175-T7351 aluminium and P91 steel can be seen in Figure 5.34. For 7175-T7351 aluminium, the result that is similar to its standard counterpart is the room temperature result, while for P91, neither of the results are similar to the standard testing results.

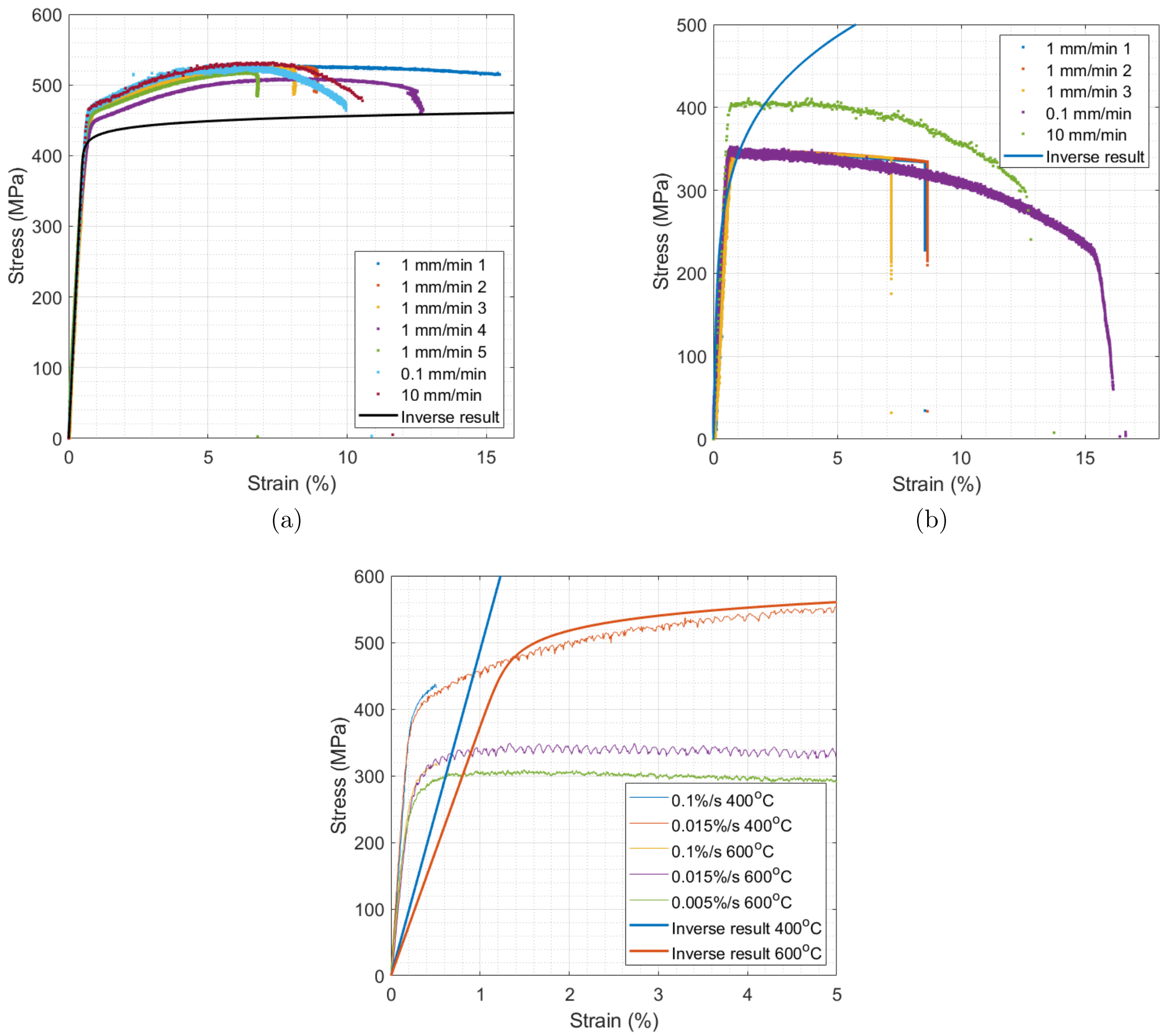

(c)

Figure 5.34: Recalculated stress-strain curves using inverse analysis of (a) 7175-T7351 aluminium at RT; (b) 7175-T7351 aluminium at 160^{o}C; (c) 7175-T7351 aluminium at 200^{o}C; (d) P91 steel.

As large datasets of both 2014A-T6 aluminium and 6082-T6 aluminium were available due to the time constraints it was not feasible to recalculate stress-strain behaviour from all testing results. Instead, stress-strain behaviour was recalculated from a force-displacement curve on the upper boundary of the set and the lower boundary of the set for each alloy in order to compare them to the experimental distribution of standard test stress-strain behaviour. The resulting stress-strain curves can be seen in Figure 5.35. Due to the results of the parameters n and α, the stress-strain curves for 2014A-T6 aluminium do not encompass a range of results, they cross-over.

The results for 6082-T6 do encompass a range of results, which is expected.

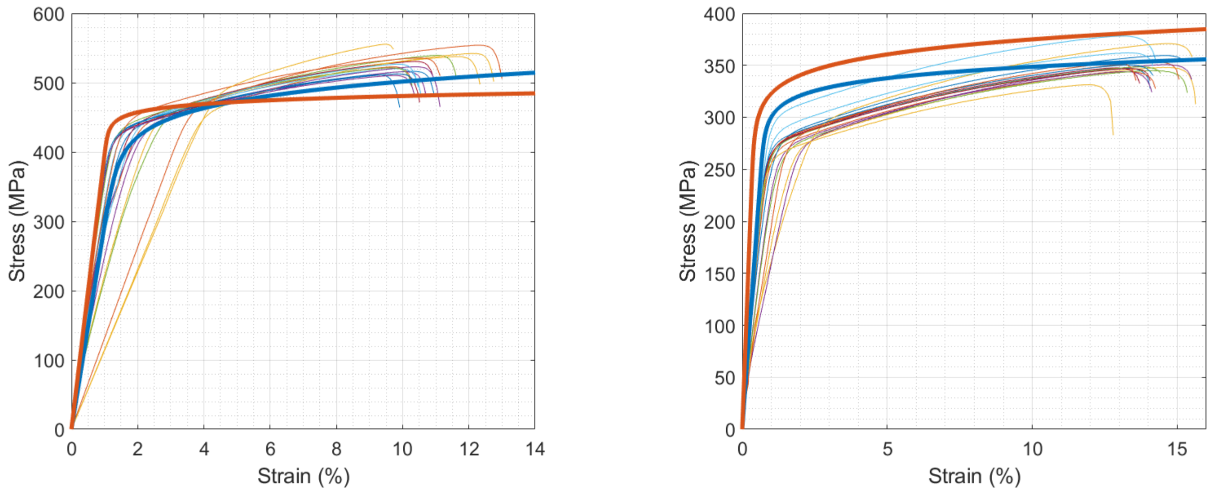

(a) (b)

Figure 5.35: Recalculated stress-strain curves using inverse analysis from 2 of the 20 repeats of (a) 2014A-T6 aluminium; (b) 6082-T6 aluminium.

5.8 Misalignment

Misalignment is a very important aspect of the small ring tensile testing. There are three types of misalignment possible in the loading setup that affect the deformation of the ring: yaw misalignment, pitch misalignment and offset misalignment. Yaw misalignment is when the pins are angled against each other, but remain on parallel planes, illustrated in Figure 5.36 (a). Pitch misalignment is when the pins are angled against each other and are not on parallel planes, illustrated in Figure 5.36 (b). Offset misalignment is when one of the pins is offset to the side, as per Figure 5.36 (c). The first two types of misalignment and their effects were investigated using a full ring FEA model, described in Section 4, while the effect of offset misalignment was investigated analytically, assuming a linear elastic material for the sake of simplicity.

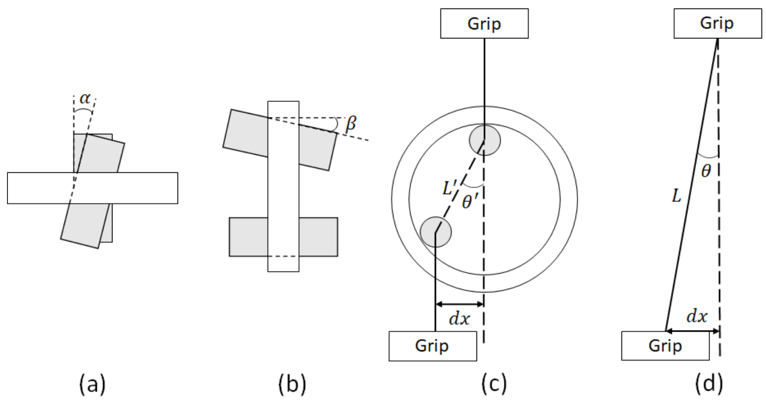

Figure 5.36: Misalignment illustrations. (a) Yaw misalignment. (b) Pitch misalignment. (c) Offset misalignment. (d) Misalignment of a standard specimen equivalent to offset misalignment.

Maximum pitch and offset misalignments are limited by the alignment of the machine, while yaw misalignment is limited by the visual inspection of the loading setup. As this tensile testing technique is being developed with a view to extend it to fatigue testing, the load train is aligned to Class 5 alignment of BS ISO 23788:2012 [184]. It specifies that the maximum misalignment for an alignment cell is that strain due to bending is either 50 microstrain at zero force or 5 % of applied uniaxial strain, whichever one is bigger, which is expressed as Equation 5.22. Uniaxial strain according to Figure 5.36 (d) in Equation 5.23, while bending strain is shown in Equation 5.24. When those equations are substituted into Equation 5.22, Equation 5.25 is the result, which can then be simplified to Equation 5.26.

$$\varepsilon_{uniaxial} \times 5\% \geq \varepsilon_{bending} \tag{5.22}$$

$$\varepsilon_{uniaxial} = \frac{\sigma}{E} = \frac{P}{AE} = \frac{P}{\frac{\pi r_s^2}{4}E} = \frac{4P}{\pi r_s^2 E} \tag{5.23}$$

$$\varepsilon_{bending} = \frac{M r_s^2}{EI} = \frac{PLsin\theta r_s}{\frac{\pi r_s^4}{4}E} = \frac{4PLsin\theta}{\pi r_s^3 E} \tag{5.24}$$

$$\frac{4P}{\pi r_s^2 E} \times 5\% \geq \frac{4PLsin\theta}{\pi r_s^3 E} \tag{5.25}$$

$$5\% \geq \frac{Lsin\theta}{r_s} \tag{5.26}$$

In this case L is 80 mm, as that is the length of the standard creep specimen and r_s is 5 mm, as that is the radius of the gauge section of the standard creep specimen. After substituting those values into Equation 5.26, the angle θ needs to be less or equal to 0.179°. This is the value of maximum pitch misalignment as well, as illustrated in Figure 5.37.

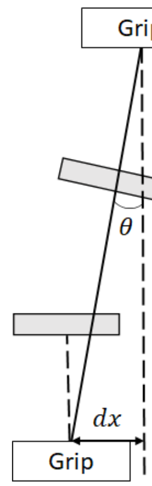

Figure 5.37: Pitch misalignment with relation to the machine alignment.

This results in a maximum dx value of $Lsin\theta = 0.05$ mm. As the level of offset misalignment affecting the small ring specimen is of interest, this value needs to be converted to θ', shown in Figure 5.36 (c). According to the inscribed angle theorem, all angles inscribed in a circle on the same arc length are equal, and they are also equal to half of the central angle on the same arc, making the angle between L' and e 90^o. Because of this, Equation 5.27 is valid. As the angle between $(2R - 2r_{pin})$ and dx is also 90^o, Equation 5.28 is also valid and can be combined with Equation 5.27 to get Equation 5.29, then the maximum angle θ' can be found to be 0.8815^o according to Equation 5.30. Using this angle to calculate the error in force and displacement measurements results in less than 1 % difference from actual values.

$$L' = (2R - 2r_{pin}) \times cos\theta' \tag{5.27}$$

$$L' = \frac{dx}{sin\theta'} \tag{5.28}$$

$$\frac{dx}{2R - 2r_{pin}} = sin\theta' cos\theta' = \frac{1}{2} sin\,(2\theta') \tag{5.29}$$

$$\theta' = \frac{1}{2} arcsin \frac{dx}{R - r_{pin}} \tag{5.30}$$

The maximum yaw misalignment was assumed to be 5^o, as larger misalignments would be noticed during setup and corrected. It was implemented in the model by rotating one of the pins by 5^o. Pitch misalignment was implemented in the same way. The effect of misalignment on the FEA results can be seen in Figure 5.38.

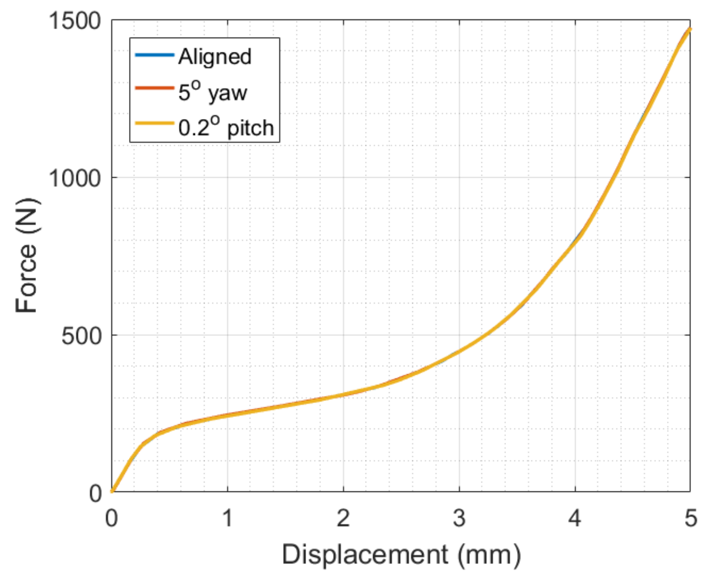

Figure 5.38: The effect of pitch and yaw misalignment on the force-displacement results.

Neither yaw nor pitch misalignment (of this magnitude) were found to have a significant effect on the results. It is concluded that pin misalignment does not have a significant effect on the results provided it can be kept to within small values. The potential of a small amount of misalignment in the small ring experimental data presented is therefore considered insignificant.

5.9 Discussion

The reasons for differences between the small ring test results and conventional test results, as well as the differences between different small ring test results and different standard test results are rate dependence, the possibility of ageing and different duration of ageing when heating up the specimens.

When observations regarding rate dependence are made, similarities in behaviour between standard test results and small ring specimen test results are seen. At room temperature for 7175-T7351 aluminium and at 400^{o}C for P91 steel, rate dependence is not present in both standard test results and small ring specimen test results. This shows that the rates chosen for those small ring tests were appropriate and the results should be comparable to standard test results, provided an appropriate interpretation method can be developed.

When rate dependence is present and ageing does not occur, at 600^{o}C for P91 steel, the trends in the results from the standard specimen tests and small ring specimen tests agree with each other. The slow loading rates result in lower force (or stress) than the two faster ones, which are approximately the same. This also shows that the rates chosen were comparable for the small ring tests and standard tests and that small ring specimens are suitable for testing rate dependent materials that do not age.

When both rate dependence and ageing are present, at elevated temperatures for 7175-T7351 aluminium, both standard test results and small ring specimen test results exhibit significant rate dependency, however the effect is not consistent, as it is also combined with ageing. At 160^{o}C the fast loading rate (4.08 mm/min in the case of ring specimens and 10 mm/min in the case of conventional specimens) result in higher force (or stress) than the slower ones, the results from which are mostly the same for standard test results. The lower rate small ring results are very similar as well, with 2.04 mm/min and 0.204 mm/min R1 being the closest and R2 being more similar to slower rates. This could have been caused by the material ageing as it was being heated up or tested or the small ring specimen tensile testing loading rate selected being not representative of the slow loading rate used with conventional tensile specimens.

At 200^{o}C there is a significant difference in response across the rate in both standard test results and small ring specimen results, as the trends between standard tests and small ring tests do not agree. The force at 4.08 mm/min loading rate for the small ring test initially was not the highest out of all the results of the tests done at 200^{o}C. The small ring results at the 0.0204 mm/min R1 do not exhibit the initial slope seen in all the other small ring test results either. As according to the previous investigation this material ages very quickly, especially at 200^{o}C, this could have been caused by the material ageing as it was being tested or by it ageing as it stayed at elevated temperature before the test began. Another potential explanation for the lack of the initial slope could be the transition between the first and the second slope (region I and region III) being at a very low force and the specimen being pre-tensioned before the test, however this is not supported by the results from the repeat, which is initially similar to 0.204 mm/min R1. This could potentially be improved in future testing by induction heating, as it would bring the specimen up to temperature quickly and reduce the potential for ageing prior to testing. An undergraduate project student investigated the suitability of different heating element arrangements for induction heating, discovering that it is a promising method for heating small ring specimens (C. S. Harper, MEng, University of Nottingham, document, 2017).

Regarding failure, the more ductile materials identified from standard specimen test results tend to fail in a more ductile way when tested as ring specimens, with higher displacements to failure and sudden failure as opposed to progressive failure. Regarding the effect of temperature, the fracture results from the P91 steel do not show significant temperature dependence, which does not agree with standard test results, which show a significant difference in fracture between different rates. There is a significant temperature effect for 7175-T7351, most likely caused by ageing. An interesting thing to note is that the 7175-T7351 small ring specimen tested at room temperature at 0.0204 mm/min loading rate failed at a significantly higher displacement than the other specimens. As the standard testing results do not support the idea that this material is more ductile at slower loading rates, this result is likely an outlier.

If a small ring specimen was noted to have thinning by the pin, its tensile test results showed a large deformation between peak load and failure. This is particularly visible on the P91 specimens tested at 600^{o}C. Therefore it can be argued that the deformation past the peak load coincides with localized thinning (necking), which is a similar phenomenon to the necking that occurs in standard specimens, but experienced through different geometry.

The results from the small ring specimens are more consistent, with the variation of the initial slope for 2014A-T6 being between -54.3 % and 32.5 % and for 6082-T6 - between -27.1 % and

+29.4 %. Due to how the small ring specimens are loaded slip is not possible, which eliminates one of the potential sources of error during the setup.

All aluminium rings exhibit bending inwards after testing, but the steel rings do not. This could be caused by a difference in viscous behaviour. Another potential reason for this could be that the ring straightens out at higher displacements, which were not reached by the aluminium rings as they failed earlier. Differences in Poisson's ratio are unlikely to have caused this difference in behaviour as Poisson's ratio of all these materials is between 0.3 and 0.33.

As 7175-T7351 aluminium ages quickly and has a significant rate dependence at elevated temperatures, those small ring specimen test results are not suitable for interpreting them by any of the methods developed. The Young's modulus and yield stress could potentially be determined, the latter depending on the appropriate loading rate being chosen and the material being aged the same amount while it is being brought up to testing temperature, which is not likely to have happened. Another issue is that the first slope is very short, making the data difficult to interpret. Testing a thicker ring would have made the evaluation of Young's modulus more accurate. The experimental results for P91 steel at both temperatures are significantly different from anything achieved when material model parameters were varied, in particular the first and second transitions being at significantly higher displacements. This makes the suitability of these results for any of the methods investigated questionable, even though standard testing results from P91 steel can be described with a Ramberg-Osgood material model up to a certain strain. All other experimental results look suitable for interpretation.

Experimental data being scattered is a significant issue for all methods, as is poorly zeroed data. A wide force-displacement curve causes issues when fitting the Equation 5.13, as the distribution of the scatter is not necessarily even, potentially introducing errors. Poorly zeroed data makes it unclear where the loading actually begins potentially affecting both Young's modulus and yield strength that are being evaluated.

The results from using the methods for recalculating stress-strain behaviour will be discussed beginning with the most appropriate materials, 7175-T7351, 2014A-T6 and 6082-T6 aluminium alloys tested at room temperature. When Young's modulus was evaluated for 7175-T7351 aluminium, direct correlations offered the most accurate results. Inverse analysis overestimated the results by about 13 %. OLS method underestimated two of the results by about 30 %, with the third being within 10 %, while direct correlations overestimated one of the results by around 30 % with the other two being accurate. Neural networks underestimated Young's modulus by at least 20 %. For 2014A-T6 aluminium direct correlations and inverse analysis resulted values on the higher end of the standard range or above it, while OLS and neural networks resulted in values on the lower end of standard range or below it. All methods when used for 6082-T6 aluminium tend to overestimate Young's modulus in comparison to the standard results, with some overlap of the evaluated range of Young's modulus and standard testing Young's modulus.

As for the yield stress for 7175-T7351 aluminium at room temperature, it appears to have been evaluated quite accurately using inverse analysis, within 10 % of standard testing results. The neural network results look about as accurate, however that yield stress is a value that repeats in Table 5.17, making it seem that it is a limitation of the model instead of a genuine result. The results from both direct correlations and OLS are higher than standard values, by around 25 %. For 2014A-T6 aluminium and 6082-T6 aluminium yield stress was consistently higher than standard values when direct correlations (at least 45 %), OLS (at least 36 %) and inverse analysis (at least 36 %) were used. The neural networks appear to have encountered the limitation in this data as well, making their results unreliable.

Then, moving on to P91, for which the quality of the data was questionable. Young's modulus was between 2.5 (neural networks for 600^{o}C), 4 (direct correlations, OLS and inverse analysis) and 20 times (neural networks for 400^{o}C) lower that identified from standard testing.

Yield stress in most cases was between 2 (inverse analysis for 600^{o}C) and 4 (inverse analysis for 400^{o}C and direct correlations) times higher than identified from standard testing. The results from neural networks appear to have been affected by a limitation of the method, making them unreliable, apart from one which is 20 % higher than identified from standard testing. Using direct correlations, the yield stress found from the test at 600^{o}C was 20 % lower, 10 % higher or 70 % higher that evaluated from standard testing. And using OLS resulted in yield stresses 30 % lower, 10 % lower and 50 % higher than the yield stress evaluated from standard testing.

Overall, none of the methods were able to evaluate either Young's modulus or yield stress for P91 steel consistently and accurately. This could be due to the lack of accurate LVDT measurements and the error contributions being inaccurate, which is the most likely reason, the material being unsuitable for a Ramberg-Osgood material model or the microstructure making it not suitable to be tested as a small ring specimen.

Finally, the results which were not suitable for the methods developed, 7175-T7351 aluminium at elevated temperatures. At 160^{o}C Young's modulus was close to standard results in some cases. Using direct correlations one result was close to the highest standard result, one to the lowest, but the other ones were around 43 % higher and 21 % lower. Using OLS, it was at least 32 % lower than the lowest standard results, using neural networks one result was close to the lowest standard result, one to highest, but the other ones were at least 30 % higher and 25 % lower. Inverse analysis resulted in Young's modulus that was twice the magnitude of standard, which is likely caused by the scatter in the experimental data.

At 200^{o}C some values of Young's modulus were close to standard results as well. When direct correlations were used the middle value agreed well with the 10 mm/min standard test result, but the other ones were 45 % higher or lower. Two of the OLS results were negative due to a combination of parameters being unexpected, but the other two agreed with standard results well. Two of the neural network results were 15 % higher than standard results, and one was about 20 times lower. The result from inverse analysis was 25 % lower than standard results.

When yield stress was evaluated for the 160^{o}C test results and direct correlations and OLS were used, the middle calculated values were close to the 1 mm/min standard test results, but the higher values were about 5 times too high and the lower values about 50 % too low. The higher neural network result appears to be affected by the limitation of the method and the lower value is about 50 % too low, with a middle value close to standard result. When inverse analysis was used the result was 30 % lower than standard.

For 200°C test results using both direct correlations and OLS the middle calculated values were close to the 10 mm/min standard test results, the higher values were about 5 times too high and the lower values were about 50 % too low. The higher neural network results appears to be influenced by the limitation, which makes them inaccurate and the lower result is 5 times too low. Inverse analysis resulted in yield stress value that was 43 % lower than standard.

Overall, neural networks do not seem suitable for these results due to the limitations they currently have. The inverse analysis results are significantly affected by the scatter in the data. Some of the results using OLS and direct correlations are close to standard, which means that the amount of ageing the material experienced happened to be similar and those rates chosen were appropriate.

As for the hardening behaviour, OLS, neural networks and inverse analysis are all technically capable of evaluating it. OLS did not result in a strong correlation when tested on virtual data, which means that the results from real data would not be accurate either. Neural networks appear to encounter a limitation in the majority of cases when calculating parameter α, making the hardening behaviour calculated inaccurate. Inverse analysis does not have any inherent issues with calculating hardening behaviour, however the results are very dependent on accurate evaluation of yield stress. When yield stress was calculated to be close to standard results, the hardening behaviour looks similar to standard results, but when it was not a good comparison cannot be made.

As misalignment of the magnitudes seen during experimental testing was found to have no significant effect on small ring testing results the disagreement between interpreted stress strain results and experimental stress-strain results cannot be explained that way. Compliance calculated at room temperature was found to not have a significant effect either.

5.10 Summary and Conclusions

This chapter described the small ring specimen tensile testing technique, followed by the small ring specimen test results. The trends in the conventional test results and the small ring specimen test results and the repeatability of both tests were compared. Several interpretation methods for calculating bulk material tensile data from small ring specimen tensile test data were developed. The performance of those methods was then evaluated using the conventional test results and small ring specimen test results.

The main conclusions from this chapter are as follows:

- The trends related to rate dependency tend to agree between standard test results and small ring test results.
- Similarly to standard test results, more ductile materials fail in a more ductile manner, while more brittle materials fail in a more brittle manner.
- The deformation past the peak load in small ring specimen test results indicates localized thinning (necking).
- The current version of the analytical solution is suitable for evaluating Young's modulus using inverse analysis, additional work is needed for it to be suitable for the stress-strain behaviour.
- Scattered experimental data should be smoothed before interpreting it.
- LVDT readings are necessary for the small ring tensile results to be interpreted accurately, especially at elevated temperatures, as using crosshead displacements results in the recalculated bulk material properties several times lower than standard.
- The current version of direct correlations method is suitable for an initial estimate of Young's modulus and yield stress.

- The OLS and PCA methods are inherently limited by assumed linear relationships between the parameters and the current versions are limited by the dataset used to fit them.
- The current version of neural network method is inaccurate due to the dataset used to train it not being appropriate, as coefficients fitted to experimental results are out of the bounds of the coefficients used to train the neural network.
- The current inverse analysis method is the most consistently accurate method, however it is very computationally expensive.

6 Small Ring Specimen Cyclic Modelling

6.1 Introduction

Having confirmed that small ring specimens are suitable for tensile testing and that unixaial-equivalent stress-strain data can be calculated from the small ring specimen tensile test results in Chapter 5, the suitability of small ring specimens for cyclic testing had to be investigated.

The deformation of the small ring specimen under cyclic loading needs to be accurately modelled, which led to two FEA models being developed: a 1/8th model (due to symmetry) for the majority of the modelling work and a full ring FEA model used to investigate misalignment. Initial modelling studies were done to verify the FEA model by fitting a combined hardening material model to the standard cyclic test results of copper annealed at 600^{o}C and 700^{o}C, then using those model parameters to run simulations and compare the results to experimentally acquired results. Modelling work was then carried out to investigate how varying material and geometry parameters affect the force-time and force-displacement results.

6.2 FEA Models

6.2.1 1/8th 3D Model

The FEA model is based on the experimental setup for small ring cyclic testing described in detail in Section 7. The model itself consists of a pin, a clamp and the ring, similar to the 1/8th FEA model developed for the investigation of small ring specimen tensile loading, described in Section 4. Due to the setup being symmetrical 1/8th of the setup is modelled, with symmetry boundary conditions applied on all planes of symmetry. The ring has an inner radius of 4.5 mm and outer radius of 5.5 mm, half thickness of 1 mm and is modelled as a deformable body. The pin has a radius of 1.25 mm and a half length of 2 mm and is modelled as a deformable body. The clamp has a half width and half length of 2 mm and a thickness of 0.2 mm, it is modelled as a deformable body. It is rectangular instead of circular because the difference in the area of contact between the ring and the clamp is negligible and a better model of contact is achieved, as the contact is more consistent due to the nodes being arranged in an orderly fashion. The model is shown in Figure 6.1.

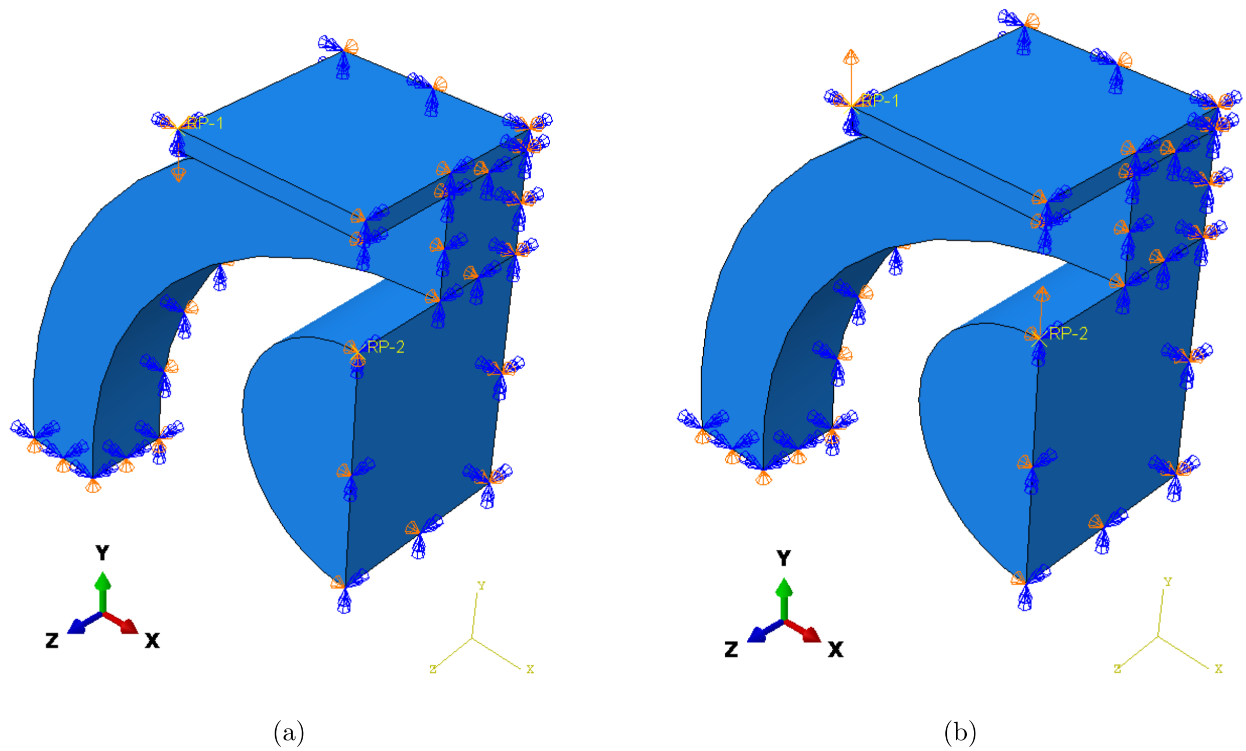

Figure 6.1: 1/8th cyclically loaded small ring specimen FEA model during (a) clamping; (b) cycling.

Both the pin and the clamp are modelled as elastic-only. This was chosen because two analyses were run: one with elastic-only pin and clamp, one with elastic-plastic pin and clamp, and there was no difference between the results. Also, no permanent deformation was noted on the clamping rods and the pins after cyclic small ring specimen testing. As the pin is made from Nimonic, the Young's modulus is set to be 200 GPa. The clamp is made from silvered steel, as it is modelled shorter than the actual clamping rod, in order to ensure it deforms the same amount the Young's modulus is set to 0.94 GPa. In order to define the material, a combined hardening model was used. The equations for it can be seen in Equations 2.19 and 2.20. Material constants were determined by fitting the model to stress-strain curves acquired from standard testing (using specimens shown in Figure 3.4) for copper annealed at 600^{o}C and 700^{o}C. The curves were fitted using Matlab Optimization toolbox, as described in Section 3.6.2.

The comparison of the experimental and simulated stress-time behaviour for the 600^{o}C anneal is shown in Figure 6.2 (a) to (c). The comparison of the experimental and simulated stress-time behaviour for the 700^{o}C anneal is shown in Figure 6.2 (d) to (f). As simulated stress-time behaviour is based on rate independent material model the time in simulated behaviour is arbitrary, therefore having no units. Both saturation stress and speed to saturation agree well for the 700^{o}C anneal, while for the 600^{o}C anneal test 1 results appears to be missing data points at the beginning, but there is good agreement between the simulated results and the test 2 results.

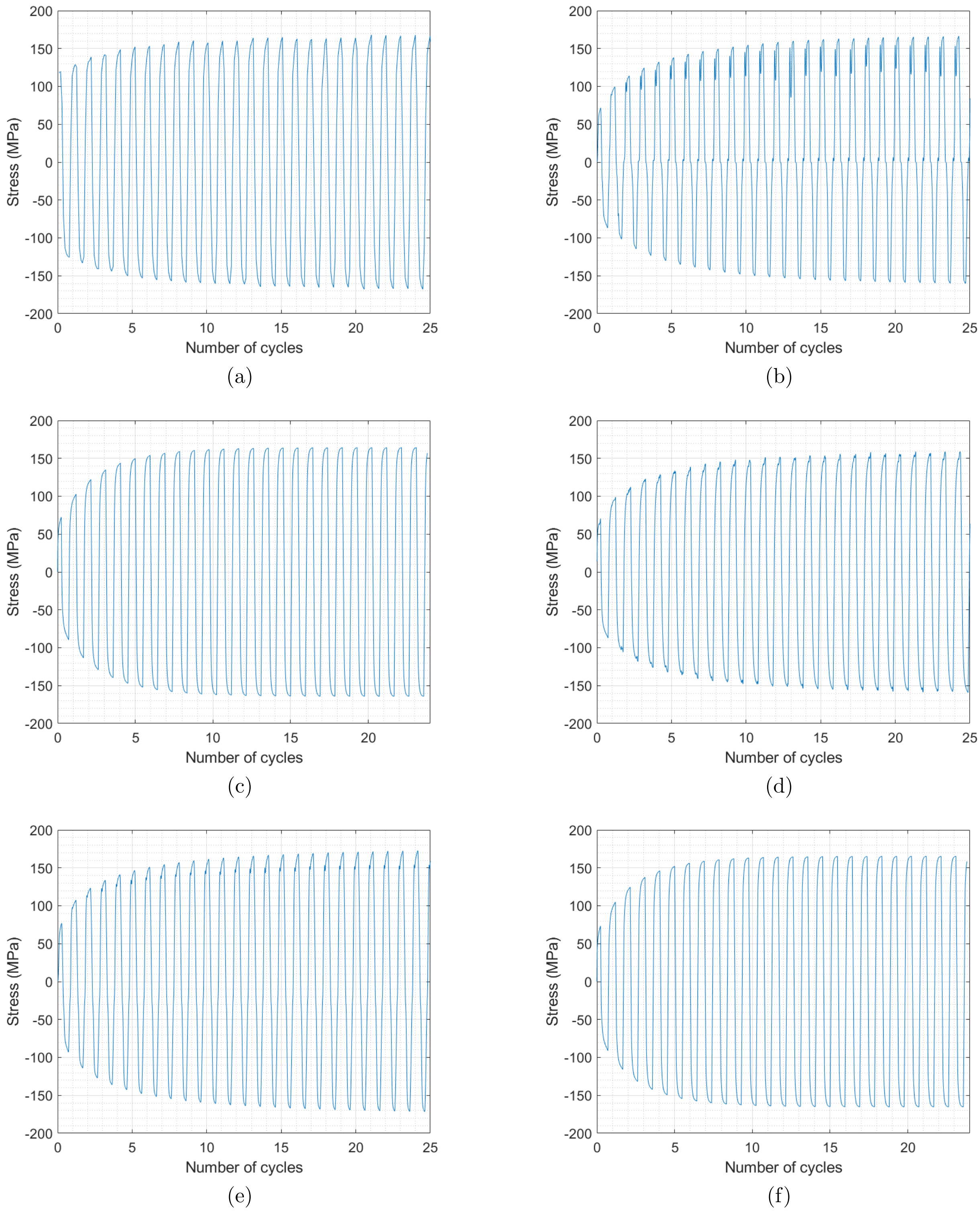

Figure 6.2: (a) Copper annealed at 600^{o}C test 1 experimental result; (b) copper annealed at 600^{o}C test 2 experimental; (c) simulation using parameters fitted to copper annealed at 600^{o}C experimental results; (d) copper annealed at 700^{o}C test 1 experimental result; (e) copper annealed at 700^{o}C test 2 experimental; (f) simulation using parameters fitted to copper annealed at 700^{o}C experimental results.

The conventional testing results for the 600^{o}C anneal can be seen in Figure 6.3. The kinks through zero load in the second test occurred due to the specimen bending during the test, which resulted in the top and bottom fixture not being aligned. As the testing machine is displacement controlled and the displacement is taken from averaging the displacements measured by two LVDTs (one on each side of the specimen) this particularly affects the test results around zero load, causing the kinks. The strain range in the first test (Figure 6.3 (a)) is about 0.05 % larger than the range in the second test (Figure 6.3 (b)), resulting in about 5 MPa larger stress for the first test (Figure 6.3 (c)) than for the second test (Figure 6.3 (d)). Overall, the results for the initial part of the cyclic response agree with the literature well (saturation stress of around 160 MPa), but they diverge when close to failure [167].

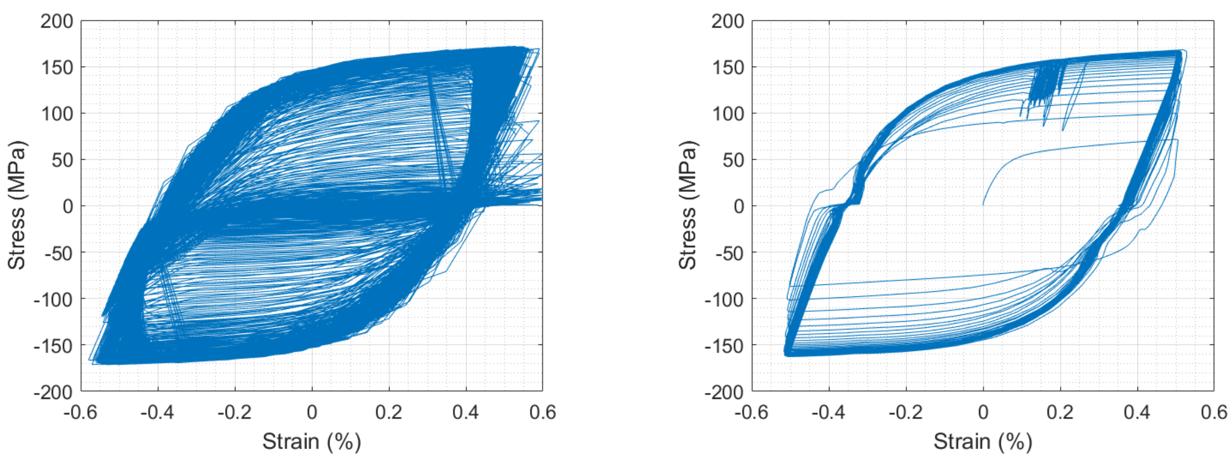

(a) (b)

Figure 6.3: Standard testing results of the 600^{o}C anneal (a) test 1 stress-strain; (b) test 2 stress-strain.

The results from the 700^{o}C anneal can be seen in Figure 6.4. The strain range in the second test (Figure 6.4 (b)) is about 0.04 % higher than in the first test (Figure 6.4 (a)), resulting in a saturation stress that was about 10 MPa larger for the second test (Figure 6.4 (d)) than for the first test (Figure 6.4 (c)). There appears to have been some issue with stress-strain recordings at around 0.075 % strain on the tensile side of the cycle. Overall, the saturation stress is about 40 MPa higher than reported in literature.

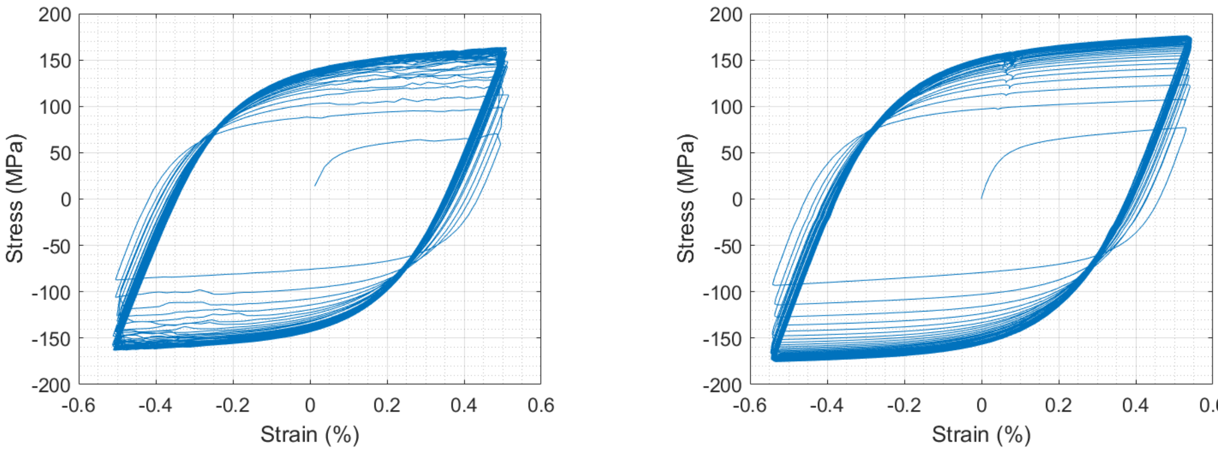

(a) (b)

Figure 6.4: Standard testing results of the 700^{o}C anneal (a) test 1 stress-strain; (b) test 2 stress-strain.

Selected cycles (cycle 1, cycle 5 and cycle 24) of the standard specimen test results and the fitted material model were compared as well. They were selected as cycle 1 shows how well the initial cyclic behaviour is fitted, cycle 5 shows how well the model represents the intermediate cycles and cycle 24 shows the stabilized cycles. For both anneals the results can be seen in Figure 6.5. For the 600^{o}C anneal the regularly shaped cycles fit well, for the 700^{o}C anneal the first cycle fits well and the later ones are slightly different, around the transitions between the straight lines specifically. Cycle 1 was not plotted for the 600^{o}C anneal test 1 because the results were significantly different from both FEA and test 2 and it was likely missing initial data points.

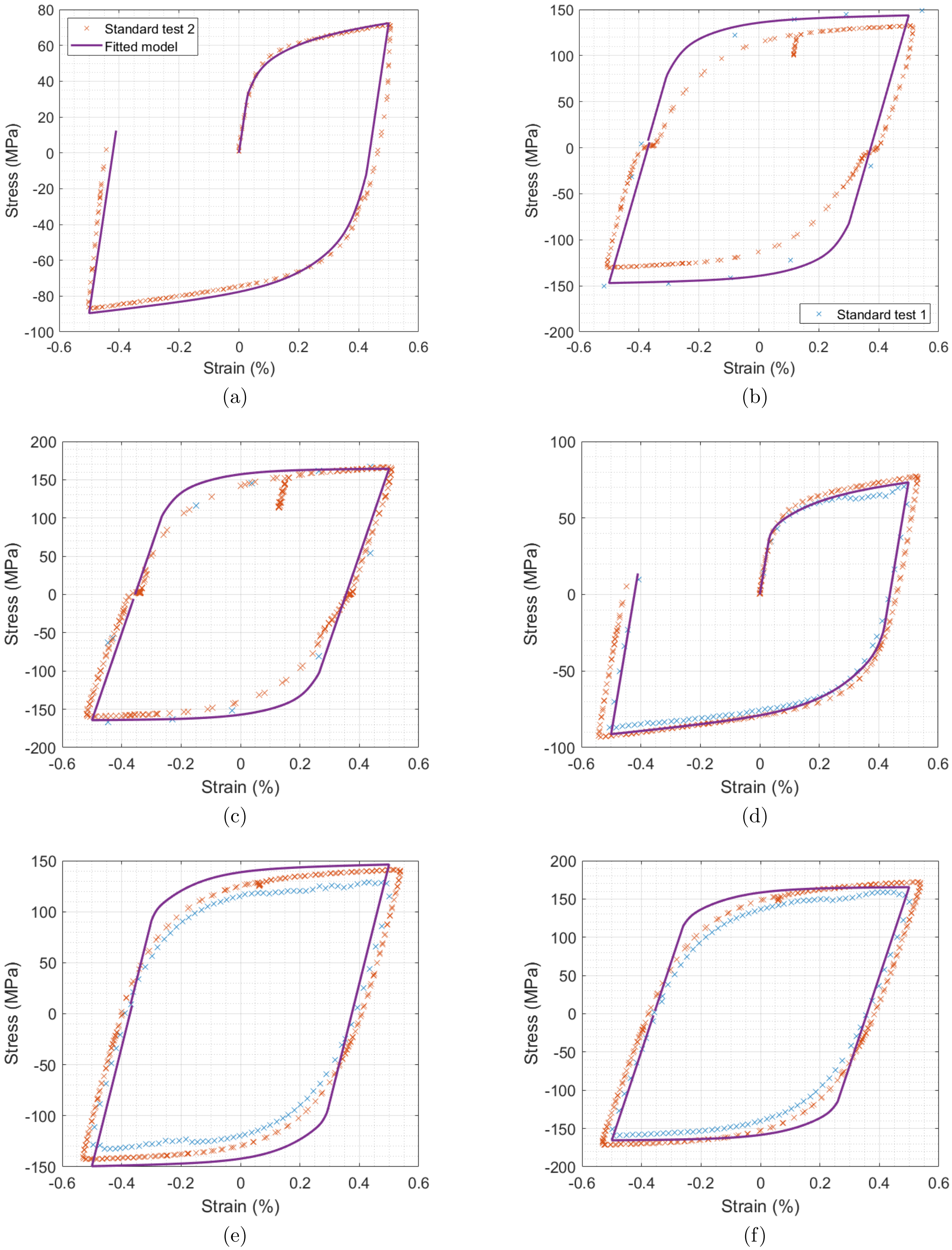

Figure 6.5: Comparison of selected cycles from standard test experimental results and simulations using parameters fitted to those results (a) 600^{o}C anneal cycle 1; (b) 600^{o}C anneal cycle 5; (c) 600^{o}C anneal cycle 24 (stabilized); (d) 700^{o}C anneal cycle 1; (e) 700^{o}C anneal cycle 5; (f) 700^{o}C anneal cycle 24 (stabilized).

The material model parameters fitted to the experimental results are summarized in Table 6.1. Poisson's ratio was taken from a datasheet as opposed to experimentally investigated, a sensitivity study for it was done, details are shown in Section 6.4.

Table 6.1: Combined hardening material model parameters fitted to conventional experimental data.

Anneal temperature (^{o}C)	E (GPa)	σ_y (MPa)	C (GPa) (1; 2)	γ (1, 2)	b_i	Q_∞ (MPa)
600	113.2	32	15.25; 60.93	820; 5313	23.44	101.45
700	116.6	37.6	72.47; 17.75	16870; 885.5	24.65	102.31

The step used was static general, with non-linear geometry enabled, due to large deformations occurring during the analysis. Time period (the duration of the step) was set in order to define how many cycles of loading should be completed. Static general step neglects inertia effects and time dependent effects, but takes rate dependent effects into account. This step was suitable because the accelerations during small ring specimen cyclic testing are small, making inertia effects appropriate to ignore, and creep is not being taken into account. The amplitudes are tabulated, with the amplitude for the clamp being shifted due to it being displaced in the first step in order to clamp while the pin is stationary.

Surface-to-surface contact was set up between the ring and the pin, with the pin being the master surface as it is stiffer than the ring and the ring being the slave surface due to being less stiff. Sliding formulation was finite sliding, as it continuously tracks which parts of the master surface are in contact with which parts of the slave surface. Discretization method was surface to surface, as two smooth surfaces are in contact with each other. Surface smoothing was enabled due to surfaces being circular. The effect of coefficient of friction was investigated for a set clamping displacement, it is discussed in Section 6.4. The majority of simulations were done with a coefficient of friction set to 0.4, apart from the ones investigating its effects. Normal behaviour was set up as "Hard" contact, same as for the small ring tensile modelling, due to the same reasons. Surface-to-surface contact was also set up between the ring and the clamp, with the clamp being the master surface as it is stiffer and the ring being the slave surface due to being less stiff. All other features are identical to those used in the ring to pin contact.

Deformation is set up using boundary conditions. There are symmetry boundary conditions set up on all planes of symmetry. The pin is displaced and therefore the ring is deformed by applying a displacement boundary condition onto the reference point of the pin. A clamping load is applied by displacing the clamp while the pin is kept stationary and squashing the ring between them by a set displacement value. Both the pin and the clamp are only allowed to move vertically. When the cyclic load is applied, both the pin and the clamp move in phase. The displacements prescribed depend on what experimental amplitude the results are being compared to.

Element size chosen for the ring was about 0.2 mm x 0.2 mm x 0.2 mm, resulting in 5 elements across the thickness of the ring. This size was determined to be appropriate according to a mesh density study shown in Figure 6.6 (a). As the force-displacement curve for 5 elements is smooth (apart from spikes in force in the first cycle, caused by the nodes coming into contact as the small ring specimen is loaded) and does not differ from the larger number of elements, showing convergence. Mesh controls were set up to a structured mesh with hex elements. The elements used were Standard 3D stress elements that were quadratic, with reduced integration (C3D20R), due to them being suitable for modelling curved surfaces. An example mesh can be seen in Figure 6.6 (b).

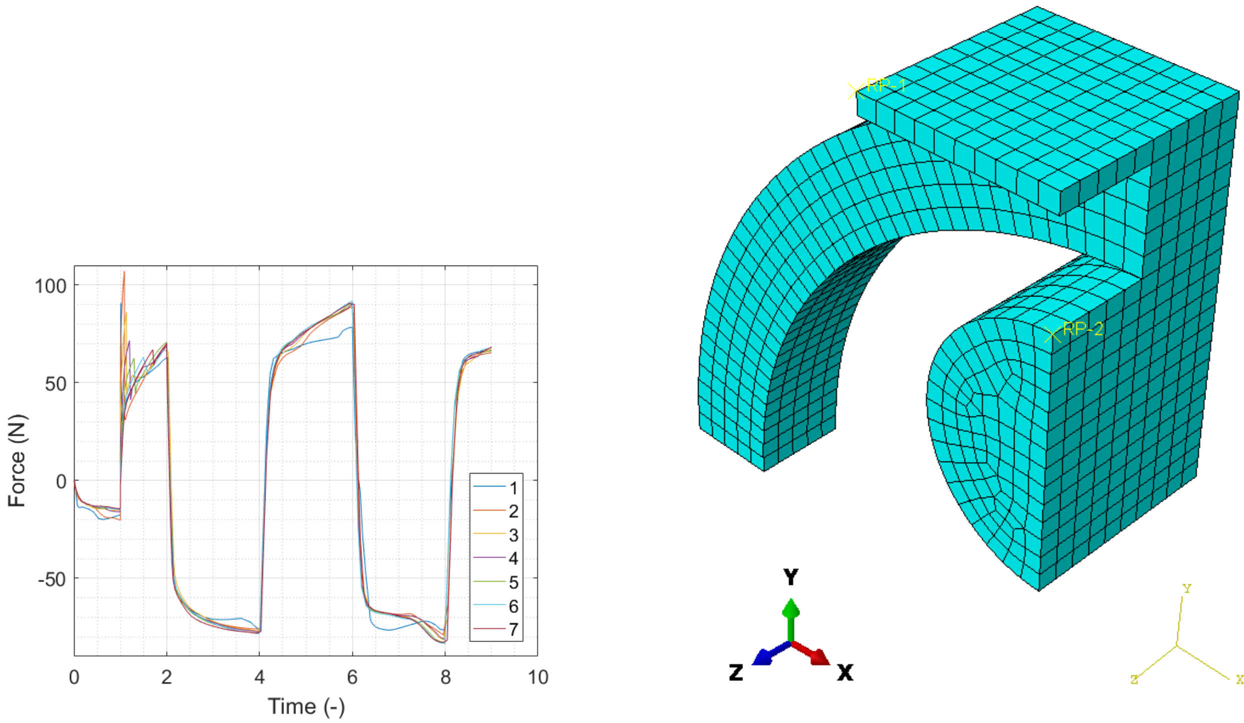

(a) (b)

Figure 6.6: (a) Mesh convergence study, with the number of elements across the ring in the legend; (b) Meshed 1/8th FEA model.

6.2.2 Full Ring 3D Model

The full ring model was developed in order to investigate the effect of misalignment. When the pins are misaligned with respect to the ring the whole setup becomes asymmetric and makes the 1/8th model not suitable.

The model consists of two pins, two clamps, and a ring. The ring has an inner radius of 4.5 mm, outer radius of 5.5 mm and thickness of 2 mm, the same as the small ring specimen used for testing. The pins have a radius of 1.25 mm and a length of 4 mm, the clamps have a length and width of 4 mm and a thickness of 0.2 mm. All are modelled as deformable bodies, as in the 1/8th model. The model itself can be seen in Figure 6.7.

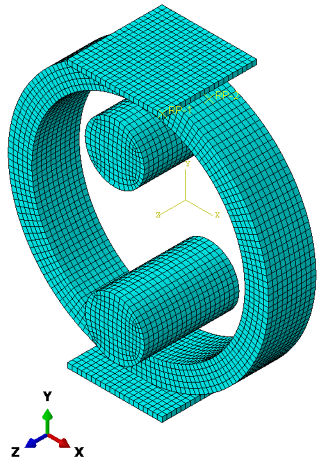

Figure 6.7: Full ring cyclic model.

The material model used was the combined hardening model. Static general step with non-linear geometry enabled was used, with the time period set according to the number of cycles needed. The contact between the pins and the ring, as well as the clamps and the ring, was set up as surface-to-surface contact, with pin surfaces and clamp surfaces as master surfaces and ring surfaces as slave surfaces. The sliding formulation was finite sliding, discretization method was surface to surface. Due to the ring and the pins being circular, surface smoothing was enabled. Tangential behaviour was set to be 0.4 coefficient of friction, as friction would have an effect when the pins are misaligned and 0.4 is a realistic coefficient of friction. Normal behaviour was set up as "Hard" contact.

The boundary condition for the bottom pin is encastre, as it stays stationary during testing, and the bottom clamp is displaced vertically during the first step, then kept stationary for the cyclic loading. The top pin is kept stationary during the first step, while the top clamp is displaced vertically to clamp the ring, then in the second step they move in phase applying cyclic loading. The element size and type was the same as for the 1/8th model, about 0.2 mm x 0.2 mm x 0.2 mm, with 5 elements across the radial thickness and 10 along the lateral thickness. The elements used in the model were C3D20R.

6.3 Preliminary Modelling Analysis

This section provides a detailed discussion of the reason for the spikes in the simulated force values, the accuracy of the FEA model described in Section 6.2, by comparing the simulated test results to experimental test results. The evolution of equivalent gauge length and section, as defined in Section 4.2.3 was investigated to see how much of an effect rate dependency could have.

The previous section showed that there are spikes in the force-time curves of the small ring specimen due to the nodes coming into contact. Figure 6.8 shows what happens when cyclic loading is applied. Some nodes come into contact properly (the rightmost ones), while the nodes further away from the right edge are offset between the ring and the pin, causing the oscillatory stiffness. This offset is dependent on the material properties used in the model, therefore a non-material specific mesh which does not have those spikes cannot be found.

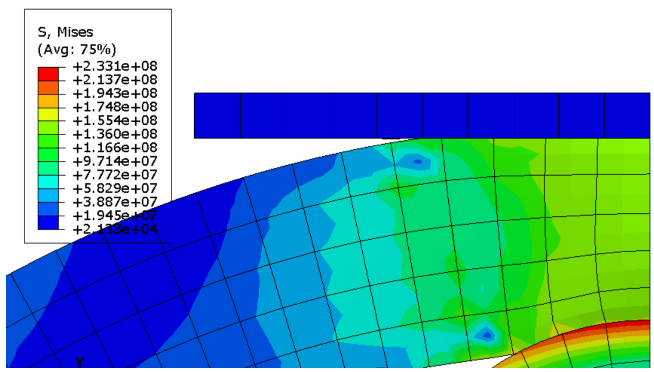

Figure 6.8: Illustration of nodes coming into contact with other nodes during cyclic small ring specimen loading.

Figure 6.9 shows the comparison of force-time results acquired from cyclically loading a small ring specimen and FEA simulations by using material model parameters fitted to the conventional test results. For the 600^{o}C anneal the simulated peak tensile and compressive loads are 75 N and 70 N respectively, while the experimental peak loads are 140 N and 95 N. For the 700^{o}C anneal the simulated peak tensile and compressive loads are 72 N and 65 N respectively, while the experimental peak loads are 130 N and 90 N. The simulated peak loads are significantly lower than experimental peak loads, which continues as the loading progresses as well. The 600^{o}C anneal has higher peak loads both experimentally and as simulated. Due to such significant differences further comparison of the experimental and simulated results was not performed.

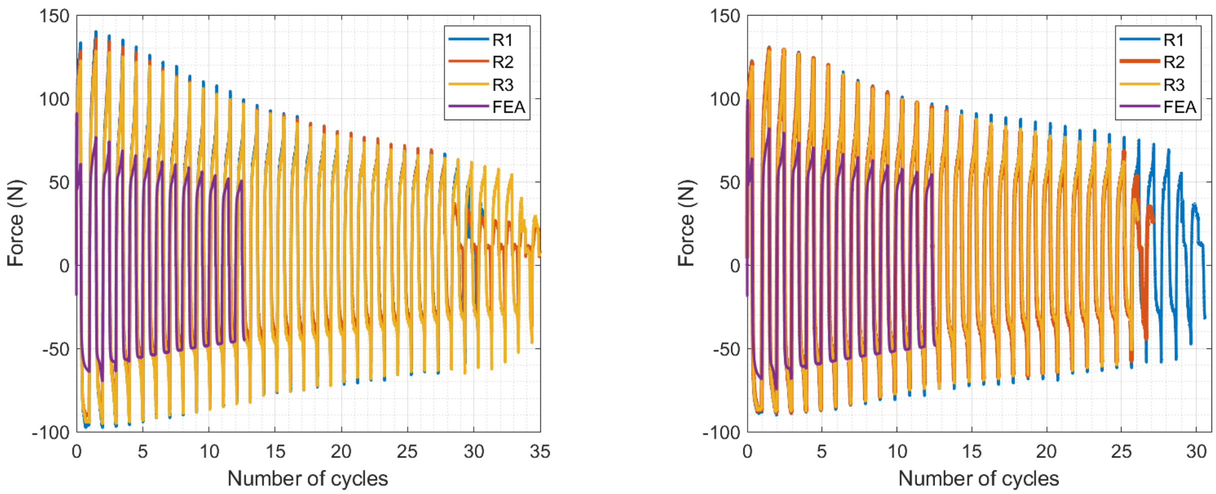

(a) (b)

Figure 6.9: Force-time curves from FEA modelling of (a) 600^{o}C anneal fit and experimental results; (b) 700^oC anneal fit.

Similarly to the modelling of small ring specimen under tensile load, the evolution of gauge length and section was investigated during cyclic loading, the resulting plots are shown in Figure 6.10. The values were acquired in the same way as described in Chapter 4. If both the strain and displacement are negative, or if both are positive then the equivalent gauge length is positive. If the strain is negative but displacement is positive, the equivalent gauge length is negative. When the strains are small with respect to displacement the equivalent gauge length is large and when the strain goes through zero and switches signs from negative to positive the equivalent gauge length switches from a large negative value to a large positive value. As the number of cycles increases strain switches signs at increasingly positive displacement. Also, tensile strains are higher than compressive strains and as the number of cycles increases tensile strains reduce then increase, while compressive strains consistently reduce. In general the curves in the top right are similar to the equivalent gauge length graphs in Section 4.2.3. This variation in equivalent gauge length of more than 5 times during the cyclic loading suggests that small ring specimen cyclic testing is not suitable for strain rate sensitive materials.

Unlike equivalent gauge length, which is plotted against the value it is calculated from, equivalent gauge section is plotted against displacement as opposed to force. This was done as the force range varies during cyclic loading, while the displacement amplitude remains constant. As the number of cycles increases equivalent gauge section reduces, which makes sense as the forces go down as the number of cycles increases. The values outside of the range of 0 mm^2 to 0.5 mm^2 are caused by small stresses in the first cycle and loss of contact in later cycles. The discontinuity in the first cycle arises from the force changing sign (negative to positive) before the stress changes sign in the first cycle, causing a sudden drop of equivalent gauge section around zero displacement, then it abruptly changes sign due to the stress changing sign as well and jumps to a positive value.

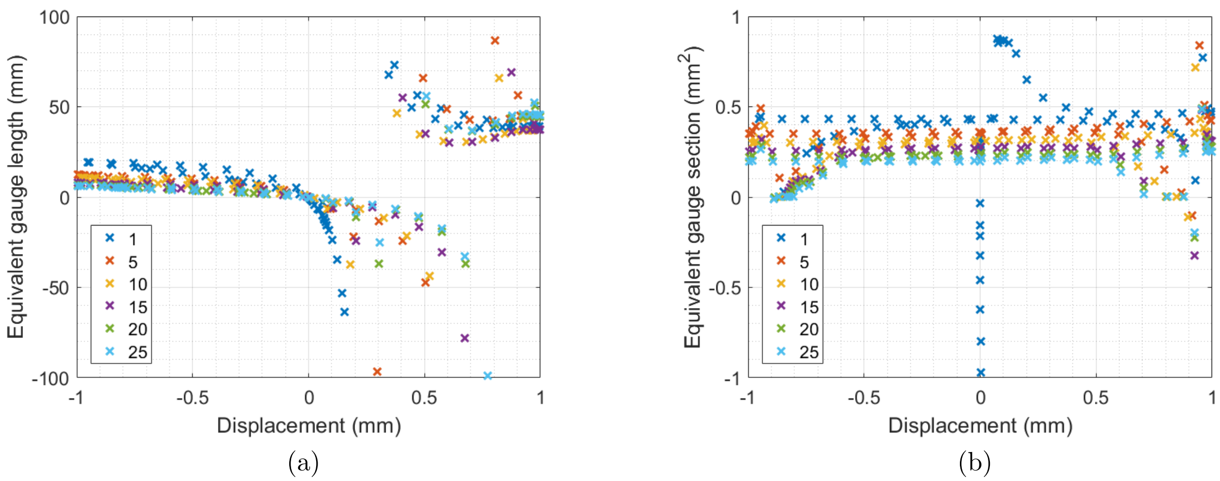

Figure 6.10: The evolution of (a) equivalent gauge length as the number of cycles increases; (b) equivalent gauge section as the number of cycles increases.

6.4 Varied Material and Geometry Parameters

It is important to evaluate how varying material parameters and geometry parameters influences the small ring specimen test results. The effects of constitutive behaviour are important for developing a method to calculate bulk material stress-strain behaviour, while the effect of coefficient of friction shows if it is a significant contributor to the deformation and therefore a potentially significant source of error in test results. While geometry parameters were not varied experimentally, it is important to know how they would affect the test results, as changing them could affect the sensitivity to certain material model parameters, making the calculation of bulk material behaviour easier and more reliable.

6.4.1 Material

The combined hardening material model parameters and the coefficient of friction were varied in order to see how they would affect the results of the small ring specimen tensile FE analysis and to provide a direction for making a method to interpret the experimental data. The parameters varied were Young's modulus, yield stress, parameter C, parameter γ, parameter Q_∞, parameter b, Poisson's ratio and the coefficient of friction. They were varied one at a time, while keeping the other parameters constant to evaluate the magnitude of the effect of each parameter.

Young's modulus was varied between 50 GPa (applicable for tin) and 190 GPa (applicable for wrought iron), the effects of this variation on the small ring cyclic force-number of cycles and force-displacement curves can be seen in Figure 6.11. Unlike in the tensile modelling, in cyclic modelling Young's modulus affects only the slopes of the elastic loading in the first cycle and elastic unloading during cycling. Increasing the Young's modulus increases the slopes, while decreasing the Young's modulus decreases the slopes and the area enclosed by the hysteresis loops. The peak loads are not affected at all, the hardening curve for the around 0.5 mm before the peak load is not affected either.

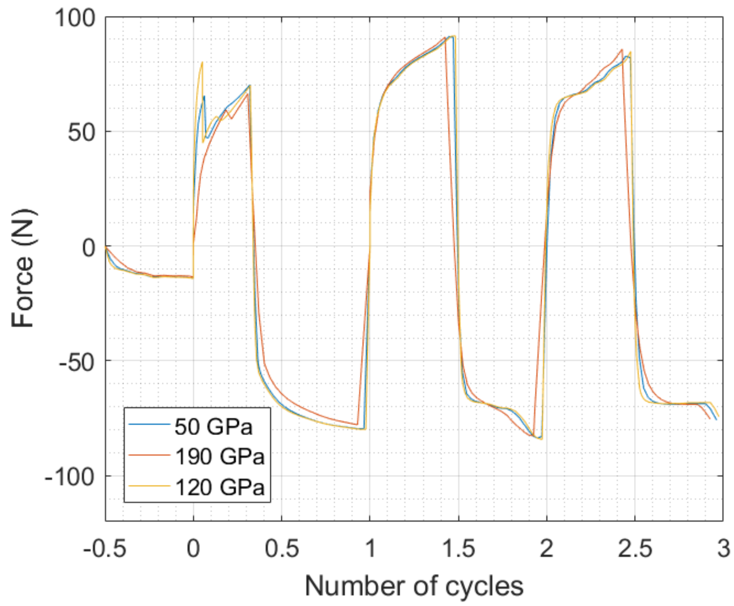

(a)

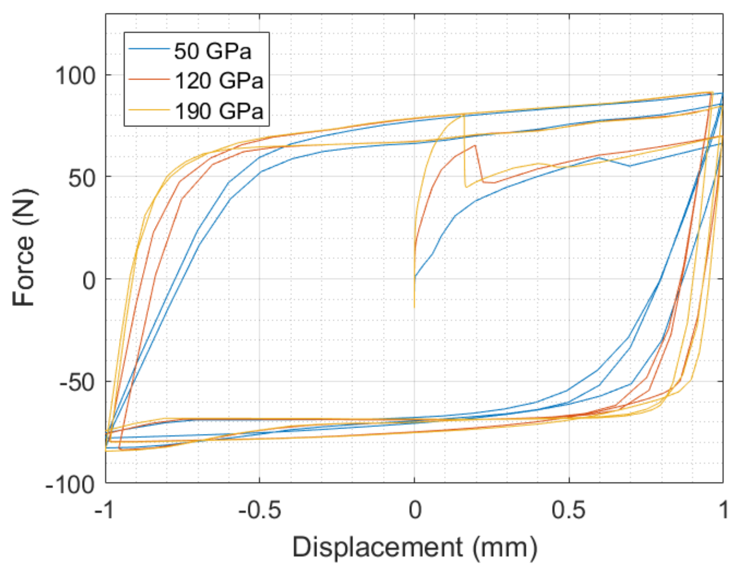

(b)

Figure 6.11: The effect of varied Young's modulus on small ring cyclic (a) force-number of cycles results; (b) force-displacement results.

As for the yield stress, it was varied between 30 MPa (applicable for the annealed copper used in this project) and 370 MPa (applicable for structural stainless steel) with the effects on the force-number of cycles and force-displacement curves shown in Figure 6.12. It does not affect the unloading slopes, unlike Young's modulus, however it affects the length of those slopes, as increasing yield stress increases the length of them. The slope of the hardening curve leading to the peak load is also affected, with the higher yield stress resulting in a steeper slope. This suggests that as the cyclic loading progresses, a greater proportion of the ring section yields.

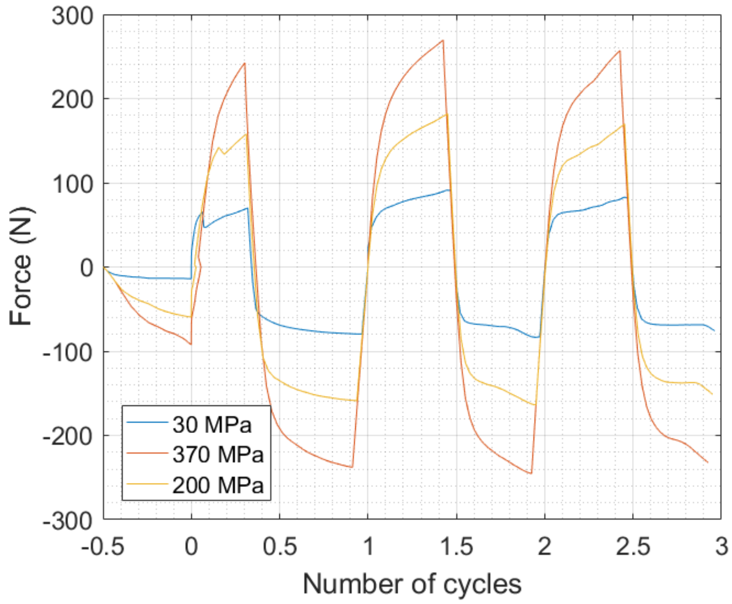

(a)

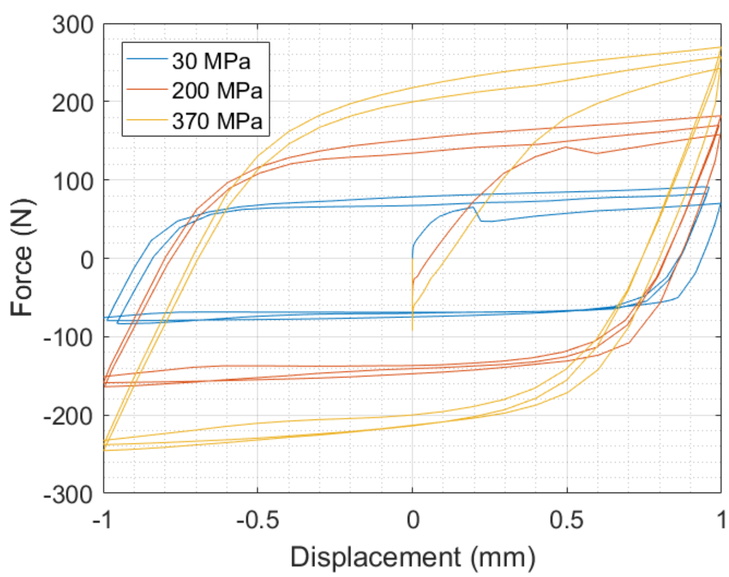

(b)

Figure 6.12: The effect of varied yield stress on small ring cyclic (a) force-number of cycles results; (b) force-displacement results.

The magnitude of the effect of varied C is very dependent on the magnitude of the isotropic hardening component as well. If the isotropic component is significantly larger, then the variation in the kinematic parameters would not have an effect, however, if there is an effect the general trends would be the same no matter what the isotropic component is, as the signs in the combined hardening equations remain the same. The effects of varied parameter C, when it is varied between the values of 20 MPa and 100 GPa, are shown in Figure 6.13. Increasing C increases the peak loads and the plastic hardening part of the curves, there is no effect on the linear unloading part of the curves.

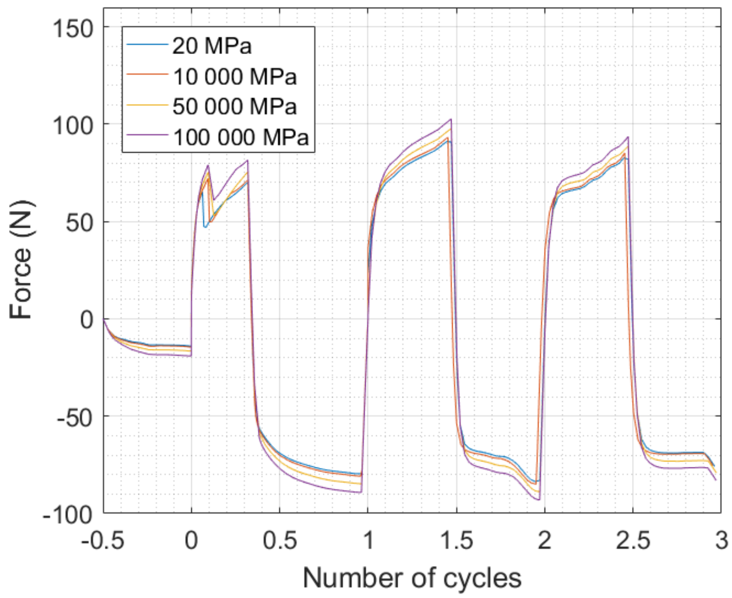

(a)

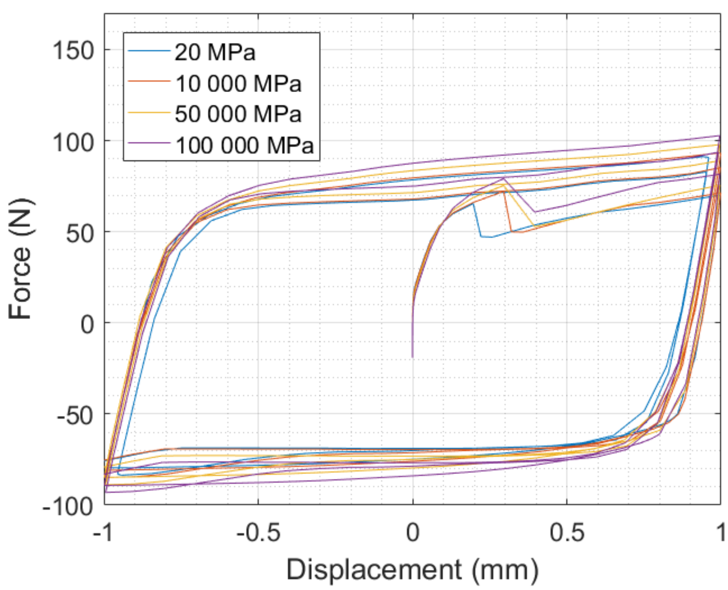

(b)

Figure 6.13: The effect of varied parameter C on small ring cyclic (a) force-number of cycles results; (b) force-displacement results.

The effects of varying parameter γ between 500 and 1500 on the small ring specimen force-number of cycles and force-displacement curves are shown in Figure 6.14. As γ is a part of the kinematic components of the combined hardening model, it would also not have an effect on the small ring results if the isotropic components is significantly larger than the kinematic component. Generally increasing γ reduces the peak loads and lowers the plastic hardening part of the curves, which is the opposite to the effect of parameter C.

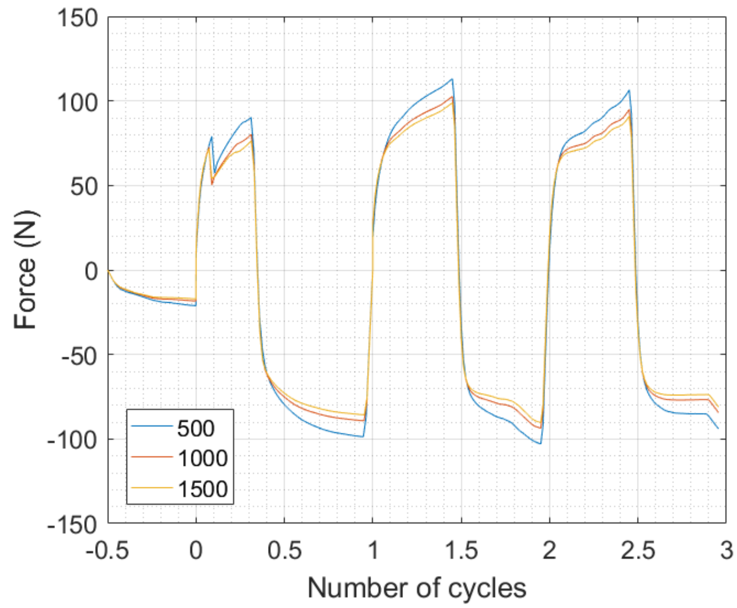

(a)

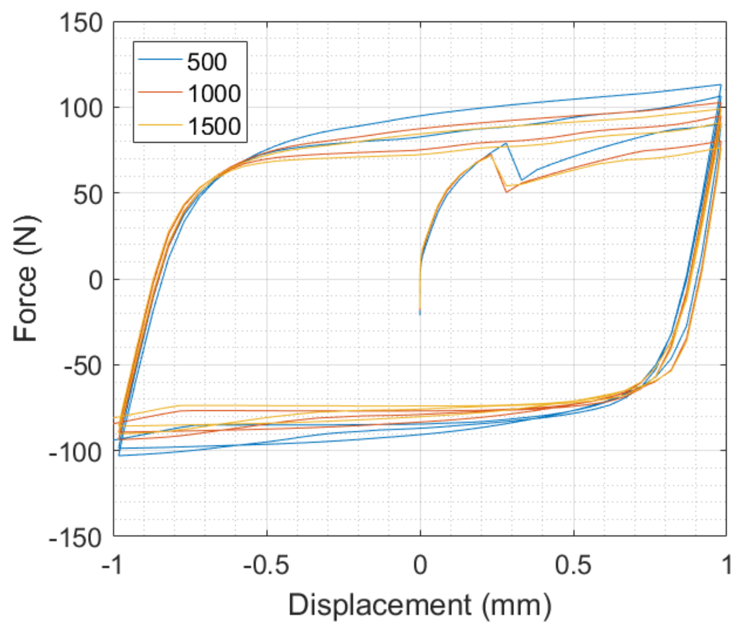

(b)

Figure 6.14: The effect of varied parameter γ on small ring cyclic (a) force-number of cycles results; (b) force-displacement results.

Similarly to how varying the coefficients in the kinematic part of the combined hardening model can have no effect if the isotropic component is significantly larger, varying the coefficients of the isotropic part of the combined hardening model can have no effect if the kinematic components are significantly larger. Ensuring that varying Q_{∞} has an effect and varying it between 150 MPa and 350 MPa has the effect on the force-number of cycles and force-displacement curves shown in Figure 6.15. Increasing Q_∞ increases peak loads and makes the line leading up to the peak load steeper.

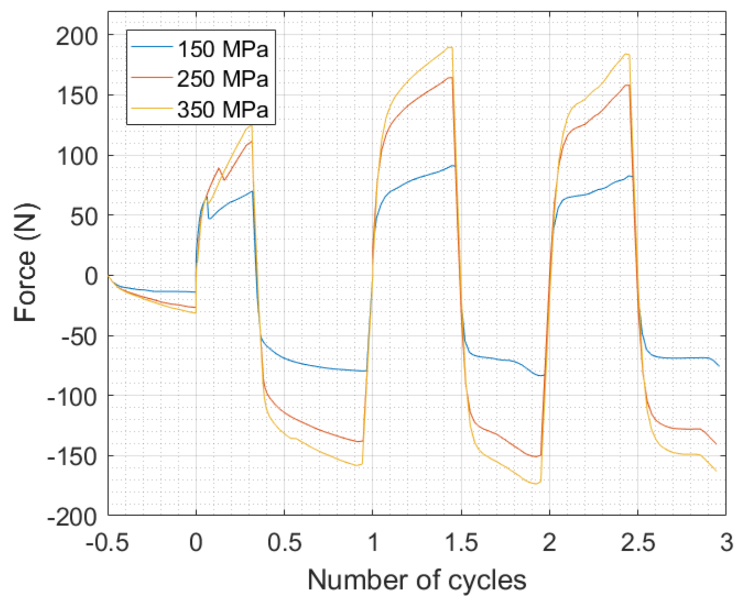

(a)

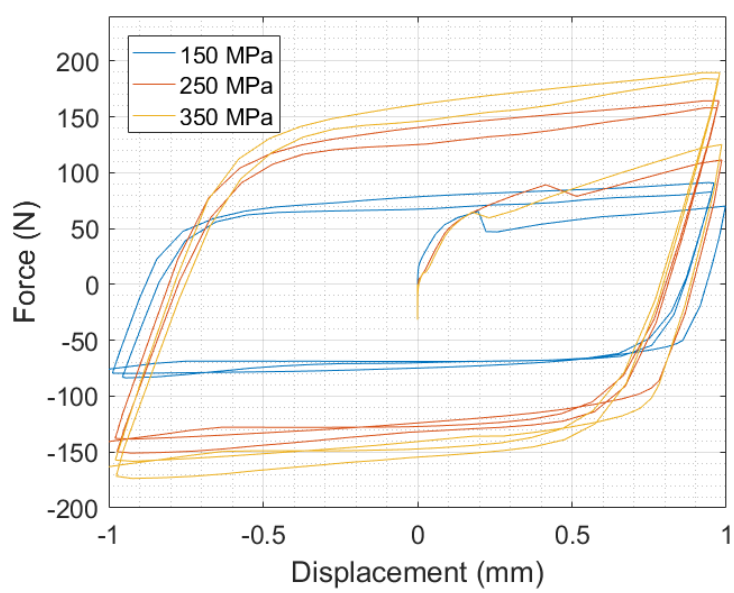

(b)

Figure 6.15: The effect of varied parameter Q_∞ on small ring cyclic (a) force-number of cycles results; (b) force-displacement results.

As parameter b is also a coefficient in the isotropic part of the combined hardening model, varying it would have no effect if the kinematic part is too large. Figure 6.16 shows the effect of varying parameter b between 5 and 70 on the force-number of cycles and force-displacement curves. It can be seen that increasing b raises the peak load and the plastic hardening part of the curves. It also changes the shape of the compressive part of the curves, from a smooth increase to the peak load to a smooth increase to a steep slope to the peak load, seen particularly well at the values of b at 40 and 70 and cycle 2, however, this effect could be caused by this specific combination of combined hardening parameters and should not be used to infer that if such features exist in the force-number of cycles curve the value of b is high.

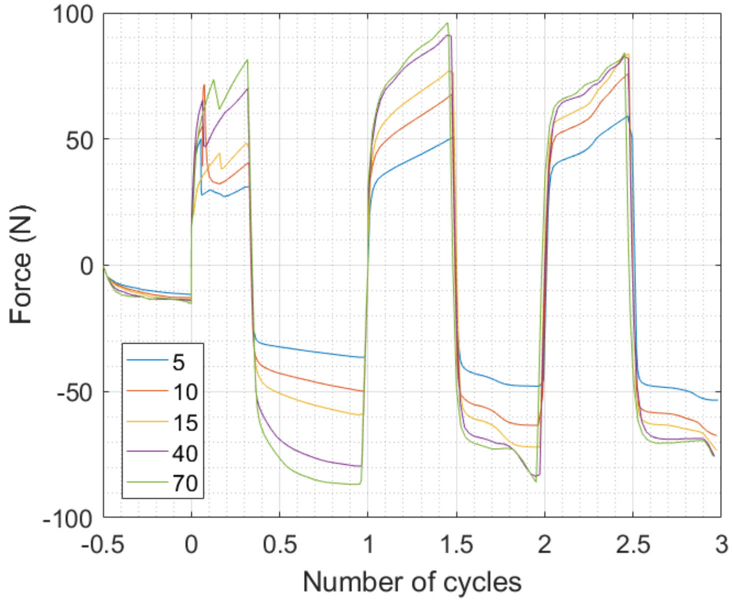

(a)

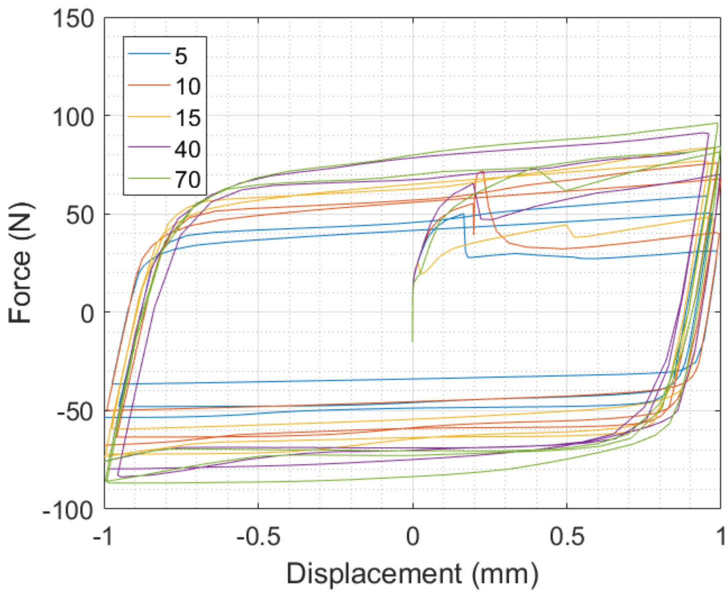

(b)

Figure 6.16: The effect of varied parameter b on small ring cyclic (a) force-number of cycles results; (b) force-displacement results.

The effect of Poisson's ratio varied between 0.2 and 0.4 on the force-number of cycles and force-displacement curves can be seen in Figure 6.17. The effect is minimal, therefore it can be stated that an accurate value of Poisson's ratio is not necessary for an accurate simulation of the force-number of cycles and force-displacement behaviour.

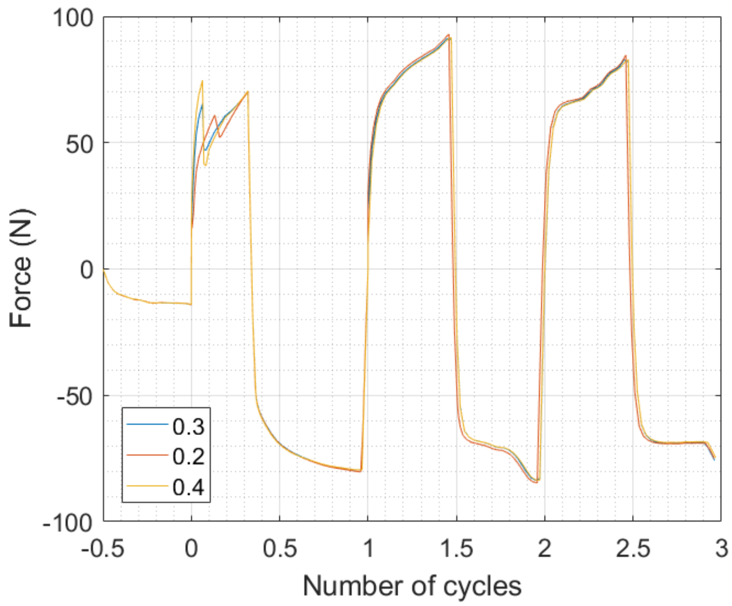

(a)

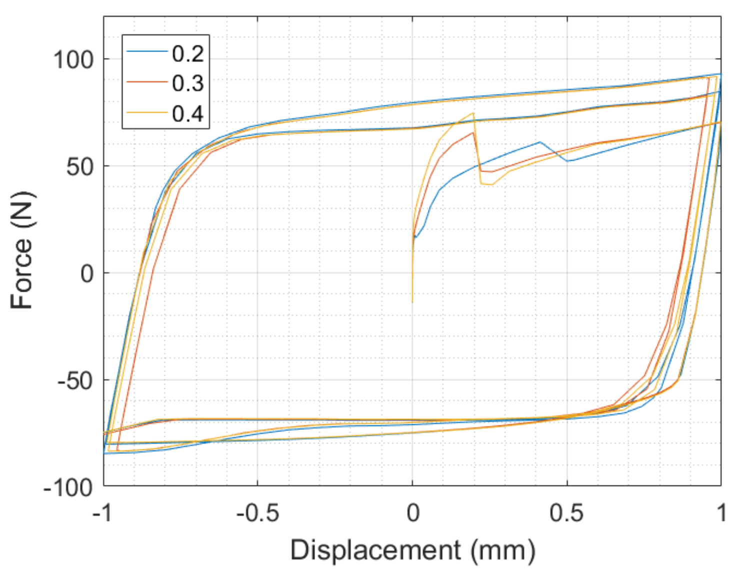

(b)

Figure 6.17: The effect of varied Poisson's ratio on small ring cyclic (a) force-number of cycles results; (b) force-displacement results.

The coefficient of friction was varied between frictionless behaviour and 1, the effect of this variation on the force-number of cycles and force-displacement curves is shown in Figure 6.18. The effect is significantly larger than the effect of varied coefficient of friction on small ring specimen tensile results, which is likely caused by the presence of clamping, as it increases the area of contact and introduces a new contact, between the ring and the clamp. Higher coefficients of friction result is less relative movement of the surfaces in contact, which causes higher peak loads and changes the shape of the curves. This suggests that lubricating the rings would affect the test results significantly, however, as the loading progresses the lubricant could get squeezed out from the contact area, which would change the coefficient of friction during the test and make the results less accurate. It would be advisable to test the specimens unlubricated, as then the change in coefficient of friction during loading would be less likely.

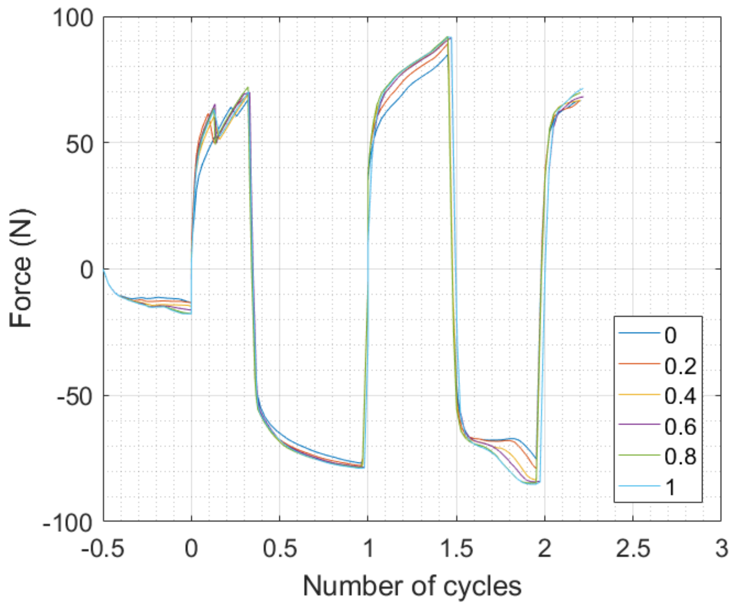

(a)

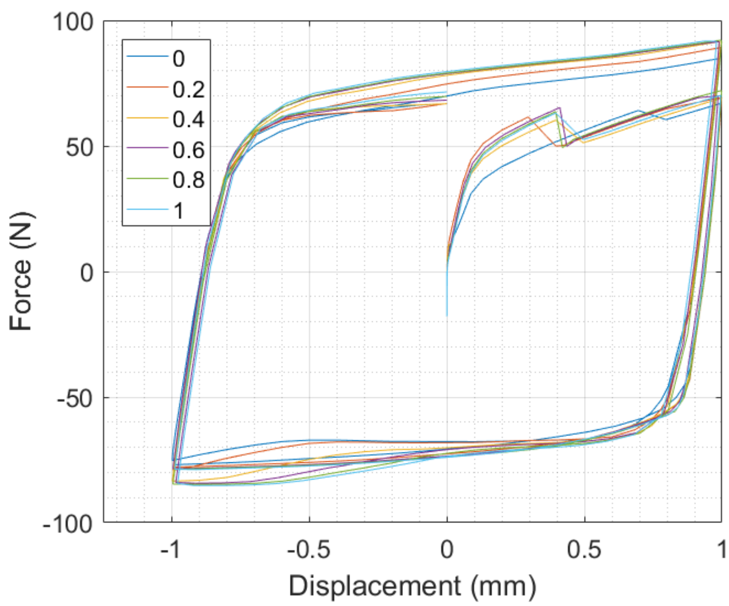

(b)

Figure 6.18: The effect of varied coefficient of friction on small ring cyclic (a) force-number of cycles results; (b) force-displacement results.

Overall, due to the nature of the combined hardening model, apart from the effect of Young's modulus, all other parameters affect the force-displacement results in the same way, with only the relative magnitudes of the coefficients influencing the significance of the effects. No parameters apart from Young's modulus affecting the linear unloading regions suggests that those regions are elastic-only, or close to elastic-only. Poisson's ratio has a negligible effect and the coefficient of friction is significant.

6.4.2 Geometry

The geometry parameters of the small ring cyclic testing setup were varied in order to see how it would affect the sensitivity of the test and to provide a direction for improvements to the setup for future testing depending on what specific part of the response is of interest. The ring parameters varied were the radius at load application making the ring elliptical vertically before it is deformed, also the radial thickness (the difference between the outer and inner radius of the ring), lateral thickness making the cross-section differently proportioned and the test parameters: the clamping displacement and the loading amplitude. The parameters were varied one at a time, while keeping the other parameters constant to evaluate the magnitude of the effect of each parameter.

Unlike tensile small ring specimen modelling, the effect of making the ring into horizontal ellipse was not investigated, as this would reduce the available maximum displacement amplitude due to the necessity for the pins to be closer together. The effect of using elliptical pins was also not investigated, as the investigation into the effects on the tensile small ring results did not show a significant effect, they would also be difficult to make and use.

The radius of the ring at load application (parameter b in Figure 4.4 (a)) was varied between 5 mm and 7 mm making the ring into a vertical ellipse before loading begins. The effects of this variation can be seen in Figure 6.19. Higher radius and a more elliptical ring results in lower peak loads, however the effect is small, as for a 2 mm increase in the radius the force is reduced by 10 N at most. This is promising as using an already elliptical ring would increase the maximum displacement amplitude, which could allow for a more thorough investigation into the fatigue life of the specimen. This observation also agrees with the similar observation made when the small ring specimen loaded in tension was modelled.

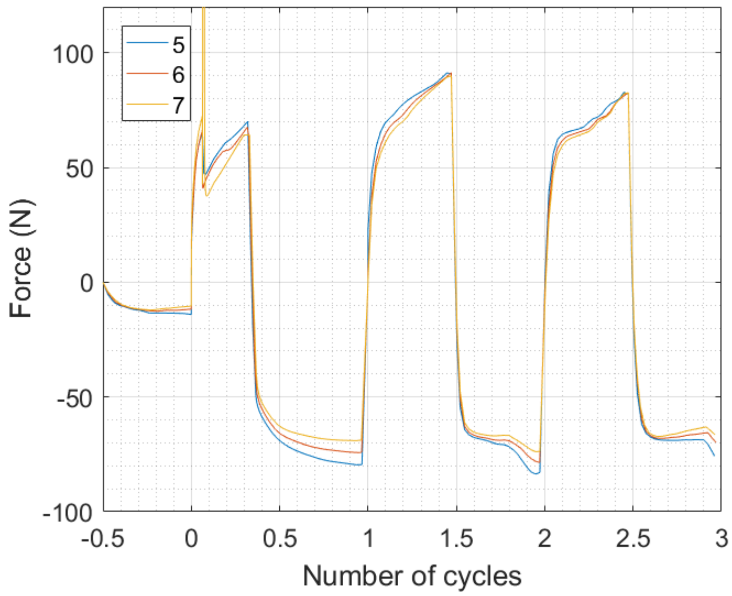

(a)

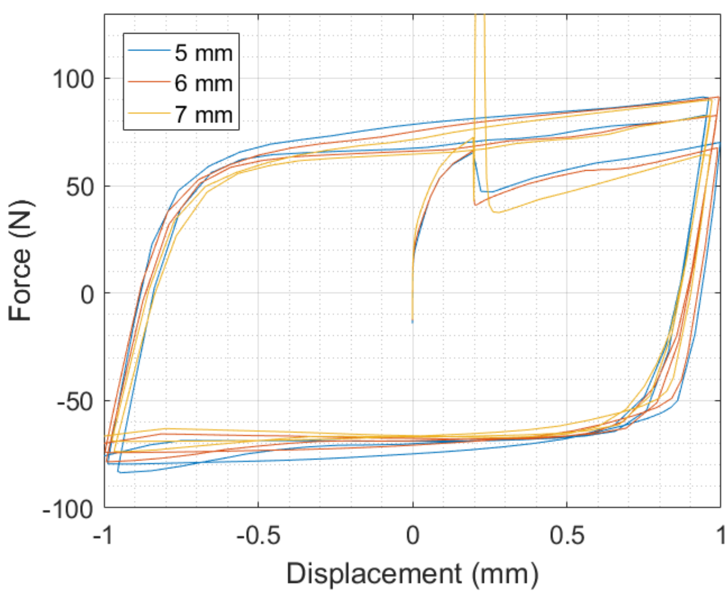

(b)

Figure 6.19: The effect of changing the ring into a vertical ellipse (varying the semi-major radius) shown in (a) force-number of cycles results; (b) force-displacement results.

Figure 6.20 shows the effect of the radial thickness varied between 1 mm and 1.5 mm on the small ring specimen force-number of cycles and force-displacement curves. Increasing the thickness results in steeper elastic unloading and higher tensile and compressive forces, however the slopes leading to the peak load appear to be unaffected.

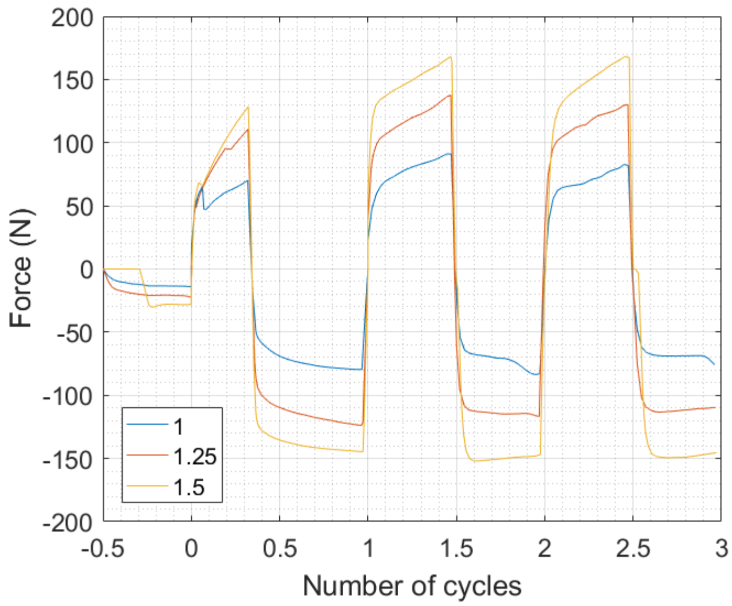

(a)

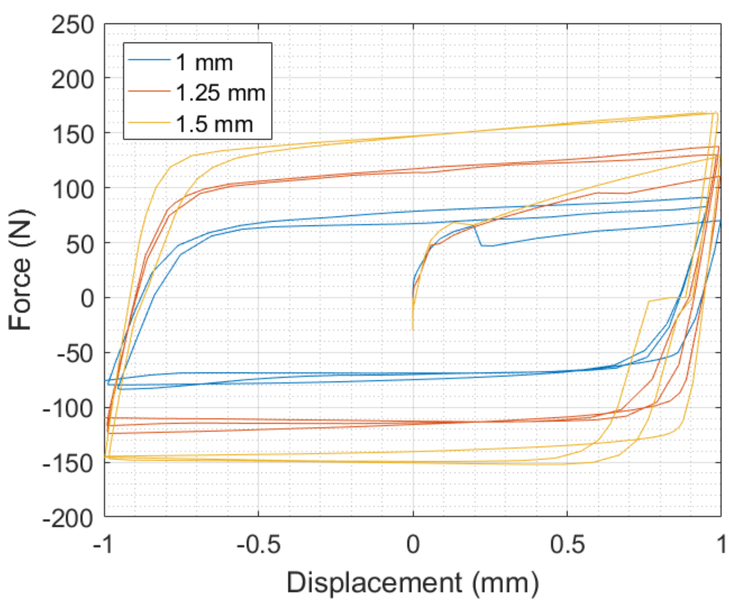

(b)

Figure 6.20: The effect of change in radial thickness shown in (a) force-number of cycles results; (b) force-displacement results.

Varying lateral thickness between 0.6 mm and 1.4 mm has the effect on the force-number of cycles and force-displacement curves that is shown in Figure 6.21. The effect of essentially the same as when radial thickness is varied.

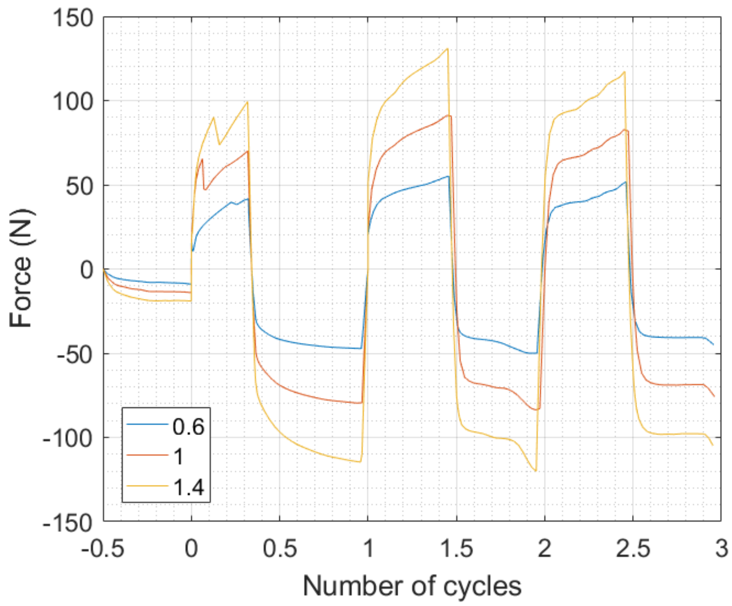

(a)

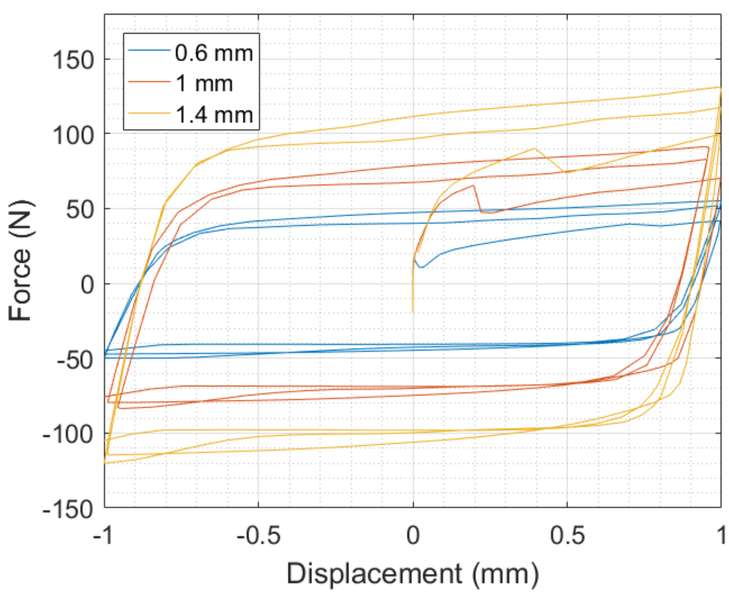

(b)

Figure 6.21: The effect of change in lateral thickness shown in (a) force-number of cycles results; (b) force-displacement results.

Moving on to the experimental parameters and how they affect the simulation results, the effect of varying the clamping displacement between 0.1 mm and 0.3 mm on the force-number of cycles and force-displacement results is shown in Figure 6.22. Clamping displacement has a significant effect, with higher displacement resulting in higher peak forces, and lower displacements resulting in negative stiffness in compressive cycles. The effects also appear to increase as the number of cycles increases. As it is unclear what applied clamping torque corresponds with what clamping displacement, this cannot be directly compared to experimental results.

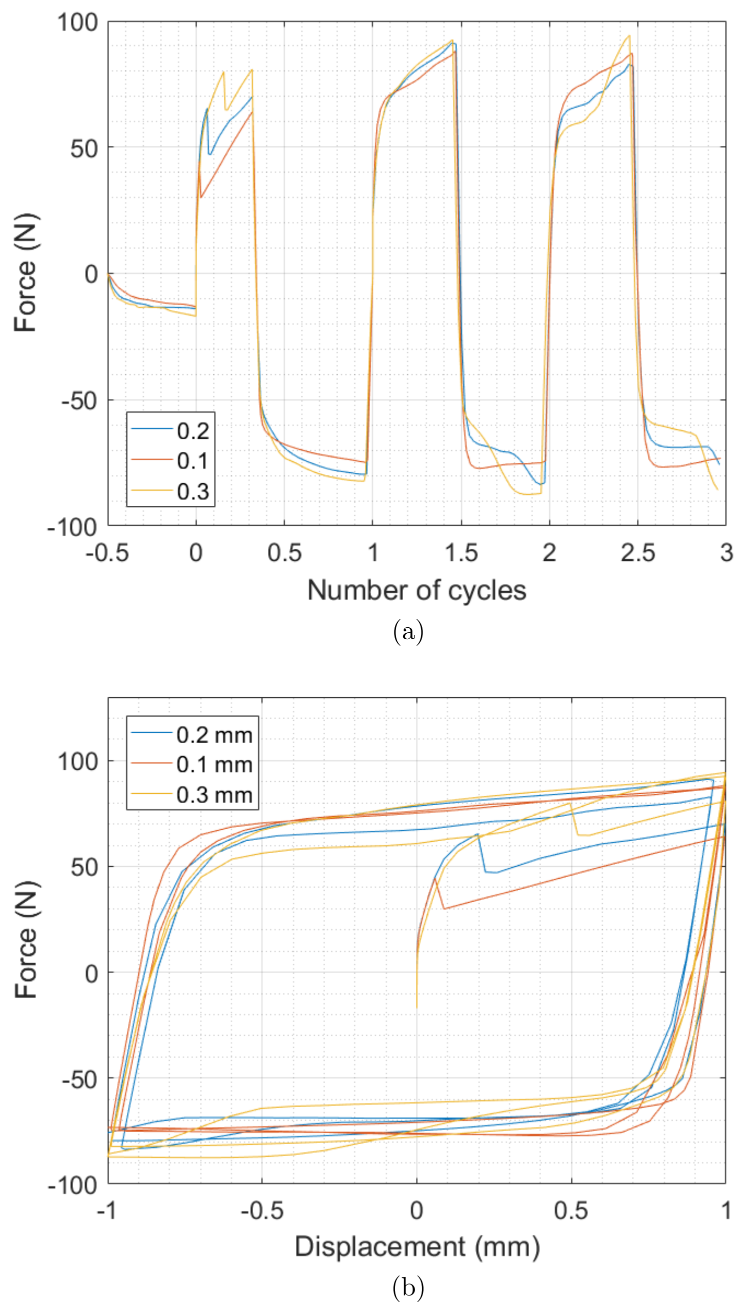

Figure 6.22: The effect of change in clamping displacement shown in (a) force-number of cycles results; (b) force-displacement results.

The effect of the loading amplitude depends on the material properties. If the low loading amplitude is elastic-only, and the higher loading amplitude goes into plasticity, the difference between the cyclic results is going to be very significant, as the elastic-only results might not even form a hysteresis loop. If the range of amplitudes is fully in the plastic region and the standard cyclic hardening curve is shallow, there might not be any effect of the variation of amplitudes on the small ring results. An intermediate situation is shown in Figure 6.23, where the loading amplitude is varied between 0.25 mm and 0.75 mm. In the first two cycles the higher loading amplitude results in higher peak loads, however, that effect essentially disappears in the third cycle. This could be due to the fact that some type of saturation stress-state is reached and the different loading amplitudes having no effect, however, this does not agree with the observation regarding varied yield stress, as that observation suggests that the material continues to yield as the loading progresses.

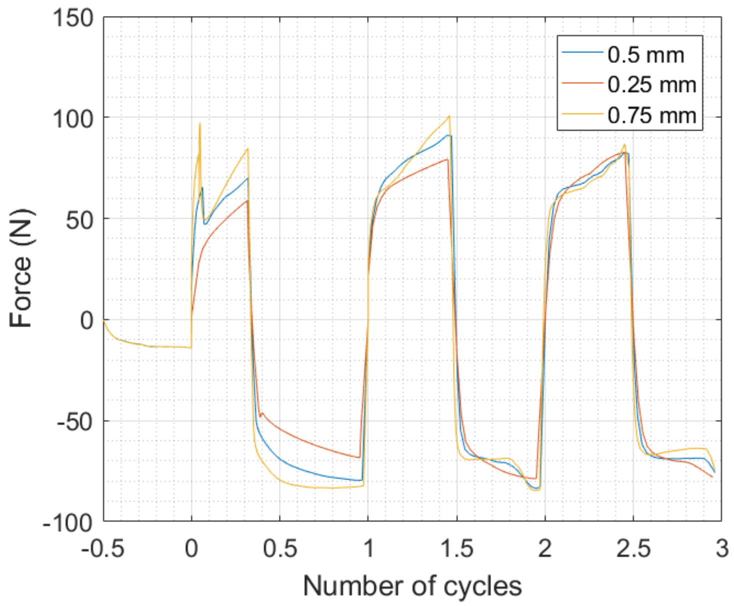

(a)

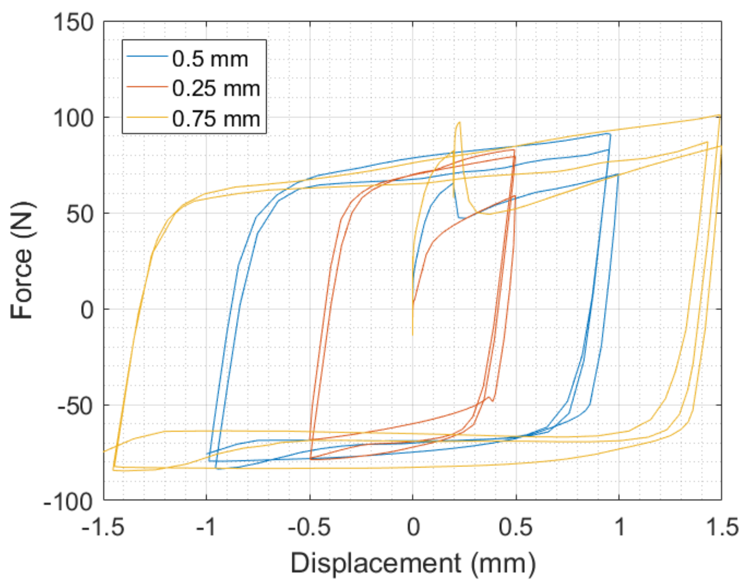

(b)

Figure 6.23: The effect of change in loading amplitude shown in (a) force-number of cycles results; (b) force-displacement results.

Overall, using a ring shaped like a vertical ellipse shows a lot of potential for small ring specimen fatigue life testing, as increasing the range of amplitudes would allow for a fuller investigation into the the fatigue life curve, however this should be investigated experimentally to be sure. Other geometry variations investigated do not seem to be interesting for further investigation, apart from clamping amplitude, which should be investigated experimentally as well.

6.5 Discussion

The FEA model developed for modelling small ring specimen under cyclic loading was shown to not be representative, as the experimental test results are significantly higher than simulated test results. As the material model was fitted to the standard test results appropriately, the other possible explanation is that the material hardened when it was being machined. Machining introduces compressive stresses on the surface and the affected depth depends on the manufacturing method, cutting speed and the material being manufactured. In order to avoid this, conventional copper specimens in literature were annealed in vacuum after they were manufactured or electropolished.

The specimens used in this study were made from a previously annealed material and while that did not result in consistently higher stresses for conventional test results than in literature, it could be that the affected layer was thin enough on the conventional specimen to not affect the results, but thick enough to affect the results of the small ring specimen cyclic test results.

When a material is machined, the properties of the resulting mechanically affected zone are non-uniform, following a smooth curve, with the peak residual stress being below the surface. The affected layer depth for simple machining operations, such as turning or cutting is between 20 μm and 50 μm [185]. Taking the higher value of the affected layer thickness, this results in the percentage affected area for a conventional specimen would be 3.96 %, while the percentage affected area for a small ring specimen would be 14.5 %. As the affected layer thickness increases, the percentage affected area increases more for a small ring specimen than for a conventional specimen. Assuming the average residual stress is around the yield stress of the annealed copper, this would increase the effective yield stress by 14.5 %. Residual stress was assumed because copper is mainly used for drawn tubing, which is a different manufacturing process from turning, making residual stress fields not accurate. Alternatively, residual stresses can be calculated according to models, but the manufacturing parameters required were unknown. While the residual stress calculation does not fully explain why the experimentally acquired force values are higher than simulated force values, it is a step is the right direction and further investigations, discussed in detail in Section 8 will provide a more complete explanation.

The coefficient of friction has a more significant effect than when tensile loading is considered. As it would be undesirable for the coefficient of friction to vary during the test, because it has such a significant effect, it would be best to test clean unlubricated samples. If a liquid lubricant is used, it could be squeezed out from the contact area during testing, which would make the coefficient of friction vary during the test and make the results less accurate. However, if clean samples are tested, the coefficient of friction would rely on the combination of materials in contact, making it different for every different material tested, which could make the development of an interpretation method more complicated. Using a dry lubricant would also be appropriate, as it is suitable for large applied pressures and would not get squeezed out. This would eliminate the dependence of the coefficient of friction from the combination of the ring, clamp and pin materials.

Similarly to tensile testing, for cyclic testing varying geometry parameters is not particularly relevant for interpreting the experimental results, it is more useful for planning future testing. The only parameter which appears to be useful to vary is the shape of the ring (making it into a vertical ellipse), as this would extend the range of amplitudes the small ring specimen could be tested with. This is only relevant for ductile materials, such as copper, as more brittle materials, such as the 2014A-T6 have been shown to break before the maximum fully reversible cyclic setup displacement is reached. Regarding misalignment, the misalignments investigated do not affect the testing results due to small maximum magnitudes.

6.6 Summary and Conclusions

This chapter described the modelling work done for cyclically loaded small ring specimen. The effects of varied material model and geometry parameters were investigated. Additional investigations are needed in order to develop a representative model of a small ring specimen under cyclic loading.

The main conclusions from this chapter are as follows:

- An FEA model representative of cyclically loaded small ring specimen experimental test results was not developed due to inherent limitations of FEA when modelling contact.

- Due to the nature of the combined hardening model it is difficult to decouple all the parameters and develop an interpretation method.
- An interpretation method for the small ring specimen cyclic test results was not developed.
- Misalignment does not have a significant effect on testing results.

7 Small Specimen Cyclic Testing

7.1 Introduction

Small specimen cyclic test results are presented and discussed in this chapter. The overview of cyclic material behaviour is in Section 2.3.2. From Chapter 4 it was identified that the equivalent gauge length, as it was defined for tensile loading, does not vary over a large range when different material properties were investigated, which allowed the assumption of an equivalent gauge length for calculating the loading rates of cyclic small ring tests. The aim of the whole project is to develop a small ring specimen cyclic testing technique, which requires a method to load the small ring specimens cyclically, an understanding of how the stress-state and deformation of the ring evolve during loading, and a way to calculate the standard-equivalent cyclic material properties.

The method for cyclically loading the small ring specimen was developed, and there are several variables that have an effect on the testing results which can be controlled during the setup. They are the clamping torque applied to clamp the small ring specimen, the displacement amplitude and the loading rate. Their effects on the results were investigated, along with the repeatability of tests with the same values of these variables. As this method has potential to be applied to both cyclic plasticity and fatigue testing, small ring specimen test results associated with both of these were investigated.

7.2 Novel Small Ring Specimen Cyclic Loading Fixture Design

Applying cyclic bending was identified to be the best way to load a small ring specimen cyclically. It is intended to deform the ring into a vertical ellipse, then into a horizontal ellipse, until the ring broke, as illustrated in Figure 7.1.

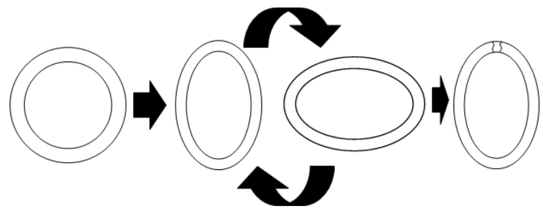

Figure 7.1: Generalized small ring specimen cyclic loading.

Three design concepts for such cyclic loading were considered:

- 2 actuator concept
- Linkage concept
- Clamped ring concept

The 2 actuator concept is illustrated by Figure 7.2. There is an actuator on the x-axis and another on the y-axis. When one actuator is engaged and deforming the ring the other is allowed to move freely. When maximum displacement is reached the first actuator would disengage and the second one would start deforming the ring in the opposite direction. This would continue until the ring failed.

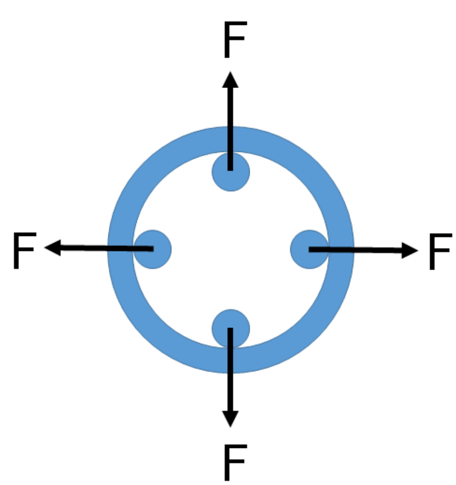

Figure 7.2: 2 actuator design concept diagram.

The main advantage of this concept was that, provided it is implemented appropriately, the ring would definitely be deformed as expected. However, there were also several disadvantages, the combination of which resulted in this concept not being chosen. To begin with, synchronization is an issue, as the actuators would have to engage and disengage on time. If that is not the case the ring would be deformed incorrectly. Secondly, space and interfacing with the existing testing machines would be an issue. In order to keep the setup stiff and due to the space constraints, as illustrated in Figure 7.3, one pair of pins would have to be longer, which would introduce additional error into measurements and control of that displacement.

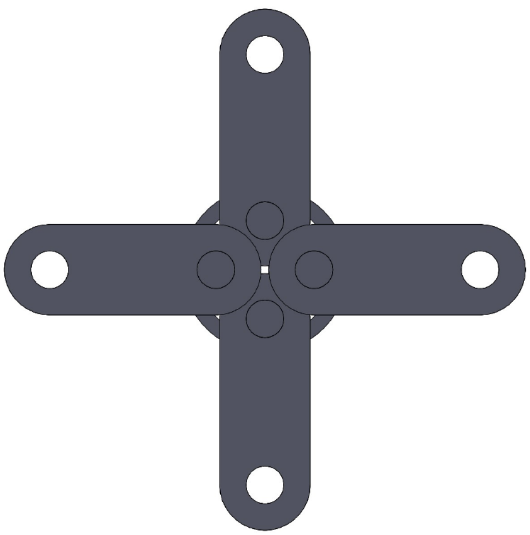

(a)

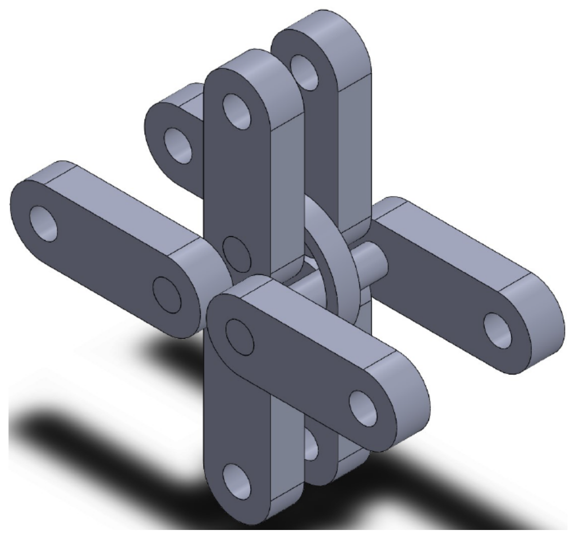

(b)

Figure 7.3: Mock up design of the 2 actuator concept. The ring in the mock up is the size of the real ring.

Also, available testing machines are all uniaxial, so a second actuator would have to be added and making it fit would be difficult. Thirdly, alignment and centering is an issue, as when the ring deforms it elongates and the center moves. The second actuator would have to move with it while both ends of it are allowed to move freely. This most likely would have to be implemented by having 4 actuators instead of 2, making the synchronization even more difficult. Lastly, when the actuator is allowed to move freely it would still exhibit some resistance to the other actuator deforming the ring, which would influence the test results.

The linkage concept is illustrated by Figure 7.4. There is an actuator on the y-axis only. When the ring is deformed into a vertical ellipse the linkages on the x-axis would move away from the inside of the ring and when the loading is reversed the linkages would deform the ring into a horizontal ellipse.

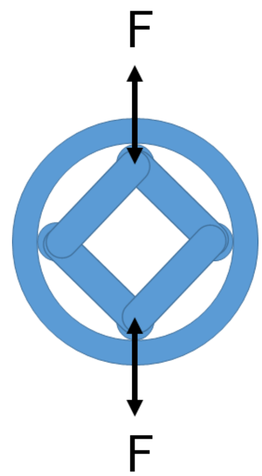

Figure 7.4: Linkage design concept diagram. The ring in the mock up is the size of the real ring.

The main advantage of this concept was that only one actuator would be needed, as opposed to several in the case of the 2 (or 4) actuator concept and synchronization would not be an issue. However, there were also several disadvantages, the combination of which also resulted in this concept not being chosen. Firstly, friction would be an issue, as in order to ensure that the setup does not deform significantly there would have to be a lot of linkages and pins interacting with each other, as illustrated by Figure 7.5. This would affect the testing results.

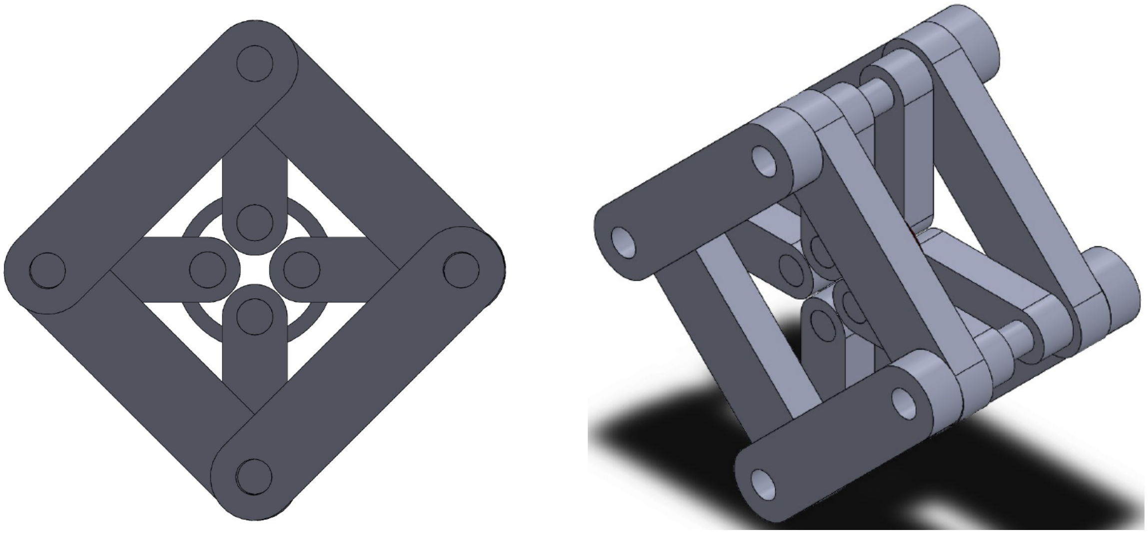

(a) (b)

Figure 7.5: Mock up design of the linkage concept.

Secondly, space would be an issue, as to minimize the deformation of the setup the linkages would have to be large in comparison to the ring and everything might not fit in and around the ring. Thirdly, centering and appropriate deformation would be an issue, in particular as the ring gets longer when it is deformed, therefore the linkages would not be able to apply appropriate deformation due to not accounting for that. Lastly, the long setup times caused by the requirement to disassemble and reassemble the setup for every test make this method impractical.

The clamped ring concept is illustrated by Figure 7.6. There is an actuator on the y-axis only, which pulls the ring into a vertical ellipse, then when the direction of the movement is reversed, pushes the ring into a horizontal ellipse.

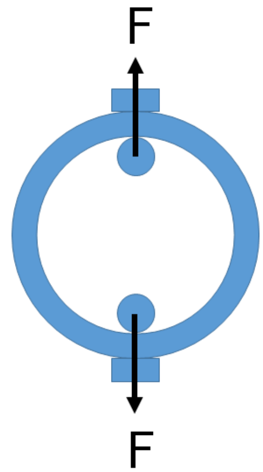

Figure 7.6: Clamp design concept diagram.

The first advantage of this setup is that it does not take up a lot of space. The second one is that it is simple, as no complicated fixtures are needed. The third advantage is that friction would not be a significant issue as there are not many points of contact. Several disadvantages were identified as well, but they were not as severe as for the other concepts, resulting in this concept being chosen. Firstly, slip could occur if not enough clamping is applied and this would affect the test results. Secondly, clamping could affect the stress state in the ring and therefore the results. Lastly, clamping could also result in early failure at the clamping location which would make it less suitable for fatigue life testing.

7.2.1 Final Design

After careful consideration of the advantages and disadvantages of each concept, the clamped ring concept was chosen to be the basis of the final design. There were several iterations before the design was finalized, the simplicity of use, interfacing with the testing machine and potential for introducing errors into the test results all being factors which had to be accounted for prior to finalisation.

The final design of the small ring specimen cyclic loading setup consists of two forks, two pins, two clamping rods, two clamping screws and an a U-shaped aligner. The detailed drawings of all the components can be seen in Appendix A.

The fork can be seen in Figure 7.7. The collar interface was designed to fit with the collar which clamps the fork to the loading arm of the testing machine. The circular cross-section was designed this way to make the manufacture easier and the circular cross-section has flats to allow the interfacing with the aligner to keep the setup aligned as the test is being set up. The distance between the flats was chosen so that the pins already available and previously used for small ring specimen creep testing could be used. The hole for the pin is positioned in a way that the amount of material under the hole is the same as in the small ring specimen creep loading setup. More material would reduce the maximum reversible loading amplitude and less material could deform during loading and introduce errors into the measured force-displacement results. The fork is made from EN24 steel, due to its high stiffness and being easy to machine. As tests at elevated temperatures were not planned, reduction in material properties at elevated temperatures was not of interest. The pins are made from Nimonic due to its high stiffness and good creep resistance properties at elevated temperatures.

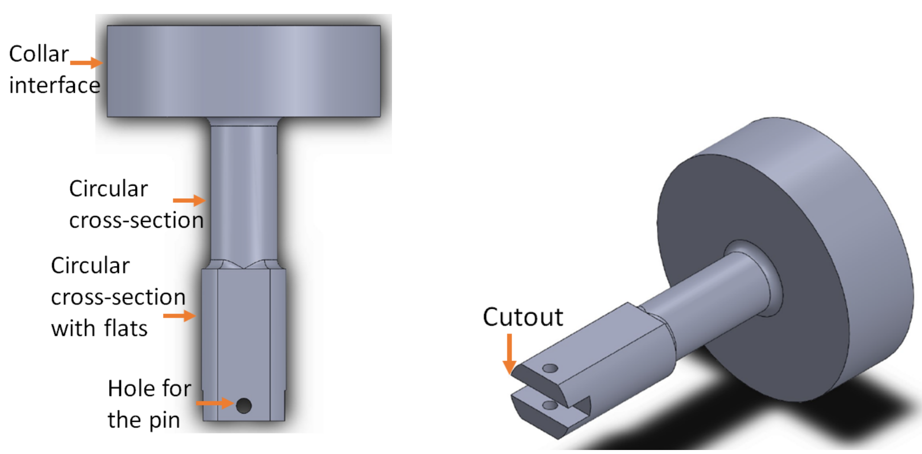

(a) (b)

Figure 7.7: The fork of the small ring specimen cyclic loading setup with features labelled. The hole for the clamping rod and the screw is not shown.

The clamping rods fit with the hole in the fork with a clearance fit, to allow unimpeded movement and no loss in the clamping force applied. They are made from silver steel, as due to the rod being made to tight tolerance it only needed to be cut to length. The clamping screws are M5 socket head screws which fit into the counterbore machined in the fork and can be tightened while in it. If the head of the screw was above the surface of the collar interface, it would not be flush with the loading arm and the fork would be misaligned.

The section view of the assembled setup can be seen in Figure 7.8. For everything to be assembled without interference, clearance fits are needed between all components. The current setup with the current ring geometry allows for the maximum compressive displacement of 1.5 mm before the forks impinge on each other.

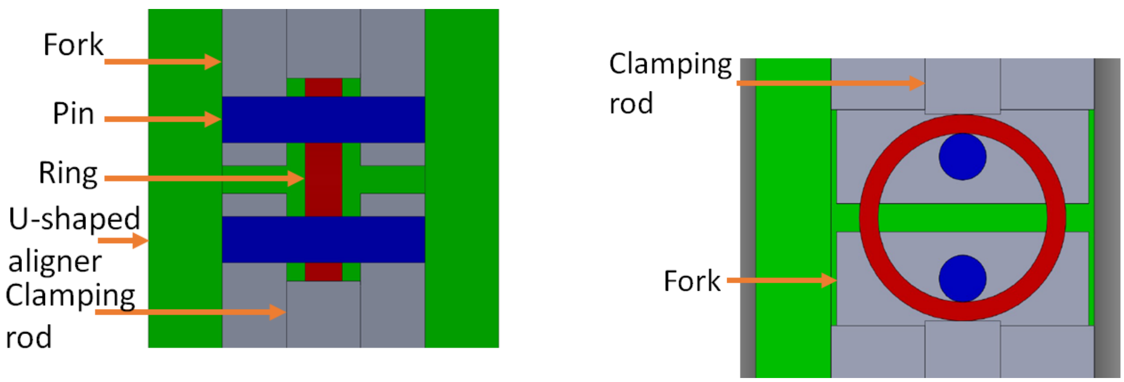

(a) (b)

Figure 7.8: Section view of assembled small ring specimen cyclic loading setup with components labelled.

The model and photo of the final design without the aligner can be seen in Figure 7.9.

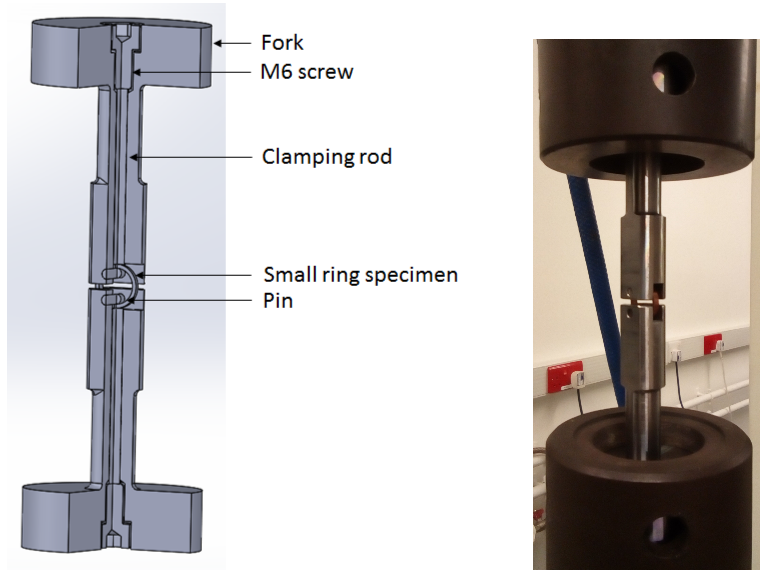

(a) (b)

Figure 7.9: (a) Model and (b) photo of the final small ring specimen cyclic testing design.

7.2.2 Fixture Compliance

The clamping to the small ring specimen is applied by applying torque to the clamping screw. That torque is then transferred into clamping force, which causes deformation in the clamping rod, small ring specimen and pin bending. Equation 7.1 describes the relationship between applied torque and axial force generated, where T is the applied torque, K is a bolt constant, d is the nominal bolt diameter, F is the axial bolt force and l is the lubrication factor. For a zinc-plated screw, which is the type of screw used in the setup, K is equal to 0.2. The screw is an M5 screw, making the nominal diameter 5 mm and it is unlubricated, making the lubrication factor 0. This results in Equation 7.2.

$$T = KFd(1-l) \tag{7.1}$$

$$F = \frac{T}{0.2 \times 5 \times 10^{-3}} = T \times 10^{3} \tag{7.2}$$

If a torque of 2 Nm is applied, the resulting clamping force is 2000 N. This results in the compression of the clamping rod described in Equation 7.3, assuming the force is evenly distributed across the cross-sectional area and the deformation is elastic only. Equation 7.4 describes the deformation of the ring when it is being clamped, assuming constant area and elastic only deformation. The area increases as the clamping force is applied and the deformation quickly becomes plastic, however, these approximations are good enough for a quick estimate of the deformation. As for the bending of the pin when clamping is applied, it is described by Equation 7.5, assuming that the boundary conditions are somewhere between simply supported and built-in (this is explained in more detail in Section 5.2.1), and the deformation is elastic only.

$$\Delta L_{rod} = \frac{FL}{AE} = \frac{2000 \times 44 \times 10^{-3}}{\pi(2 \times 10^{-3})^2 \times 207 \times 10^9} = 0.34 \times 10^{-4}\text{mm} \tag{7.3}$$

$$\Delta L_{ring} = \frac{FL}{AL} = \frac{2000 \times 1 \times 10^{-3}}{2 \times 10^{-3} \times 0.5 \times 10^{-3} \times 120 \times 10^9} = 0.017\text{mm} \tag{7.4}$$

$$w_{pin} = \frac{F \times 46.5 \times 10^{-9}}{48 \times EI} = \frac{2000 \times 46.5 \times 10^{-9}}{48 \times 200 \times 10^9 \times \frac{\pi}{4} \times (1.25 \times 10^{-3})^4} = 0.51 \times 10^{-4}\text{mm} \tag{7.5}$$

Then, when the loading begins and the ring is put in tension, the tensile load adds onto the load bending the pin and subtracts from the load deforming the clamping rod. The deformation of the rest of the loading setup is the same as described in Section 5.2.1. When tensile load is applied the deformations are as described there, when the load is reversed they unload, then when compressive load is applied the clamping rod is additionally compressed.

Moving on to setting up the test, it is important to estimate how much the forks are displaced with respect to each other when the collars are being tightened, as that only depends on the friction between them, the aligner and the clamp used. The clamp is made from mild steel, so all contact is steel on steel. No surface is lubricated on purpose, but they are not cleaned before each test either, resulting in a coefficient of friction likely between 0.3 and 0.4. The clamp is tightened by hand using a metal screw and the coefficient of friction between skin and metal is assumed to be 0.8. The grip strength of a person depends significantly on their age, gender and level of fitness, the estimate of the operator's (25 years old, female, not fit) grip strength is 270 N [186]. The force that is transferred to the screw to generate torque is $270 \times 0.8 = 216$ N. The diameter of the screw head is 25 mm, resulting in a $216 \times 12.5 \times 10^{-3} = 2.7$ Nm torque. As the nominal diameter of the screw is 8 mm, and assuming the screw is slightly lubricated, as the clamp has been in use for many years in the vicinity of lubricants, the clamping force is $\frac{T}{KD} = \frac{2.7}{0.18 \times 8 \times 10^{-3}} = 1875$ N. Assuming the coefficient of friction to be on the lower end of the estimate, 0.3, the maximum force which would allow for the forks to stay in place during setup is $1875 \times 0.3 = 562.5$ N.

When the tests were being set up, specifically, the top collar was being tightened, the force readings were observed, as it was necessary to know when the collar could continue to be tightened. The maximum force achieved during the setup, depending on how carefully the test was set up, was noted to be between around 30 N and around 200 N. One test was done to see if the ring can be deformed during the set up and it was found that it can, even if the maximum force recorded was nowhere near 500 N. This means that some of the estimates used to calculate the maximum force with which the ring is not deformed are likely incorrect and care needs to be taken when setting up the tests so as to not pre-tension the ring before cycling begins, ensuring the force readings do not exceed 50 N.

7.3 Methodology

7.3.1 Methodology Development

When the cyclic small ring specimen test is being set up there are several necessary steps: the ring needs to be clamped on both sides, the setup needs to be aligned, the collars need to be tightened onto the loading arms, the LVDT needs to be assembled, the test run and the ring removed after the test. Photographs of the labelled setup can be seen in Figure 7.10. Both sides of the ring are clamped, the bottom collar is tightened and the specimen is aligned.

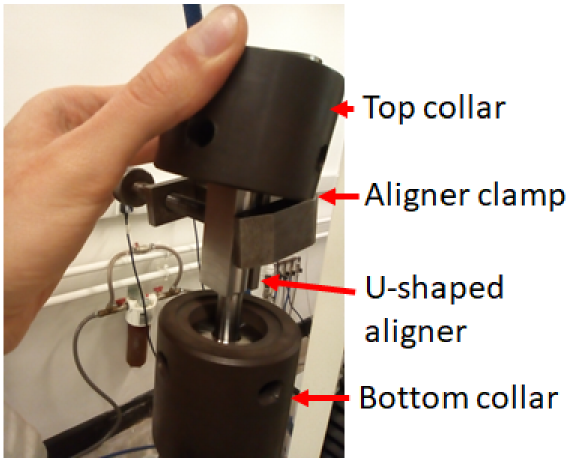

(a)

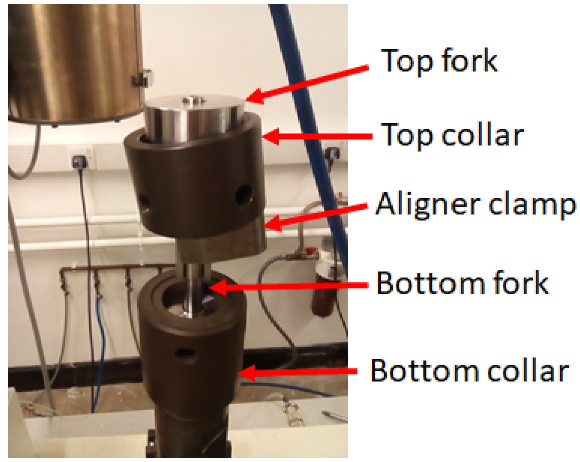

(b)

Figure 7.10: Labelled small ring specimen cyclic loading setup photographs showing all the components.

First of all, there are several theoretically viable ways to assemble the loading setup. Two main ones are the assembling of the setup separately and mounting it onto the machine, and the assembly of the loading setup directly on the loading machine. The former would have the collars on the forks, as they cannot be assembled in any other way, the ring would be assembled between the pins in the forks, the aligner would be applied and clamped to keep it in place, then the ring would be clamped and the setup assembled onto the machine. The latter would have the one side of the ring clamped and the fork assembled onto one loading arm with a collar, then the second collar would be placed onto the first, the second fork assembled, aligned and the second side of the ring clamped, then the second collar would be screwed onto the second loading arm. Afterwards the LVDT would need to be assembled onto the setup, the test run and the ring removed.

The first way would be more difficult to assemble and the ring could get misaligned while it is being clamped without it being seen until the setup is assembled onto the machine and the clamp and aligner removed. The second way keeps the specimen visible as it is being clamped on the first side, therefore misalignment would be visible. The second way of assembling the setup directly onto the testing machine was chosen.

The ring could be either hand clamped or clamped with a tool which applies a set amount of torque, such as a torque wrench. Both were attempted, the results can be seen in Figure 7.11.

When the ring was hand clamped the displacement over which there is no resulting force is very large, while when it is clamped with a torque wrench that displacement is significantly smaller, if present at all. Assuming this displacement is due to loss of contact, the values for hand clamped results are unrealistically large, making clamping with a torque wrench a more appropriate method. Using a torque wrench also allows to control the applied clamping force to an extent and investigate the effect of it on the small ring specimen cyclic testing results.

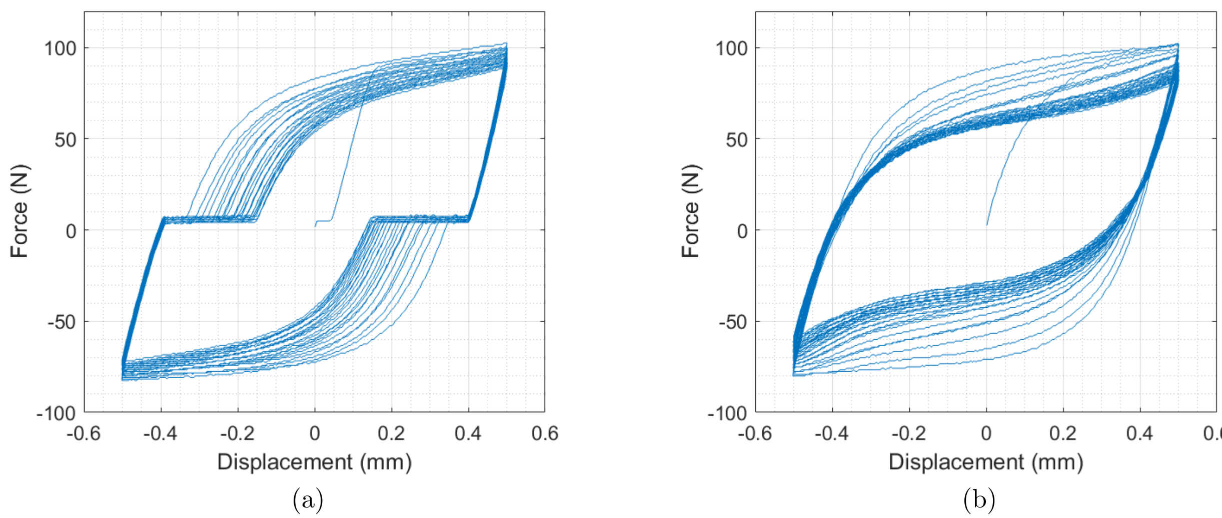

Figure 7.11: (a) Hand tightened test result; (b) Torque wrench tightened test result.

As for alignment, it is essential to apply the clamp in the direction it is shown in Figure 7.10, as otherwise the clamp does not keep both forks aligned while the second collar is being screwed onto the loading arm.

The finalized testing procedure is described step-by-step in Appendix B.

Misalignment Similarly to the misalignment possible for the tensile small ring specimen testing setup discussed in Section 5.8, cyclic small ring specimen testing setup can also experience yaw misalignment, pitch misalignment and offset misalignment. Yaw misalignment is different from the yaw misalignment experienced by the tensile setup, as, while the cyclic test is set up, the pins are kept in alignment with an aligner, within a small manufacturing tolerance. However, there is nothing keeping the ring perpendicular to the pins, especially when it is being clamped with a torque wrench. This causes the ring to be misaligned with respect to both pins, as shown in Figure 7.12 (a), as opposed to one pin being misaligned with respect to the other. The maximum possible misalignment of this type is around 10^o, as higher values make the ring impinge on the setup and the effect of this misalignment would be combined with the effect of friction of the ring and the setup. As this is to be avoided during experimental setup, a maximum of 10^o was chosen for the FEA investigation.

There are two types of pitch misalignment possible in the small ring specimen cyclic loading setup, one type is when the surface of the clamping rod and the pin are not parallel due to the manufacturing tolerances, shown in Figure 7.12 (b). In order to show the effect better, in the FEA investigation it was exaggerated to 3^o, while the real magnitude is 1^o, as that is the angular tolerance in the drawing. The other type of pitch misalignment is when the testing machine is misaligned, causing one pair of clamping rod and pin to be misaligned with respect to the other pair. This is illustrated in Figure 7.12 (c). This was also set to a maximum value of 3^o, as larger values would be noticed and fixed during setup, especially as a clamp and aligner are used to keep them aligned.

Finally, offset misalignment is illustrated in Figure 7.12 (d). It is likely to occur if the test is not set up carefully, when the top of the ring is being clamped, if it is clamped not directly above the bottom clamping location. The aligners and further setup would force the pins into alignment, however, one side of the ring would be under more tension/compression due to the arc being shorter on one side.

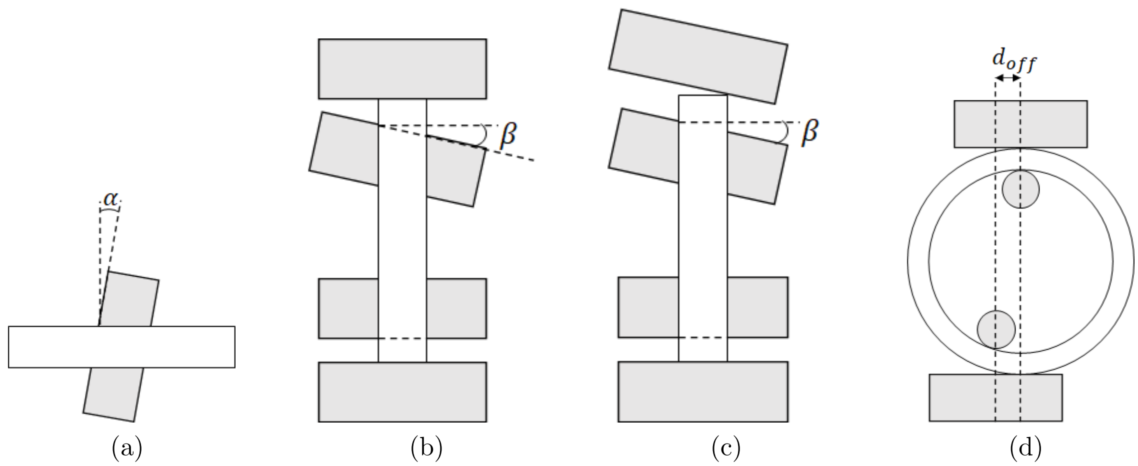

Figure 7.12: Illustrations of different types of misalignment. (a) Yaw misalignment; (b) Pitch misalignment when only the pin is misaligned; (c) Pitch misalignment when both pin and clamping rod are misaligned; (d) Offset misalignment.

The effect of misalignment can be seen in Figure 7.13. Ignoring the effects likely caused by mesh interactions, especially in the case of aligned ring, pitch of the pin had the most significant effect, with others having next to no effect, and, as the magnitude of pitch misalignment was exaggerated, it can be stated that for the cyclic loading, realistic misalignment has next to no effect. The observation about yaw misalignment is further proved by the experimental results, as there was a large number of misaligned specimens and it did not seem to affect the results. This should be further investigated when a representative FEA model is developed.

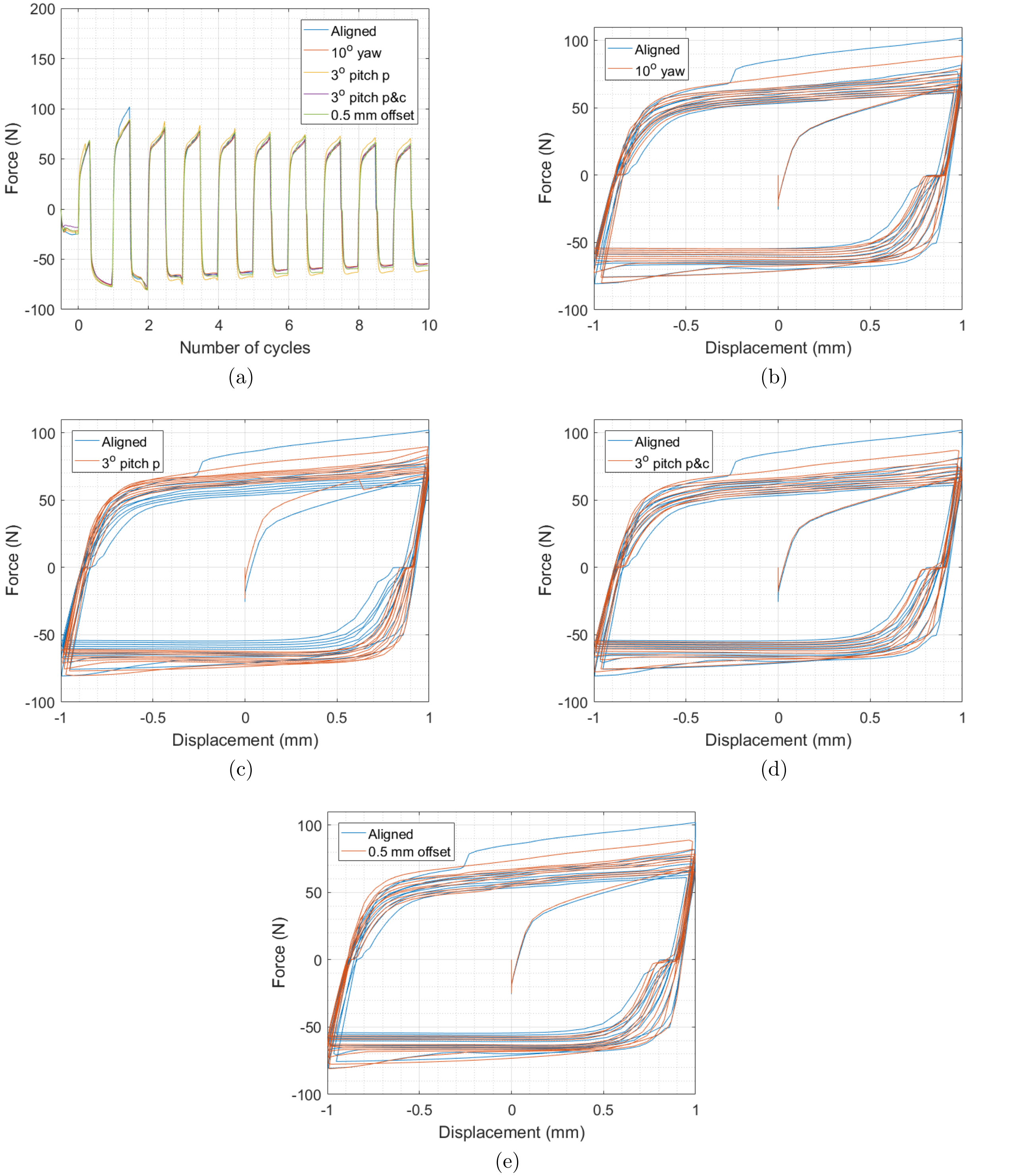

Figure 7.13: The effect of misalignment shown in (a) force-number of cycles results; (b) a comparison between aligned and yaw misalignment; (c) a comparison between aligned and pitch misaligned pin; (d) a comparison between aligned and pitch misaligned pin and clamp; (e) a comparison between aligned and offset misaligned.

7.3.2 Testing Programme

The testing programme, including all different factors that were varied and test end conditions is shown in Table 7.1.

Table 7.1: Copper ring cyclic testing matrix.

Anneal temperature (^oC)	Loading rate (mm/min)	Clamping torque (Nm)	Amplitude (mm)	End condition	Number of repeats	Number of cycles to failure
600	2.4	5	0.25	failure	1	1220
			0.50	failure	1	89
			0.75	failure	2	46, 45
			1.00	failure	6	35, 31, 30, 30, 29, 29, 26
			1.25	failure	1	23
			1.50	failure	1	21
		2	0.50	failure	3	123, 111, 100
			1.00	failure	1	34
			1.50	failure	1	20
		8	0.50	failure	2	107, 104
			1.00	failure	1	31
		None	0.50	30 cycles	1	N/A
		N/A	0.50	failure	1	92
			1.00	failure	1	34
			1.50	failure	1	18, 18, 17
700	2.46	5	0.25	26 cycles	1	N/A
			0.50	failure	1	128, 110, 26
	0.246	5	0.50	failure	1	110
	2.46	5	0.75	failure	1	60
			1.00	failure	1	27
	0.246	5	1.00	failure	1	28
	2.46	5	1.25	failure	1	20
			1.50	failure	1	19
		2	1.00	failure	1	25
			1.50	failure	1	19
		8	1.00	failure	1	28
			0.50	26 cycles	2	N/A

7.4 Grain Structures

Figure 7.14 shows the grain structure of C110 copper annealed at 600^{o}C for 1 hour. The grains were evaluated to be around 90 μm, regularly shaped and there are definitely enough grains in the cross-section for the specimens to be suitable for being tested as small ring specimens.

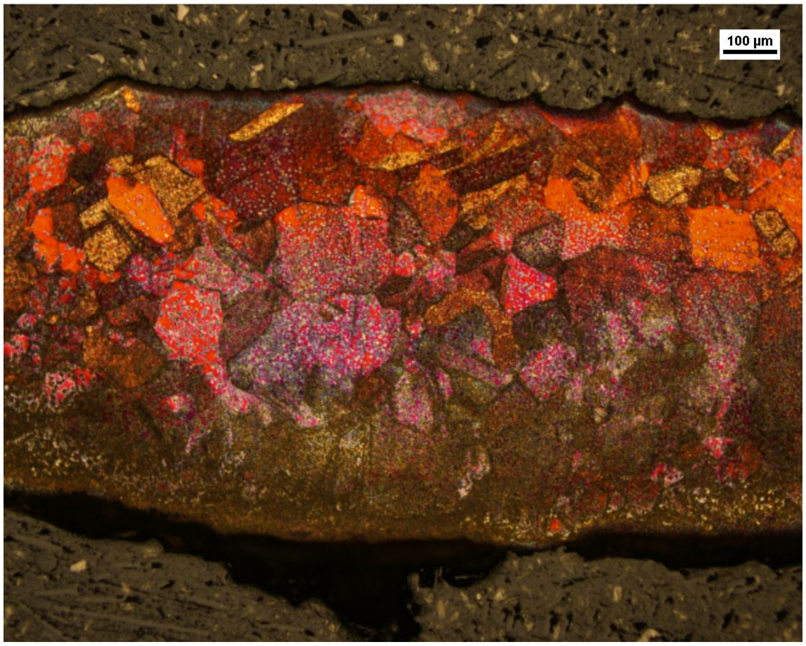

(a)

(b)

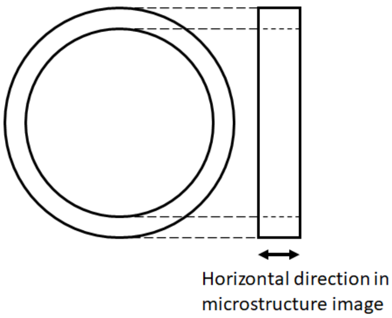

(c)

Figure 7.14: Grain structure of C110 copper annealed at 600^{o}C for 1 hour.

As for the grain structure of C110 copper annealed at 700^{o}C for 1 hour, it is shown in Figure 7.15. The grains are larger here, around 200 μm on average. This results in around 5 grains in the cross-section in some places, which is the limit number of grains for representative small specimen test results.

(a)

(b)

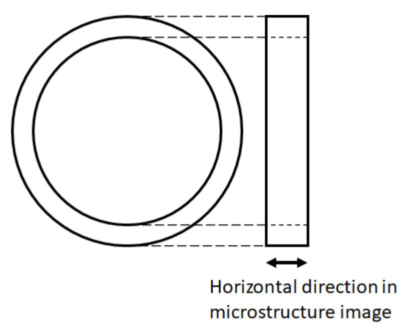

(c)

Figure 7.15: Grain structure of C110 copper annealed at 700^{o}C for 1 hour.

7.5 Small Ring Specimen Cyclic Testing Results

When small ring specimens are loaded cyclically, the force data and displacement data is collected with respect to time, which was then converted to number of cycles. The tests were done in 4 batches: the first batch was done in order to learn how to use the setup and develop an appropriate testing procedure, the second and third batches were done to collect sufficient data to draw conclusions and the fourth batch was done in order to fill in the gaps and replace results significantly affected by pre-tensioning and pre-compression. Most of the tests in the first batch were hand tightened as opposed to using a torque wrench as the testing procedure was being developed. Figure 7.16 shows an example plot of force-number of cycles results. Maximum tensile and compressive force can be identified. Maximum tensile force occurred in the second cycle in the majority of the tests (n=35), in other tests it occurred in the third cycle (n=3) and first cycle (n=1). Maximum compressive force also occurred in the second cycle in the most tests (n=27), in other tests it occurred in the first cycle (n=12), third cycle (n=2) and fourth cycle (n=2). Unlike standard specimen test results, there is no saturation stress.

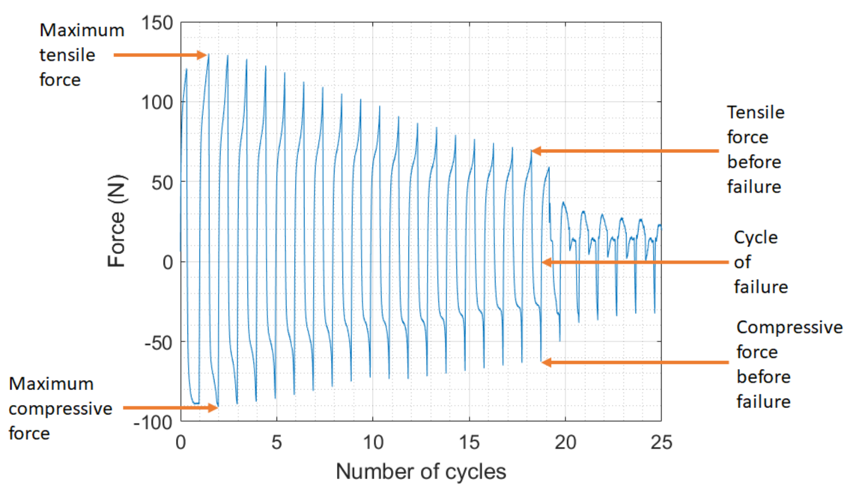

Figure 7.16: Example force-number of cycles result from cyclic small ring testing (700^{o}C anneal, 5 Nm clamping torque, 1.25 mm amplitude, 2.46 mm/min loading rate).

Tensile and compressive forces one cycle before failure can also be identified in order to evaluate the reduction in force during loading. In all tests the specimen failed during the tensile part of the cyclic loading, resulting in a sharp drop of force. In this case failure is defined by the ring fully separating into an arc. After failure the specimens were able to support a limited amount of tensile load due to the pin interacting with the sides of the crack. They were also able to support a significant compressive load after failure as the failed rings could be compressed without being significantly affected by the crack due to the geometry of the loading setup.

A plot of selected cycles of the force-displacement data is shown in Figure 7.17. Negative stiffness can be observed in the first cycle on the compressive side, when the displacement increases, but the resulting force decreases. Out of all the tests done, negative stiffness occurred in the first cycle in all cases apart from two, where the negative stiffness developed in later cycles. There were 6 test results with negative stiffness, two of them were at 1 mm amplitude and four at 1.5 mm amplitude. There were also 29 tests with a zero stiffness in that region, 8 of them were at 1 mm amplitude, 9 at 0.5 mm, 3 at 0.75 mm, 2 at 1.25 mm and 1 at 1.5 mm. The remaining 7 tests showed only positive stiffness or developed negative stiffness in later cycles, 5 of them were at 0.5 mm amplitude and 2 were at 0.25 mm amplitude.

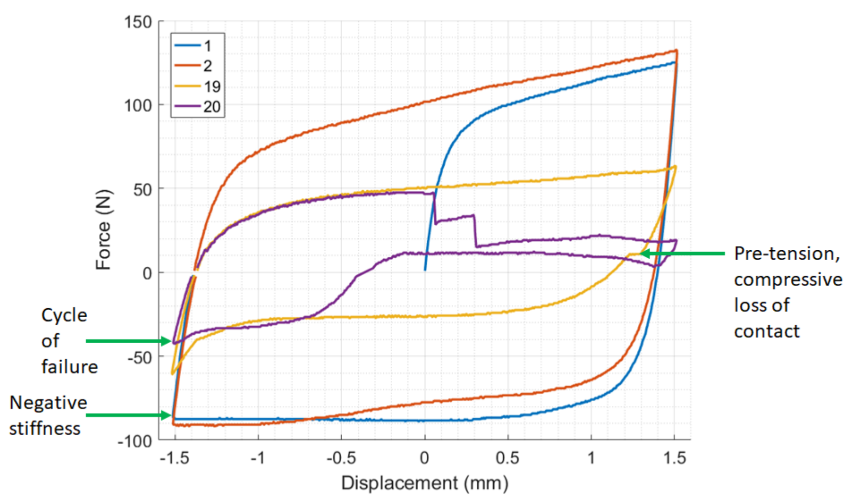

Figure 7.17: Selected cycles in the form of force-displacement curves from cyclic small ring testing (700^{o}C anneal, 2 Nm clamping torque, 1.5 mm amplitude, 2.46 mm/min loading rate).

Loss of contact can be seen in the compressive side of cycle 19. It can manifest on both the tensile and compressive side of the cycle and generally increases as the number of cycles increases. The loss of contact allows to identify pre-tension or pre-compression that occurs due to inaccuracies in setting up the test and then adjust the test results accordingly. Pre-tension of around 10 N can be seen in Figure 7.17, and the adjustment would artificially zero the results by moving the loss of contact to zero force by subtracting it from the results. The force-displacement plot is also particularly suitable to identify failure, as the sharp drop in force can be easily seen, in this case it happened in cycle 20.

Overall, the cycles are not symmetric, with the tensile side of the cycle reaching higher force and having a positive incline towards it, while the compressive side initially has an effectively flat region (between 0.5 mm and -1.5 mm in cycle 1), progressing to a flat region with a sharp peak (cycle 19) as the cycling progresses.

Due to the fact that small ring specimen cyclic test results do not have a saturation force, unlike standard specimen cyclic test results, alternative parameters have to be investigated. Maximum tensile force is one of them, as similarly to saturation stress in standard specimen test results, it is reached within a few cycles from the beginning of the test. If it is indeed similar to saturation stress, it should increase with increasing loading amplitude and if clamping affects the stress state in the small ring specimen significantly, the effect of clamping torque should be significant. Maximum tensile force, shown in Figures 7.18 (a) and (b), seems to increase as the loading amplitude increases. There is a large spread of values and it does not appear to be consistently affected by the clamping torque. Some of this could be due to a large variation in the pre-tension and pre-compression values, therefore Figures 7.18 (c) and (d) show the maximum force values adjusted by the pre-load identified from the loss of contact. If there was no loss of contact the values were not adjusted. This adjustment results in a clearer correlation between displacement amplitude and maximum tensile force. The effect of clamping torque remains inconclusive.

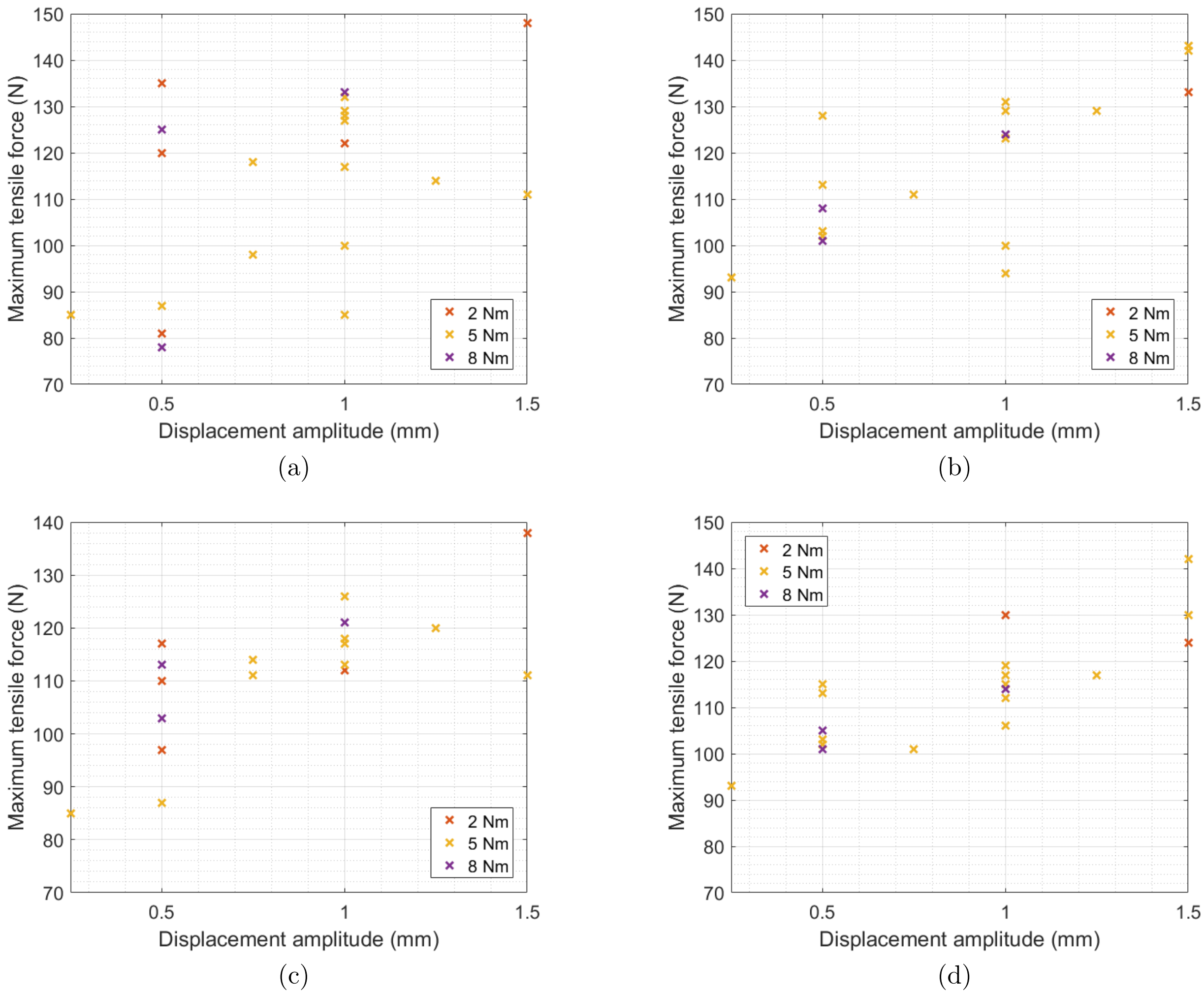

Figure 7.18: Maximum tensile force for cyclic testing of the (a) 600^{o}C anneal; (b) 700^{o}C anneal; (c) 600^{o}C anneal adjusted by pre-load; (d) 700^{o}C anneal adjusted by pre-load.

As the cycles are asymmetrical, maximum compressive force has to be investigated separately, it is shown in Figures 7.19 (a) and (b). Similarly to maximum tensile force, it also seems to increase as the loading amplitude increases and also has a large spread of values that are not consistently affected by the clamping torque. Figures 7.19 (c) and (d) were made by adjusting the maximum compressive force by the pre-load identified from loss of contact. This adjustment results in a clearer correlation between displacement amplitude and maximum tensile force. The effect of clamping torque remains inconclusive.

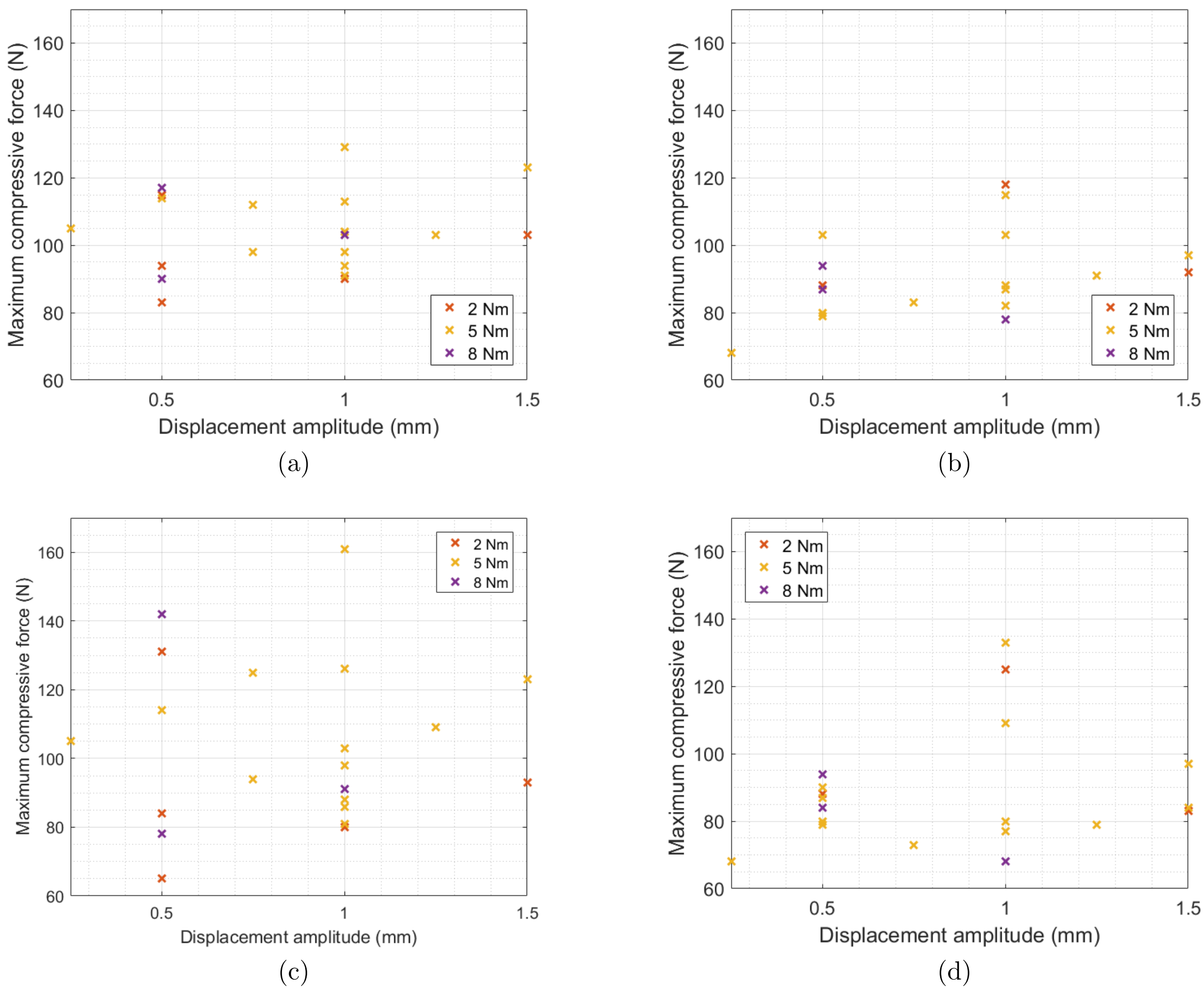

Figure 7.19: Maximum compressive force for cyclic testing of (a) 600^{o}C anneal; (b) 700^{o}C anneal; (c) 600^{o}C anneal adjusted by pre-load; (d) 700^{o}C anneal adjusted by pre-load.

In order for the small ring specimen to be a viable fatigue testing technique cycles to failure should reduce as the loading amplitude is increased. If, as identified when evaluating this small ring specimen cyclic testing setup design concept, clamping makes the specimen fail early, increasing the clamping torque should reduce the cycles to failure. Figure 7.20 shows the cycles to failure for both anneals of the copper. Generally the number of cycles to failure increases as the loading amplitude decreases, there is a large jump in the cycles to failure when the amplitude is decreased to 0.25 mm. Regarding repeatability, it was inspected where several tests at the same loading amplitude were carried out. For the 600^{o}C anneal, at 0.5 mm amplitude the mean was 104 cycles and the range was from -14.4 % to +18.3 %, at 1 mm amplitude the mean was 31 cycles and the range was from -16.1 % to 12.9 %, and at 1.5 mm amplitude the mean was 19 cycles and the range was from -10.5 % to +10.5 %. For the 700^{o}C anneal, at 0.5 mm amplitude the mean was 88 cycles and the range was from -70.5 % to +45.5 %, at 1 mm amplitude the mean was 27 cycles and the range was from -7.4 % to +11.1 %. There is one significantly lower value of cycles to failure at 700^{o}C anneal at 0.5 mm amplitude. There does not appear to be a conclusive effect of the clamping torque on the cycles to failure

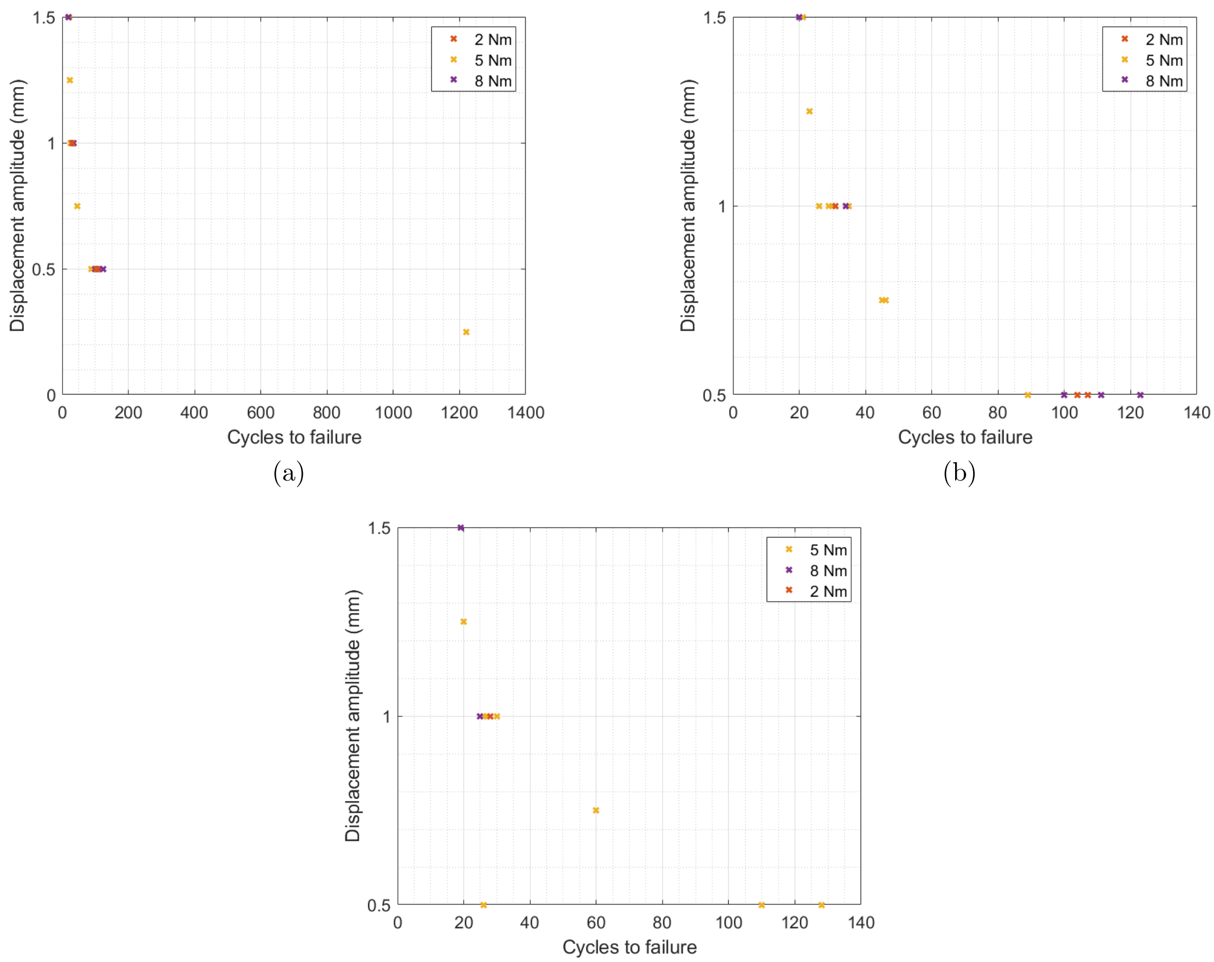

Figure 7.20: Cycles to failure for cyclic testing of (a) 600^{o}C anneal; (b) 600^{o}C anneal zoomed in; (c) 700^{o}C anneal.

Similarly to the maximum force, due to the lack of a saturation stress, the tensile load before failure is of interest. The plot of the tensile load before failure against loading amplitude is shown in Figures 7.21 (a) and (b). There is a wide scatter and no clear correlations. In order to see if it is affected by the pre-tension or pre-compression, Figures 7.21 (c) and (d) were made. There is a clearer correlation between tensile load and displacement amplitude for the 600^{o}C anneal. No clear correlation can be seen for the 700^{o}C anneal, but adjusting the results by the pre-load value reduces the spread.

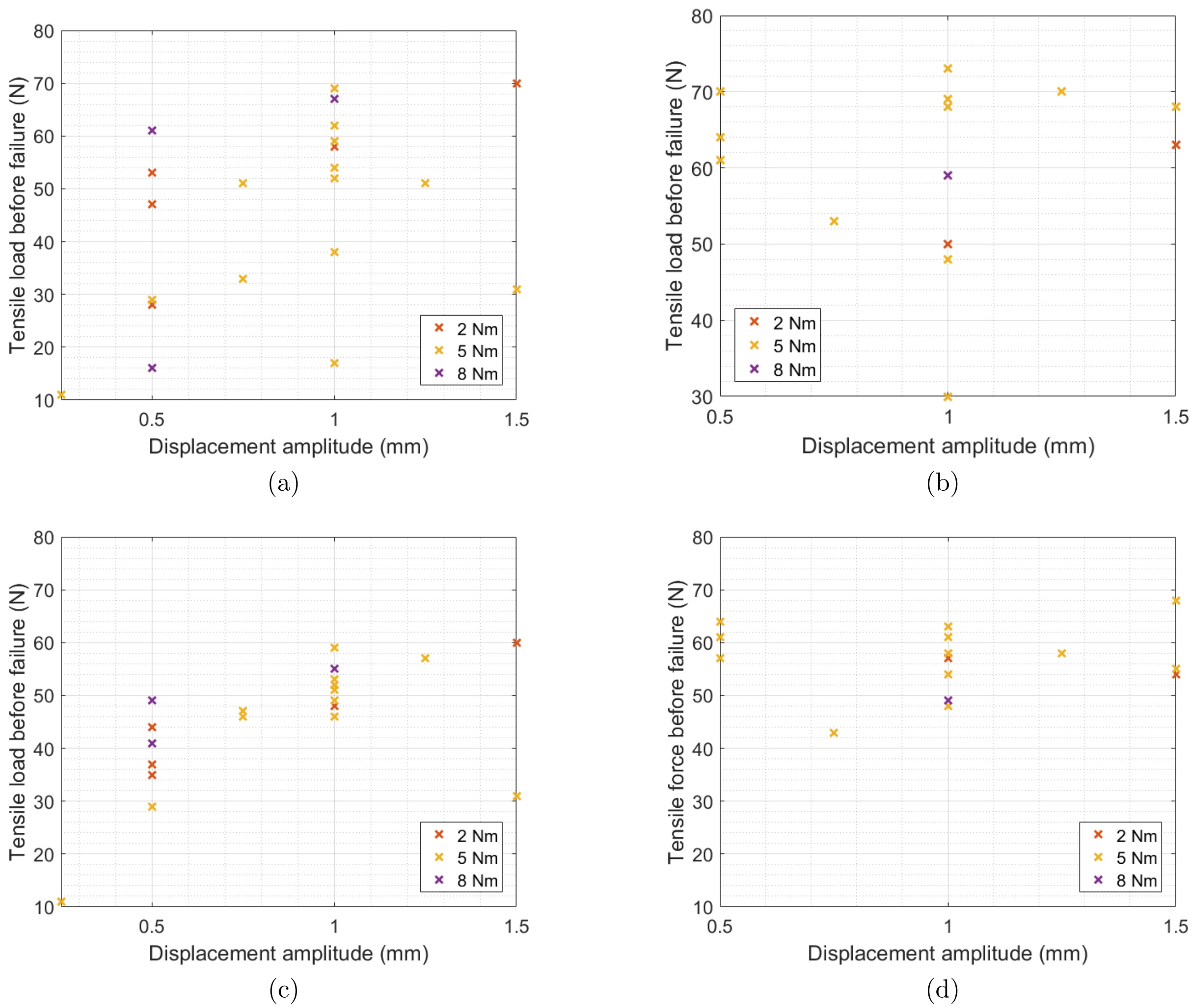

Figure 7.21: Tensile force 1 cycle before failure for cyclic testing of (a) 600^{o}C anneal; (b) 700^{o}C anneal; (c) 600^{o}C anneal adjusted by pre-load; (d) 700^{o}C anneal adjusted by pre-load.

As for compressive load before failure, it is shown in Figures 7.22 (a) and (b). Similarly to tensile load before failure, there is also a wide scatter and no clear correlations. These results were adjusted by the pre-load values and plotted in Figures 7.22 (c) and (d). Higher clamping torque results in higher compressive load before failure, but due to the wide range of values it is hard to say for certain.

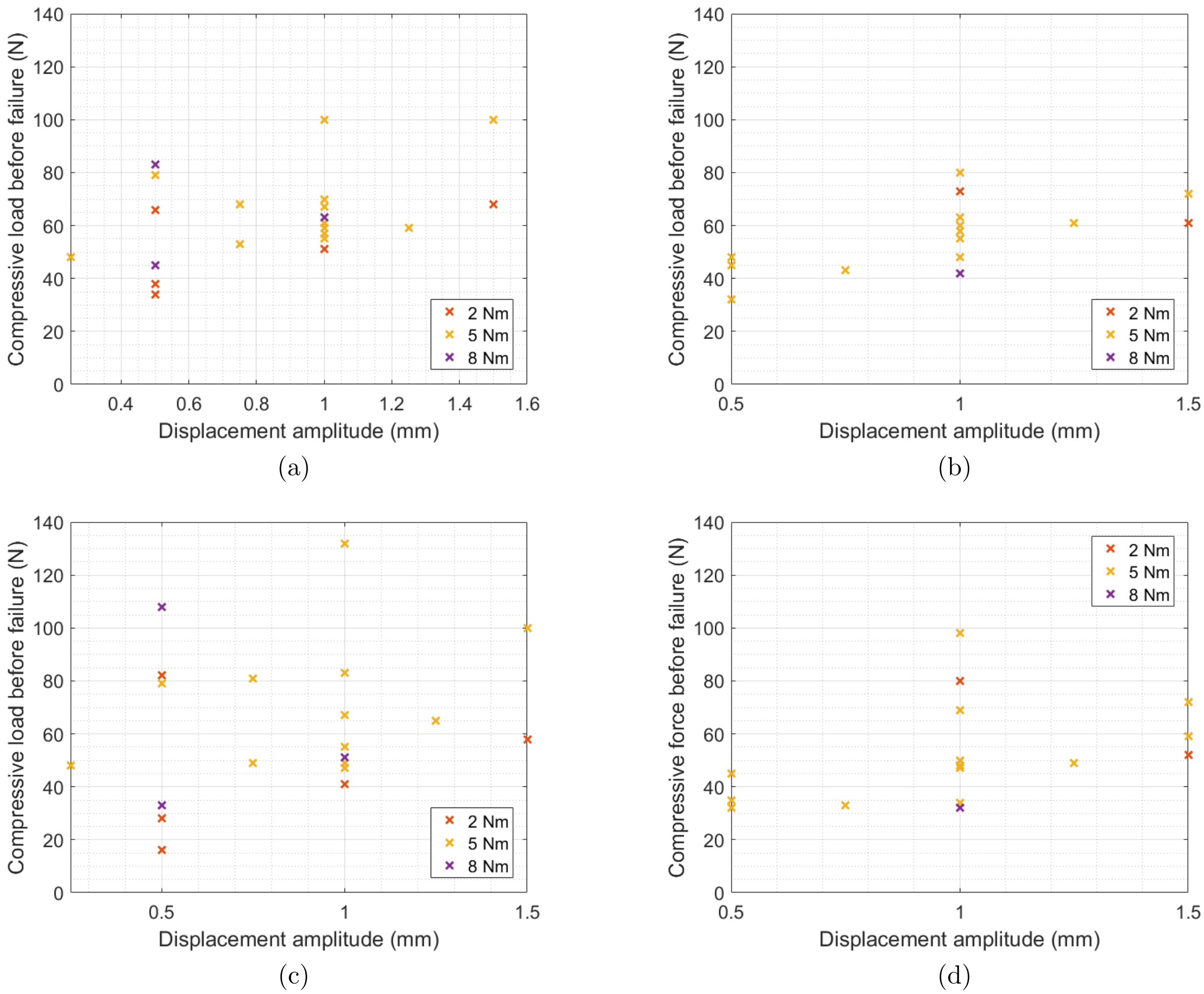

Figure 7.22: Compressive force 1 cycle before failure for cyclic testing of (a) 600^{o}C anneal; (b) 700^{o}C anneal; (c) 600^{o}C anneal adjusted by pre-load; (d) 700^{o}C anneal adjusted by pre-load.

Percentage reduction in tensile force, compressive force and overall force are parameters that combine maximum forces and forces before failure, with a view to minimize the effect of pre-load and find clearer correlations between the parameter of interest and loading amplitude or the effect of clamping torque. Figures 7.23 (a) and (b) show the percentage reduction in tensile force during cyclic loading. There does not appear to be a clear correlation between displacement amplitude and percentage reduction. There is no conclusive effect provided by the clamping torque. Percentage reduction in compressive force is also of interest, it is shown in Figures 7.23 (c) and (d). A weak correlation can be seen between percentage reduction and displacement amplitude. There is a lot of scatter as well and the clamping torque has no consistent effect. The overall reduction in force range combines the previous two sets of data and is shown in Figures 7.23 (e) and (f). There is a weak correlation visible in the 600^{o}C anneal data, but not in the 700^{o}C anneal data, with lower displacement amplitude resulting in higher reduction in force. Overall the percentage reduction is at least 40 % in the majority of the cases, which is a significant amount.

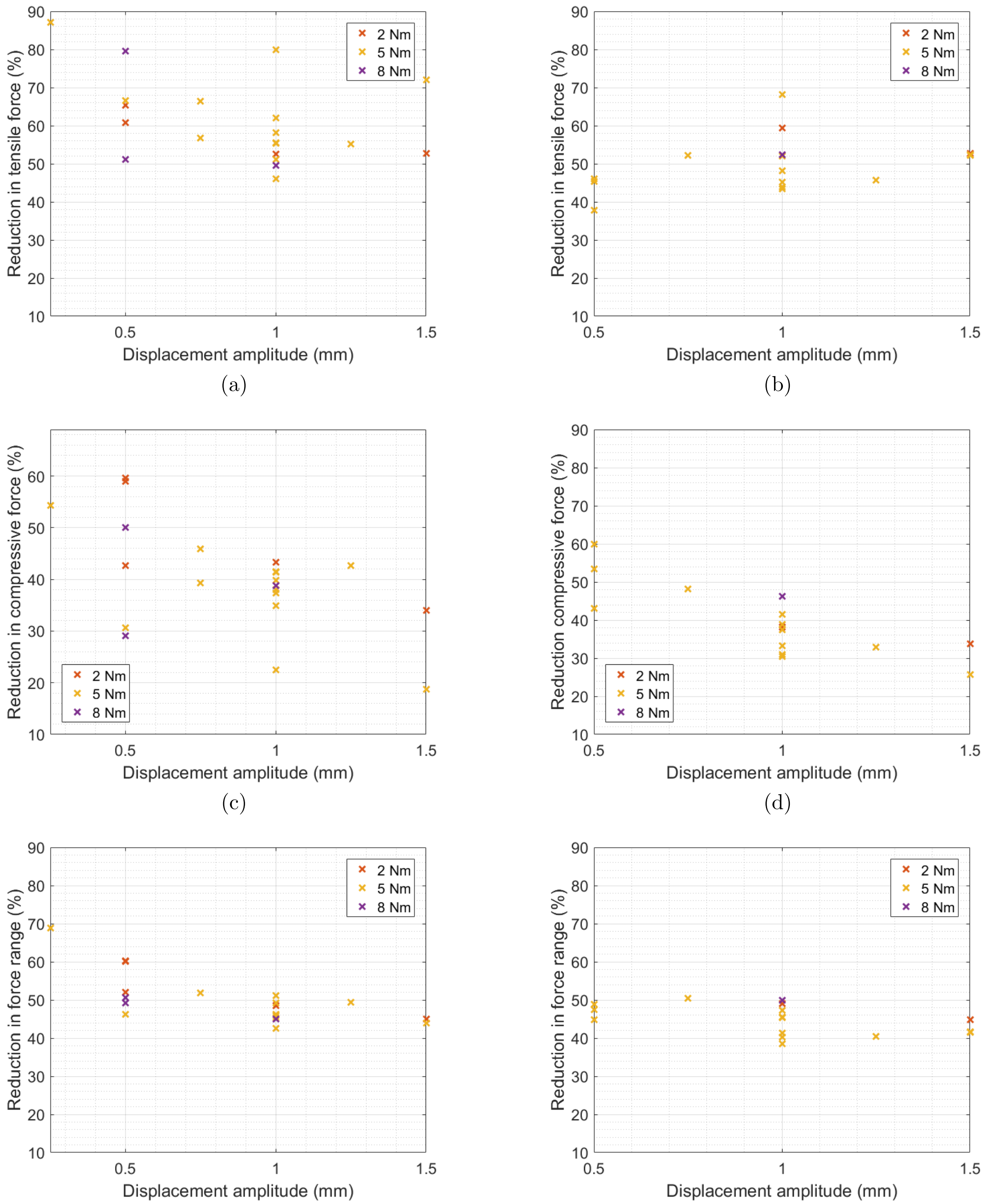

Figure 7.23: Percentage reduction during cyclic loading in (a) tensile force for 600^oC anneal; (b) tensile force for 700^oC anneal; (c) compressive force for 600^oC anneal (d) compressive force for 700^oC anneal; (e) force range for 600^oC anneal; (f) force range for 700^oC anneal.

As mentioned before, loss of contact is important to find the pre-load in order to adjust the results according to it. Higher clamping torque is expected to reduce the loss of contact, as it would result in higher compression of the clamping rod and bending of the pin, which then would support higher level of thinning in the small ring specimen as it is loaded. Tensile loss of contact, shown in Figures 7.24 (a) and (b), occurred in 6 tests, and it was only notable for the 600^{o}C anneal. It was larger when the clamping torque was lower and did not exist at all at clamping torque of 8 Nm. Compressive loss of contact, shown in Figures 7.24 (c) and (d), occurred in 32 cases, which is significantly more than for tensile loss of contact. It appears that the compressive loss of contact is also larger when the clamping torque is lower, however that is not consistent, as there was no loss of contact observed at 2 Nm in the data from the 700^{o}C anneal.

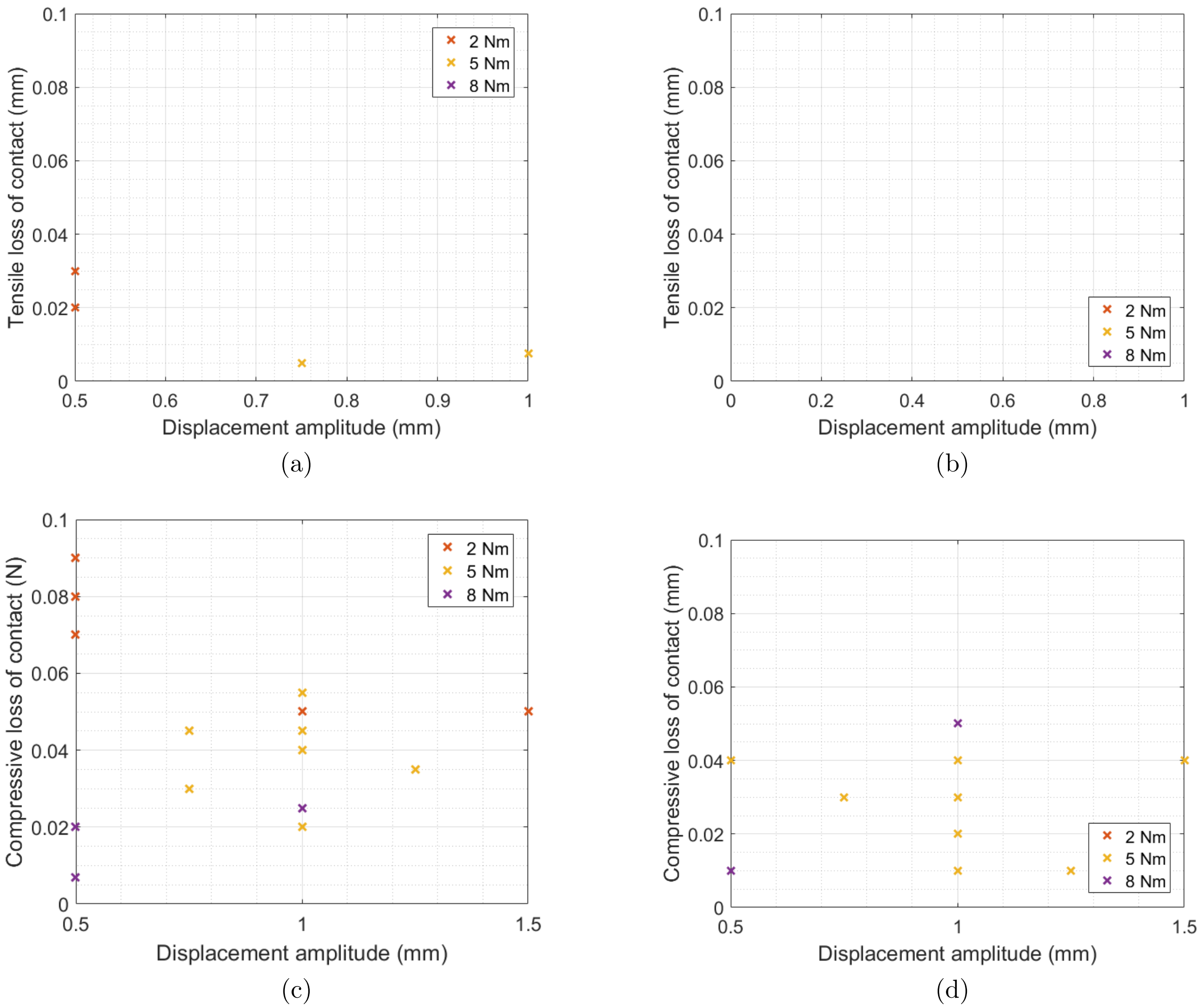

Figure 7.24: Loss of contact for (a) 600^{o}C anneal on the tensile side of the cycle; (b) 700^{o}C anneal on the tensile side of the cycle; (c) 600^{o}C anneal on the compressive side of the cycle; (d) 700^{o}C anneal on the compressive side of the cycle.

Repeats of the same material, clamping torque, loading rate and displacement amplitude were done in order to investigate the repeatability of small ring specimen cyclic test results. The pre-tension/compression values in general varied between -32 N and 18 N for the 600^{o}C anneal tests and between -18 N and 14 N for the 700^{o}C anneal. 6.7 N of the pre-tension can be accounted for by the weight of the top half of the small ring specimen cyclic testing setup.

The comparison of the repeats as force-number of cycles data can be seen in Figure 7.25. When the pre-load values are comparable, there is good agreement for a large proportion of cycles for both anneals. The agreement for 600^{o}C anneal only worsens when the rings fail. The cycles to failure are 29, 31 and 34, which are close together. The agreement for 700^{o}C diverges earlier by about 5 N, but still is broadly good. The cycles to failure are 28, 29 and 30, which are close together as well. When the pre-load values are not comparable, the agreement is less good, however, the biggest difference arises from noise, in particular seen in Figure 7.25 (d) at -10 N.

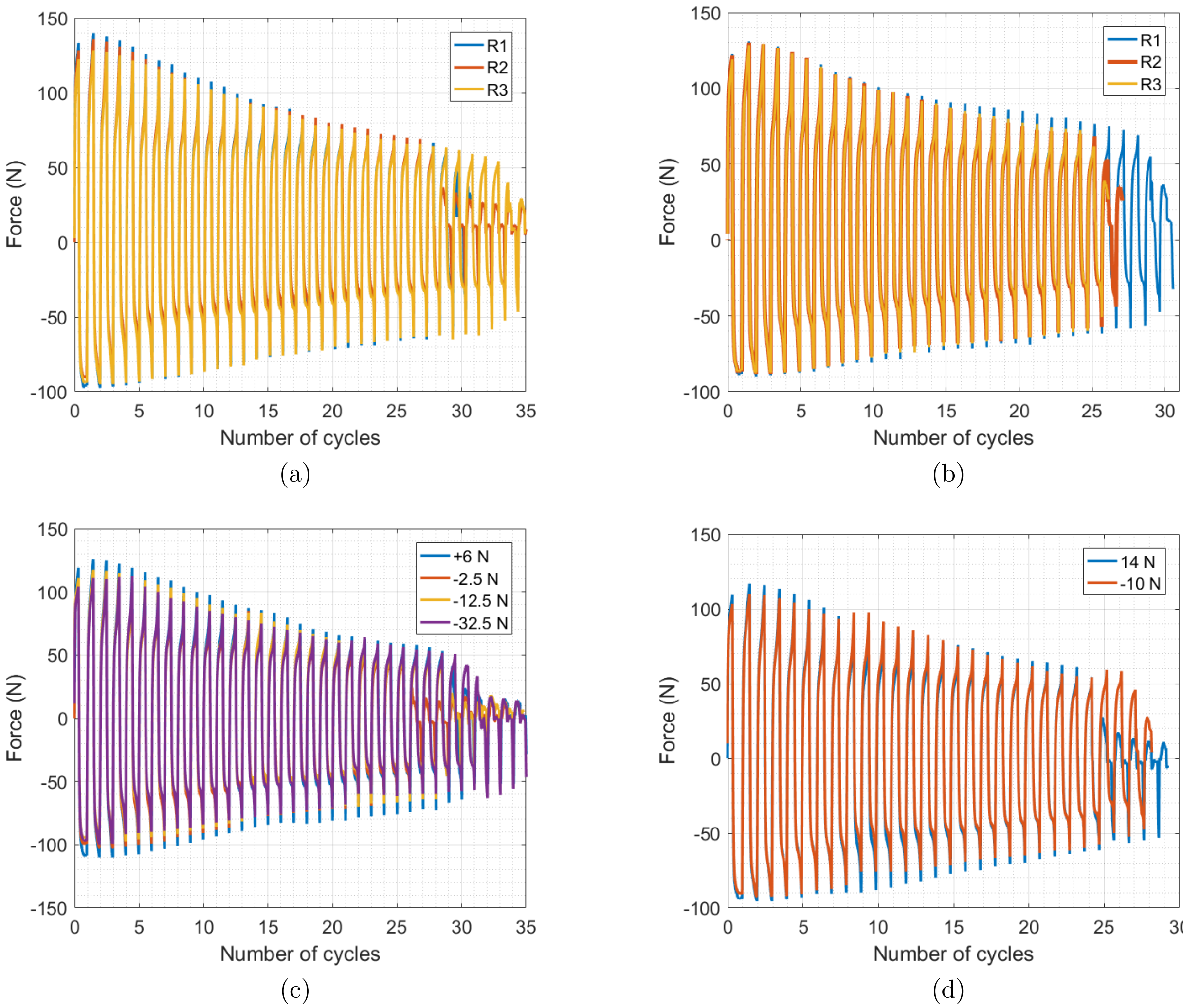

Figure 7.25: Comparison of the repeats (force-number of cycles) at 5 Nm clamping torque and 1 mm displacement amplitude of the (a) 600^{o}C anneal with comparable pre-load; (b) 700^{o}C anneal with comparable pre-load; (c) 600^{o}C anneal with different pre-loads; (d) 700^{o}C anneal with different pre-loads.

Figure 7.26 shows the first two cycles from the repeats plotted as force-displacement graphs. The first and second cycle of 600^{o}C has a slightly wider scatter (around 15 N at the widest part) than the scatter for 700^{o}C anneal (around 5 N at the widest part). The repeats with comparable pre-load values are more similar to each other than to the ones with significantly different pre-load values.

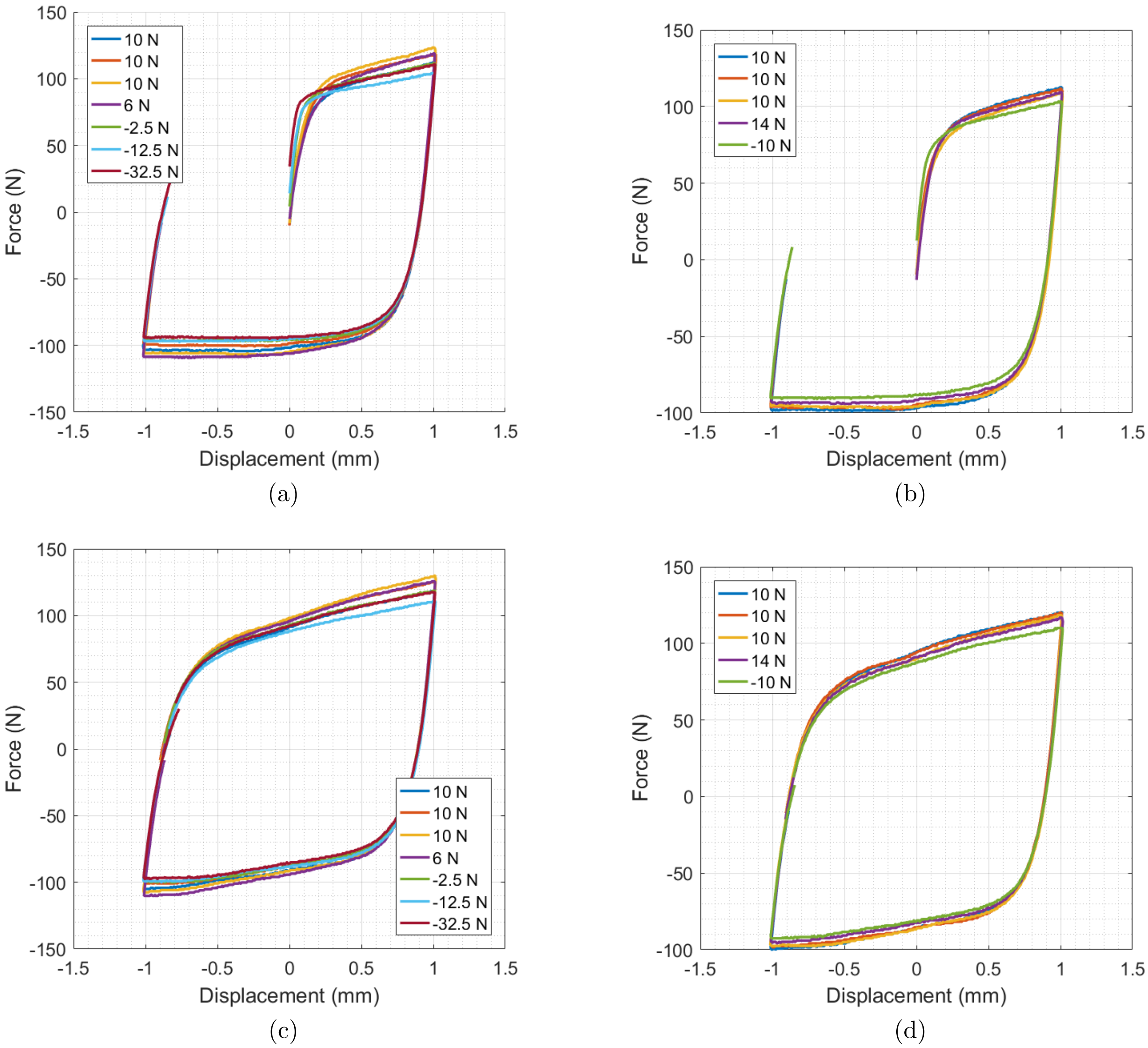

Figure 7.26: Comparison of the repeats (force-displacement) at 5 Nm clamping torque and 1 mm displacement amplitude of the (a) 1st loop of 600^{o}C anneal; (b) 1st loop of 700^{o}C anneal; (c) 2nd loop of 600^{o}C anneal; (d) 2nd loop of the 700^{o}C anneal.

Cycles 15 and 25 from the repeats plotted as force-displacement graphs can be seen in Figure 7.27. The shape of the loops changed significantly between the first two cycles and the 15th cycle. It did not change between the 15th cycle and the 25th cycle, however, the force range and the area enclosed by the loop both go down significantly. Similarly to the first two cycles, the scatter is wider for 600^{o}C anneal than 700^{o}C anneal.A small amount of loss of contact can be seen in all images, which increases as the number of cycles increases. A wider spread of pre-load values results in a wider spread of the 600^{o}C anneal hysteresis loops than in the 700^{o}C anneal hysteresis loops. The first of the 700^{o}C anneal rings fails at cycle 25, the 14 N pre-load one.

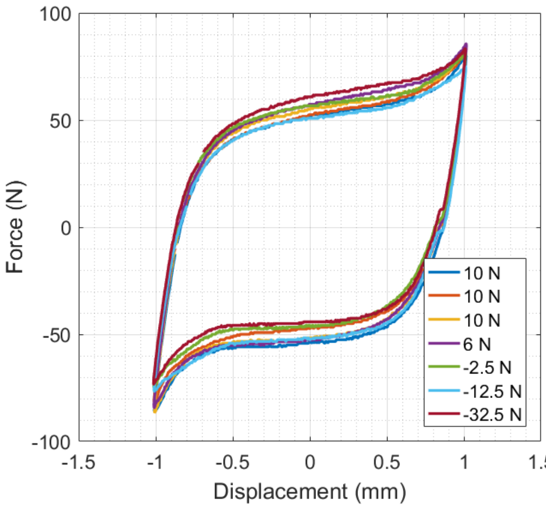

(a)

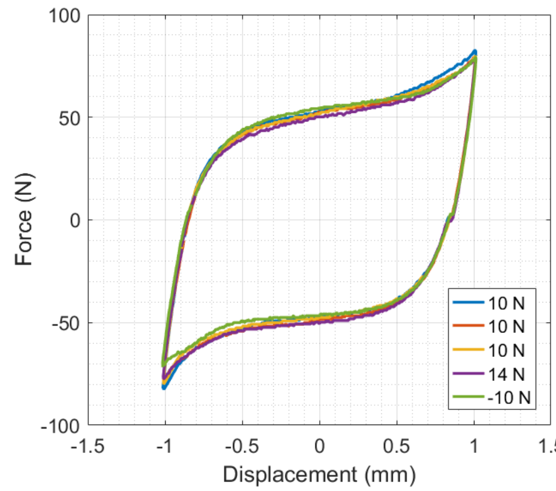

(b)

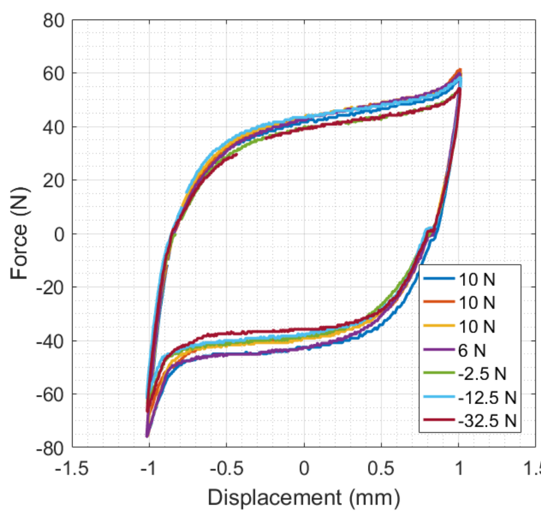

(c)

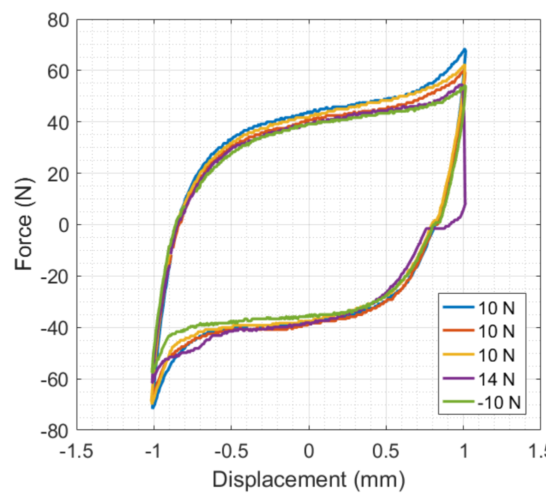

(d)

Figure 7.27: Comparison of the repeats (force-displacement) at 5 Nm clamping torque and 1 mm displacement amplitude of the (a) 15th loop of 600^{o}C anneal; (b) 15th loop of 700^{o}C anneal; (c) 25th loop of 600^{o}C anneal; (d) 25th loop of the 700^{o}C anneal.

The cycles when failure occurs are shown in Figure 7.28. There is a good agreement between the different repeats up to the ring failing. The rings fail on the tensile side of the loop in all cases, sometimes in sudden failure and sometimes in progressive failure. That can be seen particularly well in Figure 7.28 (c) and (e). The irregular loop shape is a good indication of failure, as it is not necessarily easy to see in a force-time plot. In the case of a small ring specimen under cyclic loading, failure is full separation of the ring into an arc, which is indicated by a sharp drop in tensile load and irregular loop shape.

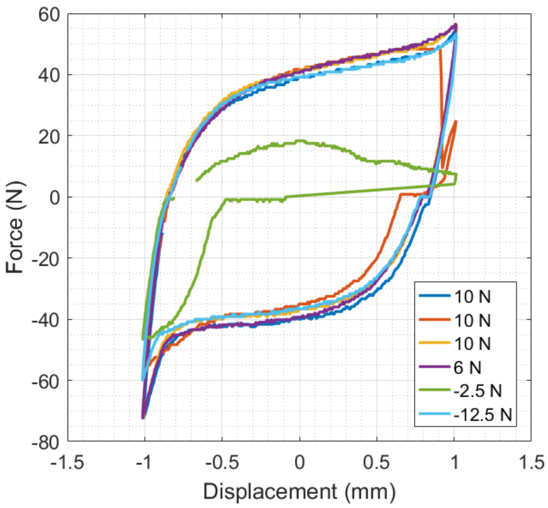

(a)

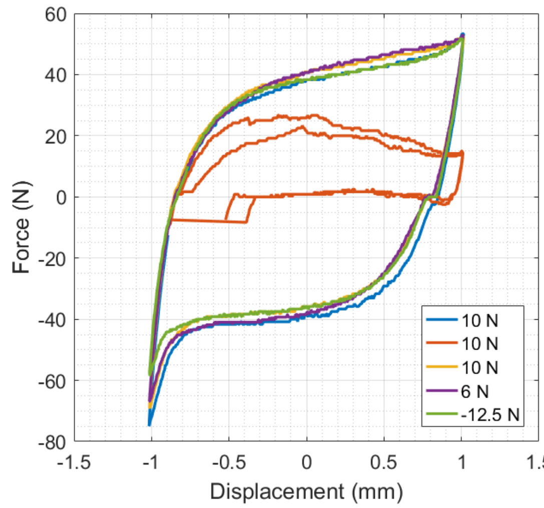

(b)

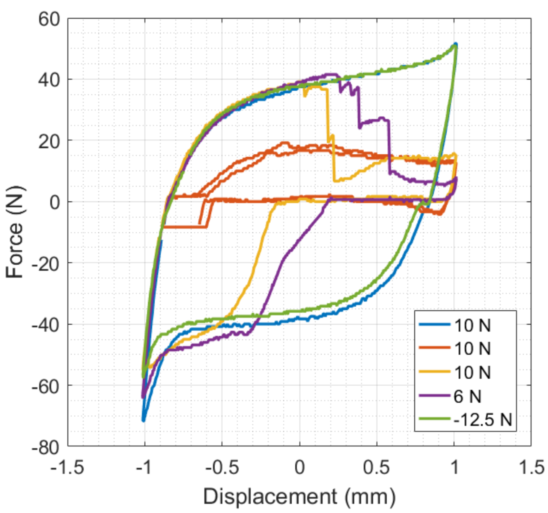

(c)

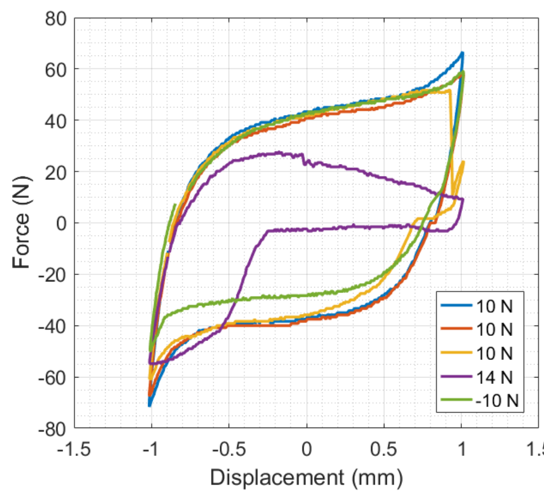

(d)

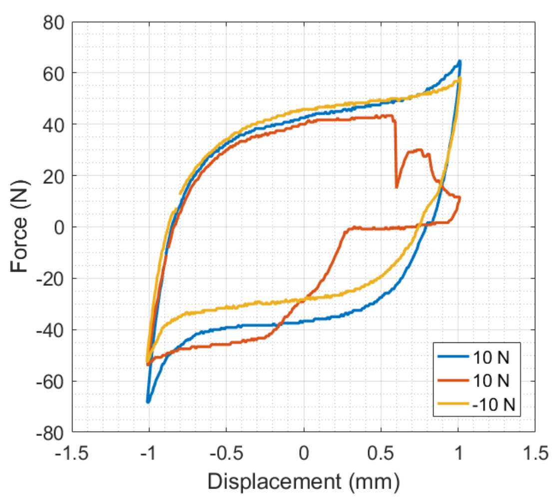

(e)

Figure 7.28: Comparison of the repeats (force-displacement) at 5 Nm clamping torque and 1 mm displacement amplitude of the (a) 28th loop of 600^{o}C anneal; (b) 29th loop of 600^{o}C anneal; (c) 30th loop of 600^{o}C anneal; (d) 26th loop of the 700^{o}C anneal; (e) 27th loop of the 700^{o}C anneal.

An investigation was done to see if a faster loading rate could be used to test the 700^{o}C anneal, as the loading rate suggested by the literature was very slow (0.246 mm/min) and a single test would have taken about 1 day to run. The force-number of cycles curves of that investigation can be seen in Figure 7.29. The plot of the 1 mm amplitude tests can be seen in (a) and (b), with (b) being adjusted by the pre-tension/compression value identified from loss of contact. After the adjustment the agreement between the tests at different rates is good. The plot of the 0.5 mm amplitude tests can be seen in (c). The agreement between the tests at different rates is not as good as for the 1 mm amplitude, the noticeable noise in force in both 2.46 mm/min and 0.246 mm/min test results contribute to that. The number of cycles to failure is higher for the slower loading rate.

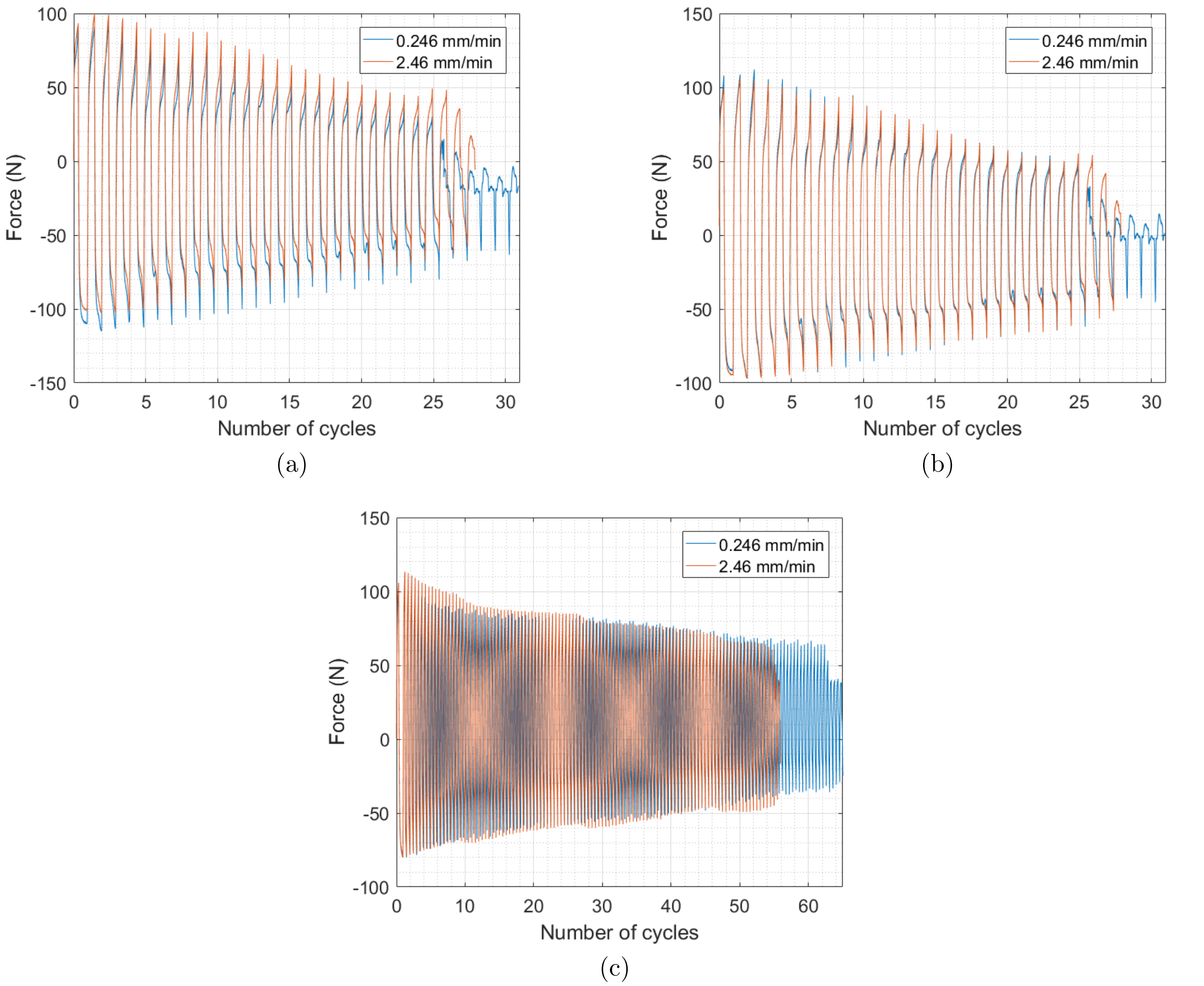

Figure 7.29: Comparison of force-number of cycles response of the 700^{o}C anneal at 5 Nm clamping torque, different loading rates (a) and 1 mm amplitude; (b) and 1 mm amplitude adjusted for pre-tension/compression; (c) and 0.5 mm amplitude.

Regarding the agreement between selected cycles, they are shown in Figure 7.30 (a) to (d), it is pretty good for the first cycle apart from the peak in the 0.246 mm/min results. For the other cycles the agreement is less good, with differences up to 10 N in parts of the hysteresis loops. The shapes of the loops agree generally well. As for the cycles close to failure, they are shown in Figure 7.30 (e) and (f). The shape of the loops does not agree well between the different loading rates, the 0.246 mm/min test shows negative stiffness in cycle 25 and the loss of contact during the 2.46 mm/min test on the 26th cycle is not present as a step any more. The level of agreement is similar to what was expected, as, when rate dependency was investigated with standard specimens, no significant effects were observed.

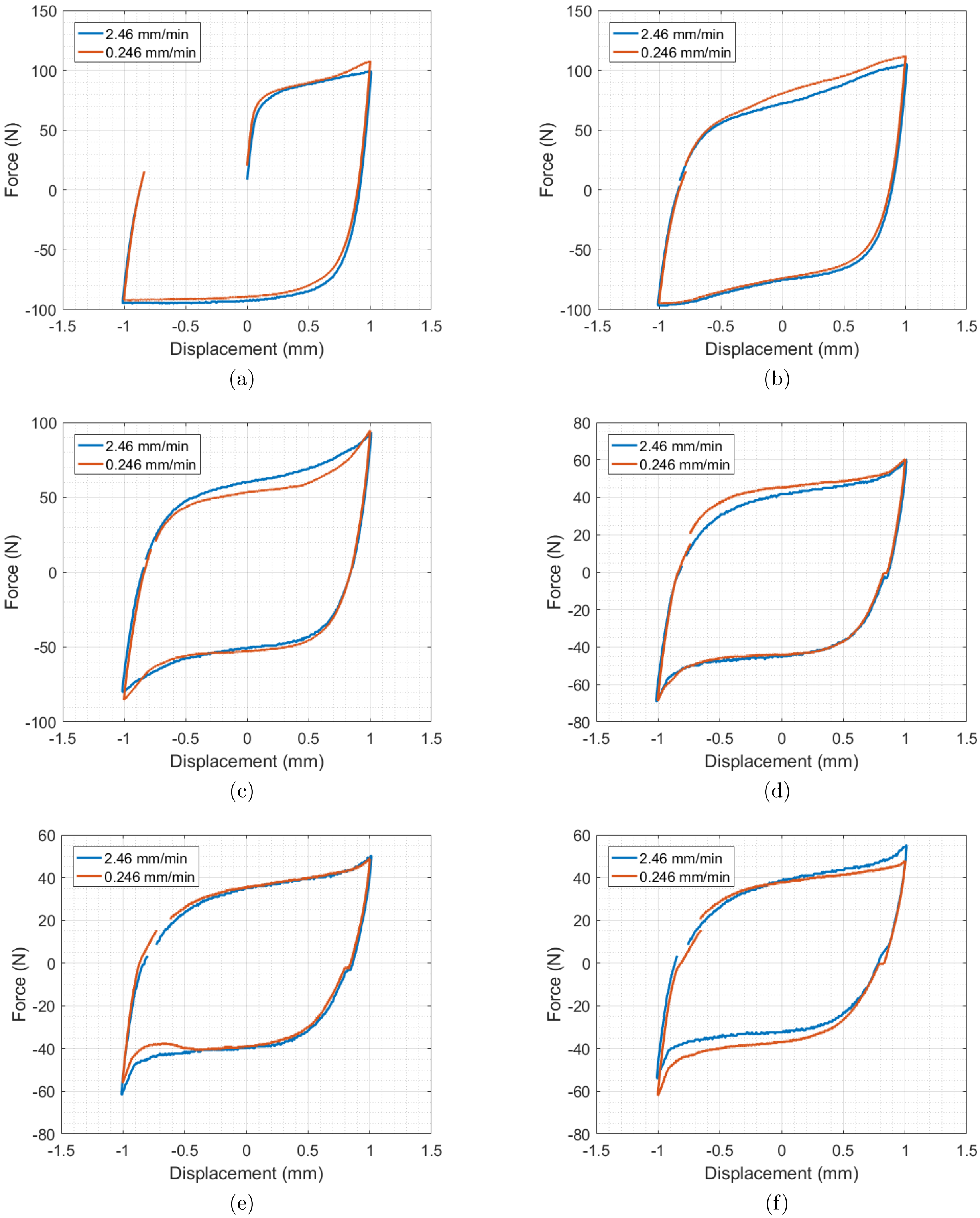

Figure 7.30: Comparison of force-displacement response of the 700°C anneal at 5 Nm clamping torque, different loading rates at (a) 1st cycle; (b) 3rd cycle; (c) 10th cycle; (d) 20th cycle; (e) 25th cycle; (f) 26th cycle.

Figure 7.31 shows examples of ring specimens used for cyclic loading. Ring (a) was not cycled, as while it was being clamped it was misaligned enough to touch the fork, which could have affected the results. Ring (b) was cycled until failure, it did not develop a plastic hinge at the bottom. Neither did ring (c), but it was deformed into a horizontal ellipse and the crack was opened significantly in comparison to other rings shown. Ring (d) developed a plastic hinge at the bottom, the crack is at the top. Ring (e) was deformed into this shape when the pin was going into the compressive stroke and one side of the crack slipped past it and the other side was bent down.

(a) (b) (c) (d) (e)

Figure 7.31: Examples of failed copper ring specimens. (a) 8 Nm clamping, no loading. (b) 600^oC anneal, 8 Nm clamping, 0.5 mm amplitude. (c) 700^oC anneal, 5 Nm clamping, 0.75 mm amplitude. (d) 700^oC anneal, 5 Nm clamping, 1.25 mm amplitude. (e) 600^oC anneal, 5 Nm clamping, 1.5 mm amplitude.

Location of failure was noted for 9 tests of the 600^oC anneal and 11 tests of the 700^oC anneal. For the 600^oC anneal failure occurred at the top pin in 6 cases and at the bottom pin in 3 cases. For the 700^oC anneal failure occurred at the top pin in 5 cases and at the bottom pin in 6 cases.

After testing the small ring specimens were inspected for misalignment. If the sides of the contact area between the small ring specimen and the pins were not perpendicular to the small ring specimen the ring was considered to be misaligned. It was noted for 19 tests of the 600^oC anneal and 18 tests of the 700^oC anneal. For the 600^oC anneal 8 specimens were visibly misaligned, 2 of them were clamped with 2 Nm, 5 with 5 Nm and 1 with 2 Nm. The ones not visibly misaligned were 1 clamped with 2 Nm, 7 with 5 Nm and 1 with 8 Nm. For the 700^{o}C anneal 6 specimens were visibly misaligned, none were clamped with 2 Nm, 5 with 5 Nm and 1 with 8 Nm. The ones not visibly misaligned were 2 clamped with 2 Nm, 5 with 5 Nm and 1 with 8 Nm. When setting up the tests using higher clamping torque, especially 8 Nm, some specimens had to be scrapped, as they were misaligned by the clamping enough to impinge on the setup, which would potentially affect the results due to friction. Test results from misaligned specimens were not excluded. The effects of misalignment were further discussed in Chapter 6. No visible signs of slip or rotation were noted on any specimens, however the magnitudes of both are likely to be too small to see with a naked eye.

7.6 Fractography Results

Figure 7.32 shows the fracture surface of small ring specimen made from C110 copper tested under cyclic loading. Beach lines indicating fatigue failure are visible on all fracture surfaces. The width of the lines increases as the loading amplitude increases, as the number of cycles to failure for higher amplitudes is lower, which requires the same area of specimen to be fractured with fewer lines. It appears that there are multiple cracks propagating at the same time, as the direction of beach marks is different in different locations on the specimen, seen particularly well in figure 7.32 (a). Due to a lack of depth of focus it is difficult to count the number of beach marks accurately to evaluate when the cracks initiated. Multiple cracks propagating at the same time is also an issue for counting as it is not clear which crack initiated first. Taking SEM images of fracture surfaces would be beneficial to evaluate when cracks initiated.

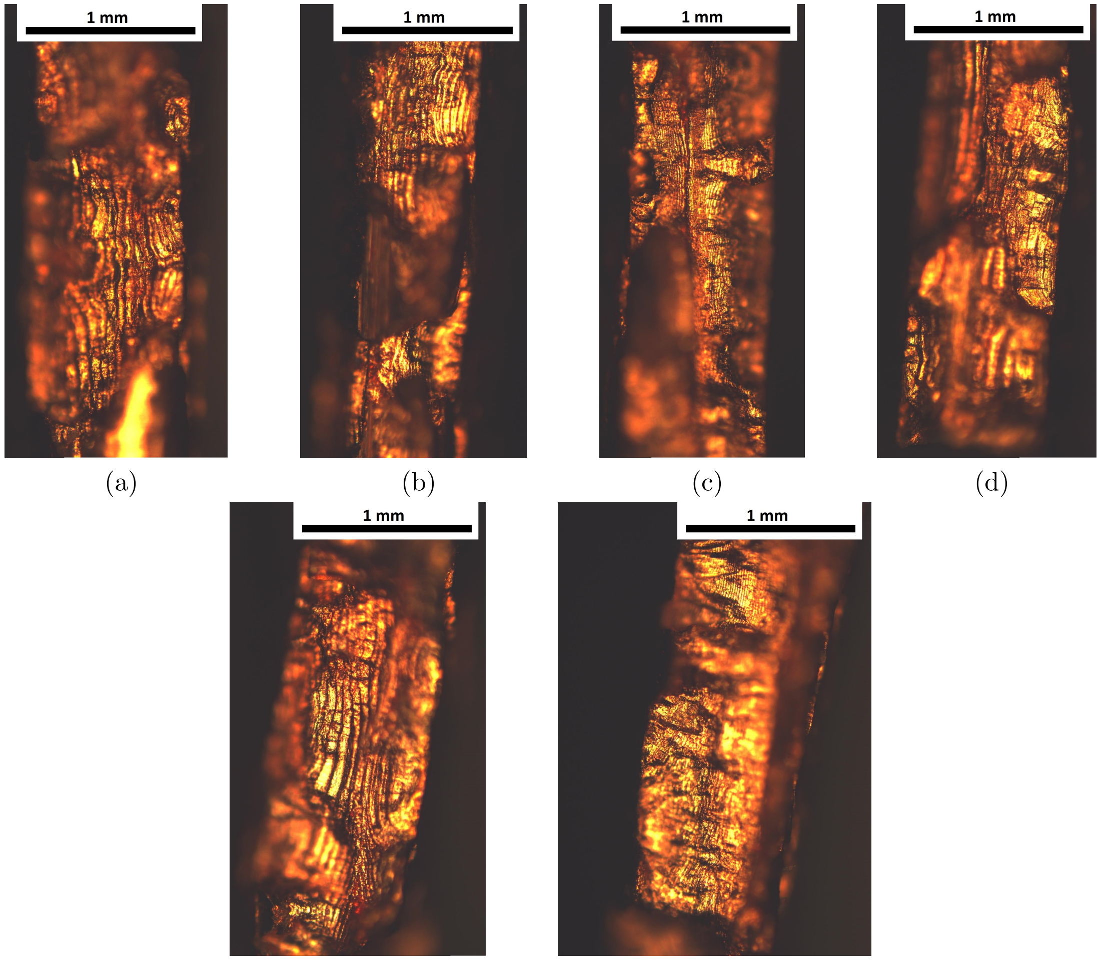

(a) (b) (c) (d) (e) (f)

Figure 7.32: Fracture surface of C110 copper annealed at (a) 600^{o}C and tested at 1.5 mm amplitude; (b) 600^{o}C tested at 1 mm amplitude; (c) 600^{o}C tested at 0.5 mm amplitude; (d) 700^{o}C tested at 1.5 mm amplitude; (e) 700^{o}C tested at 1 mm amplitude; (f) 700^{o}C tested at 0.5 mm amplitude.

7.7 Discussion

Maximum tensile force occurring in the second cycle is caused by cyclic hardening, similarly to how the maximum stress per cycle increases with the first few cycles when standard specimens are tested. Some of the higher cycle numbers for the maximum force could have been caused by the specimen rotating after the first few cycles and a step occurring. There is a very clear difference between maximum tensile force in the first and second cycle in most cases.

Maximum compressive force was usually very similar in the first and second cycle, as shown in the example Figure 7.17. If the tests where the maximum compressive force occurs in the first and second cycle were taken together, they would be the absolute majority of all tests (39 tests out of 43). The remaining four tests, which had the maximum compressive force occurring in the third and fourth cycles, could be showing this result due to stepped reduction in force, as two of them have clear steps in the force data, and two are unclear.

In all cases the small ring specimens failed on the tensile side of the hysteresis loop. In a lot of cases tensile and compressive load can be supported by the specimen after failure, that depends on the loading amplitude and the interactions of the pin and the sides of the crack, as one half could slip past the pin on the compressive stroke, as it occurred in the case of Figure 7.31 (e). Out of the specimens for which the location of failure was noted, it was evenly distributed between the top and the bottom pin, which suggests that there is no bias in stress introduced due to the way the cyclic tests are set up.

As seen from the evolution of the shape of the hysteresis loops, as the number of cycles increases the area enclosed by the loop decreases. The shape of the loop itself changes from similar to a parallelogram to a rounded parallelogram with peaks at maximum tension and maximum compression. This is likely partially caused by the thinning of the ring, the interaction of the clamps and the ring and the cyclic hardening of the material.

Generally, as displacement amplitude increases, so do the maximum forces and forces before failure (Figures 7.18, 7.19, 7.21 and 7.22), however the correlations are weak. The values of percentage reduction plots are too scattered to make any useful insights.

The relationship between the number of cycles to failure and the loading amplitude (Figure 7.20) is similar in shape to conventional fatigue life curves. This indicates the potential of the small ring specimens under cyclic loading to be used for determining fatigue life, provided a method to correlate the small ring results and standard testing results is developed. On the other hand, as all rings failed at the clamping location, it is possible that only the material that was clamped is being tested for fatigue life as opposed to the whole ring, which would likely make the results less useful.

Clamping torque does not have a consistent effect on anything, apart from loss of contact, which is unexpected. If it was the main reason why failure occurred at the clamp, the higher clamping torque should reduce the number of cycles to failure. That not being the case could mean that the scatter in the data obscures the effect of clamping, or that it indeed does not affect the cycles to failure.

The significant difference in loss of contact for tensile and compressive side of the cycle could be explained by it being governed both by the thinning of the ring at the clamping location and by the deformation of the loading setup (bending of the pin and compression of the clamping rod). While they are made from materials with similar stiffness, their geometry is significantly different. This was confirmed in Chapter 6.

Repeatability between small ring tests is very good, but it does depend on pre-load. If the pre-loads are more than a few newtons different, the resulting force-displacement curves can differ by up to 25 N, even after the pre-load is adjusted for and when the range of force is 125 N this is significant. The good agreement between the repeats ends when the specimens start to fail. When cycles to failure are considered, they are also close, within around 10 % of each other.

As small rings were being tested and the testing method was being refined, several observations about the practicality of various aspects of the testing were noted. To begin with, the current loading setup relies significantly on friction to keep the ring unloaded as the test is being set up. Considering the large variety of pre-load values observed from loss of contact, the test has to be set up very carefully in order to minimize the pre-load variation between tests and have good repeatability. If loss of contact is present the pre-load can be adjusted for, however, it is not always there.

Secondly, using a torque wrench with a set torque to clamp the rings results in significantly more consistent and realistic results. This can be seen when results from hand tightened tests are compared with the results from tests tightened with a torque wrench, especially when loss of contact is considered. Lower clamping torque has the advantage of resulting in a loss of contact more consistently, as well as not misaligning the specimen to impinge onto the setup and lead to scrapping. A good improvement to the loading setup would be to remove the torque transfer from the screw to the rod. This could be done by inserting a ball between them, however, it could easily be lost when the tests are being set up or the setup is disassembled.

Finally it is a good idea to observe the force-displacement plot as the test is going, as failure, indicated by a sharp drop of force, can be seen very clearly. This allows for the test to be stopped as soon as the specimen fails and time to not be wasted cycling a failed specimen.

Regarding the development of an interpretation method for cyclic small ring specimen test results, unlike with the development of a small ring specimen tensile test result interpretation described in Chapter 5, varying the material model parameters one at a time did not provide useful direction. Due to the FEA model having issues on the first cycle, it could not be explicitly checked whether yield stress can be determined from the first quarter cycle, similarly to how it is determined from standard cyclic results. From Chapter 5 it was concluded that Young's modulus and yield strength can be evaluated from a small ring specimen tensile test results and from this chapter it was concluded that clamping torque does not have a significant effect on the test results, it can be assumed that the first quarter cycle of the small ring specimen cyclic test is equivalent to the small ring specimen tensile test result, therefore yield stress can be calculated.

When the isotropic component of the combined hardening model is fitted to the standard cyclic test results, it requires the yield stress to have been identified, the cumulative plastic strain to have been calculated and the peak tensile and compressive stresses found. If an analogous method was investigated for small ring specimen cyclic test results, the yield stress could be evaluated as described previously, the cumulative plastic displacement could be evaluated similarly to how cumulative plastic strain was evaluated, and the peak tensile and compressive loads can be found. The main problems with this are that the compressive peak loads are lower in magnitude than tensile peak loads and that both tensile and compressive peak loads increase for a couple of cycles, then start decreasing. This means that the form of equation used for fitting the isotropic hardening component parameters cannot be used and a similar fitting method cannot be used either. The method of fitting the kinematic hardening component relies on the isotropic component having been fitted beforehand, therefore it cannot be used either. Potentially a different form of equation could be fitted to the peak loads of the small ring specimen cyclic test results and a relationship between that equation and the isotropic hardening equation could be found, however, the peak loads could depend on the materials the pin and the clamp are made from. This should be investigated using FEA as a part of Future work. As inverse analysis was the most promising method for calculating uniaxial-equivalent tensile stress-strain results, it is likely to be suitable for calculating standard-equivalent cyclic stress-strain results, provided a representative FEA model is developed. Young's modulus and yield stress can be evaluated separately, leaving potentially four coefficients for the inverse analysis to calculate. If more than one backstress is needed, that number increases to six, and, as longer simulations would be needed to match the experimental results, this method would be very computationally expensive.

7.8 Summary and Conclusions

This chapter described the development of the fixture and the testing method for loading small ring specimens cyclically. Afterwards the small ring specimen cyclic testing results are presented and discussed in relation to conventional specimen cyclic and fatigue test results.

The main conclusions from this chapter are as follows:

- Small ring specimen cyclic testing shows potential for cyclic plasticity and fatigue life testing.
- Repeatability of small ring cyclic results is good, both for cycles to failure and hysteresis loops.
- Development of an interpretation method for small ring specimen cyclic test results is more complicated than for tensile test results.

- Small ring cyclic testing setup relies significantly on friction which reduces the accuracy of the results.
- There are weak correlations between forces developed during testing and displacement amplitude.

8 Conclusions and Future Work

The objectives of this PhD project were as follows:

1. Develop a testing method for small ring specimens under tensile loading;
2. Develop a representative model for a small ring specimen under tensile loading;
3. Develop a method to calculate the bulk stress-strain behaviour from a small ring specimen tensile test results;
4. Evaluate the suitability of the small ring specimen for tensile testing;
5. Design a fixture for small ring specimens to be loaded cyclically;
6. Develop a testing method for small ring specimens under cyclic loading;
7. Develop a representative model for a small ring specimen under cyclic loading;
8. Develop a method to calculate the bulk cyclic plasticity behaviour from a small ring specimen cyclic test results;

The 1st objective was shown to be achieved in Chapter 5. A small ring specimen tensile testing method was developed based on the small ring specimen creep testing method, using the same loading setup as small ring specimen creep tests. The loading rates should be chosen according to the findings from varying the material model parameters in the representative FEA model. As the equivalent gauge length was found to vary between around 50 mm and around 30 mm for small ring specimens made of different materials and during the test, for materials which do not exhibit significant rate dependence, loading rates calculated based on those equivalent gauge length values are appropriate. To summarize the small ring specimen tensile testing method, the specimen is placed between two pins, an appropriate loading rate is applied and the test is stopped when the ring fails.

Chapter 4 shows that the 2nd objective was achieved. A representative FEA model for a small ring specimen under tensile loading was developed, using symmetry to simplify the model to a 1/8th ring model when alignment is not a concern and a full ring model when it is. It was verified by fitting a Ramberg-Osgood material model to standard specimen tensile test results, using the fitted coefficients to simulate a small ring specimen tensile test result and finding good agreement between that and experimental small ring specimen tensile test results. In the future, the following work should be completed to further develop this objective:

- Investigating compliance using FEA, including the effects of elevated temperature on setup materials;
- Developing an analytical model based on Timoshenko beam theory;
- Using a full stress-strain curve as opposed to a material model.

Chapter 5 also shows steps were taken towards achieving the 3rd objective. Several methods for recalculating bulk material stress-strain behaviour from small ring specimen tensile test data were investigated, with inverse analysis being the most successful and consistently applicable. In the future, the following work should be completed to further develop this objective:

- Implementing the use of a piecewise inverse analysis as opposed to varying material model parameters;
- Teaching the neural network with a wider set of data;
- Utilizing full force-displacement curves and full stress-strain curves as opposed to fitted models to reduce error.

It can be stated that the 4th objective was achieved as well, as an overall conclusion of Chapters 4 and 5. The small ring specimens were found to be suitable for tensile testing. Misalignment was found to have no significant effect on the results, which is a significant advantage over a lot of other small specimen testing techniques. In the future, the following work should be completed to further develop this objective:

- Using an induction heating setup;
- Investigating the effect of significant material anisotropy;
- Investigating the effect of different surface roughness;
- Investigating the effect of different manufacturing methods;
- Validating the effect of varied geometry;
- Testing a wider variety of materials;
- Investigating compliance experimentally and using FEA;
- Validating the effects of misalignment experimentally;
- Developing a method to calculate UTS from small ring specimen tensile testing results.

Moving on to the cyclic loading of a small ring specimen, the 5^{th} and 6^{th} objectives were shown to be achieved in Chapter 7. The fixture suitable for loading the small ring specimen cyclically was developed based on a clamped ring concept and an appropriate method to use it was established, partially based on the design of the setup itself and partially on what was found to work well during testing. It performed well, but shortfalls were identified, which would require design improvements and a new fixture to be made.

Steps were taken towards achieving the 7^{th} objective, using a method analogous to the one used to develop a representative model for a small ring specimen under tensile loading, as described in Chapter 6. The model has issues with modelling contact, due to nodes in the FEA model coming into contact as the cyclic loading progresses. Another issue was that the forces in the simulated small ring specimen cyclic test results were significantly lower than the forces in the experimental small ring specimen cyclic test results. This could be caused by the surface hardening which occurred due to machining the specimens. In the future, the following work should be completed to further develop this objective:

- Eliminating the spikes in force-displacement curves by
  - Using a coupled finite element and boundary element model;
  - Splicing together the results of a tensile model and a cyclic model, with the tensile model used for the first quarter cycle;
  - Using a material-specific mesh to avoid the spikes;
- Investigating the effects of pin and rod material properties on the results;
- Incorporating pre-tension and pre-compression into the FEA model to investigate their effects;
- Investigating compliance using FEA;
- Developing a relationship between ring clamping torque and deformation resulting from clamping;
- Performing interrupted testing and measuring dislocation density to validate the development of the stress state modelled using FEA;

As the 7$^{\text{th}}$ objective was not achieved, the 8$^{\text{th}}$ objective could not be achieved either. However, it was found that misalignment had no significant effect on the test results, and that cyclic loading of small ring specimens is a promising technique for calculating cyclic plasticity parameters and potentially even fatigue life, provided accurate calculation methods are developed. In the future, the following work should be completed to further develop this objective:

- Investigating the effect of significant material anisotropy;
- Investigating the effect of different surface roughness;
- Investigating the effect of different manufacturing methods;

- Validating the effect of varied geometry;
- Testing a wider variety of materials;
- Investigating compliance experimentally and using FEA;
- Validating the effects of misalignment experimentally;
- Validating the effects of coefficient of friction experimentally;
- Testing at lower displacement amplitudes.

While developing a method to evaluate fatigue life using small ring specimens was not an objective of this project, small ring specimen test results do show promise for this. In the future, the following work should be completed to further explore it:

- Further investigation of small ring specimen cyclic testing fracture surfaces to verify fatigue damage using SEM;
- Provided fatigue failure is confirmed, a method to reconstruct an S-N curve from small ring specimen test results could be developed, both experimentally and numerically.

9 References

[1] T. H. Hyde and W. Sun. A novel, high-sensitivity, small specimen creep test. *Journal of Strain Analysis for Engineering Design*, 44(3):171–185, 2009.

[2] R. E. Smallman and A. H. W. Ngan. *Physical Metallurgy and Advanced Materials.* Elsevier, Oxford, UK, 7th edition, 2007.

[3] A. Kelly and K. M. Knowles. *Crystallography and Crystal Defects.* John Wiley & Sons, Incorporated, New Jersey, USA, 2020.

[4] R. E. Smallman and R. J. Bishop. *Modern Physical Metallurgy and Materials Engineering - Science, Process, Applications.* Elsevier, Oxford, UK, 6th edition, 1999.

[5] P. P. Benham. *Mechanics of engineering materials.* Longman, Harlow, UK, 2nd edition, 1996.

[6] R. Hooke. De potentia restitutiva. 1678.

[7] S. D. Poisson. Mémoire sur l'Équilibre et le mouvement des corps Élastiques. 1828.

[8] R. V. Mises. Mechanik der festen korper im plastiseh-deformablen zustand. *Naehr. kgl. Ges. Wiss. Gottingen, Math Phys Klasse*, pages 582–592, 1913.

[9] H. Tresca. Memoire sur l'ecoulement des corps solids. *Memoire Presentes par Divers Savants, Acad Sci Paris*, 20:75–135, 1872.

[10] N. E. Dowling. *Mechanical behavior of materials : engineering methods for deformation, fracture, and fatigue.* Pearson, Harlow, UK, 4th international edition, 2013.

[11] J. L. Chaboche, K. Dang-Van, and G. Cordier. Modelization of the strain memory effect on the cyclic hardening of 316 stainless steel. *Berlin*, 1979.

[12] J. L. Chaboche and G. Rousselier. On the plastic and viscoplastic constitutive equations, parts I and II. *Pressure Vessel Piping*, 105:153–164, 1983.

[13] L. F. Coffin. A study of the effects of cyclic thermal stresses on ductile metal. *Trans ASME*, 76:931–950, 1954.

[14] S. S. Manson. Behaviour of materials under conditions of thermal stress. *In: NACA TN-2933, National Advisory Committee for Aeronautics*, 1954.

[15] F. C. Campbell, editor. *Phase diagrams [electronic resource] : understanding the basics*. ASM International, Ohio, USA, 2012.

[16] R. Foret, Z. Hodis, and J. Sopousek. Redistribution of carbon and nitrogen in heterogeneous weld joints of creep-resistant steels (P91/P22). *METAL 2012 - Conference Proceedings, 21st International Conference on Metallurgy and Materials*, pages 478–484, 2012.

[17] The Engineering ToolBox. Young's modulus of elasticity for metals and alloys. https://www.engineeringtoolbox.com/young-modulus-d_773.html, 2004. Accessed 2020-11-15.

[18] G. E. Dieter. *Mechanical metallurgy*. McGraw-Hill, London, UK, SI metric edition, 1988.

[19] G. N. Vigilante, A. Fish, G. P. O'Hara, D. Crayon, and T. Hickey. Elevated temperature properties of steels. Technical report, US Army Armament Research, Developement and engineering center, 1996.

[20] The British Standards Institution. BS ISO 12106:2017 Metallic materials — Fatigue testing — Axial-strain controlled method, 2017.

[21] D. W. A. Rees. *Basic engineering plasticity : an introduction with engineering and manufacturing applications*. Elsevier, Amsterdam, the Netherlands, 2006.

[22] The British Standards Institution. BS EN ISO 6892-1:2019 Metallic materials. Tensile testing. Method of test at room temperature, 2016.

[23] The British Standards Institution. BS EN 2002-1:2005 Aerospace series. Metallic materials. Test methods. Tensile testing at ambient temperature, 2005.

[24] The British Standards Institution. BS EN ISO 4136:2012 Destructive tests on welds in metallic materials. Transverse tensile test, 2012.

[25] The British Standards Institution. BS EN ISO 6892-2:2018 Metallic materials. Tensile testing. Method of test at elevated temperature, 2018.

[26] The British Standards Institution. BS EN 2002-2:2005 Aerospace series. Metallic materials. Test methods. Tensile testing at elevated temperature, 2005.

[27] The British Standards Institution. BS EN ISO 6892-3:2015 Metallic materials. Tensile testing. Method of test at low temperature, 2015.

[28] The British Standards Institution. BS ISO 6892-4:2015 Metallic materials. Tensile testing. Method of test in liquid helium, 2015.

[29] The British Standards Institution. BS EN ISO 26203-1:2018 Metallic materials. Tensile testing at high strain rates. Elastic-bar-type systems, 2018.

[30] The British Standards Institution. BS ISO 16842:2014 Metallic materials. Sheet and strip. Biaxial tensile testing method using a cruciform test piece, 2014.

[31] The British Standards Institution. BS EN ISO 8496:2013 Metallic materials. Tube. Ring tensile test, 2013.

[32] The British Standards Institution. BS ISO 1099:2017 Metallic materials — Fatigue testing — Axial force-controlled method, 2017.

[33] The British Standards Institution. BS 3518-1:1993 Methods of fatigue testing — Part 1: Guide to general principles, 1993.

[34] The British Standards Institution. BS 7270:2006 Metallic materials – Constant amplitude strain controlled axial fatigue – Method of test, 2006.

[35] The British Standards Institution. BS 3518-3:1963 Methods of fatigue testing — Part 3: Direct stress fatigue tests, 1963.

[36] The British Standards Institution. BS ISO 12111:2011 Metallic materials — Fatigue testing — Strain-controlled thermomechanical fatigue testing method, 2011.

[37] The British Standards Institution. BS EN ISO 3928:2016 Sintered metal materials, excluding hardmetals. Fatigue test pieces, 2006.

[38] The British Standards Institution. PD ISO/TR 12112:2018 Metallic materials — Principles and designs for multiaxial fatigue testing, 2018.

[39] The British Standards Institution. BS ISO 12110-1:2013 Metallic materials. Fatigue testing. Variable amplitude fatigue testing. General principles, test method and reporting requirements, 2013.

[40] The British Standards Institution. BS ISO 1352:2011 Metallic materials — Torque controlled fatigue testing, 2011.

[41] The British Standards Institution. BS ISO 1143:2010 Metallic materials — Rotating bar bending fatigue testing, 2010.

[42] H. Liu, R. Chen, M. Wen, L. Zhang, and Y. Shen. Optimizing parallel section length for small tensile specimen with fabrication non-uniformity in thickness. *Fusion Engineering and Design*, 147, 2019.

[43] G. E. Lucas, G. R. Odette, and J. W. Sheckherd. *The Use of Small-Scale Specimens for Testing Irradiated Material, ASTM STP S88.* American Society for Testing and Materials, Philadelphia, 1986. pp. 112-140.

[44] D. Holländer, D. Kulawinski, A. Weidner, M. Thiele, H. Biermann, and U. Gampe. Small-scale specimen testing for fatigue life assessment of service-exposed industrial gas turbine blades. *International Journal of Fatigue*, 92:262–271, 2016.

[45] D. Holländer, D. Kulawinski, M. Thiele, C. Damm, S. Henkel, H. Biermann, and U. Gampe. Investigation of isothermal and thermo-mechanical fatigue behavior of the nickel-base su-

peralloy IN738LC using standardized and advanced test methods. *Materials Science and Engineering A*, 670:314–324, 2016.

[46] H. Sakasegawa, X. Chen, T. Kato, H. Tanigawa, M. Ando, J. W. Geringer, S. Ukai, and S. Ohtsuka. Strain evaluation using a non-contact deformation measurement system in tensile tests of irradiated F82H and 9Cr ODS steels. *Nuclear Materials and Energy*, 16:108–113, 2018.

[47] P. Konopik, R. Prochazka, M. Rund, and J. Dzugan. Novel methods for high-cycle fatigue life determination. *Key Engineering Materials*, 810:40–45, 2019.

[48] E. Nakayama, M. Fukumoto, M. Miyahara, K. Okamura, H. Fujimoto, K. Fukui, and T. Kitamura. Evaluation of local fatigue strength in spot weld by small specimen. *Fatigue and Fracture of Engineering Materials and Structures*, 33(5):267–275, 2010.

[49] G. M. Castelluccio, A. A. Yawny, J. E. Perez Ipiña, and H. A. Ernst. In situ evaluation of tensile properties of heat-affected zones from welded steel pipes. *Strain*, 48(1):68–74, 2012.

[50] A. Hojna, F. Di Gabriele, H. Hadraba, R. Husak, I. Kubena, L. Rozumova, P. Bublikova, J. Kalivodova, and J. Matejicek. Fracture behaviour of the 14Cr ODS steel exposed to helium and liquid lead. *Journal of Nuclear Materials*, 490:143–154, 2017.

[51] X. Chen, Z. Liu, G. He, and H. Xie. A novel integrated tension-compression design for a mini split Hopkinson bar apparatus. *Review of Scientific Instruments*, 85(3), 2014.

[52] M. Sanders, F. Di Bella, and H. Liang. Small-scale mechanical characterization of aluminum and titanium alloys. *Journal of Testing and Evaluation*, 39(1):9–15, 2011.

[53] A. Husain, D. K. Sehgal, and R. K. Pandey. An inverse finite element procedure for the determination of constitutive tensile behavior of materials using miniature specimen. *Computational Materials Science*, 31(1-2):84–92, 2004.

[54] S. Knitel, P. Spätig, and H. P. Seifert. An inverse method based on finite element model to derive the plastic flow properties from non-standard tensile specimens of Eurofer97 steel. *Nuclear Materials and Energy*, 9(Supplement C):311 – 316, 2016.

[55] Z. Špirit, M. Chocholoušek, and M. Šíma. Mechanical testing of anisotropy in ODS steel tubes. In *IOP Conference Series: Materials Science and Engineering*, volume 179. Institute of Physics Publishing, 2017.

[56] S. Szávai, P. Rózsahegyi, J. Dudra, R. Beleznai, Z. Bézi, and S. Jónás. Determination of mechanical properties of operating components using instrumented hardness testing, small punch and small size tensile testing techniques. *Lecture Notes in Mechanical Engineering*, pages 135–150, 2017.

[57] H. Ge, Q. Huang, J. Xin, and K. Sun. Small specimen test techniques applied to evaluate the mechanical properties of CLAM steel. *Journal of Fusion Energy*, 34(5):1124–1128, 2015.

[58] M. Březina, J. Petzová, L. Kupča, and M. Kapusňák. Utilization of SPT techniques for evaluation of changes in the properties of the VVER-440 reactor pressure vessel steels after their irradiation in the research and power reactors. volume 1A. American Society of Mechanical Engineers (ASME), 2015.

[59] B. J. Kim, R. Kasada, and A. Kimura. Effects of chemical composition on the impact properties of A533B steels. *Materials Science Forum*, 654-656:2895–2898, 2010.

[60] B. J. Kim, R. Kasada, A. Kimura, and H. Tanigawa. Evaluation of grain boundary embrittlement of phosphorus added F82H steel by SSTT. *Journal of Nuclear Materials*, 421(1-3):153–159, 2012.

[61] ASTM International. ASTM E384-17 Standard test method for microindentation hardness of materials, 2017.

[62] K. Kumar, A. Pooleery, K. Madhusoodanan, R. N. Singh, A. Chatterjee, B. K. Dutta, and R. K. Sinha. Optimisation of thickness of miniature tensile specimens for evaluation of mechanical properties. *Materials Science and Engineering A*, 675:32–43, 2016.

[63] M. N. Gussev, R. H. Howard, K. A. Terrani, and K. G. Field. Sub-size tensile specimen design for in-reactor irradiation and post-irradiation testing. *Nuclear Engineering and Design*, 320:298–308, 2017.

[64] N. Kashaev, M. Horstmann, V. Ventzke, S. Riekehr, and N. Huber. Comparative study of mechanical properties using standard and micro-specimens of base materials Inconel 625, Inconel 718 and Ti-6Al-4 V. *Journal of Materials Research and Technology*, 2(1):43–47, 2013.

[65] W. Vandermeulen, J. L. Puzzolante, and M. Scibetta. Understanding of tensile test results on small size specimens of certified reference material BCR-661. *Journal of Testing and Evaluation*, 45(2):695–703, 2017.

[66] I. V. Lomakin, A. R. Arutyunyan, R. R. Valiev, F. A. Gadzhiev, and M. Y. Murashkin. Design and evaluation of an experimental technique for mechanical and fatigue testing of sub-sized samples. *Experimental Techniques*, 42(3):261–270, 2018.

[67] T. E. García, B. Arroyo, C. Rodríguez, F. J. Belzunce, and J. A. Álvarez. Small punch test methodologies for the analysis of the hydrogen embrittlement of structural steels. *Theoretical and Applied Fracture Mechanics*, 86:89–100, 2016.

[68] T. E. García, C. Rodríguez, F. J. Belzunce, and I. I. Cuesta. Development of a new methodology for estimating the CTOD of structural steels using the small punch test. *Engineering Failure Analysis*, 50:88–99, 2015.

[69] M. Fernández, C. Rodríguez, F. J. Belzunce, and T. E. García. Mechanical behaviour estimation of synchronizer hubs using miniaturized specimens. European Powder Metallurgy Association (EPMA), 2015.

[70] M. Song, K. Guan, W. Qin, J. A. Szpunar, and J. Chen. Size effect criteria on the small punch test for AISI 316L austenitic stainless steel. *Materials Science and Engineering A*, 606:346–353, 2014.

[71] S. D. Norris and J. D. Parker. Deformation processes during disc bend loading. *Materials Science and Technology*, 12(2):163–170, 1996.

[72] T. E. García, C. Rodríguez, F. J. Belzunce, and C. Suárez. Estimation of the mechanical properties of metallic materials by means of the small punch test. *Journal of Alloys and Compounds*, 582:708–717, 2014.

[73] I. Klevtsov, A. Dedov, and A. Molodtsov. Measurement of the tensile and yield strength of boiler steels by small punch and tensile test methods [aurukatlateraste tõmbetugevuse ja voolepiiri mõõtmine kuuliga surumise ning tõmbekatse meetodil]. *Estonian Journal of Engineering*, 15(2):99–107, 2009.

[74] J. Isselin and T. Shoji. Yield strength evaluation by small-punch test. *Journal of Testing and Evaluation*, 37(6):531–537, 2009.

[75] R. V. Prakash, T. Ramesh, N. Raju, and S. Suresh. Correlation of tensile properties of pressure vessel steels by shear punch and small punch test methods. In *International Mechanical Engineering Congress and Exposition - 2012, vol 3, Pts A-C: Design, Materials, and Manufacturing*, pages 635–640, 2013. ASME International Mechanical Engineering Congress and Exposition, Houston, TX, Nov 09-15, 2012.

[76] E. Fleury and J. S. Ha. Small punch tests to estimate the mechanical properties of steels for steam power plant: I. mechanical strength. *International Journal of Pressure Vessels and Piping*, 75(9):699–706, 1998.

[77] V. Karthik, K. Laha, P. Parameswaran, K. V. Kasiviswanathan, and B. Raj. Small specimen test techniques for estimating the tensile property degradation of mod 9Cr-1Mo steel on thermal aging. *Journal of Testing and Evaluation*, 35(4):438–448, 2007.

[78] M. M. Assas, A. Husain, and D. K. Sehgal. Identification of mechanical characteristics of materials using diminutive specimen - an empirical study. In *Procedia Engineering*, volume 10, pages 3109–3116. Elsevier Ltd, 2011.

[79] C. Rodríguez, J. García Cabezas, E. Cárdenas, F.J. Belzunce, and C. Betegón. Mechanical properties characterization of heat-affected zone using the small punch test. *Welding Journal (Miami, Fla)*, 88(9):188–192, 2009.

[80] S. Arunkumar and R. V. Prakash. Estimation of tensile properties of pressure vessel steel through automated ball indentation and small punch test. *Transactions of the Indian Institute of Metals*, 69(6):1245–1256, 2016.

[81] P. Maksimkin, S. V. Ruban, Y. Y. Nurgaly, and M. P. Short. Studying the changes in the mechanical properties of neutron-irradiated chromium-nickel steels using the "shear punch" method. *Problems of Atomic Science and Technology*, 120(2):82–90, 2019.

[82] E. Priel, B. Mittelman, S. Haroush, A. Turgeman, R. Shneck, and Y. Gelbstein. Estimation of yield and ultimate stress using the small punch test method applied to non-standard specimens: A computational study validated by experiments. *International Journal of Mechanical Sciences*, 135:484–498, 2018.

[83] R. Kopriva, M. Brumovský, M. Kytka, M. Lasan, J. Siegl, and K. Matocha. Application of miniature small punch test specimen in determination of tensile properties. volume STP1576-EB, pages 1–8. ASTM International, 2015.

[84] I. I. Cuesta and J. M. Alegre. Hardening evaluation of stamped aluminium alloy components using the small punch test. *Engineering Failure Analysis*, 26:240–246, 2012.

[85] S. Davies, S. Jeffs, R. Lancaster, and G. Baxter. High temperature deformation mechanisms in a DLD nickel superalloy. *Materials (Basel, Switzerland)*, 10(5):457, 2017.

[86] P. M. Bravo Díez, M. Preciado Calzada, D. Cárdenas Gonzalo, and J. Calaf Chica. Change of mechanical properties of AM60B alloy with heat treatments and its correlation with small punch tests. *Theoretical and Applied Fracture Mechanics*, 86:101–108, 2016.

[87] R. V. Kulkarni, K. V. Mani Krishna, S. Neogy, D. Srivastava, E. Ramadasan, R. S. Shriwastaw, B. N. Rath, N. Saibaba, S. K. Jha, and G. K. Dey. Mechanical properties of Zr-2.5to heat treatments in α+ βphase field. *Journal of Nuclear Materials*, 451(1-3):300–312, 2014.

[88] Y. C. Kim, K. H. Kim, and D. Kwon. Nondestructive mechanical property assessment using instrumented indentation testing. In *Proceedings of the International Offshore and Polar Engineering Conference*, volume 4, pages 312–315, 2010.

[89] S. Ghosh, S. Yadav, and G. Das. Ball indentation technique: A currently developed tool to study the effect of various heat treatments on the mechanical properties of En24 steel. *Materials Letters*, 62(24):3966–3968, 2008.

[90] T. Ramesh, R. V. Prakash, S. Suresh, and N. Raju. Evaluation of tensile properties of pressure vessel materials by shear punch test method. *Applied Mechanics and Materials*, 187:53–57, 2012.

[91] D. D. Awale, A. R. Ballal, M. M. Thawre, V. D. Vijayanand, J. G. Kumar, and G. V. P. Reddy. Microstructural investigation and mechanical properties evaluation using miniature specimen testing of various constituents of dissimilar weld joint. *Journal of Nuclear Materials*, 532, 2020.

[92] T. Suresh Kumar, A. Nagesha, J. Ganesh Kumar, P. Parameswaran, and R. Sandhya. Influence of thermal aging on tensile and low cycle fatigue behavior of type 316LN austenitic stainless steel weld joint. *Metallurgical and Materials Transactions A: Physical Metallurgy and Materials Science*, 49(8):3257–3273, 2018.

[93] S. Nagaraju, J. GaneshKumar, P. Vasantharaja, M. Vasudevan, and K. Laha. Evaluation of strength property variations across 9Cr-1Mo steel weld joints using automated ball indentation (ABI) technique. *Materials Science and Engineering A*, 695:199–210, 2017.

[94] R. Pamnani, V. Karthik, T. Jayakumar, M. Vasudevan, and T. Sakthivel. Evaluation of mechanical properties across micro alloyed HSLA steel weld joints using Automated Ball Indentation. *Materials Science and Engineering A*, 651:214–223, 2016.

[95] D. R. Barbadikar, A. R. Ballal, D. R. Peshwe, J. Ganeshkumar, K. Laha, and M. D. Mathew. A study on the effect of tempering temperature on tensile properties of P92 steel by automated ball indentation technique. volume 86, pages 910–918. Elsevier Ltd, 2014.

[96] J. Brumek, B. Strnadel, and I. Dlouhý. New approach to stress-strain curve prediction using ball indentation test. volume 1, pages 1049–1054, 2011.

[97] J. G. Kumar, V. D. Vijayanand, and K. Laha. Finite element simulation of plastic deformation of 316ln stainless steel during automated ball indentation test. *Journal of Testing and Evaluation*, 48(4), 2020.

[98] B. Li, S. Zhang, J. Li, J. Wang, and S. Lu. Quantitative evaluation of mechanical properties of machined surface layer using automated ball indentation technique. *Materials Science and Engineering A*, 773, 2020.

[99] J. Ganesh Kumar and K. Laha. Influence of some test parameters on automated ball indentation test results. *Experimental Techniques*, 42(1):45–54, 2018.

[100] M. Das, T.K. Pal, and G. Das. Use of portable automated ball indentation system to evaluate mechanical properties of steel pipes. *Transactions of the Indian Institute of Metals*, 65(2):197–203, 2012.

[101] M. Puchnin, O. Trudonoshyn, O. Prach, and F. Pešlová. Comparison of ABI technique and standard methods in measuring mechanical properties of aluminium Al-aloys. *Manufacturing Technology*, 16(3):37–38, 2016.

[102] O. Trudonoshyn, M. Puchnin, and O. Prach. Use of the ABI technique to measure the mechanical properties of aluminium alloys: Effect of heat-treatment conditions on the mechanical properties of alloys. *Materiali in Tehnologije*, 50(3):427–431, 2016.

[103] D. C. Patil, K. Venkateswarlu, S. A. Kori, G. Das, M. Das, S. N. Alhajeri, and T. G. Langdon. Mechanical property evaluation of an Al-2024 alloy subjected to HPT processing. volume 63. Institute of Physics Publishing, 2014.

[104] H.R. Ammar, F.M. Haggag, A.S. Alaboodi, and F.A. Al-Mufadi. Nondestructive measurements of flow properties of nanocrystalline Al-Cu-Ti alloy using automated ball indentation (ABI) technique. *Materials Science and Engineering A*, 729:477–486, 2018.

[105] F. Wang, J. Zhao, and N. Zhu. Constitutive equations and ANN approach to predict the flow stress of Ti-6Al-4V alloy based on ABI tests. *Journal of Materials Engineering and Performance*, 25(11):4875–4884, 2016.

[106] H. Wang, T. Xu, and B. Shou. Determination of material strengths by hydraulic bulge test. *Materials*, 10(1):23, 2017.

[107] S. Jitsukawa, M. Kizaki, A. Umino, K. Shiba, and A. Hishinuma. Methods and devices for small specimen testing at the Japan atomic energy research institute. Number 1204, pages 289–307. Publ by ASTM, Philadelphia, PA, United States, 1993.

[108] J. Džugan, R. Prochazka, and P. Konopik. *Micro-Tensile Test Technique Development and Application to Mechanical Property Determination*. 2015.

[109] M. Gussev. Role of scale factor during tensile testing of small specimens. *Small Specimen Test Techniques*, 6:1–19, 01 2014.

[110] A. Kolhatkar, V. Karthik, G. M. S. K. Chaitanya, A. Kumar, and D. Ramchandran. Development and validation of a miniature tensile specimen for determination of mechanical properties. *Journal of Testing and Evaluation*, 47(5), 2019.

[111] G. Chen, S. C. Shan, X. Chen, and H. Yuan. Ratcheting and fatigue properties of the high-nitrogen steel X13CrMnMoN18-14-3 under cyclic loading. *Computational Materials Science*, 46(3):572–578, 2009.

[112] K. Kumar, A. Pooleery, K. Madhusoodanan, R. N. Singh, J. K. Chakravartty, R. S. Shriwastaw, B. K. Dutta, and R. K. Sinha. Evaluation of ultimate tensile strength using miniature disk bend test. *Journal of Nuclear Materials*, 461:100–111, 2015.

[113] S. Nogami, W. Guan, M. Toyota, and A. Hasegawa. Fatigue life prediction of ferritic/martensitic steels based on universal slope equations and tensile properties obtained using small specimen. *Fusion Engineering and Design*, 125:330–336, 2016.

[114] S. Nogami, W. Guan, M. Toyota, and A. Hasegawa. Fatigue life prediction of ferritic/martensitic steels based on universal slope equations and tensile properties obtained using small specimen. *Fusion Engineering and Design*, 125:330–336, 2017.

[115] K. Milička and F. Dobeš. Small punch testing of P91 steel. *International Journal of Pressure Vessels and Piping*, 83(9):625–634, 2006.

[116] S. Ghosh, M. Tarafder, S. Sivaprasad, and S. Tarafder. Experimental and numerical study of ball indentation for evaluation of mechanical properties and fracture toughness of structural steel. *Transactions of the Indian Institute of Metals*, 63(2-3):617–621, 2010.

[117] H. R. Abedi, A. Zarei-Hanzaki, E. Karimi, and N. Haghdadi. The shear punch jump test - a novel application of a small specimen testing technique for rapid evaluation of deformation mechanisms. *Experimental Mechanics*, 55(8):1569–1573, 2015.

[118] T. E. García, C. Rodríguez, F. J. Belzunce, I. Pe nuelas, and I. I. Cuesta. Estimation of the fracture toughness of structural steels by means of the CTOD evaluation on notched small punch specimens. *Procedia Materials Science*, 3(Supplement C):861 – 866, 2014.

[119] M. Abendroth and M. Kuna. Determination of ductile material properties by means of the small punch test and neural networks. *Advanced Engineering Materials*, 6(7):536–540, 2004.

[120] M. Abendroth and M. Kuna. Identification of ductile damage and fracture parameters from the small punch test using neural networks. *Engineering Fracture Mechanics*, 73(6):710–725, 2006.

[121] T. Linse and M. Kuna. Characterization of reactor vessel steels in the brittle-ductile transition region. In *17th European Conference on Fracture 2008: Multilevel Approach to Fracture of Materials, Components and Structures*, volume 1, pages 765–772, 2008.

[122] T. Kato, M. Ohata, S. Nogami, and H. Tanigawa. Evaluation of impacts of stress triaxiality on plastic deformability of RAFM steel using various types of tensile specimen. *Fusion Engineering and Design*, 109(B):1631–1636, 2016.

[123] C. Kannan, S. Bhattacharya, D. K. Sehgal, and R. K. Pandey. Effect of specimen thickness and punch diameter in evaluation of small punch test parameters toward characterization of mechanical properties of Cr-Mo steels. *Journal of Testing and Evaluation*, 42(6):1501–1509, 2014.

[124] J. Siegl, P. Haušild, A. Janča, R. Kopřiva, and M. Kytka. Characterisation of mechanical properties by small punch test. *Key Engineering Materials*, 606:15–18, 2014.

[125] R. Lacalle, J.A. Álvarez, and F. Gutiérrez-Solana. Analysis of key factors for the interpretation of small punch test results. *Fatigue and Fracture of Engineering Materials and Structures*, 31(10):841–849, 2008.

[126] D. Sunjaya, T. Wei, R. Harrison, and W. Y. Yeung. Finite element modelling of small punch test on 304H stainless steel. *Key Engineering Materials*, 345-346 II:1165–1168, 2007.

[127] J. S. Cheon and I. S. Kim. Evaluation of thermal aging embrittlement in CF8 duplex stainless steel by small punch test. *Journal of Nuclear Materials*, 278(1):96–103, 2000.

[128] M. D. Richardson, S. Connolly, M. Gorley, B. P. Wynne, and E. Surrey. Influence of surface finish on small punch testing of 9Cr Eurofer-97 steel. *Journal of Testing and Evaluation*, 48(2):1310–1318, 2020.

[129] H. T. Pham and T. Iwamoto. An evaluation of fracture properties of type-304 austenitic stainless steel at high deformation rate using the small punch test. *International Journal of Mechanical Sciences*, 144:249–261, 2018.

[130] C. Ye, J. B. Vogt, and I. Proriol Serre. Liquid metal embrittlement of the T91 steel in lead bismuth eutectic: The role of loading rate and of the oxygen content in the liquid metal. *Materials Science and Engineering A*, 608:242–248, 2014.

[131] J. Mak, T. Wei, R. Wuhrer, W. Yeung, G. Heness, and Z. Di. A solution for estimating the tensile yield strength from small specimens. *Journal of Testing and Evaluation*, 41(4):647–650, 2013.

[132] I. Simonovski, S. Holmström, and M. Bruchhausen. Small punch tensile testing of curved specimens: Finite element analysis and experiment. *International Journal of Mechanical Sciences*, 120(Supplement C):204 – 213, 2017.

[133] R. V. Prakash and S. Arunkumar. Influence of friction on the response of small punch test. *Transactions of the Indian Institute of Metals*, 69(2):617–622, 2016.

[134] S. Nogami, T. Itoh, H. Sakasegawa, H. Tanigawa, E. Wakai, A. Nishimura, and A. Hasegawa. Study on fatigue life evaluation using small specimens for testing neutron-irradiated materials. *Journal of Nuclear Science and Technology*, 48(1):60–64, 2011.

[135] S. Nogami, Y. Sato, A. Tanaka, A. Hasegawa, A. Nishimura, and H. Tanigawa. Effect of specimen shape on the low cycle fatigue life of reduced activation ferritic/martensitic steel. *Journal of Nuclear Science and Technology*, 47(1):47–52, 2010.

[136] S. W. Kim, H. Tanigawa, T. Hirose, and A. Kohyama. Effects of surface morphology and distributed inclusions on the low cycle fatigue behavior of miniaturized specimens of F82H steel. volume 1502 STP, pages 159–169. American Society for Testing and Materials, 2009.

[137] S. Nogami, C. Hisaka, M. Fujiwara, E. Wakai, and A. Hasegawa. High temperature fatigue life evaluation using small specimen. *Plasma and Fusion Research*, 12:1405022–1–1405022–6, 2017.

[138] P. S. De, C. M. Obermark, and R. S. Mishra. Development of a reversible bending fatigue test bed to evaluate bulk properties using sub-size specimens. *Journal of Testing and Evaluation*, 36(4):402–405, 2008.

[139] P. S. De, R. S. Mishra, and C. B. Smith. Effect of microstructure on fatigue life and fracture morphology in an aluminum alloy. *Scripta Materialia*, 60(7):500–503, 2009.

[140] R. V. Prakash and A. Subbiah. Evaluation of fatigue data through miniature specimen test techniques. In *American Society of Mechanical Engineers, Pressure Vessels and Piping Division (Publication) PVP*, volume 1A. American Society of Mechanical Engineers (ASME), 2015.

[141] M. Hayakawa, E. Nakayama, K. Okamura, M. Yamamoto, and K. Shizawa. Development of micro-shear fatigue test and its application to single crystal of pure iron. In I. F. Pariente,

J. A. F. O. Correia, A. M. P. De Jesus, Belzunce F. J., and A. Fernandez-Canteli, editors, *Procedia Engineering*, volume 160, pages 167–174. Elsevier Ltd, 2016.

[142] J. Volák and Z. Bunda. Comparison of selected fatigue characteristics of P92 steel and 15CH2NMFA steel. pages 885–890. Tanger Ltd., 2016.

[143] S. Nogami, A. Nishimura, E. Wakai, H. Tanigawa, T. Itoh, and A. Hasegawa. Development of fatigue life evaluation method using small specimen. *Journal of Nuclear Materials*, 441(1-3):125–132, 2013.

[144] T. Sugimoto, T. Itoh, M. Sakane, and C. Hisaka. Development of fatigue testing machine for small sized specimen in liquid environment. *Key Engineering Materials*, 734:185–193, 2017.

[145] T. Hirose, H. Tanigawa, M. Ando, A. Kohyama, Y. Katoh, and S. Jitsukawa. Small specimen test technology for evaluation of fatigue properties of fusion structural materials. *Materials Transactions*, 42(3):389–392, 2001.

[146] I. Černý, D. Mikulová, and I. Fürbacher. Fatigue strength and failure mechanisms of nitrided small parts of a 30CrMoV9 steel. *Materials and Manufacturing Processes*, 26(1):1–6, 2011.

[147] Y. Murase, J. Nagakawa, and N. Yamamoto. In-beam fatigue behavior of 20% cold-worked 316 stainless steel at 300 °C. *Fusion Engineering and Design*, 81(8-14 Part B):999–1003, 2006.

[148] S. I. Komazaki, R. Jojima, N. Muraoka, S. Nogami, M. Kamaya, C. Hisaka, M. Fujiwara, and A. Nitta. Development of small bulge fatigue testing technique using small disk-type specimen. *Fatigue and Fracture of Engineering Materials and Structures*, 43(16), 2019.

[149] M. M. Parvez, Y. Chen, and F. Liou. Comparison of fatigue performance between additively manufactured and wrought 304L stainless steel using a novel fatigue test setup. 2020.

[150] A. S. Haidyrah, J. W. Newkirk, and C. H. Castaño. Weibull statistical analysis of Krouse type bending fatigue of nuclear materials. *Journal of Nuclear Materials*, 470:244 – 250, 2016.

[151] R.V. Prakash, P. Dhaka, G.V. Prasad Reddy, and R. Sandhya. Understanding the fatigue response of small volume specimens through novel fatigue test methods – experimental results and numerical simulation. *Theoretical and Applied Fracture Mechanics*, 103, 2019.

[152] Q. Wang and W. Zhang. Fatigue life prediction of smooth and circular-hole specimens based on equivalent initial flaw size. In Wang Z. Zhang S., editor, *Proceedings of 2015 the 1st International Conference on Reliability Systems Engineering, ICRSE 2015*. Institute of Electrical and Electronics Engineers Inc., 2015.

[153] D .T. S. Lewis, R. J. Lancaster, S. P. Jeffs, H. W. Illsley, S. J. Davies, and G. J. Baxter. Characterising the fatigue performance of additive materials using the small punch test. *Materials Science and Engineering A*, 754:719–727, 2019.

[154] R.V. Prakash, M. Thomas, A.R. Prakash, and C.K. Mukhopadhyay. Online acoustic emission monitoring of cyclic ball indentation testing - correlation with hysteresis area response. volume 28, pages 1629–1636. Elsevier B.V., 2020.

[155] R. J. Lancaster, S. P. Jeffs, H. W. Illsley, C. Argyrakis, R. C. Hurst, and G. J. Baxter. Development of a novel methodology to study fatigue properties using the small punch test. *Materials Science and Engineering A*, 748:21–29, 2019.

[156] M. Bruchhausen, S. Holmström, I. Simonovski, T. Austin, J.-M. Lapetite, S. Ripplinger, and F. de Haan. Recent developments in small punch testing: Tensile properties and DBTT. *Theoretical and Applied Fracture Mechanics*, 86:2–10, 2016.

[157] C. C. Dyson, W. Sun, C. J. Hyde, S. J. Brett, and T. H. Hyde. Use of small specimen creep data in component life management: a review. *Materials Science and Technology (United Kingdom)*, 32(15):1567–1581, 2016.

[158] T. H. Hyde, C. J. Hyde, and W. Sun. Theoretical basis and practical aspects of small specimen creep testing. *Journal of Strain Analysis for Engineering Design*, 48(2):112–125, 2013.

[159] T. H. Hyde, B. S. M. Ali, and W. Sun. Interpretation of small ring creep test data. *Journal of Strain Analysis for Engineering Design*, 48(4):269–278, 2013.

[160] M. F. Lam Wing Cheong. *Experimental and Numerical Investigations into the Behaviour of a 7175-T7351 Aluminium Alloy for Aerospace Gearbox Housing Applications at Elevated Temperatures*. PhD thesis, University of Nottingham, 2018.

[161] G. E. Lucas. Review of small specimen test techniques for irradiation testing. *Metallurgical Transactions A*, 21(5):1105–1119, 1990.

[162] Smiths Metal Centres Limited. 2014a aluminium technical datasheet. https://www.smithmetal.com/pdf/aluminium/2xxx/2014a.pdf, 2020. Accessed: 2020-07-24.

[163] Smiths Metal Centres Limited. 6082 aluminium technical datasheet. https://www.smithmetal.com/pdf/aluminium/6xxx/6082.pdf, 2020. Accessed: 2020-07-24.

[164] A. A. Saad. *Cyclic plasticity and creep of power plant materials*. PhD thesis, University of Nottingham, 2012.

[165] Hebei Metals Industrial Limited. P91 steel technical datasheet. http://www.metalspiping.com/t91-p91-steel.html#: :text=Designated2020. Accessed: 2020-07-24.

[166] M. C. Murphy. The engineering fatigue properties of wrought copper. *Fatigue & Fracture of Engineering Materials & Structures*, 4(3):199–234, 1981.

[167] J. Polák, K. Obrtlík, M. Hájek, and A. Vašek. Cyclic stress-strain response of polycrystalline copper in a wide range of plastic strain amplitudes. *Materials Science and Engineering: A*, 151(1):19 – 27, 1992.

[168] J. H. You and M. Miskiewicz. Material parameters of copper and CuCrZr alloy for cyclic plasticity at elevated temperatures. *Journal of Nuclear Materials*, 373(1):269 – 274, 2008.

[169] Smiths Metal Centres Limited. C110 technical datasheet. https://www.smithmetal.com/pdf/copper-brass-bronze/copper/c110.pdf, 2020. Accessed: 2020-07-24.

[170] C.J. Hyde, T.H. Hyde, W. Sun, and A.A. Becker. Damage mechanics based predictions of creep crack growth in 316 stainless steel. *Engineering Fracture Mechanics*, 77(12):2385 – 2402, 2010.

[171] J. P. Rouse, Hyde C. J., W. Sun, and T. H. Hyde. Comparison of several optimisation strategies for the determination of material constants in the Chaboche visco-plasticity model. *The Journal of Strain Analysis for Engineering Design*, 48(6):347–363, 2013.

[172] E. Paul (Ernest Paul) DeGarmo. *Materials and processes in manufacturing / E. Paul DeGarmo, J.T. Black, Ronald A. Kohser.* Wiley, New York, 8th ed. edition, 1999.

[173] The Engineering ToolBox. Grit size vs. surface roughness. https://www.engineeringtoolbox.com/grit-size-surface-roughness-d$_2096.html, 2018. Accessed 2021-06-06.$

[174] C. J. Hyde, W. Sun, and S. B. Leen. Cyclic thermo-mechanical material modelling and testing of 316 stainless steel. *International Journal of Pressure Vessels and Piping*, 87(6):365–372, 2010.

[175] E. Kreyszig. *Differential Geometry.* Dover Publications, Inc., New York, USA, 1991.

[176] X. Mao and H. Takahashi. Development of a further-miniaturized specimen of 3 mm diameter for TEM disk (ø 3 mm) small punch tests. *Journal of Nuclear Materials*, 150(1):42–52, 1987.

[177] J. P. Rouse, C. J. Hyde, and J. Kazakeviciute. Investigations into Taylor-Quinney coefficient determination for a 7000 series aluminium alloy using a novel small specimen test technique. *Ubiquity Proceedings*, 1:42, 2018.

[178] J. Woolman and R. A. Mottram. En 24 - per cent nickel-chromium-molybdenum steel. In J. Woolman and R.A. Mottram, editors, *The Mechanical and Physical Properties of the British Standard EN Steels (B.S. 970–1955)*, pages 72 – 110. Pergamon, 1966.

[179] AZO Materials. Super alloy nimonic 101 datasheet. https://www.azom.com/article.aspx?ArticleID=7688, 2012.

[180] F. Hayashi. *Econometrics*. Princeton University Press, New Jersey, USA, 2000.

[181] S. Sharma. *Applied multivariate techniques*. J. Wiley, New York, USA, 1996.

[182] C. R. Alavala. *Fuzzy logic and neural networks [electronic resource] : basic concepts and application*. New Age International P Ltd., Publishers, New Delhi, India, 2008.

[183] A. Benaarbia, J. P. Rouse, and W. Sun. A thermodynamically-based viscoelastic-viscoplastic model for the high temperature cyclic behaviour of 9–12% Cr steels. *International Journal of Plasticity*, 107:100 – 121, 2018.

[184] The British Standards Institution. BS ISO 23788:2012 Metallic materials. Verification of the alignment of fatigue testing machines, 2012.

[185] W. Grzesik. *Advanced Machining Processes of Metallic Materials, 2nd Edition*. Elsevier, 2016.

[186] V. Mathiowetz, N. Kashman, G. Volland, K. Weber, M. Dowe, and S. Rogers. Grip and pinch strength: Normative data for adults. *Archives of physical medicine and rehabilitation*, 66:69–74, 1985.

10 Appendix

10.1 Appendix A — Small Ring Specimen Cyclic Loading Design Drawings

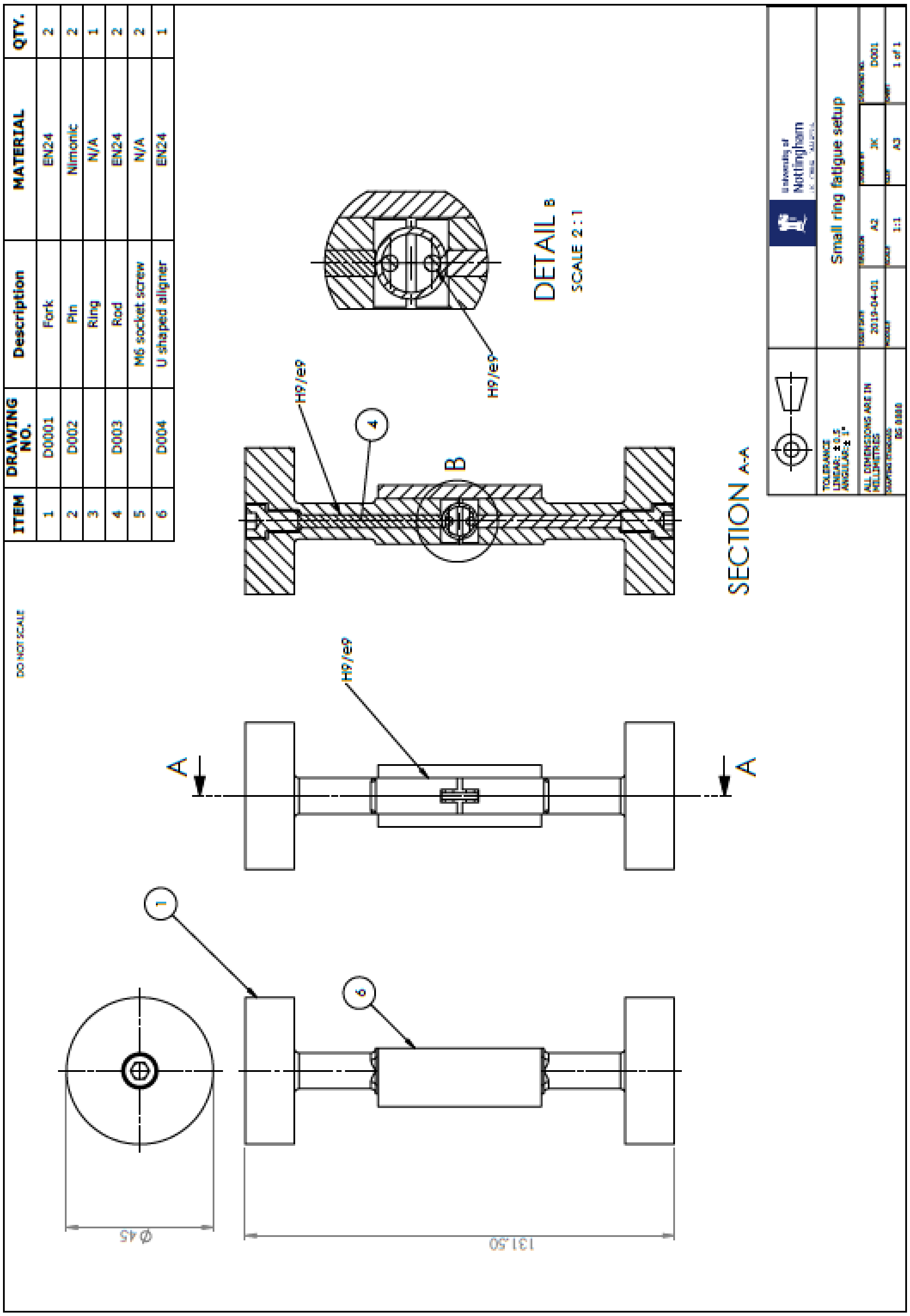

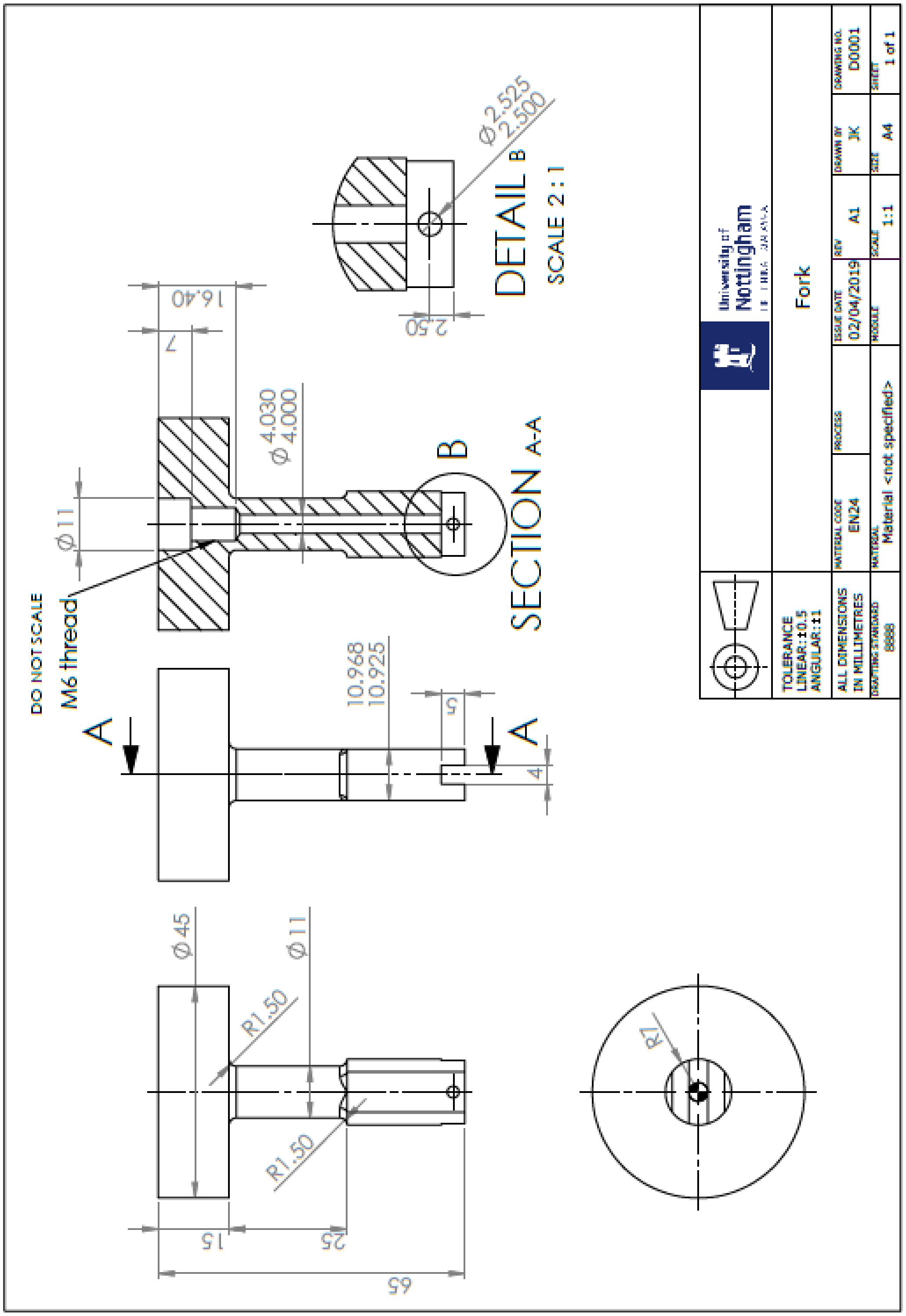
DO NOT SCALE
M6 thread
Ø 11
A
Ø 45
15
R1.50
R1.50
Ø 11
25
65
7
16.40
Ø 4.030
4.000
10.968
10.925
5
4
A
B
SECTION A-A
2.50
Ø 2.525
2.500
DETAIL B
SCALE 2 : 1
R7
University of Nottingham
TOLERANCE
LINEAR: ±0.5
ANGULAR: ±1
Fork
ALL DIMENSIONS IN MILLIMETRES
DRAFTING STANDARD
8888
MATERIAL CODE
EN24
PROCESS
ISSUE DATE
02/04/2019
REV
A1
DRAWN BY
JK
DRAWING NO.
D0001
MATERIAL
Material <not specified>
MODULE
SCALE
1:1
SIZE
A4
SHEET
1 of 1

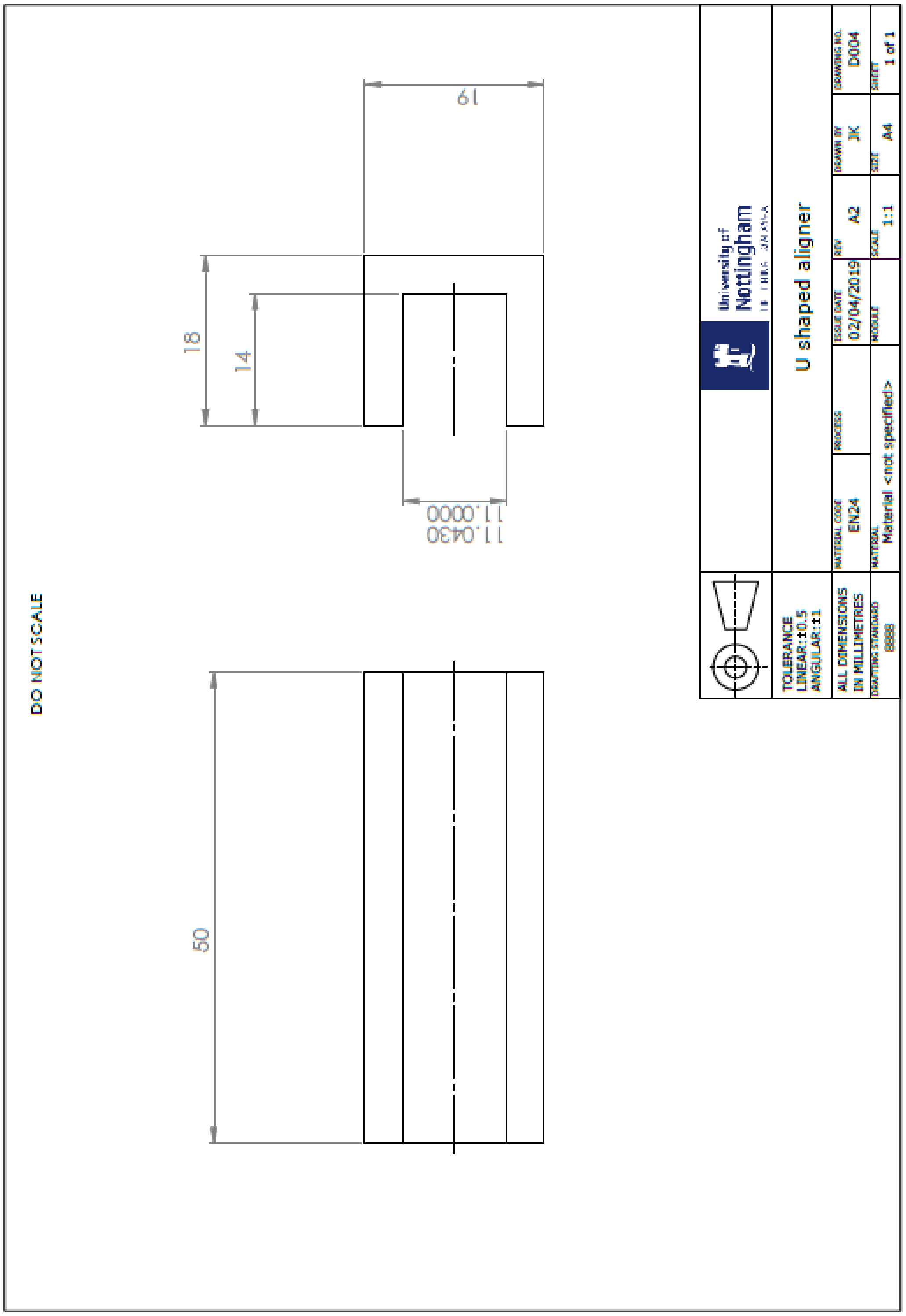
DO NOT SCALE
19
18
14
11.0000
11.0430
50
University of Nottingham
U shaped aligner
TOLERANCE
LINEAR: ±0.5
ANGULAR: ±1
ALL DIMENSIONS IN MILLIMETRES
8888
EN24
Material <not specified>
02/04/2019
A2
JK
D004
1:1
A4
1 of 1

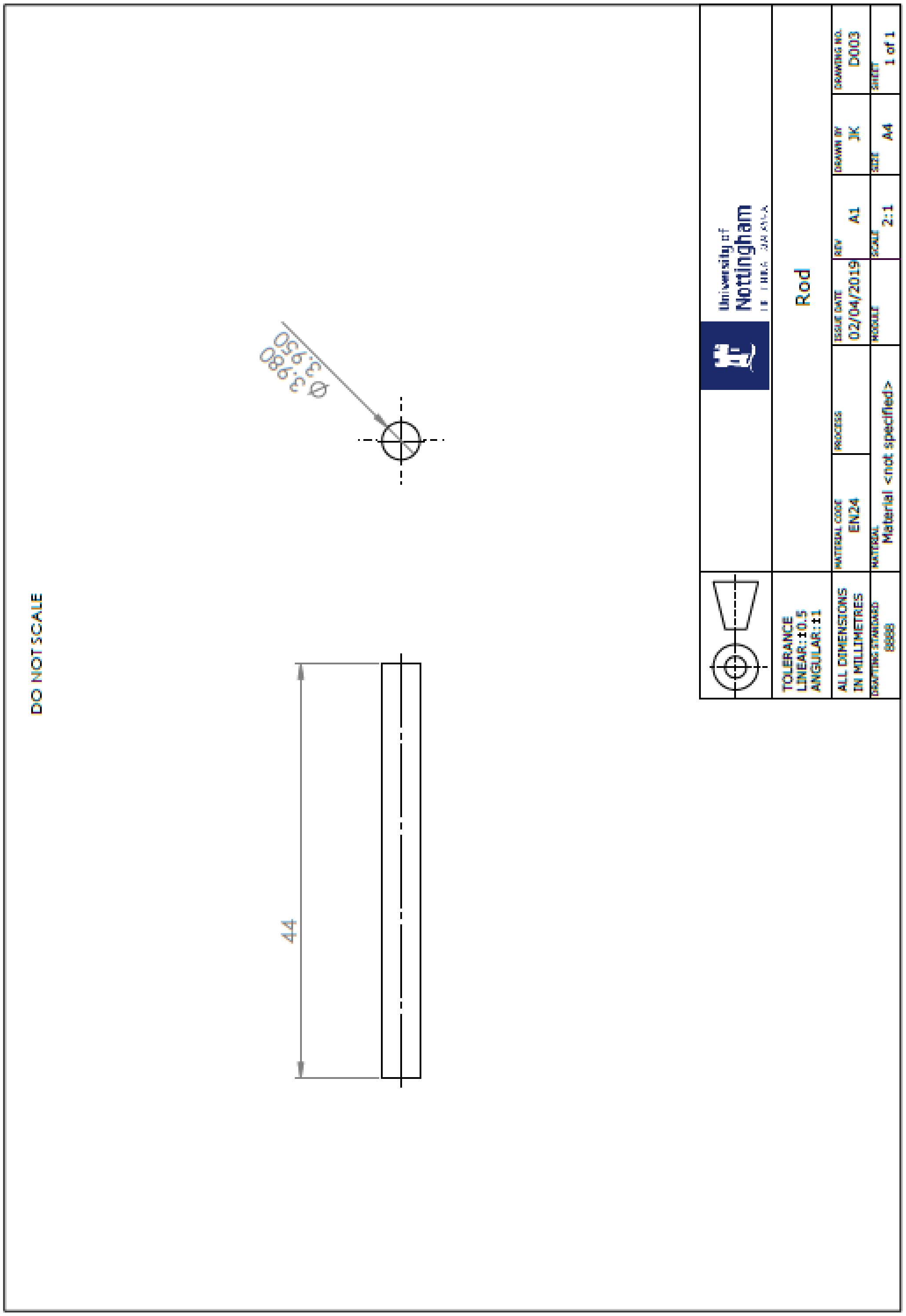
DO NOT SCALE
44
Ø3.980
3.950
University of
Nottingham
Rod
TOLERANCE
LINEAR: ±0.5
ANGULAR: ±1
ALL DIMENSIONS
IN MILLIMETRES
MATERIAL CODE
EN24
PROCESS
MATERIAL
Material <not specified>
ISSUE DATE
02/04/2019
MODULE
REV
A1
SCALE
2:1
DRAWN BY
JK
SIZE
A4
DRAWING NO.
D003
SHEET
1 of 1

10.2 Appendix B — Small Ring Specimen Cyclic Loading Setup

1. Loading arms on the machine with no additional fixtures

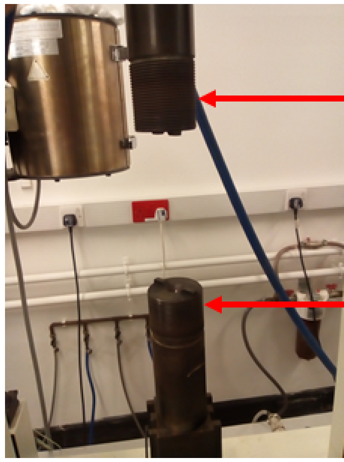

Top loading arm

Bottom loading arm

2. Clamp the bottom fork into the aligner clamp

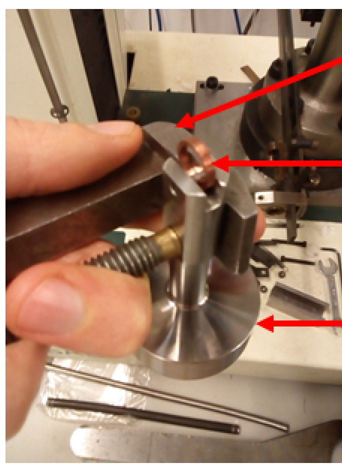

Aligner clamp

Small ring specimen

Bottom fork

3. Put the ring into the groove, insert the pin

4. Turn it over, insert the rod, insert the screw

5. Turn the ring so that it is against the right side of the groove of the fork

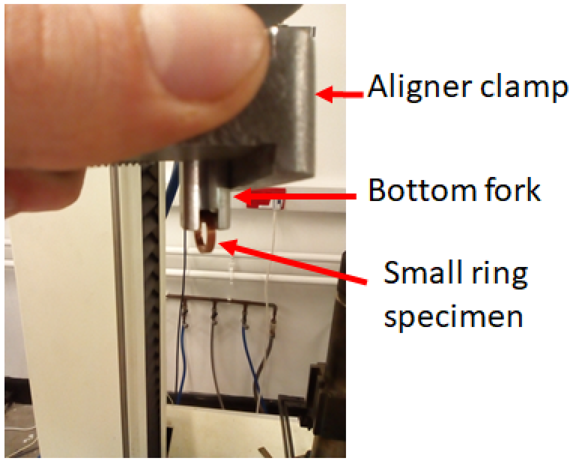

6. Tighten the screw with the torque wrench which aligns the ring towards the middle

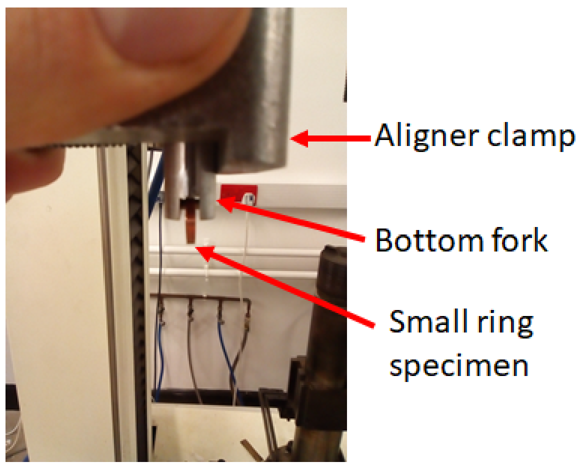

7. Put the bottom fork on the bottom arm of the machine

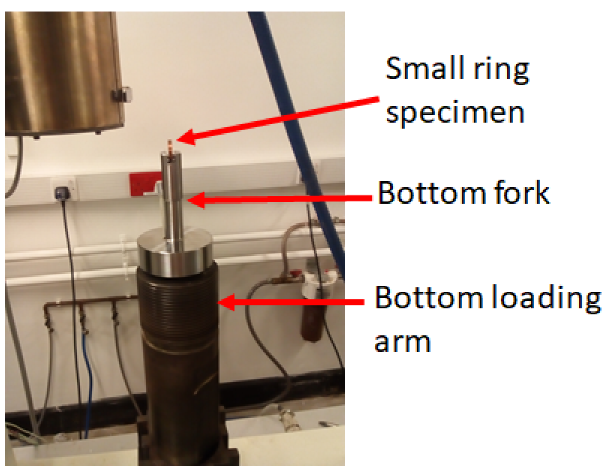

8. Screw on the bottom collar (the taller one), tighten with a bar

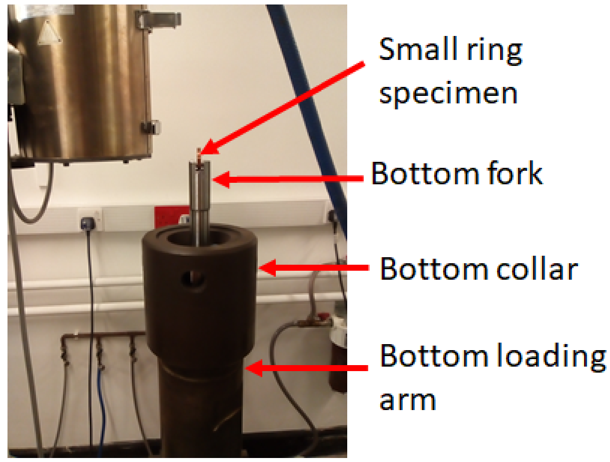

9. Stack the top collar on the bottom collar

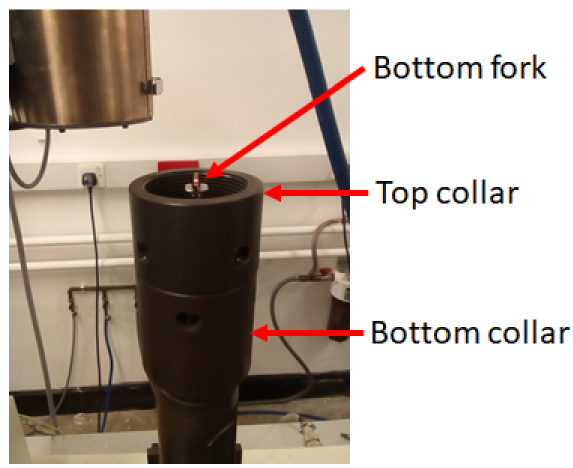

10. Put the top fork above the bottom fork, insert the pin

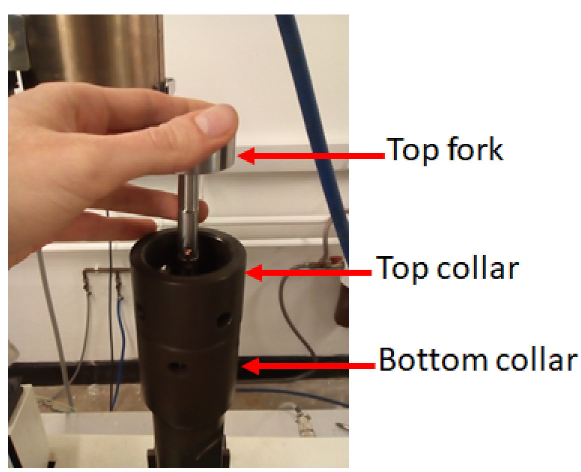

11. Lift the top collar to allow for alignment

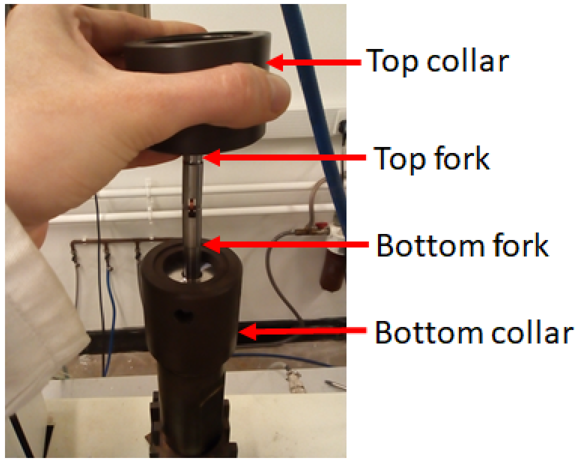

12. Put the U-shaped aligner on

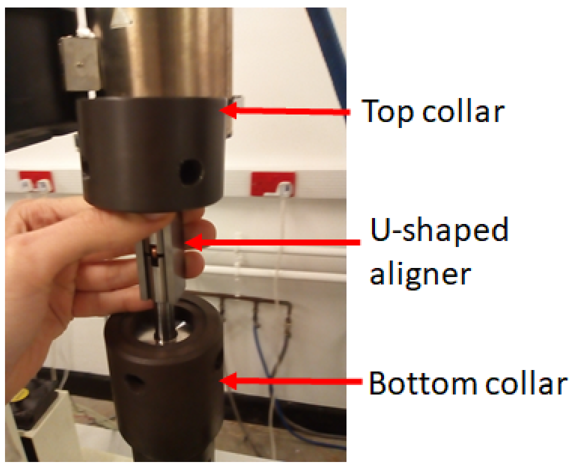

13. Attach the aligner clamp, make sure the top fork cannot move back and forth, as that would introduce misalignment. The collar is now hanging on the aligner clamp

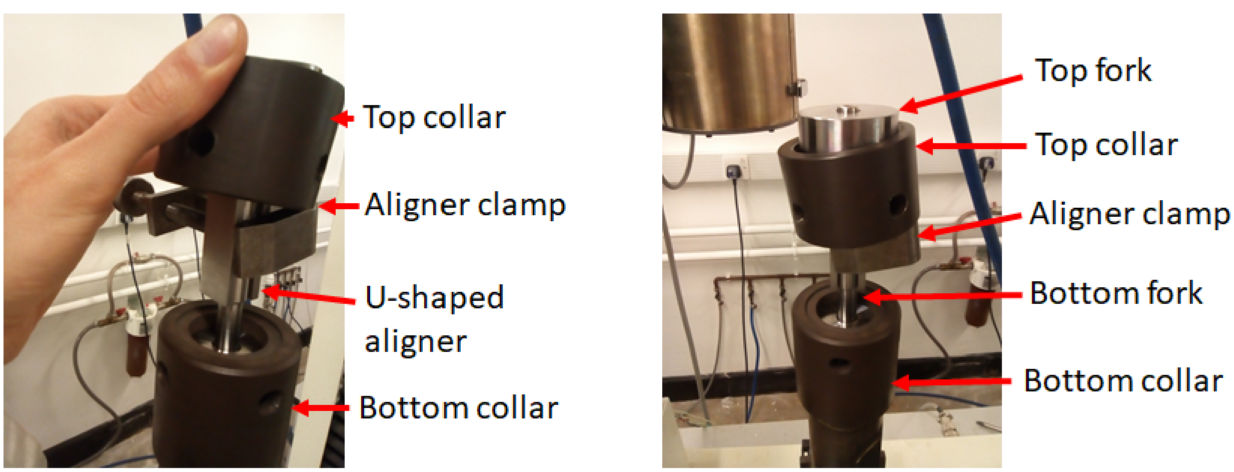

(a) (b)

14. Tighten the top screw with a torque wrench

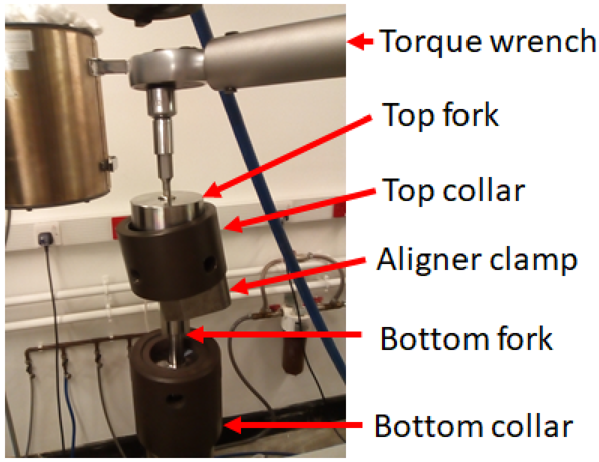

15. Lower the top arm of the machine until a small gap remains. If the setup appears to be offset and the top collar impossible to screw on, loosen the bottom collar and align the setup, then tighten the collar again

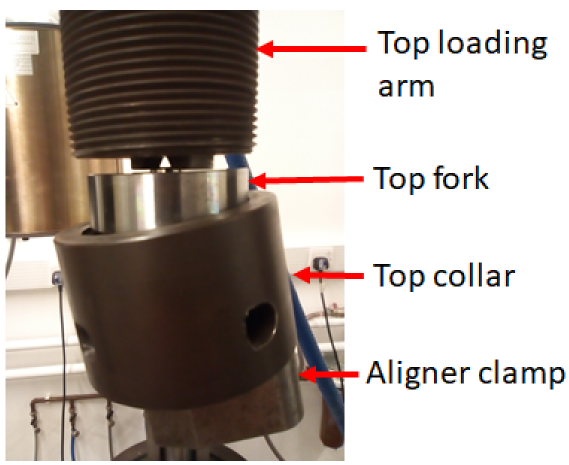

16. Zero the load cell

17. Start the programme (Horizon), which is meant to keep the setup at zero pre-load

18. Start screwing on the top collar by hand

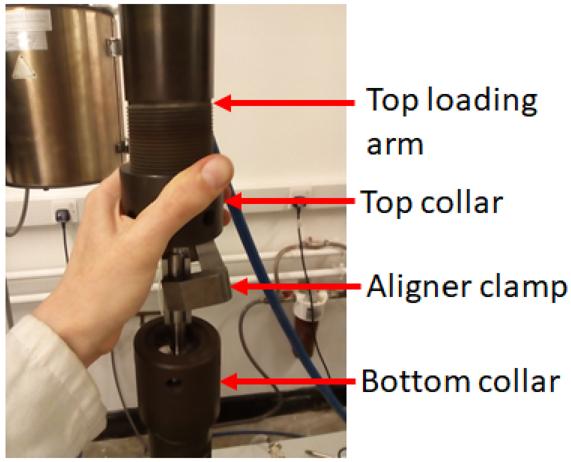

19. When the force readings go up, allow time for the loading arm to go down to get back to zero or near zero force

20. When the collar cannot be tightened any more by hand, tighten with bars

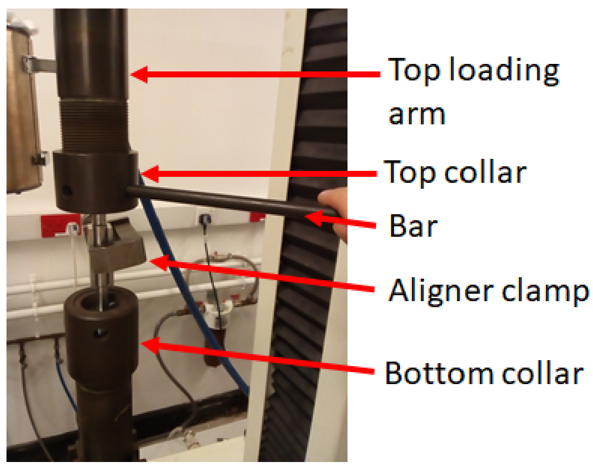

21. Remove the aligner clamp. The U-shaped aligner will likely stay on due to friction and the slight allowable misalignment

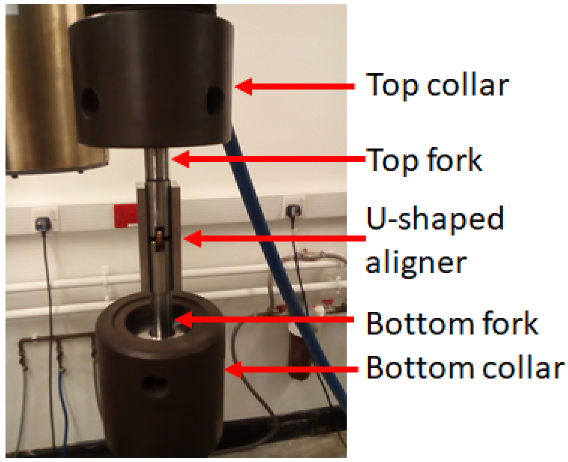

22. Remove the U-shaped aligner carefully

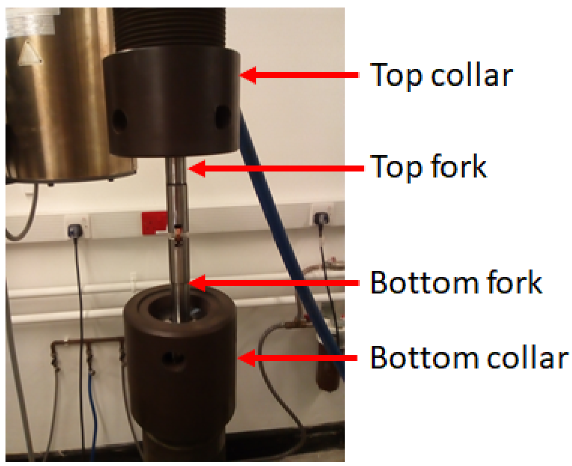

23. Put the LVDT setup on, with slip gauges as shown in the image to keep the spacing consistent for different tests

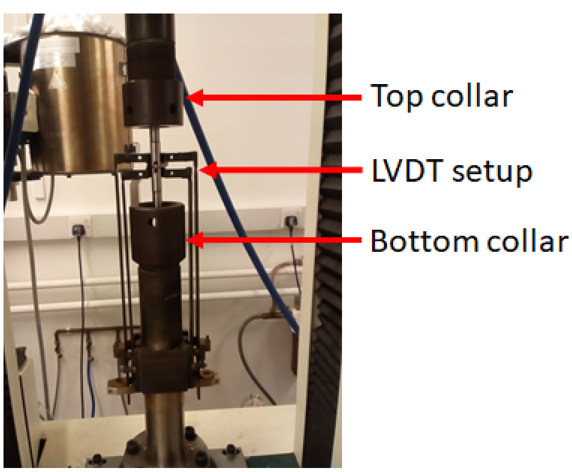

(c)

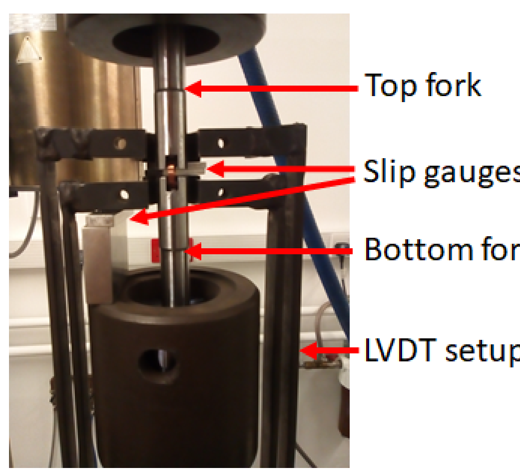

(d)

24. Attach the clamps and tighten the screws

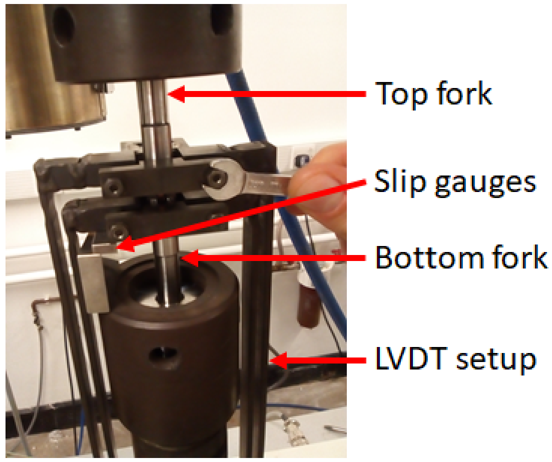

25. Remove the slip gauges

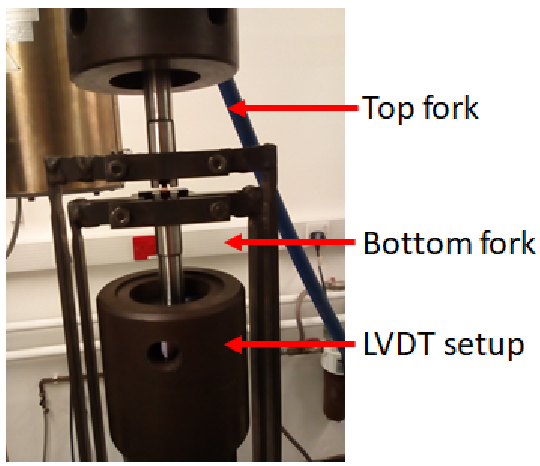

26. Put the springs on the bottom of the LVDT setup

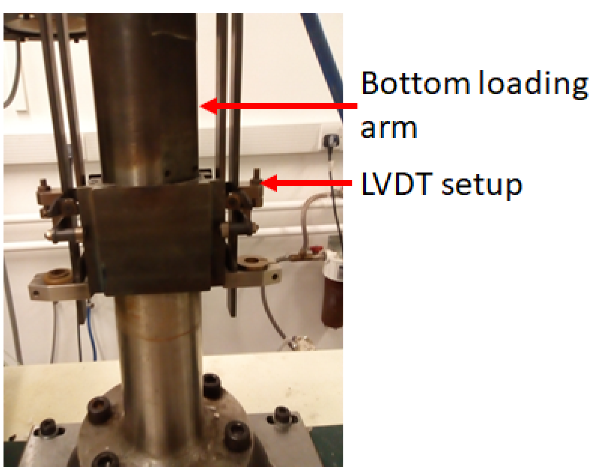

(e)

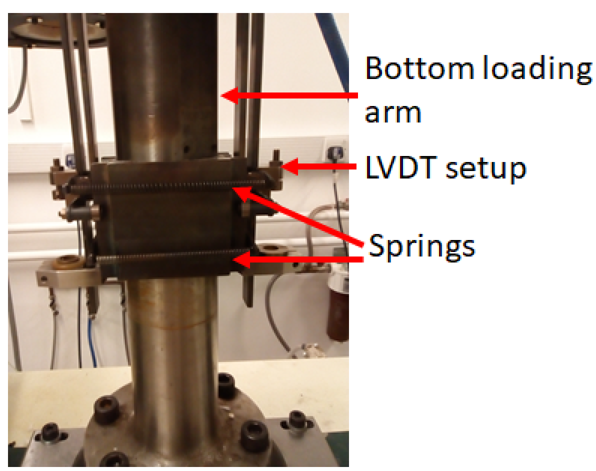

(f)

27. Insert the LVDT and tighten the screw so that the reading is about the middle of the travel length

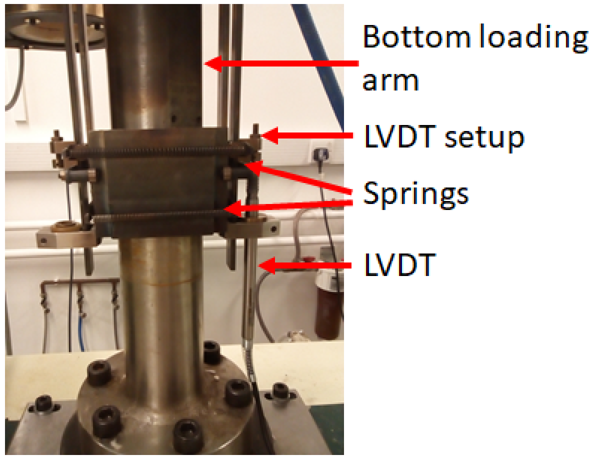

28. Stop the programme (Horizon), as the setup took about 10 minutes to complete and there are a lot of increases in force in the force-time plot due to completing the setup

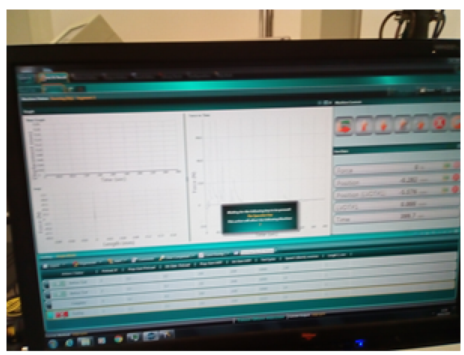

29. Start the programme again, observe carefully for the first cycle to make sure nothing unexpected happens

30. Stop when required

31. Move the loading arm so that the load reading is close to zero or zero if possible

32. Put the U-shaped aligner on and the aligner clamp on

33. Loosen the top collar

34. Move the top loading arm out of the way

35. If either pin can be removed, then remove it to take the setup apart, if not, loosen the top screw and remove the top pin

36. Identify whether the small ring specimen failed at the top clamp or the bottom clamp

37. Loosen the other screw and take the ring out